Investigations of
derivatives of triacetoneamine
for reactive CO_2-absorption

Vom Fachbereich Maschinenbau und Verfahrenstechnik

der RPTU Kaiserslautern-Landau

zur Verleihung des akademischen Grades

Doktor-Ingenieur (Dr.-Ing.)

genehmigte

Dissertation

von

Elmar Kessler

aus Reutlingen

Dekan: Prof. Dr.-Ing. Tilmann Beck
Berichterstatter: Prof. Dr.-Ing. Hans Hasse
                         Prof. Dr.-Ing. Erik von Harbou

Tag der mündlichen Prüfung: 21.04.2023

D 386

Abstract

A new class of amines that are promising solvents for reactive CO_2-absorption processes was thoroughly investigated in a comprehensive experimental study. The amines are all derivatives of triacetoneamine and differ only in the substituent of the triacetoneamine ring structure. These amines are abbreviated by the acronym EvA with a consecutive number that designates the derivatives. About 50 EvAs were considered in the present study, from which 26 were actually synthesized and investigated as aqueous solvents. The investigated properties were: solubility of CO_2, rate of absorption of CO_2, liquid-liquid and solid-liquid equilibrium, speciation (qualitative and quantitative), pK-values, pH-values, foaming behavior, density, dynamic viscosity, vapor pressure, and liquid heat capacity. All 26 EvAs were assessed in an experimental screening. The results were compared with the results of two standard solvents from industry: aqueous solvents of monoethanolamine (MEA) and a solvent blend of methyl-diethanolamine and piperazine (MDEA/PZ). Detailed studies were carried out for two EvAs that revealed significantly improved performance compared to MEA and MDEA/PZ: EvA34 combines favorable properties of MEA and MDEA/PZ in one molecule. EvA25 reveals a liquid-liquid phase split that reduces the solubility of CO_2 in the solvent and shifts the CO_2 into the aqueous phase. This allowed the design of a new CO_2-absorption process, that takes advantage of the liquid-liquid phase split. Finally, the chemical speciation in 16 EvAs was investigated by NMR spectroscopy. From the results, relationships between the chemical structure of the EvAs and the observed speciation, basicity, and application properties were established. This enabled giving guidelines for the design of new amines and proposing new types of amines, which were called ADAMs.

Kurzfassung

Eine neue und vielversprechende Klasse von Aminen für den Einsatz als wässrige Lösungsmittel für die Reaktivabsorption von CO_2 aus gasförmigen Medien wurde in einer experimentellen Studie detailliert untersucht. Die untersuchten Amine sind Derivate des Triacetonamins und unterscheiden sich ausschließlich durch unterschiedliche Substituenten am Triacetonaminring. Abgekürzt wurden die Derivate durch das Akronym EvA mit einer fortlaufenden Nummer, die zur Identifikation des Derivats dient. Insgesamt wurden 50 EvAs in Betracht gezogen, von denen 26 synthetisiert und untersucht wurden. Die untersuchten Eigenschaften der EvA-basierten Lösungsmittel waren: Löslichkeit von CO_2, Absorptionsgeschwindigkeit von CO_2, Flüssig-Flüssig- und Fest-Flüssig-Gleichgewichte, Speziesaufklärung und -verteilung, pK-Werte, pH-Werte, spezifische Wärmekapazität, Schaumbildung, Dichte und dynamische Viskosität, sowie der Dampfdruck. Zunächst wurden die 26 EvAs in einem experimentellen Screening bewertet. Dazu wurden die Ergebnisse der EvAs mit denen von zwei wässrigen Standardlösungsmitteln aus der Industrie verglichen: Lösungsmittel mit Monoethanolamin (MEA) und mit einem Gemisch aus Methyldiethanolamin und Piperazin (MDEA/PZ).

Zwei der EvAs, welche die Ergebnisse von MEA und MDEA/PZ deutlich übertrafen, wurden daraufhin eingehender untersucht: EvA34 vereint die vorteilhaften Eigenschaften von MEA und MDEA/PZ in einem Molekül. EvA25 zeigt eine Flüssig-Flüssig-Phasentrennung, die die Löslichkeit von CO_2 im Lösungsmittel verringert und das CO_2 in die wässrige Phase zwingt. Dies ermöglichte das Design eines neuen Verfahrens zur Absorption von CO_2, welches sich die Flüssig-Flüssig-Phasentrennung zunutze macht. Abschließend wurde die Speziesverteilung in insgesamt 16 EvA-basierten Lösungsmitteln mittels NMR-Spektroskopie untersucht. Anhand der Ergebnisse wurden Zusammenhänge zwischen der chemischen Struktur der EvAs, der auftretenden Speziesverteilung, der Basizität und den daraus folgenden Eigenschaften der EvAs, wie beispielsweise die Löslichkeit von CO_2, abgeleitet. Aus diesen Zusammenhängen konnten Leitlinien für das Design neuer Amine erstellt und auch angewendet werden. Die daraus neu kreierten Amine wurden mit dem Akronym ADAM abgekürzt.

Contents

1 Introduction

Post combustion carbon capture, the CO_2-absorption from flue gas of power plants, is an essential technique to achieve the worlds climate goals [1–4]. Furthermore, The removal of CO_2 from gaseous streams is an important task in many large scale industrial operations. The major applications for CO_2-absorption in industry are the purification of natural gas, refinery gases, or synthesis gas with more than five billion tons of products each year, from which CO_2 has to be removed [5–12]. High requirements have to be met in the purification tasks, e.g., the concentration of CO_2 in the purified gas must often be decreased down to a few ppm. The state-of-the-art process for this purpose is reactive CO_2-absorption, with a reactive solvent that selectively absorbs CO_2 at low temperature in an absorber column, and is regenerated at increased temperature in a desorber column. The choice of the solvent is thereby crucial. Common solvents are aqueous solutions of amines, of which many have been described in the scientific and patent literature [13–23]. The major advantages of aqueous solutions of amines are their high selectivity for absorbing CO_2, as well as their ability to capture high amounts of CO_2 even at very low partial pressures of CO_2. A drawback, however, is the high energy demand that is required for their regeneration [5, 6]. Reducing it is an important goal, both economically and ecologically. One of the most important approach to achieve this goal is the development of improved amine based solvents for reactive CO_2-absorption [24, 25]. Furthermore, the CO_2-absorption process must be adapted to the properties of the solvent and of the purification task [6, 26].

An interesting class of amines for improving the performance of reactive CO_2-absorption processes are derivatives of triacetoneamine. This class of amines was revealed for the first time recently in patents of Evonik [27, 28]. The amines are abbreviated by the acronym EvA with a consecutive number that designates the derivative. The EvAs share the triacetoneamine ring structure but differ in one substituent. About 50 EvAs were considered for the study, from which 26 were actually synthesized and investigated as aqueous solvents. Most of the EvAs were developed and synthesized specifically for being applied as solvents for CO_2-absorption. The chemical structures of the investigated EvAs are shown in Figure 1. The abbreviation of the amines (EvA + number) is used in the present work not only for identifying the amines. For brevity, it is also used for designating aqueous solvents that contain the respective amine. This short-cut notation is used only where the context excludes any confusion with the pure amines.

The present work is a cumulative thesis that summarizes the results of publications on studies of EvAs [29–34] and puts them into context. The results were obtained in a cooperation project with Evonik and thyssenkrupp that was financially supported by the

Federal Ministry of Economic Affairs and Energy of the Federal Republic of Germany (grant no. 03ET1098). The first step was a comprehensive experimental screening of all synthesized EvAs (cf. Section 3). Seven apparatuses were used to study nine properties of the solvents. The properties were chosen such as to characterize the solvents with regard to their industrial application for CO_2-removal: CO_2-loading, rate of absorption of CO_2, pK-values, foaming behavior, solid precipitation, solubility in water, liquid-liquid demixing temperature, density, dynamic viscosity, and CO_2-solubility isotherms. Furthermore, the NoVa short-cut method [35] was used to estimate the energy demand and recirculation rate of two typical purification tasks: the purification of natural gas and of synthesis gas. All results from the screening were compared to corresponding data for two amines that are widely used for CO_2-absorption: monoethanolamine (MEA) and a blend of methyl-diethanolamine and piperazine (MDEA/PZ). From the screening, EvA02, EvA03, EvA25, and EvA34 emerged as the most promising candidates, which surpassed the performance of MEA and MDEA/PZ in many properties. They were investigated more in detail. The results of the detailed studies of EvA25 and EvA34 are shown in the second part of the present work, given in Section 4 and Section 5. The detailed studies for EvA02 and EvA03 are not part of the present work. EvA02 shows solid precipitation even at moderate mass fractions of amine in the unloaded solvent, which makes the solvent unattractive for industrial CO_2-absorption [29]. In contrast, EvA03 has already proven its commercial applicability as constituent of an amine blend [36], which, however, makes its data subject to confidentiality.

In the detailed study of EvA34 (cf. Section 4), a comprehensive set of experimental data of unloaded and CO_2-loaded aqueous solutions of EvA34 was measured and compared to corresponding data for aqueous solutions of MEA and MDEA/PZ. The investigated properties were: CO_2-solubility, loadings of CO_2-containing species, pK-values, pH-values, density, liquid heat capacity, vapor pressure, dynamic viscosity. The comparison revealed that EvA34 combines favorable properties of MEA and MDEA/PZ in one molecule.

In the detailed study of EvA25 (cf. Section 5), the focus was on the phase behavior of the system (EvA25 + H_2O + CO_2). Aqueous solutions of EvA25 show the particularity of a liquid-liquid phase split in a temperature range that is interesting for the design of an adapted CO_2-absorption process. The liquid-liquid phase split occurs above about $t > 60\,°C$. As a consequence, a liquid-liquid phase split can be avoided at low absorption temperatures, whereas at high desorption temperatures, the liquid-liquid phase split occurs. The basic idea is that the occurrence of a new phase leads to an accumulation of CO_2 in only one of the phases and the hope is that a process can be designed in such a way as to make use of this [37–45]. Hence, a comprehensive experimental study was performed for the system (EvA25 + H_2O + CO_2) from which data for the liquid-

liquid (LLE) and vapor-liquid equilibrium (VLE) was obtained. The system (EvA25 + H_2O + CO_2) can also form a solid phase when the temperature is low and the mass fraction of amine in the CO_2-loaded solvent is high. The occurrence of a solid phase is unwanted in the new process design. To be able to avoid solid precipitation, also the solid-liquid equilibrium (SLE) was investigated. The results of the LLE, VLE, and SLE were linked to determine the solid-liquid-liquid-vapor equilibrium (SLLVE) of the system (EvA25 + H_2O + CO_2). This approach yielded an overview of the phase behavior of the system, which, in turn, was the basis for a sound discussion of benefits that could be drawn from the liquid-liquid phase split in the design of advanced CO_2-absorption processes. The phase split leads to a lowering of the overall CO_2-capacity, compared to a homogeneous solvent at desorption. Further improvements seem possible by an adapted process design, for which a concept was proposed.

The investigations of the EvAs are concluded with a study of the relationships between the chemical structure of the amines and properties of the solvents that are relevant for CO_2-absorption processes (cf. Section 6). To tackle this task, several consecutive steps were performed. Initially, the knowledge of the speciation in aqueous solutions of EvAs was extended. Therefore, in total, sixteen CO_2-loaded aqueous solutions of EvAs were investigated by NMR spectroscopy over a wide range of temperature and CO_2-loading. The resulting concentrations of the CO_2-containing species bicarbonate and carbonate, carbamates, alkylcarbonates, and molecular CO_2 were combined with results for the pK-values from Section 3, from which relationships between the chemical structure of the amine and the basicity and speciation of CO_2-containing species were established. That knowledge was then related to application properties that are relevant for a CO_2-absorption process, e.g., CO_2-solubility and rate of absorption of CO_2. From this, guidelines for the design of new amines were derived. Finally, these guidelines were applied and three basic structures as well as several promising derivatives of these compounds, that can be customized with regard to the requirements of the purification task, were designed.

2 Experimental

2.1 Chemicals

The investigated EvAs were provided by Evonik. They were synthesized by reductive amination using a noble metal catalyst [46, 47]. Either 2,2,6,6-tetramethyl-4-piperidone or 2,2,6,6-tetramethyl-4-amino-piperidine, was used as base chemical to which different substituents were added in the synthesis of the EvAs. After hydrogenation at elevated temperature and pressure, the EvAs were purified by vacuum distillation and filtration. The chemical structures of the synthesized EvAs are shown in Figure 1. Greek letters are used to designate the amino groups. The amount of the individual EvAs that were initially synthesized for the screening was between 80 g and 350 g. For the detailed studies, the synthesized amount of the EvAs was in the range of a few kg.

The purified EvAs were analyzed by GC-MS, Karl-Fischer titration and $^{13}C\{^1H\}$ inverse gated NMR spectroscopy. The purities and major impurities are specified in Table 1. Also the molar mass M and the aggregate state of the synthesized EvAs at ambient pressure and 25 °C are reported in Table 1. In most cases purities larger than 0.96 g/g were reached. The major impurities for these EvAs were the educts (2,2,6,6-tetramethyl-4-piperidone, 2,2,6,6-tetramethyl-4-piperidinol, or 2,2,6,6-tetramethyl-4-amino-piperidine, as well as the substituents that were used for the synthesis of the EvAs) and H_2O. For EvA19, EvA22, EvA33, and EvA41, for which the purity was lower than 0.96 g/g, as well as for EvA25 and EvA34, which were part of a the detailed study (cf. Section 4 and Section 5), the major impurities were quantified and are stated in Table 1. EvA29 and EvA30 were obtained in a single synthesis and could not be separated. Therefore only the mixture EvA29/30 was investigated.

Table 2 gives a survey of the chemicals that were used in the present work besides the EvAs. H_2O was purified by ion-exchange and filtration with a Siemens TWF/EI-Ion UV Plus water purification system. All other chemicals were purchased and used without further purification. The presence of impurities is not considered in the estimates of experimental uncertainties.
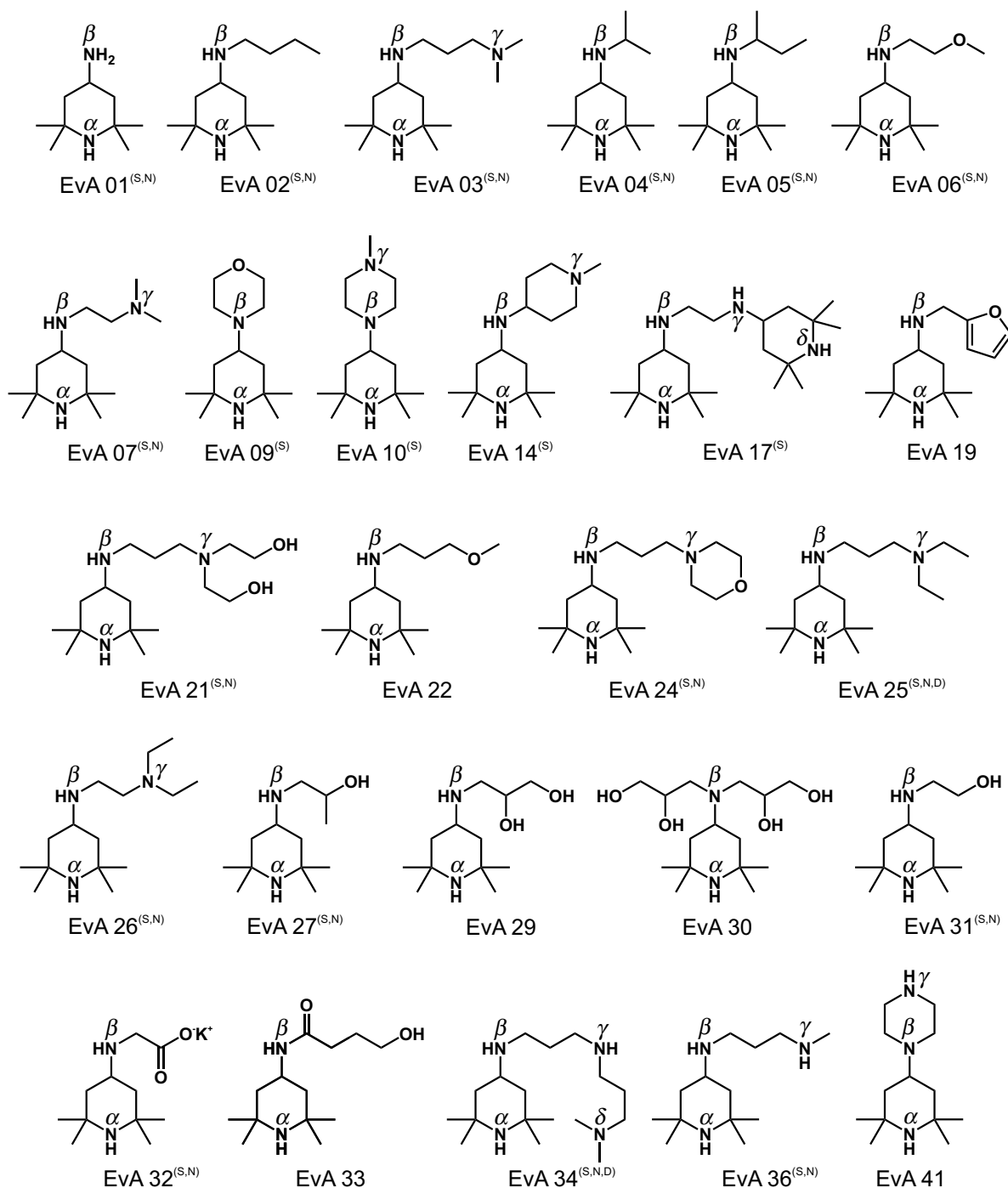
Figure 1: Chemical structures of the EvAs that were studied experimentally in the present work. Greek letters label the different amino groups. [S]EvAs that were taken into account for developing structure-property relationships (cf. Section 6). [N]EvAs for which a species elucidation in CO_2-loaded aqueous solution was performed (cf. Section 6). [D]EvAs for which a detailed study is presented in the present work (cf. Section 4 and Section 5).

Table 1: Properties and purities of the synthesized EvAs.

	M g/mol	AS	purity[a] g/g
EvA01	156.3	liquid	≥ 0.96
EvA02	212.4	liquid	≥ 0.96
EvA03	241.4	liquid	≥ 0.96
EvA04	198.4	liquid	≥ 0.96
EvA05	212.4	liquid	≥ 0.96
EvA06	214.4	liquid	≥ 0.96
EvA07	227.4	liquid	≥ 0.96
EvA09	226.4	solid	≥ 0.96
EvA10	239.4	solid	≥ 0.96
EvA14	253.4	liquid	≥ 0.96
EvA17	338.6	solid	≥ 0.96
EvA19	236.4	liquid	$\geq 0.74^{b}$
EvA21	301.5	solid	≥ 0.96
EvA22	228.4	liquid	$\geq 0.76^{c}$
EvA24	283.5	liquid	≥ 0.96
EvA25	269.4	liquid	$\geq 0.96^{d}$
EvA26	255.4	liquid	≥ 0.96
EvA27	214.4	solid	≥ 0.96
EvA29/30*	230.3 304.4	solid	≥ 0.96
EvA31	200.3	solid	≥ 0.96
EvA32	252.4	solid	≥ 0.96
EvA33	242.4	solid	$\geq 0.84^{e}$
EvA34	298.5	liquid	$\geq 0.97^{f}$
EvA36	227.4	liquid	≥ 0.96
EvA41	225.4	solid	$\geq 0.87^{g}$

M: molar mass, AS: pure component aggregate state at ambient pressure and $t = 25\,°C$, *mixture of EvA29 (0.56 g/g) and EvA30 (0.44 g/g) with $M_{\text{EvA29/30}} = 257.4$ g/mol. ^{a}Impurities in all EvAs are educts and H_2O. Additional impurities are: ^{b}EvA01/triacetoneamine (≤ 0.07 g/g) and furan compounds (≤ 0.15 g/g), ^{c}EvA01/triacetoneamine (≤ 0.08 g/g) and 3-methoxy-propylamine (≤ 0.12 g/g), ^{d}N-ethyl-propylene-triacetonediamine (≤ 0.02 g/g), 2,2,6,6-tetramethyl-4-piperidone or 2,2,6,6-tetramethyl-4-piperidinol (≤ 0.02 g/g) and H_2O (≤ 0.01 g/g), ^{e}EvA01/triacetoneamine (≤ 0.12 g/g), ^{f}2,2,6,6-tetramethyl-4-piperidone or 2,2,6,6-tetramethyl-4-piperidinol (≤ 0.02 g/g) and H_2O (≤ 0.01 g/g), ^{e}piperazine (≤ 0.09 g/g).

Table 2: Chemicals that were used in the present work besides EvAs.

name (CAS)	source	purity
Ethanol (Uvasol) (64-17-5)	Merck	0.999 g/g
H_2O (7732-18-5)	Siemens TWF/EI-Ion UV Plus	0.99999 g/g
CO_2 (124-38-9)	Air Liquide	0.99995 mol/mol
$CO_2/O_2/N_2$ (-) 14/6/80 vol. %	Air Liquide	0.999 mol/mol
MEA (141-43-5)	Sigma-Aldrich	0.99 g/g
MDEA (105-59-9)	Sigma-Aldrich	0.99 g/g
PZ (110-85-0)	Sigma-Aldrich	0.99 g/g
1 M HCl (7647-01-0)	Carl Roth	0.998 mol/mol
1 M NaOH (1310-73-2)	Carl Roth	0.998 mol/mol
KOH (1310-58-3)	Fluka	0.99 g/g
$KHCO_3$ (298-14-6)	Sigma Aldrich	0.995 g/g
KH_2PO_4 (7778-77-0)	Bernd Kraft	0.99 g/g
Na_2HPO_4 (7558-79-4)	Bernd Kraft	0.99 g/g
Titrisol pH-buffer (-)	Merck	not stated by supplier
Reagents for Karl-Fischer titration (-)	Fluka	not stated by supplier

2.2 Specification of the composition

The concentration of the amine in the solvent is specified in three different ways in this work, depending on the context: the molality of amine $\tilde{m}_{\mathrm{amine}}$, the mass fraction of amine in the unloaded solvent $\tilde{w}^0_{\mathrm{amine}}$, and the mass fraction of amine $\tilde{w}_{\mathrm{amine}}$

$$\tilde{m}_{\mathrm{amine}} = \frac{\tilde{W}_{\mathrm{amine}}}{M_{\mathrm{amine}} \cdot \tilde{W}_{\mathrm{H_2O}}} \tag{1}$$

$$\tilde{w}^0_{\mathrm{amine}} = \frac{\tilde{W}_{\mathrm{amine}}}{\tilde{W}_{\mathrm{amine}} + \tilde{W}_{\mathrm{H_2O}}} \tag{2}$$

$$\tilde{w}_{\mathrm{amine}} = \frac{\tilde{W}_{\mathrm{amine}}}{\tilde{W}_{\mathrm{amine}} + \tilde{W}_{\mathrm{H_2O}} + \tilde{W}_{\mathrm{CO_2}}} \tag{3}$$

where $\tilde{W}_{\mathrm{amine}}$ is the overall mass of amine, $\tilde{W}_{\mathrm{H_2O}}$ is the overall mass of H_2O, and $\tilde{W}_{\mathrm{CO_2}}$ is the overall mass of CO_2, where overall means that all reactions in the solvent are disregarded. M_{amine} is the molar mass of amine.

The content of CO_2 in the solvent is characterized in four different ways in this work: the molality of CO_2 $\tilde{m}_{CO_2}$, the mole-related CO_2-loading $\tilde{\alpha}_{CO_2}$, the mass-related CO_2-loading $\tilde{X}_{CO_2}$, and the mass fraction of CO_2 $\tilde{w}_{CO_2}$

$$\tilde{m}_{CO_2} = \frac{\tilde{W}_{CO_2}}{M_{CO_2} \cdot \tilde{W}_{H_2O}} \tag{4}$$

$$\tilde{X}_{CO_2} = \frac{\tilde{W}_{CO_2}}{\tilde{W}_{amine}} \tag{5}$$

$$\tilde{\alpha}_{CO_2} = \tilde{X}_{CO_2} \cdot \frac{M_{amine}}{M_{CO_2}} \tag{6}$$

$$\tilde{w}_{CO_2} = \frac{\tilde{W}_{CO_2}}{\tilde{W}_{amine} + \tilde{W}_{H_2O} + \tilde{W}_{CO_2}} \tag{7}$$

where M_{CO_2} is the molar mass of CO_2. In all symbols that are used to characterize compositions in the present work, the tilde refers to the pure components amine, H_2O, and CO_2 without accounting the chemical reactions in the solvent.

2.3 Sample preparation

2.3.1 Sample preparation for the screening

For the screening of the EvAs (cf. Section 3), the solvents were prepared by mixing amine and H_2O. The amount of amine and H_2O in the unloaded aqueous solvent was determined gravimetrically with an accuracy of ± 1 mg. From this, the resulting mass fraction of the amine in the unloaded solvent $\tilde{w}^0_{amine}$ was known with a relative expanded uncertainty of $U_r(\tilde{w}^0_{amine}) = 0.001$ (0.99 level of confidence). The procedure of the CO_2-loading in the screening experiments is described in the respective experimental sections (cf. Section 2.4).

2.3.2 Sample preparation for detailed studies

For preparing the aqueous solutions of amines for the detailed studies (cf. Sections 4 - 6), firstly, dissolved gases were removed from the pure components H_2O and amine by lowering the pressure with a vacuum pump. The degassed components were mixed while maintaining the low pressure to obtain the aqueous solvent. The amount of

amine and H_2O in the solvent were determined gravimetrically with an accuracy of $\pm$ 1 mg. From this, the molality of amine $\tilde{m}_{\mathrm{amine}}$ is known with a relative expanded uncertainty of $U_r(\tilde{m}_{\mathrm{amine}}) = 0.001$ (0.99 level of confidence). The amount of solvent in the sample was determined by differential weighing in all experiments except for the gas solubility experiments in the high pressure region (cf. Section 2.7.2) and liquid-liquid equilibrium experiments (cf. Section 2.5). In these experiments, the amount of solvent was calculated from the volume that was displaced by a piston pump, the same way as described in previous works of our group [29, 48, 49].

The solvents were loaded with CO_2 by applying CO_2 onto the gas phase of a stainless steel cylinder which was partially filled with a gravimetrically determined amount of the solvent in all experiments except in liquid-liquid equilibrium experiments (cf. Section 2.5) and gas solubility experiments in the high pressure region (cf. Section 2.7.2). In these exceptions, the solvents were loaded with CO_2 inside the apparatus.

The amount of CO_2 was determined by differential weighing in all experiments except in liquid-liquid equilibrium experiments (cf. Section 2.5) and nuclear magnetic resonance (NMR) spectroscopy experiments (cf. Section 2.8.3). The accuracy of the weighing was $\pm$ 1 mg. The resulting relative expanded uncertainty in the molality of CO_2 $\tilde{m}_{\mathrm{CO_2}}$ from weighing was $U_r(\tilde{m}_{\mathrm{CO_2}}) = 0.01$ (0.99 level of confidence). However, for the experiments in which stainless steel cylinders with a riser pipe were used for the CO_2-loading, incomplete mixing may have led to an underestimation of the actual molality of CO_2. More details on this are given in Appendix A. The relative expanded uncertainties stated in the present work account for possible effects from incomplete mixing. They are $U_r(\tilde{m}_{\mathrm{CO_2}}) = 0.025$ (0.99 level of confidence). In liquid-liquid equilibrium experiments (cf. Section 2.5) and NMR spectroscopy experiments (cf. Section 2.8.3), the amount of CO_2 was determined from the $^{13}C\{^1H\}$ inverse gated NMR spectra, as described more in detail in Section 2.8.3.

2.4 Screening methods

2.4.1 Qualitative investigations

2.4.1.1 Solubility of amines in H_2O

The solubility of amines in H_2O was investigated at two mass fractions of amine in the unloaded solvent: $\tilde{w}_{\mathrm{amine}}^0 = 0.05$ g/g and $\tilde{w}_{\mathrm{amine}}^0 = 0.4$ g/g. After mixing the amine with H_2O, the solvent was stirred for 24 hours, and then stored for 7 days at $t = 25$ °C and ambient pressure. If no solids were visible after that period, the amines were classified

as soluble in H_2O. Otherwise they were classified as poorly soluble. Each experiment was performed once.

The expanded uncertainty of the mass fraction of amine in the unloaded solvent $\tilde{w}^0_{\text{amine}}$ was the same as specified in Section 2.3.1. The temperature was controlled by air conditioning. The expanded uncertainty of the temperature measurement t was $U(t) = 1\ ℃$ (0.99 level of confidence). The ambient pressure was $p = 977 \pm 20$ mbar.

2.4.1.2 Foaming behavior

The foaming behavior in the systems (amine + H_2O + CO_2) was assessed by comparing foam heights above 100 g of the aqueous solvents, through which a stream of pure CO_2 with a constant volume flow of $\dot{V} = 100$ Ncm³/min at a pressure of $p_{CO_2} = 1$ bar was bubbled inside a cylinder that had an inner diameter of 3.2 cm. The flow-saturator setup that was used for the investigation was the same as in a previous work of our group [29]. Therefore, no further details on the setup are given here. The mass fraction of amine in the unloaded solvent was $\tilde{w}^0_{\text{amine}} = 0.4$ g/g. The temperature was $t = 40\ ℃$. The foam heights were observed for 4 hours. All solvents reached their equilibrium CO_2-loading within that period. The maximum foam height that was observed for at least 5 minutes during the experiment was recorded and is considered here as the result. An aqueous solution of MEA with the same mass fraction of amine in the unloaded solvent was taken as reference. The foam height of the reference was about 7 cm. The fluctuation within the 5 minutes was about 2 cm. The foam heights of the EvAs are roughly classified as higher, equal, or lower compared to the reference. The volume flow was measured with a calibrated G51 thermal volume flow meter from MKS. The pressure was measured with a calibrated high precision pressure transducer from WIKA. The temperature of the thermostatting bath, that was used for thermostatting the cylinder, was measured with a calibrated Pt100 thermometer. Each experiment was performed once.

The expanded uncertainty of the mass fraction of amine in the unloaded solvent $\tilde{w}^0_{\text{amine}}$ was the same as specified in Section 2.3.1. The expanded uncertainty of the temperature measurement t in the thermostatting bath was $U(t) = 1\ ℃$ (0.99 level of confidence). The standard uncertainty of the partial pressure of CO_2 p_{CO_2} inside the cylinder was $u(p_{CO_2}) = 25$ mbar. The standard uncertainty of the volume flow of CO_2 $\dot{V}$ was $u(\dot{V}) = 10$ Ncm³/min.

2.4.1.3 Solid precipitation

The occurrence of solid precipitation in the systems (amine + H_2O + CO_2) was investigated by visual analysis of samples which were taken while the aqueous solutions of

amines were loaded with CO_2. Two different mass fractions of amines in the unloaded solvent were investigated: $\tilde{w}^0_{\mathrm{amine}} = 0.05$ g/g and $\tilde{w}^0_{\mathrm{amine}} = 0.4$ g/g. The samples with $\tilde{w}^0_{\mathrm{amine}} = 0.05$ g/g were taken during the bubble cell experiments which are described in Section 2.4.2.4. The samples with $\tilde{w}^0_{\mathrm{amine}} = 0.4$ g/g were taken from the flow-saturator experiments that were conducted to investigate the foaming behavior as described in Section 2.4.1.2. All samples were stored in glass vials for 7 days at $t = 25$ ℃. Zeolite chips were added to the samples as crystallization germs. A visual analysis of the samples after 7 days revealed if solid precipitation occurred. If at least one sample of a CO_2-loaded aqueous solution of a given amine revealed solid precipitation, it was classified as solid precipitating. Each experiment was performed once.

The expanded uncertainty of the mass fraction of amine in the unloaded solvent $\tilde{w}^0_{\mathrm{amine}}$ was the same as specified in Section 2.3.1. The temperature t was controlled by air conditioning. The expanded uncertainty of the temperature measurement was $U(t) = 1$ ℃ (0.99 level of confidence). The pressure inside the sample vials was not measured as it has no significant influence on the occurrence of solid precipitation.

2.4.2 Quantitative investigations

2.4.2.1 Density and dynamic viscosity

The density of the unloaded solvents was measured in a calibrated oscillating U-tube densimeter (Anton Paar DMA 4500 M). The dynamic viscosity of the unloaded solvents was measured in a calibrated falling sphere viscosimeter (HAAKE type 800-0197). Both properties were investigated with a mass fraction of amine in the unloaded solvent of $\tilde{w}^0_{\mathrm{amine}} = 0.4$ g/g at $t = 25$ ℃ and ambient pressure. The temperature was measured with a calibrated Pt100 thermometer. Each solvent was measured six times. The arithmetic mean values of the measured density and dynamic viscosity are reported here as the result.

The standard uncertainty of the measured density ρ and dynamic viscosity η was calculated from the standard deviation of the repeated measurements and the standard uncertainty from calibration. The average standard uncertainty of the density was $u(\rho) = 0.01$ g/cm^3. The average standard uncertainty of the dynamic viscosity was $u(\eta) = 2$ mPa·s. The expanded uncertainty of the mass fraction of amine in the unloaded solvent $\tilde{w}^0_{\mathrm{amine}}$ was the same as specified in Section 2.3.1. The expanded uncertainty of the temperature measurement t was $U(t) = 1$ ℃ (0.99 level of confidence). The ambient pressure was $p = 977 \pm 20$ mbar.

2.4.2.2 Demixing temperature

The liquid-liquid demixing temperature of unloaded solvents was investigated by visual analysis of samples that were thermostatted in an oven. The mass fraction of amine in the unloaded solvent was always $\tilde{w}^0_{\text{amine}} = 0.4$ g/g in the experiments. Glass vials that contained about 15 ml of the unloaded solvents were subjected to a temperature program in which, after keeping the temperature constant for 2 hours, the temperature was increased in steps of 5 ℃. A visual analysis of the samples was performed prior to each temperature increase and any occurrence of a liquid-liquid demixing was recorded. The mean temperature between the recorded demixing temperature and the previous temperature, where no demixing was observed, is reported here as the demixing temperature. The temperature inside the oven was measured with a calibrated Pt100 thermometer. Each experiment was performed twice.

The expanded uncertainty of the measured demixing temperature t_{demix} was calculated from the temperature step size and the expanded uncertainty of the temperature measurement and was $U(t_{\text{demix}}) = 2.7$ ℃ (0.99 level of confidence). The expanded uncertainty of the mass fraction of amine in the unloaded solvent $\tilde{w}^0_{\text{amine}}$ was the same as specified in Section 2.3.1. The pressure inside the glass vials was not measured as it has no significant influence on the demixing temperature.

2.4.2.3 pK-values

The molal activity-based pK-values of amines, highly diluted in H_2O, were determined by titration experiments. The equipment and the way the experiments were conducted and evaluated were the same as described in Section 2.8.1. Each experiment was performed once.

The standard uncertainty of the measured pK-value was calculated from the standard deviation of repeated experiments with EvA34 and EvA25 (cf. Section 4 and Section 5) and from calibration and was $u(\text{p}K) = 0.15$ on the pH-scale. The expanded uncertainty of the temperature measurement t was $U(t) = 1$ ℃ (0.99 level of confidence). The experiments were performed at ambient pressure, which was $p = 977 \pm 20$ mbar.

2.4.2.4 Initial rate of absorption and equilibrium CO_2-loading

The initial rate of absorption and equilibrium CO_2-loading were measured in a bubble cell, which is schematically shown in Figure 2. A gas stream of $\dot{V} = 1000$ Ncm³/min, containing 14 vol % CO_2, 6 vol % O_2 and 80 vol % N_2 from a gas cylinder, was bubbled
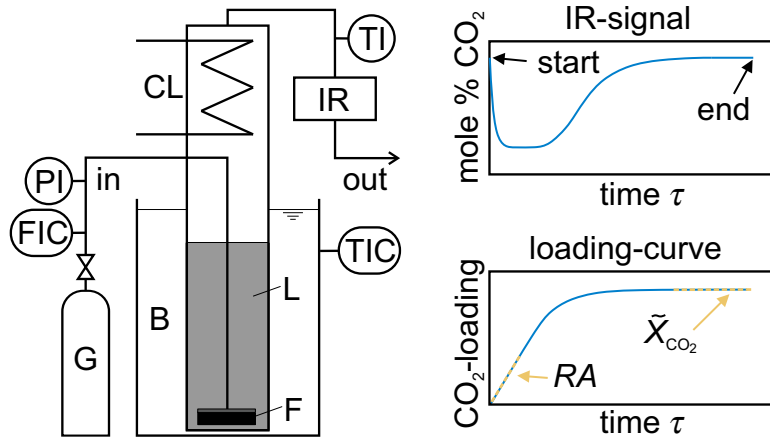
Figure 2: Experimental setup of the bubble cell. G: feed gas, L: aqueous solution of amine, F: dispersion frit, B: thermostatting bath, CL: water-cooled condenser, IR: infrared spectrometer for measuring the CO_2 concentration. The diagrams are explained in the text.

through 150 g of an aqueous solution of amine with $\tilde{w}^0_{amine} = 0.05$ g/g. The total pressure was kept constant at $p = 1$ bar. The aqueous solution of amine was thermostatted by a surrounding bath. The experiments were performed at $t = 40$ ℃ and $t = 100$ ℃. A water-cooled condenser was installed above the bubble cell. The volume flow was measured with a calibrated rotameter from Yokogawa. The pressure was measured with a calibrated pressure transducer from WIKA. The temperature of the thermostatting bath was measured with a calibrated Pt100 thermometer. The mole fraction of CO_2 leaving the bubble cell was measured by a calibrated Ansyco-G100 infrared (IR) spectrometer. A sketch of a typical resulting IR-signal is shown in the upper right part of Figure 2. From the IR-signal, the loading-curve was calculated. A sketch of a loading-curve is shown in the lower right part of Figure 2. The loading-curve was calculated by integrating the amount of CO_2 that was captured in the bubble cell over time. That amount was found from the difference between the inlet and the outlet mole fraction of CO_2 of the bubble cell. N_2 and O_2 were assumed to be inert.

Two results were obtained from the loading-curve: the equilibrium CO_2-loading $\tilde{X}_{CO_2}$ and the initial rate of absorption RA. The equilibrium CO_2-loading $\tilde{X}_{CO_2}$ was calculated by dividing the total amount of CO_2 that was captured in one experiment by the amount of amine in the bubble cell, which was known from sample preparation. The equilibrium CO_2-loading was investigated at $t = 40$ ℃ and $t = 100$ ℃. The initial rate of absorption RA was determined from a linear fit of the initial 16 minutes of the loading curve and was only evaluated at $t = 40$ ℃. Each experiment was performed once.

The experimental setup and procedure was tested with repeated experiments with aqueous solutions of MEA. The relative standard uncertainty of the measured equilibrium CO_2-loading $\tilde{X}_{CO_2}$ was calculated from the standard uncertainty of the IR-calibration

and the standard deviation of the repeated testings with MEA and was $u_r(\tilde{X}_{CO_2}) = 0.05$. This relative standard uncertainty was also taken as an estimate for the relative standard uncertainty of the measured initial rate of absorption RA: $u_r(RA) = 0.05$ and includes variations in the volume flow. The expanded uncertainty of the mass fraction of amine in the unloaded solvent $\tilde{w}^0_{amine}$ was the same as specified in Section 2.3.1. The expanded uncertainty of the temperature measurement t in the thermostatting bath was $U(t) = 1$ ℃ (0.99 level of confidence). The standard uncertainty of the partial pressure of CO_2 p_{CO_2} was $u(p_{CO_2}) = 5$ mbar.

2.4.2.5 CO$_2$-solubility isotherms

The CO_2-solubility in aqueous solutions of amines was measured by head space gas chromatography at $t = 40$ ℃ and $t = 100$ ℃. The equipment and procedure was the same as described in Section 2.7.1 with two exceptions: firstly, each sample was measured only once. Secondly, for the screening, the samples were prepared in stainless steel cells that were directly used in the head space gas chromatography apparatus, instead of the way, described in Section 2.3.2. This procedure simplified and accelerated the measurements with only little expense in the accuracy of the weighing. The amount of solvent and CO_2 was determined by differential weighing.

To obtain the measurement uncertainty of the partial pressure of CO_2 p_{CO_2}, the results from the screening for the system (EvA34 + H_2O + CO_2) were compared to the corresponding data from the detailed study (cf. Section 4). The results are in good agreement. The relative standard uncertainty of the measured partial pressure of CO_2 was calculated from the standard deviation of the comparison and the standard uncertainty of the calibration and was $u_r(p_{CO_2}) = 0.08$. The expanded uncertainty of the mass fraction of amine in the unloaded solvent $\tilde{w}^0_{amine}$ was the same as specified in Section 2.3.1. The accuracy of the weighing of CO_2 was ± 1 mg. The resulting relative expanded uncertainty of the CO_2-loading $\tilde{X}_{CO_2}$ was $U_r(\tilde{X}_{CO_2}) = 0.01$ (0.99 level of confidence). The expanded uncertainty of the temperature measurement t in the thermostatting bath was $U(t) = 0.1$ ℃ (0.99 level of confidence).

2.5 Liquid-liquid equilibrium

Liquid-liquid equilibria (LLE) were measured only in the system (EvA25 + H_2O) and (EvA25 + H_2O + CO_2) (cf. Section 5). The LLE were studied in an apparatus that was especially built for this purpose, inspired by previous related work [50, 51]. The experimental setup is shown in Figure 3. The key unit is a thermostatted high-pressure
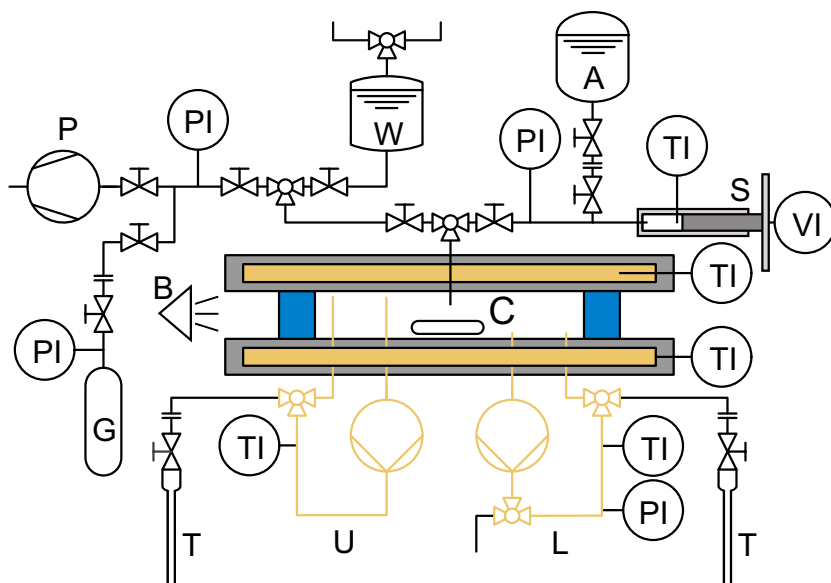
Figure 3: Experimental setup for measurements of liquid-liquid equilibria. A: Aqueous solution of EvA25, B: back-light and sapphire windows to look inside the cell, C: view cell and magnetic stir bar, G: CO_2 cylinder, L: lower circulation loop, P: vacuum pump, S: piston pump, T: sample tubes, U: upper circulation loop, W: H_2O and/or washing solution. Yellow color marks thermostatisation.

view cell (C), in which the LLE is established. The phases can be observed through sapphire windows (B). The cell is equipped with two thermostatted sampling loops (U, L), from which samples of the two liquid phases can be taken for analysis. The entire cell can be rotated, which facilitates suitable positioning of the inlet and outlet of the sampling loops in the phases. The samples circulate in the loops, driven by gear pumps. Three-way valves in the loops were used to withdraw the samples, which were collected in pressure-resistant NMR tubes (S-5-400-MW-IPV-7 from Norell or 522-QPV-7 / 524-QPV-7 from Wilmad-LabGlass) (T).

The cell was cleaned with a washing solution (W), emptied via the lower circulation loop (L), and evacuated with a vacuum pump (P) before each initial filling. The initial filling was performed the same way as in the high pressure view cell experiments [29, 31, 48, 49]: CO_2 was added from a CO_2 cylinder (G), the aqueous solution of EvA25 (A) was added from the piston pump (S). To avoid exceedingly high pressures in the apparatus, the amount was chosen such that a tiny gas bubble was present in the cell at all times. This was done manually by adjusting the amount of liquid in the cell with the piston pump. The gas bubble's only purpose was to avoid a leakage of the system as a result of a pressure increase caused by thermal expansion of the liquid. The gas bubble worked as a pressure buffer and had no influence on the measured liquid-liquid equilibrium. After setting the temperature, the mixture was stirred for 12 hours by means of a magnetic stir bar placed in the cell. Then, the stir bar was switched off and the mixture rested for another 80 hours before the samples were taken. The pumps were running at all times.

The samples from both loops were taken at the same time by simultaneously switching both sample valves from loop position to sample position for a few seconds. After the experiment was finished, the temperature of the cell was set to a new point and a new experiment was started. After taking samples at three to four temperatures, the cell was refilled.

The temperature was measured with two calibrated platinum resistance thermometers in the thermostatting liquid surrounding the cell. The CO_2-loading was measured with $^{13}C\{^1H\}$ inverse gated NMR spectroscopy. The NMR experiments were performed at $t = 20$ ℃ to ensure that the amount of CO_2 in the gas phase of the NMR tubes was negligible. More details on the $^{13}C\{^1H\}$ NMR acquisition parameters are given in the Section 2.8.3. The mass fraction of H_2O was determined with standard ^1H NMR spectroscopy, by comparing the integral of the water peak to that of all peaks that belong to EvA25. More details on the ^1H NMR acquisition parameters are given in the Appendix A. Due to uncertainties resulting from overlapping peaks at mass fractions of EvA25 in samples with $\tilde{w}_{EvA} \geq 0.65$ g/g, the mass fraction of H_2O in these samples was determined by Karl-Fischer titration. The amount of EvA25 was calculated from the mass fraction of H_2O $\tilde{w}_{H_2O}$ and the CO_2-loading $\tilde{X}_{CO_2}$. The pressure inside the apparatus was measured with a calibrated high precision pressure transducer from WIKA in the lower loop. Due to the running gear pumps, small diameters of the loop-tubes, and high viscosity of the CO_2-loaded solvent (cf. Appendix C), the accuracy of that measurement was, however, far below that of the VLE experiments (cf. Section 2.7), so that the pressure reading was only used to ensure that no exceedingly high pressures in the cell occurred during the experiments. As expected, the pressure was always in the range of the bubble point pressure of the solution, which was known from the VLE experiments (cf. Section 2.7). Due to the poor quality of that measurement, the measured pressures of the LLE experiments are not reported in the present work.

Each of the LLE experiments in the system (EvA25 + H_2O) was repeated three to five times. The arithmetic mean value is reported here as the result. The standard uncertainty of the mass fraction of H_2O $\tilde{w}_{H_2O}$ was calculated from the standard deviation of the repeated measurements and the standard uncertainty of a previously performed calibration with weighed samples. The standard uncertainty resulting from calibration was $u(\tilde{w}_{H_2O}) = 0.021$ g/g for samples which were measured with Karl-Fischer titration and $u(\tilde{w}_{H_2O}) = 0.010$ g/g for samples which were measured by ^1H NMR spectroscopy.

Experiments in the system (EvA25 + H_2O + CO_2) were performed only once. The standard uncertainty of the mass fraction of H_2O $\tilde{w}_{H_2O}$ resulting from calibration was taken as the standard uncertainty of the mass fraction of H_2O in the samples (see above). The standard uncertainty of the mass fraction of CO_2 $\tilde{w}_{CO_2}$ was calculated from the standard uncertainty of the $^{13}C\{^1H\}$ inverse gated NMR experiments (cf.

Section 2.8.3) and the standard uncertainty of a previously performed calibration. The standard uncertainty from calibration was $u(\tilde{w}_{CO_2}) = 0.014$ g/g and results mainly from sample taking and handling. The expanded uncertainty of the temperature measurement t was $U(t) = 0.1$ ℃ (0.99 level of confidence). The pressure inside the cell was not recorded (see text above) as it has no significant influence on the composition in the liquid phases.

2.6 Solid-liquid equilibrium

Solid-liquid equilibria (SLE) were measured only in the system (EvA25 + H_2O + CO_2) (cf. Section 5). In the screening (cf. Section 3), EvA25 showed solid precipitation in a composition and temperature region, where CO_2-absorption processes are usually operated. Solid precipitation is not desired in the CO_2-absorption processes that are discussed in Section 5. To avoid solid precipitation, the phase boundaries for solid precipitation must be known. This was done by measuring the liquidus temperature of CO_2-loaded aqueous solutions of EvA25. The determination of the composition in the solids was not in the scope of the present work.

The liquidus temperature was determined starting from low temperatures, where solids were present, by stepwise heating up the samples and observing the disappearance of the solids. First, samples of the CO_2-loaded solvents were filled into 10 ml glass vials and frozen at -25 ℃. The frozen samples were then put in a thermostatted water bath which was initially thermostatted at $t = 10$ ℃. The bath temperature was then increased in steps of 2 ℃ every three and a half days. This time period was sufficient to ensure the establishment of the equilibrium. Before increasing the temperature, the samples were visually inspected for solids. If no solids were found, the arithmetic mean of the last two temperatures (the last one, for which solids were found and the present one, where the solids had disappeared) was taken as the liquidus temperature. The temperature of the thermostatting bath was measured with a calibrated Pt100 thermometer. Each sample was measured at least two times. The arithmetic mean value of the measured liquidus temperatures is reported here as the result.

The standard uncertainty of the liquidus temperature t_{freeze} was calculated from the standard deviation of the repeated measurements, half the step size of the temperature increase, and the standard uncertainty from temperature calibration. The average standard uncertainty of the liquidus temperature was $u(t_{freeze}) = 2.8$ ℃. The expanded uncertainty of the liquid composition is the same as specified in Section 2.3.2. The pressure inside the vials was not measured as it has no significant influence on the measured liquidus temperature.

2.7 Gas solubility

2.7.1 Head space gas chromatography

The partial pressure of CO_2 in the gas phase above CO_2-loaded aqueous solutions of amines was measured with head space gas chromatography for pressures $p_{CO_2} < 1$ bar. The equipment and the experimental procedure were the same as employed in previous works of our group [29, 48, 49] and are therefore not described here in detail. The composition of the liquid phase was known from sample preparation and the partial pressure of CO_2 was determined by gas chromatography. The gas chromatograph (Agilent, type 6890) was equipped with a capillary column (J&M Scientific, type GS-Q, 30 m, 0.32 mm i.d.) and a thermal conductivity detector. For calibration, the sample cells were filled with pure CO_2 at a pressure ranging from 20 mbar $\leq p_{CO_2} \leq$ 900 mbar. The calibration was performed before and after each change of temperature. The temperature was measured with calibrated platinum resistance thermometer in the thermostatting liquid surrounding the cells. At least four sample cells were prepared and studied in the same way (exceptions were made for the screening (cf. Section 2.4)). The arithmetic mean values of the measured partial pressures of CO_2 are reported here as the result.

The standard uncertainty of the measured partial pressure of CO_2 p_{CO_2} was calculated from the standard deviation of the repeated measurements and the standard uncertainty from calibration. The average relative standard uncertainty of the measured partial pressure of CO_2 was $u_r(p_{CO_2}) = 0.025$. The expanded uncertainty of the liquid composition was the same as specified in Section 2.3.2. The expanded uncertainty of the temperature measurement t was $U(t) = 0.1$ ℃ (0.99 level of confidence).

2.7.2 High pressure view cell

A thermostatted high pressure view cell was used to determine the bubble point pressure of CO_2-loaded aqueous solutions of amines for pressures between 1 bar $\leq p \leq$ 100 bar. The equipment and the experimental procedure were the same as in previous works of our group [29, 48, 49] and are therefore not described here in detail. The bubble point pressure was measured with calibrated high precision pressure transducers from WIKA. The view cell's temperature was measured with calibrated platinum resistance thermometer in the thermostatting liquid surrounding the view cell. Each experiment was repeated three times. The arithmetic mean values of the measured bubble point pressures are reported here as the result.

The standard uncertainty of the measured bubble point pressure p was calculated from the standard deviation of the repeated measurements and the standard uncertainty from

calibration. The average relative standard uncertainty of the bubble point pressure was $u_r(p) = 0.005$. The expanded uncertainty of the molality of amines $\tilde{m}_{\text{amine}}$ was the same as specified in Section 2.3.2. CO_2 was added separately into the cell. The amount of CO_2 was known from weighing with an accuracy of $\pm$ 1 mg. The resulting relative expanded uncertainty of the molality of CO_2 $\tilde{m}_{CO_2}$ was $U_r(\tilde{m}_{CO_2}) = 0.001$ (0.99 level of confidence). The expanded uncertainty of the temperature measurement t was $U(t) = 0.1$ ℃ (0.99 level of confidence).

2.8 Chemical equilibrium

2.8.1 Titration

The molal activity-based pK-values of the amines, highly diluted in H_2O, were determined by titration experiments. The titration experiments were performed with a Metrohm Ti-Touch 916 Titrino, equipped with a Dosino 800. In the experiments, amine, H_2O, and 1M HCl were mixed in a double jacket thermostatted and stirred vessel. After reaching the desired temperature, 1M NaOH was titrated to the mixture. The pH-value was measured with a Metrohm LL Unitrode. The pH-electrode also contained a calibrated Pt1000 that was used for the temperature measurement. The pH-electrode was calibrated with five buffer solutions at pH = 2, 6, 8, 10, and 12 before and after each temperature change. Each experiment was performed twice (except for the screening, where the experiments were performed only once (cf. Section 2.4)). The arithmetic mean values of the obtained molal activity based pK-values are reported here as the result.

The standard uncertainty of the measured pK-value was calculated from the standard deviation of the repeated measurements and the standard uncertainty from calibration. The average standard uncertainty of the measured pK-values was $u(\text{p}K) = 0.13$ on the molal activity based pH-scale. The expanded uncertainty of the temperature measurement t was $U(t) = 0.1$ ℃ (0.99 level of confidence). All titrations were performed at ambient pressure, which was $p = 977 \pm 20$ mbar.

2.8.2 pH-meter

The pH-value of unloaded and CO_2-loaded aqueous solutions of amines was measured with a Mettler Toledo HA405-DXK-S8 pH-electrode connected to a Mettler Toledo Five Easy FE20 pH/mV bench meter. The pH-electrode was screwed into a pressure-resistant and hermetically closed stainless steel vial containing the sample. The vial was placed

into an oil bath and thermostatted by the surrounding oil. The temperature of the oil bath was measured by a calibrated digital probe thermometer from TFA Dostmann (TFA 30.1021). For an experiment with unloaded solvents, the temperature was first kept at $t = 25$ ℃ for 15 minutes. Then the temperature was increased to $t = 40$ ℃ for 30 minutes, followed by $t = 80$ ℃ and $t = 120$ ℃ for 40 minutes each. For CO_2-loaded solvents, the periods were: 20 minutes at $t = 20$ ℃ and 120 minutes at $t = 60$ ℃ and $t = 100$ ℃ respectively. These timings ensured that, at each temperature, the thermal and chemical equilibrium was reached. The pH-electrode was calibrated with 0.01 M HCl, 0.01 M KOH, 0.1 M KOH, and KH_2PO_4-Na_2HPO_4 [52] reference mixtures using the same measurement procedure as described above. The molal activity based pH-value of the reference mixtures was calculated using Pitzer's extended Debye-Hückel law [53]. Each experiment with unloaded solvents was performed three times. The experiments with CO_2-loaded solvents were performed twice. The arithmetic mean values of the measured molal activity based pH-values are reported here as the result.

The standard uncertainty of the measured pH-value was calculated from the standard deviation of the repeated measurements and the standard uncertainty from calibration. The average standard uncertainty of the measured pH-values was $u(pH) = 0.14$ on the molal activity based pH-scale. The expanded uncertainty of the composition was the same as specified in Section 2.3.2. The expanded uncertainty of the temperature measurement t was $U(t) = 0.1$ ℃ (0.99 level of confidence). The pressure inside the vials was not measured as it has no significant influence on the measured pH-value.

2.8.3 NMR spectroscopy

NMR spectroscopy was used for the elucidation and quantification of the speciation in the CO_2-loaded aqueous solutions of amines. The measurements were carried out with a Bruker Ascend 400 MHz spectrometer equipped with an Avance 3 HD 400 console and either CPPBBO or PABBO 5 mm probe heads. All samples were analyzed in pressure-resistant valved NMR tubes (S-5-400-MW-IPV-7 by Norell and 522-QPV-7 / 524-QPV-7 by Wilmad-LabGlass). The filling level inside the tubes was kept below 6 cm to ensure homogeneous thermostatisation of the liquid phase inside the NMR tube. The temperature of the samples was controlled by a thermostatted nitrogen gas flow in the NMR spectrometer. The temperature was calibrated by using the temperature dependent ^{1}H shift of methanol (25 ℃ ≤ t ≤ 60 ℃) and ethylene glycol (80 ℃ ≤ t ≤ 120 ℃) [54]. To reach chemical equilibrium, the samples were thermostatted for 4 hours in an oven before they were analyzed in the NMR spectrometer.

For the elucidation, ^{1}H, ^{13}C{^{1}H} inverse gated, and two-dimensional ^{1}H-^{13}C heteronuclear single quantum coherence (HSQC), ^{1}H-^{13}C heteronuclear multiple bond correlation

(HMBC), and 135° distortionless enhanced polarization transfer ^{13}C (DEPT135) measurements were used.

For the quantification of the CO_2-containing species, ^{13}C{^{1}H} inverse gated NMR spectra (decoupling sequence: waltz16, flip angle: between 30° and 90°, relaxation delay: 60 s to 90 s (depending on the flip angle), acquired size of FID: 128k - 256k, sweep width: 220 ppm, excitation frequency offset: 100 ppm, acquisition time: 2.97 s to 6.5 s, 128 to 1024 scans per spectra) were applied. The T_1 relaxation time was measured by inversion recovery with power gated proton decoupling and was $T_1 \leq 8$ s for a 90° flip angle for all studied systems. The recorded spectra were post-processed manually (zero filling, line broadening, phase correction, and either Whittaker-Smoother or polynomial baseline correction). The peak areas were determined by direct integration.

The concentration of the CO_2-containing species $\tilde{\alpha}_i$ were obtained by comparing the peak integrals of the different CO_2-containing species i in relation to the total peak integrals of all amine signals and are thus obtained in moles of the species per moles of all amine-species in the mixture.

In the symbols that are used to specify the concentration in the present work, the tilde refers to the measured amount of the species and include all protonated forms of the species. The sum of the concentration of all CO_2-containing species was taken as the total CO_2-loading as shown in Equation (8). The measurements as described above were carried out at different temperatures with each sample.

$$\tilde{\alpha}_{CO_2} = \sum_i \tilde{\alpha}_i \tag{8}$$

The values listed in Table 3 were taken to describe the standard uncertainty of the measured concentrations of CO_2-containing species $\tilde{\alpha}_i$. They result mainly from uncertainties in the post-processing and peak integration and stem from comparisons between the measured sums of all CO_2-containing species with their initial weighed amounts. The expanded uncertainty of the composition of the solvent was the same as specified in Section 2.3.2. The expanded uncertainty of the temperature measurement t was $U(t) = 0.1$ ℃ (0.99 level of confidence). The pressure inside the NMR tubes was not measured as it has no significant influence on the measured concentrations of CO_2-containing species.

Table 3: Standard uncertainty of the quantitative NMR investigation. $\tilde{w}^0_{\text{amine}}$: mass fraction of amine in the unloaded solvent, $\tilde{\alpha}_i$: concentration of CO_2-containing species, t: temperature, u: standard uncertainty, u_r: relative standard uncertainty.

$\tilde{w}^0_{\text{amine}}$	t	$u_r(\tilde{\alpha}_i)$; $u(\tilde{\alpha}_i)$
g/g	°C	- ; mol/mol
0.1	20 - 69	max{ 0.05 ; 0.03 }
0.4	20 - 69	max{ 0.03 ; 0.02 }
0.1 & 0.4	≥ 70	max{ 0.08 ; 0.05 }

2.9 Liquid heat capacity

The liquid heat capacity of pure amine and its mixtures with H_2O was measured in a differential scanning calorimeter (DSC) Q2000 from TA Instruments. The temperature measurement of the DSC was calibrated using melting point determination. The cell's heat flux was calibrated by melting enthalpy calibration. The heat capacity measurement was calibrated with a sapphire standard (No. 915079.902) provided by TA Instruments. For weighing the samples, a Mettler Toledo MX5 was used. For all experiments, hermetically closed Tzero Alodined pans and lids from TA Instruments were used. The pans and lids were passivated to avoid the base catalyzed formation of aluminum-hydroxide and hydrogen.

For the measurement an upward temperature ramp of 5 °C/min between $t = 20$ °C and $t = 90$ °C was applied. Each sample was measured three times in a row. Before and between each run a resting time of 5 minutes at $t = 20$ °C was given. The result of the first run was discarded. The average of the second and third run is reported here as the measured liquid heat capacity.

The standard uncertainty of the measured liquid heat capacity c_p was calculated from the standard deviation of the repeated measurements and the standard uncertainty from calibration. The average standard uncertainty of the measured liquid heat capacity was $u(c_p) = 75$ J/(kg·K). The expanded uncertainty of the composition was the same as specified in Section 2.3.2. The expanded uncertainty of the temperature measurement t was $U(t) = 0.1$ °C (0.99 level of confidence). The pressure inside the pans was not measured as it has no significant influence on the measured liquid heat capacity.

2.10 Density and dynamic viscosity

The density and dynamic viscosity of unloaded and CO_2-loaded aqueous solutions of amines were measured with an Anton Paar SVM 3000 instrument which is a combination of an oscillating U-tube densimeter and Stabinger viscosimeter. Each experiment was repeated up to five times. The arithmetic mean values of the measured densities and dynamic viscosities are reported here as the result.

The standard uncertainty of the measured density ρ and dynamic viscosity η was calculated from the standard deviation of the repeated measurements and the standard uncertainty from calibration. The average standard uncertainty of the measured density was $u(\rho) = 0.001$ g/cm³. The average relative standard uncertainty of the measured dynamic viscosity was $u_r(\eta) = 0.01$. The expanded uncertainty of the composition was the same as specified in Section 2.3.2. The expanded uncertainty of the temperature measurement t was $U(t) = 0.1$ ℃ (0.99 level of confidence). The measurements were performed at ambient pressure, which was $p = 977 \pm 20$ mbar.

2.11 Vapor pressure

The vapor pressure of pure amines was measured in a circulation still [55, 56]. In the apparatus, the pressure was set and the temperature was measured. The pressure was measured with a P-30 0.1 MPa full scale high precision capacitive pressure sensor from WIKA. The temperature was measured with a calibrated Pt100 thermometer. Due to the onset of carbonization at temperatures around $t \approx 200$ ℃, only low pressures could be studied. The pressure and temperature were recorded every 5 seconds for 30 minutes. The arithmetic mean values of the pressure and temperature are reported here as the result.

The standard uncertainty of the measured temperature t and vapor pressure p^s was calculated from the standard deviation of the recorded temperature and pressure and the standard uncertainty from temperature and pressure calibration. The average standard uncertainty of the measured temperature was $u(t) = 0.2$ ℃. The average standard uncertainty of the measured vapor pressure was $u(p^s) = 2$ mbar.

3 Screening

3.1 Introduction

Screening of solvents is usually the first step in the process of solvent selection. Bernhardsen and Knuutila [16] have recently given a good review on reports of screenings of amine based solvents. A survey of publications on such screenings is presented in Table 4. Most of the amines that were investigated in these screenings are commercially available. Only comparatively few research groups have synthesized new amines for the screening [57–66]. Bubble cell apparatuses were used to investigate the CO_2-solubility and rate of absorption of CO_2 in most of the studies. Sometimes also the enthalpy of absorption of CO_2 or acid constants of the amines were measured. A few groups used temperature dependent fits of CO_2-solubility data to calculate the enthalpy of absorption of CO_2. Besides the experimental screenings, also group-contribution-based theoretical solvent screenings have been performed [67, 68].

Table 4: Overview of publications on experimental screenings of aqueous solutions of amines for CO_2-absorption.

author	investigated amines [1] / [2]	investigated solvents	experimental setups	investigated properties
Adeosun et al. (2013)[69]*	5 / -	5	2	f
Aronu et al. (2010)[70]	5 / -	8	1	a,b,e,f
Aronu et al. (2011)[71]*	9 / -	13	1	e,f
Aronu et al. (2013)[72]	8 / -	14	2	a,d,e,f
Brœder et al. (2012)[73]	7 / -	19	1	e,f
Chen et al. (2011)[74]	6 / -	7	1	e,f,g
Chen et al. (2011)[75]*	7 / -	8	2	c,e,f,g
Choi et al. (2014)[76]	5 / -	6	4	c,e,f,g
Chowdhury et al. (2009)[57]*	22 / 4	26	3	e,f,g
Chowdhury et al. (2011)[58]*	4 / 7	11	3	e,f,g
Chowdhury et al. (2013)[59]*	14 / 7	21	3	e,f,g
Conway et al. (2014)[62]*	3 / 30	33	2	e,f,h
Conway et al. (2014)[77]	7 / -	7	1	e,f,h
Du et al. (2016)[78]	22 / -	10	2	c,e,f
Dubois et al. (2013)[79]	10 / -	12	2	e,f
El Hadri et al. (2017)[80]	30 / -	30	3	a,e,f,g
Goto et al. (2011)[60]*	10 / 1	9	3	d,e,f,g
Goto et al. (2011)[61]	6 / 4	9	3	d,e,f,g
Hartono et al. (2017)[81]*	18 / -	18	2	c,e,f

Table 4: continued from previous page

author	investigated amines [1] / [2]	investigated solvents	experimental setups	investigated properties
Hook (1997)[64]	5 / 3	8	4	a,d,e,f
Kim et al. (2014)[82]*	6 / -	6	3	d,f,g
Luo et al. (2016)[83]	5 / -	10	2	e,f
Maneeintr et al. (2009)[65]*	1 / 5	6	1	f
Mergler et al. (2011)[84]*	5 / -	5	2	d,f
Muchan et al. (2017)[85]	4 / -	4	2	e,f,g
Muchan et al. (2017)[86]	9 / -	18	3	d,e,f,g
Puxty et al. (2009)[87]*	76 / -	76	2	e,f
Singh et al. (2007)[88]*	14 / -	14	1	a,e,f
Singh et al. (2009)[89]*	35 / -	35	1	a,e,f
Singh et al. (2009)[90]	33 / -	33	1	a,e,f
Singh et al. (2011)[91]*	27 / -	30	1	a,e,f
Singto et al. (2016)[66]	2 / 5	7	3	a,d,e,f,g
Wang et al. (2013)[92]	16 / -	16	1	e,f
Wang et al. (2013)[93]	15 / -	15	1	e,f
Yang et al. (2016)[63]	3 / 30	33	1	a,f
Zhang et al. (2017)[94]	8 / -	8	2	d,e,f
Zoghi et al. (2012)[95]	6 / -	16	1	e,f
This Section	3 / 26	56	7	a,b,c,d,e,f,h

a: water solubility and/or solid precipitation, b: foaming behavior and/or liquid-liquid demixing, c: density and/or dynamic viscosity, d: information on chemical equilibrium, e.g., pK-values or NMR, e: rate of absorption of CO_2, f: equilibrium CO_2-loading, g: calculated or measured enthalpy of absorption of CO_2, h: calculated energy demand of a purification task. *stated in Bernhardsen and Knuutila [16]. [1]commercially available, [2]synthesized for the screening.

The results of the experimental screening of the 26 newly synthesized EvAs is presented in this section. Seven apparatuses were used to study nine properties of the solvents. The properties were chosen such as to characterize the solvents for industrial application for CO_2-absorption: CO_2-loading, rate of absorption of CO_2, pK-values, foaming behavior, solid precipitation, solubility in water, liquid-liquid demixing temperature, dynamic viscosity, and CO_2-solubility isotherms. The mass fraction of the amines in the unloaded solvent was either $\tilde{w}^0_{\text{amine}} = 0.05$ g/g or $\tilde{w}^0_{\text{amine}} = 0.4$ g/g. Furthermore, the NoVa short-cut method [35] was used to estimate the energy demand and recirculation rate of two typical purification tasks: the CO_2-removal from natural gas and from synthesis gas, respectively. The same procedures were applied for all amines. The results were compared to corresponding data for two amines that are widely used for CO_2-absorption: monoethanolamine (MEA) and a blend of methyl-diethanolamine (MDEA) and piperazine (PZ) with a mass ratio of 7:1 (MDEA/PZ). The aim of this comprehensive comparison was to evaluate the potential of the EvAs as an interesting class of

aqueous solvents for the CO_2-absorption. It turned out that some of the aqueous solutions of EvAs show significantly improved performance compared to aqueous solutions of MEA and MDEA/PZ.

3.2 Experimental results

3.2.1 Solubility in water, solid precipitation, and foaming behavior

Table 5 shows the results that were obtained in the qualitative assessment of the solubility in water of the systems (amine + H_2O), as well as of solid precipitation and foaming behavior of the systems (amine + H_2O + CO_2).

All EvAs are soluble in water at $\tilde{w}^0_{\mathrm{amine}} = 0.05$ g/g. At $\tilde{w}^0_{\mathrm{amine}} = 0.4$ g/g, all EvAs except EvA14, EvA17, EvA32, and EvA33 are soluble in water. From these, EvA14 is the only which is liquid as a pure component but forms solids in aqueous solution. EvA17 has the highest molar mass of all studied amines. EvA32 is the only amino-acid, and EvA33 is the only amide in the study. The aqueous solution of EvA19 is a crude-oil-like opaque black liquid. All other aqueous solutions of EvAs are translucent reddish liquids.

Table 5: Experimental results of the qualitative assessment of the solubility in water in the system (amine + H_2O), as well as solid precipitation and foaming behavior in the system (amine + H_2O + CO_2) from the screening.

	solubility in water		solid precipitation		foam height
$\tilde{w}^0_{\mathrm{amine}}$ / g/g	0.05	0.4	0.05	0.4	0.4
t / ℃	25	25	25	25	40
CO_2-loading	no	no	yes	yes	yes
MEA	soluble	soluble	no	no	reference
MDEA/PZ	soluble	soluble	no	no	similar
EvA01	soluble	soluble	no	yes	lower
EvA02	soluble	soluble	no	yes	lower
EvA03	soluble	soluble	no	no	similar
EvA04	soluble	soluble	no	yes	lower
EvA05	soluble	soluble	no	yes	lower
EvA06	soluble	soluble	no	no	lower
EvA07	soluble	soluble	no	yes	lower
EvA09	soluble	soluble	no	no	lower
EvA10	soluble	soluble	no	yes	lower
EvA14	soluble	poor	no	[a]	[a]

Table 5: continued from previous page

	solubility in water		solid precipitation		foam height
$\tilde{w}_{\mathrm{amine}}^0$ / g/g	0.05	0.4	0.05	0.4	0.4
t / °C	25	25	25	25	40
CO_2-loading	no	no	yes	yes	yes
EvA17	soluble	poor	no	[a]	[a]
EvA19	soluble	soluble	yes	yes	lower
EvA21	soluble	soluble	no	no	lower
EvA22	soluble	soluble	no	yes	lower
EvA24	soluble	soluble	no	no	lower
EvA25	soluble	soluble	no	no[b]	lower
EvA26	soluble	soluble	no	yes	lower
EvA27	soluble	soluble	no	yes	lower
EvA29/30	soluble	soluble	no	no	similar
EvA31	soluble	soluble	no	yes	lower
EvA32	soluble	poor	no	[a]	[a]
EvA33	soluble	poor	no	[a]	[a]
EvA34	soluble	soluble	no	no	lower
EvA36	soluble	soluble	no	no	lower
EvA41	soluble	soluble	no	yes	lower

$\tilde{w}_{\mathrm{amine}}^0$: mass fraction of amine in the unloaded solvent with the relative expanded uncertainty $u_r(\tilde{w}_{\mathrm{amine}}^0) = 0.001$ (0.99 level of confidence), t: temperature with the expanded uncertainty $U(t) = 1$ °C (0.99 level of confidence). [a]not available due to poor solubility in H_2O. [b]EvA25 passed the 7 days test but showed solid precipitation after several month.

In the experiments in the bubble cell (cf. Section 2.4.2.4), only the CO_2-loaded aqueous solutions of EvA19 showed solid precipitation at $\tilde{w}_{\mathrm{amine}}^0 = 0.05$ g/g. EvA19 is the only EvA that contains an aromatic furan-ring. At $\tilde{w}_{\mathrm{amine}}^0 = 0.4$ g/g, solid precipitation was observed in the flow-saturator experiments (cf. Section 2.4.1.2) for 12 of the 21 EvAs which were soluble in water. No solid precipitation was observed for EvA03, EvA06, EvA09, EvA21, EvA24, EvA29/30, EvA34, and EvA36. EvA25 also passed the 7 days test used here for the classification of solid precipitation and was therefore classified as not solid precipitating. However, after several month, solids were found in some of the CO_2-loaded samples of EvA25. A similar behavior was observed for EvA02 in a previous work of our group [29]. A pattern to establish a relation between the molecular structure of the EvAs and the occurrence of solid precipitation was not found in the present data. However, the results clearly show that the probability of solid precipitation increases with increasing mass fraction of amine in the unloaded solvent.

The observed foam height of the reference MEA was about 7 cm in the experiments. EvA03, the mixtures EvA29/30 and MDEA/PZ showed similar foam heights. For all

other studied EvAs, a distinctly lower foam height was observed. Less foaming is advantageous for the operability of CO_2-absorption plants.

3.2.2 Density, dynamic viscosity, and demixing temperature

Table 6 shows the quantitative results of the experimental studies of the density ρ, the dynamic viscosity η, and the liquid-liquid demixing temperature t_{demix} in the system (amine + H_2O).

The density of the investigated aqueous solutions of EvAs at $t = 25\,°C$ is in a range between $\rho = 0.978$ g/cm^3 for EvA05 and $\rho = 1.027$ g/cm^3 for EvA29/30 and EvA19.

The dynamic viscosity of the aqueous solutions of EvAs at $t = 25\,°C$ is in a range between $\eta = 7.9$ mPa·s for EvA01 and $\eta = 22.1$ mPa·s for EvA34. As expected, in general, the dynamic viscosity increases with increasing molar mass. Most of the studied aqueous solutions of EvAs show higher dynamic viscosities than the aqueous solutions of MEA and MDEA/PZ. Higher viscosities are disadvantageous for the mass transfer in CO_2-absorption processes.

The lowest liquid-liquid demixing temperature in the system was observed for EvA02 at $t_{demix} = 42.5\,°C$. The demixing temperature increases with increasing ratio of polar groups (hydroxy, ether, ketone, amino) to unpolar groups (hydrocarbons) in the molecule. No demixing was observed for EvAs that contain hydroxy-groups (EvA21, EvA27, EvA29/30, EvA31), primary amino groups (EvA01), or unhindered secondary amino groups (EvA34, EvA36, EvA41), respectively.

Table 6: Density, dynamic viscosity, and liquid-liquid demixing temperature of unloaded aqueous solutions of EvAs with $\tilde{w}^0_{amine} = 0.4$ g/g. Experimental results from the present work.

	ρ	η	t_{demix}
	g/cm^3	mPa·s	°C
MEA	1.016	3.7 ± 1.3	no[a]
MDEA/PZ	1.033	5.8 ± 1.6	no[a]
EvA01	0.999	7.9 ± 1.6	no[a]
EvA02	0.984	11.6 ± 1.5	42.5
EvA03	0.999	15.5 ± 2.0	107.5
EvA04	0.986	9.1 ± 2.0	62.5
EvA05	0.978	10.4 ± 1.8	47.5
EvA06	1.006	8.6 ± 1.8	117.5
EvA07	1.000	14.7 ± 2.0	122.5
EvA09	1.024	9.3 ± 1.0	82.5

Table 6: continued from previous page

	ρ	η	t_{demix}
	g/cm^3	mPa·s	℃
EvA10	1.018	17.5 ± 2.4	92.5
EvA19	1.027	9.3 ± 1.8	72.5
EvA21	1.034	11.7 ± 2.0	no[a]
EvA22	0.998	9.8 ± 1.8	87.5
EvA24	1.024	14.6 ± 2.0	127.5
EvA25	0.992	17.4 ± 2.2	67.5
EvA26	0.995	16.1 ± 2.0	72.5
EvA27	1.015	14.8 ± 2.3	no[a]
EvA29/30	1.027	13.8 ± 2.1	no[a]
EvA31	1.021	11.6 ± 1.9	no[a]
EvA34	1.002	22.1 ± 2.4	no[a]
EvA36	1.004	14.0 ± 2.0	no[a]
EvA41	1.025	9.4 ± 1.8	no[a]

$\tilde{w}^0_{\mathrm{amine}}$: mass fraction of amine in the unloaded solvent with the relative expanded uncertainty $u_r(\tilde{w}^0_{\mathrm{amine}}) = 0.001$ (0.99 level of confidence), ρ: density at the temperature $t = 25$ ℃ with the standard uncertainty $u(\rho) = 0.01$ g/cm^3 and the expanded uncertainty $U(t) = 1$ ℃ (0.99 level of confidence) η: dynamic viscosity at the temperature $t = 25$ ℃ with the intervals representing the standard uncertainty $u(\eta)$ and the expanded uncertainty $U(t) = 1$ ℃ (0.99 level of confidence), t_{demix}: liquid-liquid demixing temperature with the expanded uncertainty $U(t_{\mathrm{demix}}) = 2.7$ ℃ (0.99 level of confidence). [a]no liquid-liquid demixing observed below $t \leq 130$ ℃.

3.2.3 pK-values

The molal activity-based pK-values of the amines, highly diluted in H$_2$O, which were determined from titration experiments at $t = 20$ ℃, $t = 40$ ℃, and $t = 60$ ℃ are listed in Table 7. In Table 7, the Greek letters indicate to which amino group the pK-value corresponds (cf. Figure 1). For the mixture EvA29/30 and for EvA41 (which was contaminated with piperazine) no reliable information on the pK-values could be obtained from the titration curves.

The highest pK-value was assigned to the α-amino group for all EvAs. Literature data [29, 96, 97] and the positive inductive effect of the surrounding 2,2,6,6-tetramethyl-piperidine-ring support this assignment. The second highest pK-value was assigned to the amino group that has the highest spatial distance to the α-amino group. This is the γ-amino group for EvAs that contain three amino groups (EvA03, EvA07, EvA10, EvA14, EvA21, EvA24, EvA25, EvA26, EvA36), and the δ-amino group for EvAs that contain four amino groups (EvA17, EvA34). Literature data for similar amines support these assignments [96, 98]. The third highest pK-value of EvA34 is assigned to the

β-amino group, and the lowest pK-value of EvA34 to the γ-amino group. Arguments for these assignments are the larger inductive effect of the piperidine ring at the β-amino group compared to the γ-amino group, literature data [29] for a similar β-amino group arrangement, and a negligible influence of the steric hindrance [96, 99, 100]. The third highest pK-value of EvA17 was assigned to the γ-amino group. For EvA17, due to the lower pK-value of the δ-amino group, compared to the α-amino group, the δ-amino group is less protonated than the α-amino group. Hence, the γ-amino group is less influenced by protonated amino groups nearby than the β-amino group, and is thus expected to have a higher pK-value than the β-amino group.

Table 7: pK-values of the investigated EvAs. Experimental results from the present work. Greek letters indicate the corresponding amino group according to the designation in Figure 1.

	pK-values											
t / ℃	20				40				60			
EvA01	10.8^α	8.2^β			10.3^α	7.7^β			9.7^α	7.2^β		
EvA02	10.9^α	8.3^β			10.4^α	7.7^β			9.8^α	7.3^β		
EvA03	10.8^α	9.4^γ	6.9^β		10.2^α	8.9^γ	6.4^β		9.7^α	8.4^γ	5.9^β	
EvA04	10.8^α	8.3^β			10.3^α	7.7^β			9.7^α	7.3^β		
EvA05	10.9^α	8.3^β			10.3^α	7.8^β			9.6^α	7.3^β		
EvA06*	10.6^α	7.5^β			10.0^α	6.9^β			9.4^α	6.6^β		
EvA07	10.6^α	8.8^γ	4.8^β		10.1^α	8.4^γ	4.5^β		9.5^α	8.0^γ	4.1^β	
EvA09*	10.4^α	5.7^β			9.8^α	5.6^β			9.2^α	5.1^β		
EvA10	10.4^α	7.7^γ	2.6^β		9.9^α	7.5^γ	2.5^β		9.1^α	7.0^γ	2.4^β	
EvA14	10.7^α	9.1^γ	5.8^β		10.1^α	8.7^γ	5.4^β		9.5^α	8.2^γ	5.1^β	
EvA17	10.9^α	9.9^δ	7.5^γ	4.6^β	10.4^α	9.4^δ	7.1^γ	4.2^β	9.7^α	8.8^δ	6.6^γ	3.8^β
EvA19*	10.5^α	7.0^β			9.9^α	6.5^β			9.3^α	6.0^β		
EvA21*	10.7^α	8.6^γ	6.2^β		10.2^α	8.2^γ	5.9^β		9.6^α	7.7^γ	5.4^β	
EvA22*	10.6^α	7.9^β			10.1^α	7.5^β			9.5^α	6.9^β		
EvA24*	10.8^α	8.0^γ	6.0^β		10.1^α	7.6^γ	5.7^β		9.4^α	7.1^γ	5.3^β	
EvA25	10.9^α	9.8^γ	6.7^β		10.3^α	9.3^γ	6.4^β		9.7^α	8.7^γ	5.9^β	
EvA26	10.6^α	9.3^γ	4.9^β		10.1^α	8.9^γ	4.5^β		9.6^α	8.4^γ	4.2^β	
EvA27*	10.6^α	7.6^β			10.0^α	7.1^β			9.5^α	6.7^β		
EvA31*	10.5^α	7.5^β			10.0^α	7.1^β			9.5^α	6.7^β		
EvA32*	10.6^α	7.6^β			10.1^α	7.3^β			9.5^α	6.9^β		
EvA33*	10.5^α	9.4^β			9.9^α	9.1^β			9.4^α	8.2^β		
EvA34	10.9^α	9.8^δ	8.3^β	6.7^γ	10.3^α	9.3^δ	7.7^β	6.2^γ	9.8^α	8.9^δ	7.5^β	5.9^γ
EvA36	11.0^α	9.9^γ	6.9^β		10.4^α	9.4^γ	6.5^β		9.9^α	8.8^γ	6.0^β	

pK-values on the molal activity based pH-scale with the standard uncertainty $u(\mathrm{p}K) = 0.15$. t: temperature with the expanded uncertainty $U(t) = 1$ ℃ (0.99 level of confidence). *EvAs that contain oxygen atoms.

The pK-values are strongly influenced by the substituents. As expected, the β-amino group that links the substituent to the piperidine-ring is influenced more strongly by the nature of the substituent than the α-amino group. However, also the α-amino group is influenced by the substituent, despite the spatial distance. Substituents that contain oxygen atoms (marked with an asterisk in Table 7) reduce the pK-values. This is due to the negative inductive effect of oxygen atoms. An exception is EvA33, where the pK-value of the β-amino group is remarkably high. EvA33 contains a secondary amide group. Amides are reported to have high pK-values [101, 102]. In general, higher pK-values are advantageous for the absorption of CO_2. EvA03, EvA17, EvA25, EvA34, and EvA36 as well as EvA33 show high pK-values. In that group of EvAs only EvA33 contains an oxygen atom.

3.2.4 Equilibrium CO_2-loading

Figure 4 shows the equilibrium CO_2-loadings $\tilde{X}_{CO_2}$ in the system (amine + H_2O + CO_2) at $t = 40\,°C$ and $t = 100\,°C$ that were obtained in bubble cell experiments at a partial pressure of CO_2 of $p_{CO_2} = 140$ mbar. The mass fraction of amine in the unloaded solvent was always $\tilde{w}^0_{amine} = 0.05$ g/g in these experiments. This low mass fraction was chosen to avoid solid precipitation. The results are displayed in descending order of the difference between the equilibrium CO_2-loadings at $t = 40\,°C$ and $t = 100\,°C$. The value of this difference $\Delta\tilde{X}_{CO_2}$ is given in Figure 4 as well. The data are divided into three groups: EvAs that contain oxygen atoms, EvAs that do not contain oxygen atoms, and the references MEA and MDEA/PZ. The corresponding experimental numerical data are given in Appendix E.

In general, EvAs that do not contain oxygen atoms show higher $\tilde{X}_{CO_2}$ at $t = 40\,°C$ than EvAs that contain oxygen atoms. Oxygen atoms lower the basicity (cf. Section 3.2.3), which consequently lowers the equilibrium CO_2-loading. But also $\Delta\tilde{X}_{CO_2}$ is in general higher for EvAs that do not contain oxygen atoms than for EvAs that contain oxygen atoms. This might be related to the temperature dependency of the pK-values: high pK-values decrease stronger with increasing temperature, than low pK-values (cf. Section 3.2.3).

However, also exceptions to this general relation between the equilibrium CO_2-loading and the pK-value were found. The amide EvA33 and the amino-acid EvA32, for example, show much lower $\tilde{X}_{CO_2}$ and $\Delta\tilde{X}_{CO_2}$ than expected from their pK-values. Another exception is EvA01, for which $\Delta\tilde{X}_{CO_2}$ is very low compared to other EvAs with similar high $\tilde{X}_{CO_2}$ at $t = 40\,°C$. Here, the different functional groups (e.g., amide, amino acid, primary, secondary, or tertiary amino groups, etc.) and the equilibrium constants of
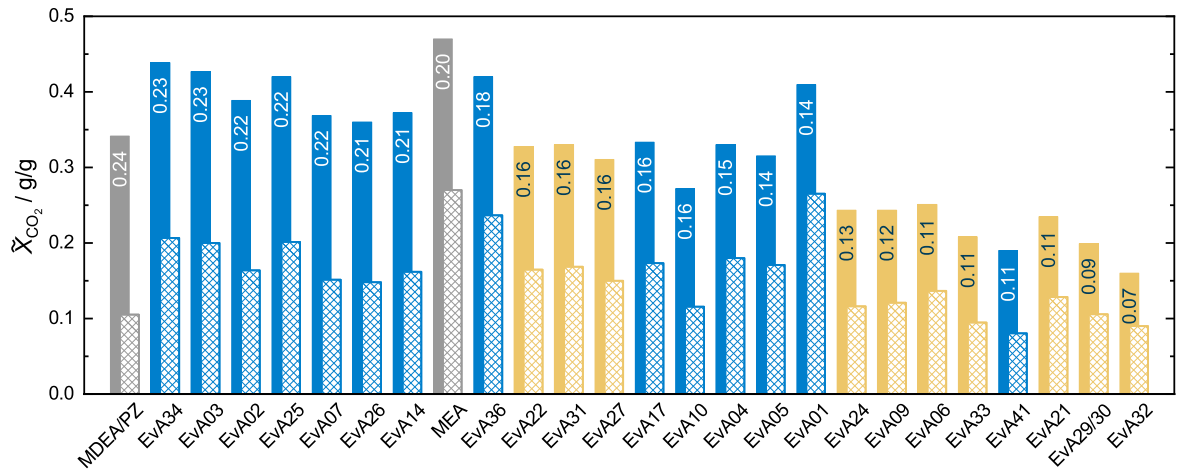
Figure 4: Equilibrium CO_2-loading in the system (amine + H_2O + CO_2) with $\tilde{w}^0_{\text{amine}} = 0.05$ g/g at $p_{CO_2} = 140$ mbar. Experimental results from bubble cell experiments of the present work. ■: $t = 40$ ℃, ⊠: $t = 100$ ℃. yellow: EvAs that contain oxygen atoms, blue: EvAs that do not contain oxygen atoms, grey: references. The number indicates the difference between the equilibrium CO_2-loadings at $t = 40$ ℃ and $t = 100$ ℃ $\Delta\tilde{X}_{CO_2}$. The results are displayed in order of descending numbers of $\Delta\tilde{X}_{CO_2}$.

the chemical reactions reveal their strong influence on the results. More details on the influence of the reactions and equilibrium constants are given in Section 6.

The highest $\Delta\tilde{X}_{CO_2}$ was found for the reference MDEA/PZ. However, $\Delta\tilde{X}_{CO_2}$ for several of the EvAs (EvA34, EvA03, EvA02, EvA25, EvA07, EvA26, and EvA14) are similar and surpass that of the reference MEA. They are all part of the group of EvAs that do not contain oxygen atoms. They show higher $\tilde{X}_{CO_2}$ than MDEA/PZ but lower $\tilde{X}_{CO_2}$ than MEA at $t = 40$ ℃ and $t = 100$ ℃, respectively. It is remarkable that five out of these seven EvAs (EvA03, EvA07, EvA14, EvA25, and EvA26) have very similar molecular structure and vary only in the length of the alkane-parts of the substituents of the tertiary γ-amino group.

3.2.5 Initial rate of absorption of CO_2

Figure 5 shows the experimental results for the initial rate of absorption of CO_2 RA as a function of the equilibrium CO_2-loading $\tilde{X}_{CO_2}$, determined from bubble cell experiments at $t = 40$ ℃ and a partial pressure of CO_2 of $p_{CO_2} = 140$ mbar. The mass fraction of amine in the unloaded solvent was $\tilde{w}^0_{\text{EvA}} = 0.05$ g/g in the experiments. This low mass fraction of amine in the unloaded solvent reduce the influence of the viscosity and surface tension on the initial rate of absorption [74] and additionally reduces the occurrence of solid precipitation. The data is divided into the same three groups as in the previous section: EvAs that contain oxygen atoms, EvAs that do not contain oxygen atoms, and
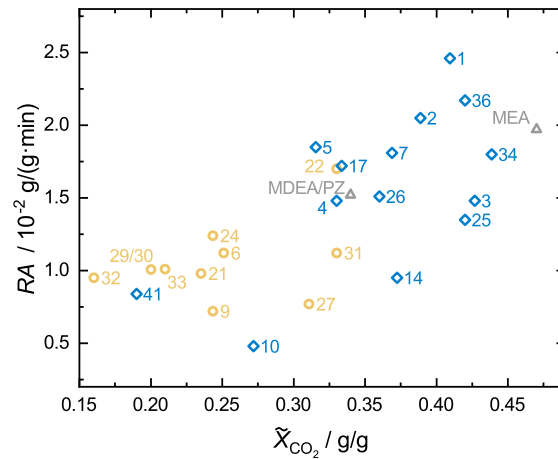
Figure 5: Initial rate of absorption of CO_2 in the system (amine + H_2O + CO_2) as a function of the equilibrium CO_2-loading at $t = 40$ °C with $\tilde{w}^0_{amine} = 0.05$ g/g at $p_{CO_2} = 140$ mbar. Experimental results from bubble cell experiments of the present work. Numbers indicate the EvA-number. ○: EvAs that contain oxygen atoms, ◇: EvAs that do not contain oxygen atoms, △: references.

the references MEA and MDEA/PZ. The corresponding experimental numerical data are given in Appendix E.

A general trend of increasing RA with increasing $\tilde{X}_{CO_2}$ is observed (cf. Figure 5). $\tilde{X}_{CO_2}$ can be seen as the driving force for the absorption, and therefore strongly influences the initial rate of absorption. This explains the importance of high equilibrium CO_2-loadings $\tilde{X}_{CO_2}$ for reaching high rates of absorption RA. As discussed in the previous section, EvAs that do not contain oxygen atoms show higher $\tilde{X}_{CO_2}$ than those that contain oxygen atoms. Consequently, most of the EvAs that do not contain oxygen atoms also show higher RA than those that contain oxygen atoms.

EvA01, EvA02, and EvA36 show the highest RA in this comparison. It is remarkable that they even surpass the RA of MEA, although MEA is known to have a high rate of absorption compared to many other amines [58, 60, 73, 81, 86, 87, 103]. As MEA has the highest $\tilde{X}_{CO_2}$, it is likely that EvA01, EvA36, and EvA02 have higher rates of reaction in the liquid phase than MEA. Other interesting candidates with high RA are EvA05, EvA07, EvA17, EvA22, and EvA34, which show similar RA as MEA and surpass that of MDEA/PZ. From these EvAs only EvA22 contains an oxygen atom.

3.2.6 CO_2-solubility isotherms

Figure 6 shows the results of the head space gas chromatography measurements, in which the CO_2-solubility isotherms in aqueous solutions of amines with $\tilde{w}^0_{amine} = 0.4$ g/g at $t = 40$ °C and $t = 100$ °C were determined. In Figure 6, the measured equilibrium
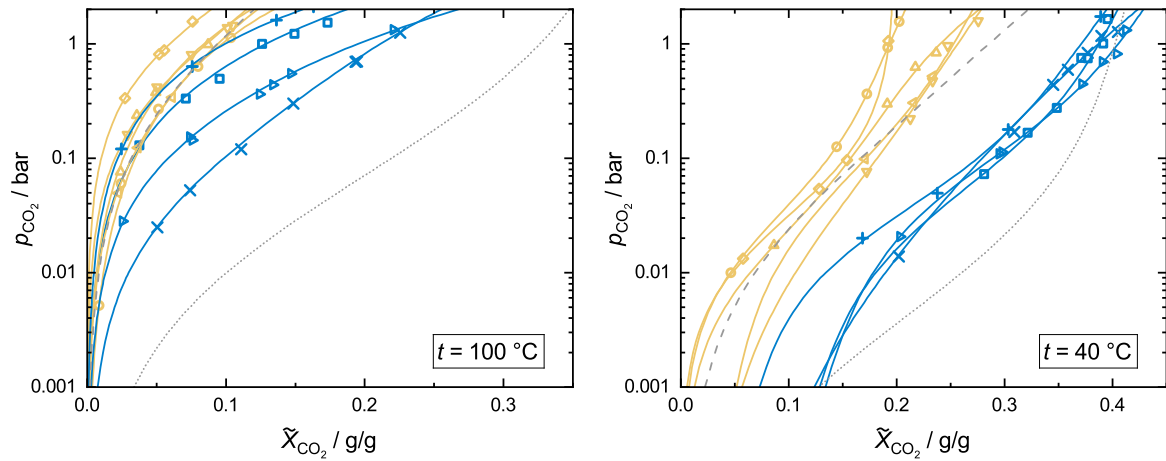
Figure 6: CO_2-solubility isotherms for the system (amine + H_2O + CO_2) with $\tilde{w}^0_{\text{amine}} = 0.4$ g/g at $t = 40\,°C$ and $t = 100\,°C$. Symbols: Experimental results from head space gas chromatography experiments of the present work. Lines: SolSOFT equation fits. Yellow: EvAs that contain oxygen atoms, blue: EvAs that do not contain oxygen atoms, grey: references. □: EvA03, ▽: EvA06, ◇: EvA09, ◁: EvA21, △: EvA24, +: EvA25, ○: EvA29/30, ▷: EvA34, ×: EvA36, dashed line: MDEA/PZ [104], dotted line: MEA [48].

partial pressure of CO_2 p_{CO_2} is plotted as a function of the CO_2-loading $\tilde{X}_{CO_2}$. The experimental results were correlated with the SolSOFT equation [35], which describes the data well. For comparison also results for MEA and MDEA/PZ are depicted, which were taken from the literature [48, 104]. Only solvents that were classified as not solid precipitating (cf. Section 3.2.1) were studied with head space gas chromatography. The data is divided into the same three groups as in the previous section. The corresponding experimental numerical data are given in Appendix E. Details on the correlation with the SolSOFT equation are given in Appendix B.

At $t = 40\,°C$, EvAs that do not contain oxygen atoms show higher CO_2-solubility than EvAs that contain oxygen atoms. This is in accordance with the results of the equilibrium CO_2-loading from bubble cell experiments with lower mass fraction of amine in the unloaded solvent (cf. Section 3.2.4). The reference MEA shows the highest CO_2-solubility at 40 °C. The CO_2-solubility in MDEA/PZ is within the range of the EvAs that contain oxygen atoms.

Also at $t = 100\,°C$, most of the EvAs that do not contain oxygen atoms show higher CO_2-solubility than the EvAs that contain oxygen atoms. Exceptions are EvA25 and partially also EvA03. The remarkable low CO_2-solubility in EvA03 and EvA25 at $t = 100\,°C$ differs from the findings from bubble cell experiments, where the CO_2-solubility in EvA25 and EvA03 at $t = 100\,°C$ is higher than that in all EvAs that contain oxygen atoms (cf. Figure 4). These differences result from the differences in the mass fraction of amine in the unloaded solvent, which was $\tilde{w}^0_{\text{amine}} = 0.4$ g/g here,

whereas it was only $\tilde{w}^0_{\text{amine}} = 0.05$ g/g in the bubble cell experiments. At $\tilde{w}^0_{\text{amine}} = 0.4$ g/g and $t = 100\,°C$, the solvent shows a large liquid-liquid miscibility gap that reduces the solubility of CO_2 in the solvent, whereas at $\tilde{w}^0_{\text{amine}} = 0.05$ g/g and $t = 100\,°C$, the miscibility gap and its effect on the CO_2-solubility is negligible (cf. Section 5). Of all studied amines, MEA shows the highest CO_2-solubility at $t = 100\,°C$. The CO_2-solubility in MDEA/PZ is within the range of the CO_2-solubility in the EvAs that contain oxygen atoms, EvA25, and EvA03.

Figure 7 shows the differences between the CO_2-solubility isotherms at $t = 40\,°C$ and $t = 100\,°C$ $\Delta\tilde{X}_{CO_2}$ for a given partial pressure of CO_2 p_{CO_2}. The displayed curves are calculated from the differences of the SolSOFT fits (cf. Figure 6). The differences between the CO_2-solubility at $t = 40\,°C$ and $t = 100\,°C$ is a particularly important parameter for the CO_2-absorption process and depends strongly on the partial pressure of CO_2. The results for $\Delta\tilde{X}_{CO_2}$ of the different amines differ strongly, however, most of the curves in Figure 7 show a distinct bulge. For MEA this bulge is at lower partial pressure of CO_2 than for the EvAs. For EvA24, EvA36, and MDEA/PZ, only a faint bulge is observed.

The results for $\Delta\tilde{X}_{CO_2}$ for the different amines follow the same trend as observed for the equilibrium CO_2-loadings (cf. Section 3.2.4): EvAs that do not contain oxygen atoms show higher $\Delta\tilde{X}_{CO_2}$ than EvAs that contain oxygen atoms. MEA shows high $\Delta\tilde{X}_{CO_2}$ only in the lower partial pressure range, MDEA/PZ only in the upper partial pressure range. The $\Delta\tilde{X}_{CO_2}$ of the reference amines are surpassed by several of the EvAs. EvA03 shows the highest $\Delta\tilde{X}_{CO_2}$. This holds for the entire range of partial pressure of CO_2.
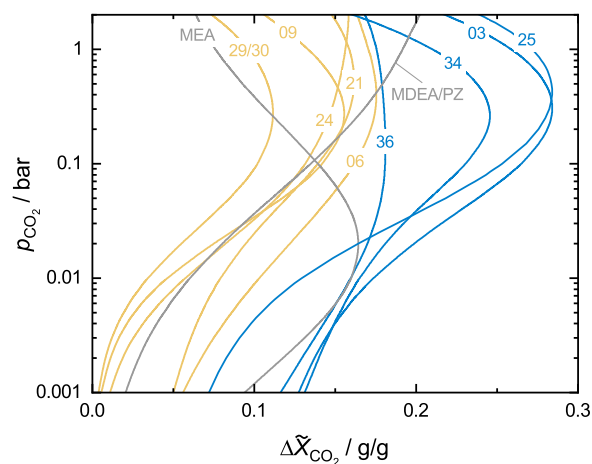
Figure 7: Differences between the CO_2-solubility isotherms at $t = 40\,°C$ and $t = 100\,°C$ (cf. Figure 6) for the system (amine + H_2O + CO_2) with $\tilde{w}^0_{\text{amine}} = 0.4$ g/g, calculated from SolSOFT fits. yellow: EvAs that contain oxygen atoms, blue: EvAs that do not contain oxygen atoms, grey: references. Numbers indicate the EvA-number.

EvA25 and EvA34 have similarly high $\Delta \tilde{X}_{CO_2}$, which are, however, slightly lower than that of EvA03, either in the lower partial pressure range (EvA25) or upper partial pressure range (EvA34). EvA36 and EvA06 also have high $\Delta \tilde{X}_{CO_2}$ compared to most of the other amines.

3.3 Estimated energy demand from NoVa short-cut method

The SolSOFT fits of the CO_2-solubility isotherms from Section 3.2.6 were used as input for a short-cut method for assessing the performance of the solvents in CO_2-absorption processes. The method that was applied for this purpose is called NoVa [35] and is an improved version of the method of Notz et al., which is known to give good results for amine based solvents [22, 105, 106]. The NoVa short-cut method yields estimates for the specific energy demand and recirculation rate for a given CO_2-removal task. It is based on an equilibrium stage model in which it is assumed that both, the absorber and the desorber, have infinite separation capacity. It is known that the method is useful for the ranking of solvents, while the absolute numbers for a given solvent should not be over-interpreted. The NoVa method is described in detail in [35], such that in the present work, the focus is on its application for assessing the EvAs.

Two purification tasks were considered as scenarios for applying the NoVa method in this work. The first scenario is inspired by natural gas purification and labeled NG here. The second scenario is inspired by synthesis gas purification and labeled SG here. The values of the input parameters for the two scenarios were selected based on averaged values from literature [1, 6, 10] and are given in Table 8. They can be divided into three sets of input parameters. The first set contains specifications that characterize the purification scenario: the partial pressure of CO_2 at the inlet $p_{CO_2}^{A,in}$ and outlet $p_{CO_2}^{A,out}$ of the absorber, the pressure in the absorber p^A, and the average molar mass of the gas that is treated M_{gas}. Here, different values for the partial pressure of CO_2 at the inlet and outlet of the absorber were chosen to specify the removal tasks of the two scenarios. The removal rate of the scenario NG is 99.5 %. The removal rate of the scenario SG is 99.97 %.

The second set of input parameters are process parameters that specify the general framework of the absorption/desorption process: the pressure in the desorber p^D, the temperature of the CO_2-loaded solvent at the desorber inlet $t^{D,rich}$, the temperature inside the desorber $t^{D,lean}$, and the temperature of the desorber condenser reflux $t^{D,cond}$. The same values of process parameters were used in both scenarios. It follows from these

choices that the heat recovery between the lean solvent and the CO_2-loaded solvent is assumed to be equal for all solvents in both scenarios.

The third set of input parameters are solvent parameters that characterize the physico-chemical properties of the solvent: the liquid specific heat capacity of H_2O c_{p,H_2O} and of the solvent $c_{p,SOL}$, the mass fraction of amine in the unloaded solvent $\tilde{w}^0_{amine}$, the enthalpy of evaporation of H_2O $\Delta h^{vap}_{H_2O}$, the enthalpy of absorption of CO_2 $\Delta h^{abs}_{CO_2}$ in the solvent (referenced to the mass of absorbed / desorbed CO_2), and the solubility of CO_2 in the solvent at absorber $\tilde{\alpha}^A_{CO_2}(p_{CO_2})$ and desorber $\tilde{\alpha}^D_{CO_2}(p_{CO_2})$ conditions, for which the SolSOFT isotherms at $t = 40\,°C$ and $t = 100\,°C$ from Section 3.2.6 were used.

Table 8: Input parameters that were used in the NoVa short-cut method for the natural gas (NG) and synthesis gas (SG) scenarios. The CO_2-solubility was described with the SolSOFT fits of the CO_2-solubility isotherms. The symbols are explained in the text.

parameter	scenario NG / SG
specifying parameters	
$p^{A,in}_{CO_2}$ / bar	2.0 / 1.5
$p^{A,out}_{CO_2}$ / bar	0.01 / 0.0005
p^A / bar	35
M_{gas} / g/mol	16
process parameters	
p^D / bar	2
$t^{D,rich}$ / °C	90
$t^{D,lean}$ / °C	100
$t^{D,cond}$ / °C	20
solvent parameters	
c_{p,H_2O} / kJ/(kg·K)	4.20
$c_{p,SOL}$ / kJ/(kg·K)	4.05
$\tilde{w}^0_{amine}$ / g/g	0.4
$\Delta h^{vap}_{H_2O}$ / kJ/g	2.21
$\Delta h^{abs}_{CO_2}$ / kJ/g	-2
$\tilde{\alpha}^A_{CO_2}(p_{CO_2})$ / g/g	cf. Table B1
$\tilde{\alpha}^D_{CO_2}(p_{CO_2})$ / g/g	

The enthalpy of absorption of CO_2 $\Delta h^{abs}_{CO_2}$ was not measured in this work. A workaround to estimate the enthalpy of absorption of CO_2 is to use a Gibbs-Helmholtz equation [107] with a temperature-dependent fit of the measured CO_2-solubility data, e.g., the temperature dependent version of the SolSOFT equation [35]. This workaround was tested but turned out to only provide strongly scattering results for $\Delta h^{abs}_{CO_2}$ as only two isotherms were measured. It was therefore assumed that $\Delta h^{abs}_{CO_2}$ is equal for all solvents. The chosen value of $\Delta h^{abs}_{CO_2} = -2$ kJ/g of absorbed CO_2 represents a crude approximation

of the enthalpy of absorption of CO_2 that is reported in literature for aqueous solutions of MEA (-2 kJ/g $\geq \Delta h_{CO_2}^{abs} \geq$ -2.5 kJ/g [6, 10, 48, 108]) and MDEA/PZ (-1.6 kJ/g $\geq \Delta h_{CO_2}^{abs} \geq$ -2.2 kJ/g [10, 109]). Using the Gibbs-Helmholtz approach did not improve the accuracy of the values.

For a given ratio of the lean solvent mass flow to the rich gas mass flow L/G, the NoVa method yields the energy demand for the removal of one gram of CO_2 q_{CO_2}. Hence, based on the results from NoVa, for all solvents, curves can be determined that show the energy demand q_{CO_2} as a function of the L/G ratio for the two scenarios. These curves are shown in the upper row diagrams of Figure 8 and are divided into the same three types of amines as in the previous sections. A detailed discussion and explanation of the basic structure of the U-shaped curves has been given in a previous work of our group [35]. The minimum of each curve is marked with an asterisk in Figure 8. It is the design point with the minimal energy demand $q_{CO_2}^{opt}$ and the optimal L/G.
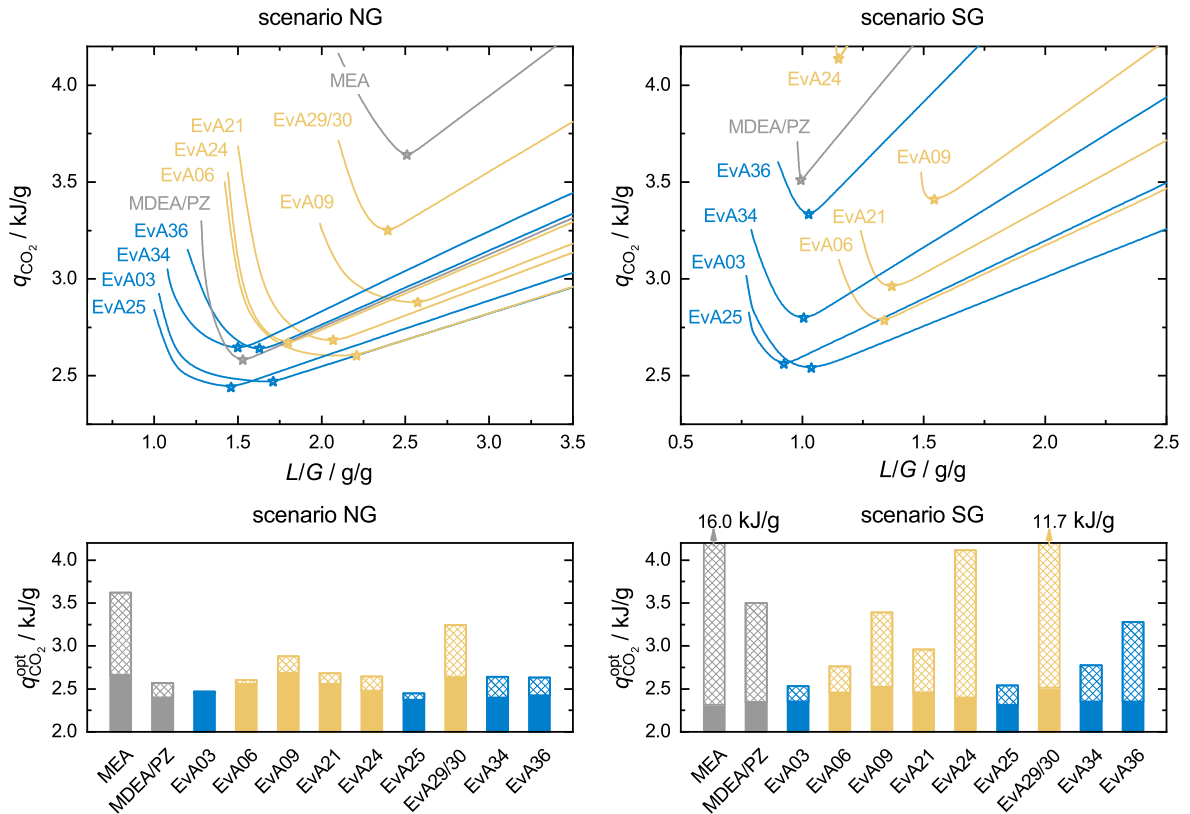
Figure 8: Results from the NoVa short-cut method for the scenario NG and SG. Upper row: estimated energy demand as a function of the liquid-to-gas ratio in the absorber. ☆: optimal operation point. Lower row: Energy contribution in the optimal operation point. ■: solvent heating, ⊠: stripping steam production. The intercept of 2 kJ/g$_{CO_2}$ equals the assumed enthalpy of desorption (see text). Yellow: EvAs that contain oxygen atoms, blue: EvAs that do not contain oxygen atoms, grey: references.

The minimal energy demand for each solvent is shown in the lower row diagrams of Figure 8. It consists of three contributions: the energy demand for the desorption of CO_2, the energy demand for solvent heating, and the energy demand for the production of stripping steam. The contribution for the desorption of CO_2 is the same for all solvents as the same amount of CO_2 is desorbed and the same enthalpy of desorption was used for all solvents (cf. Table 8). The energy demand for solvent heating and for the production of the stripping steam, as a result of the differences in their CO_2-solubility isotherms, however, vary between the solvents. Therefore, the following discussion of the results of the NoVa method focuses only on these two energy contributions.

The higher amount of CO_2 in the scenario NG leads to higher L/G ratios, compared to the scenario SG. In general, the EvAs that do not contain oxygen atoms show lower L/G ratios in the optimal operation point than EvAs that contain oxygen atoms. This comes from the higher difference between the equilibrium CO_2-loadings at $t = 40$ ℃ and $t = 100$ ℃ of EvAs that do not contain oxygen atoms (cf. Figure 7). Lower L/G ratios lead to lower energy demand for solvent heating. This is particularly relevant for purification tasks, where the amount of CO_2 in the inlet of the absorber is high and the purification requirement is low.

The higher purification requirement in the scenario SG leads to a higher energy demand for the production of stripping steam compared to the scenario NG. This amplifies the differences between the solvents. Low CO_2-solubility at $t = 100$ ℃ (cf. Figure 6) and a higher difference between the CO_2-solubility isotherms at $t = 40$ ℃ and $t = 100$ ℃ (cf. Figure 7) are favorable as they reduce the energy demand for the production of stripping steam. A comparison of the results of EvA25 and EvA34 as well as of EvA06 and EvA36 indicates that a low CO_2-solubility at $t = 100$ ℃ has stronger impact on the energy demand for the production of stripping steam than the difference between the CO_2-solubility isotherms at $t = 40$ ℃ and $t = 100$ ℃. This is particularly relevant if the purification requirement is high.

All EvAs that were studied here show a significantly lower estimated energy demand than the reference MEA in both scenarios. This result would probably remain valid if measured enthalpies of absorption of CO_2 for each solvent had been used. The difference between the estimated energy demand of the EvAs compared to that of the reference MDEA/PZ are less significant. Here, the applied assumption of equal enthalpies of absorption of CO_2 for all solvents limits the validity of the ranking. Nevertheless, most of the EvAs perform well. Especially EvA03 and EvA25 show favorable shapes of their CO_2-solubility isotherms which results in the lowest estimated energy demand in both scenarios of the assessment. In the scenario SG, the estimated energy demand of EvA03 and EvA25 is about 25 % lower than that of MDEA/PZ. Besides EvA03 and EvA25, also EvA06, EvA34 and EvA21 are interesting candidates.

3.4 Summary of results

Some of the EvAs that were synthesized for the present work turned out to be only poorly soluble in water and were not investigated further. No problems with foaming occurred in the tests with the aqueous solutions of EvAs. For two of the EvAs, the tendency for foaming was similar to that of MEA and MDEA/PZ. For all others it was distinctly lower. The dynamic viscosities of the studied aqueous solutions of EvAs were higher than those of corresponding solutions of MEA and MDEA/PZ. This is undesired, but there are many EvAs with moderate viscosities that are acceptable for applications.

In several of the studied aqueous solutions of EvAs, a liquid-liquid phase split occurs at elevated temperatures. The demixing temperatures vary strongly, depending on the substituent of the EvA. As expected, polar groups increase the demixing temperature. There was an ongoing discussion whether such a liquid-liquid phase split can be used in an advantageous way in CO_2-absorption processes [38–45, 110]. The system (EvA25 + H_2O + CO_2) was hence studied more in detail (cf. Section 5) and it turned out that the liquid-liquid phase split, that occurs at elevated temperature, does reduce the solubility of CO_2 in the solvent. After the phase split, the organic liquid phase contains only little CO_2, so that only the aqueous phase has to be regenerated. This effect is favorable and can most probably be used beneficial in advanced CO_2-absorption processes (cf. Section 5).

After loading the solvents with CO_2, solid precipitation was observed for some of the EvAs. This process can be very slow and it may take days until the solid forms. The probability of solid precipitation increases with increasing mass fraction of amine in the unloaded solvent. Solid precipitation is generally undesired. But, similar to the liquid-liquid phase split, it has been argued that also solid precipitation could be beneficially used in CO_2-absorption processes [111–113]. The basic idea is (similar to the liquid-liquid phase split) that the occurrence of a new phase leads to a split of the CO_2 between these phases and the hope is that a process can be designed in such a way as to make use of this. EvAs could also be interesting candidates for studying CO_2-absorption processes with solid precipitation.

The solubility of CO_2 in the solvents is of outstanding importance for the CO_2-absorption process and was studied with a bubble cell and by head space gas chromatography in the present screening. Two mass fractions of amine in the unloaded solvent were investigated ($\tilde{w}^0_{EvA}$ = 0.05 g/g and $\tilde{w}^0_{EvA}$ = 0.4 g/g). Generally, aqueous solutions of EvAs that do not contain oxygen atoms showed higher equilibrium CO_2-loadings than the ones that contain oxygen atoms. This holds both for the results at t = 40 ℃ and t = 100 ℃ (absorber and desorber conditions). The EvAs that do not contain oxygen atoms have also a higher difference between the equilibrium CO_2-loadings at absorption

and desorption conditions. Also the measured pK-values follow this trend: they are generally higher for EvAs that do not contain oxygen atoms.

Furthermore, rates of absorption of CO_2 were studied in bubble cell experiments. A low mass fraction of amine in the unloaded solvent was used in these studies to minimize the influence of the viscosity and surface tension. The initial rates of absorption of CO_2 in the aqueous solutions of EvAs that do not contain oxygen atoms are generally higher than those for EvAs that contain oxygen atoms. This is partially related to the fact that the EvAs that do not contain oxygen atoms also have a higher equilibrium CO_2-loading and that there is a general trend that high equilibrium CO_2-loadings lead to high rates of absorption of CO_2 as the potential difference that drives the absorption of CO_2 is higher.

The CO_2-solubility isotherms that were measured in the present work, were correlated empirically with the SolSOFT equation, which was introduced recently by our group [35]. This information enables the application of a short-cut method for assessing solvents for CO_2-absorption. The basic method for this purpose was developed some years ago by our group and is known to give good results for ranking solvents [22]. The method has recently been overhauled and the new version is called NoVa [35]. One of the advantages of NoVa is that it gives deep insight on the limitations of the absorption/desorption process. As its predecessor, NoVa yields a curve that relates the specific energy demand that is required for a given purification task to the ratio of the solvent flow rate and the feed gas flow rate. From that curve, the optimal liquid-to-gas ratio for the solvent and the minimal regeneration energy demand can be determined. The NoVa method was applied to all EvAs for which CO_2-solubility isotherms were measured, as well as to the references MEA and MDEA/PZ. The purification tasks that were considered were natural gas and synthesis gas purification. As expected, MEA is not an attractive solvent for these applications, in which MDEA/PZ is often used. Several of the EvAs outperform MDEA/PZ in this assessment. This shows the potential of the EvAs.

3.5 Conclusion

The 26 synthesized EvAs were investigated in an experimental screening. MEA and MDEA/PZ were included in the screening as references and treated the same way as the EvAs. Overall, the aqueous solutions of EvA02, EvA03, EvA25, and EvA34 emerge as the most promising candidates from the screening. EvA02 was studied in a previous work of our group [29]. Unfortunately, EvA02 shows solid precipitation even at moderate mass fractions of amine in the unloaded solvent, which makes the solvent unattractive for industrial CO_2-absorption [29]. In contrast, EvA03 has already proven its commercial

applicability as part of an amine blend [36], which, however, makes further results of EvA03 subject to confidentiality. EvA25 and EvA34 were investigated more in detail (cf. Section 4 and Section 5). The results from these investigations are in good agreement with those of the present section, revealing that both EvAs are highly interesting solvent candidates for improved CO_2-absorption.

This study provides also a broad basis for establishing structure-property relationships that relate the molecule structure of the EvAs to properties of its aqueous solution that are relevant for the CO_2-absorption. Only some aspects of this have been discussed in the present section. Many more have been elucidated after information on the chemical speciation of 16 EvAs became available. The elucidation and quantification of the chemical speciation in the EvAs as well as the relationships that were found between the chemical structure and the measured properties are presented in detail in Section 6. Based on the structure-property relationships, new advanced molecule structures for future amine based solvents for CO_2-absorption were developed (cf. Section 6).

4 Physico-chemical properties of the system (EvA34 + H$_2$O + CO$_2$)

4.1 Introduction

Aqueous solutions of EvA34 (cf. Figure 1) were found to be promising solvents for CO$_2$-absorption in the screening (cf. Section 3). The solvent EvA34 was, hence, studied in more detail. The liquid density and the dynamic viscosity was studied for pure EvA34, as well as for the systems (EvA34 + H$_2$O) and (EvA34 + H$_2$O + CO$_2$). The liquid heat capacity was studied for pure EvA34 and for the systems (EvA34 + H$_2$O). Furthermore, data on the vapor pressure of pure EvA34 was recorded. The pH-value was measured for the systems (EvA34 + H$_2$O) and (EvA34 + H$_2$O + CO$_2$) and the dissociation constants of EvA34 were determined from titration curves. Moreover, data on the solubility of CO$_2$ and data on the CO$_2$-containing species in the liquid phase of the system (EvA34 + H$_2$O + CO$_2$) were measured. Most of the new data was taken at temperatures between $t = 20\,°C$ and $t = 120\,°C$. The mass fraction of EvA34 in the unloaded solvent in studies of the system (EvA34 + H$_2$O + CO$_2$) was either $\tilde{w}^0_{\mathrm{EvA34}} = 0.1$ g/g or $\tilde{w}^0_{\mathrm{EvA34}} = 0.4$ g/g. For the system (EvA34 + H$_2$O), the mass fraction of EvA34 was varied between 0 g/g $\leq \tilde{w}^0_{\mathrm{EvA34}} \leq 1$ g/g. The CO$_2$-loading was up to $\tilde{\alpha}_{\mathrm{CO}_2} = 6.2$ mol/mol. Table 9 gives an overview of the experiments.

Table 9: Overview of the experiments with EvA34.

property	$\tilde{w}^0_{\mathrm{EvA34}}$ g/g	$\tilde{\alpha}_{\mathrm{CO}_2}$ mol/mol	p bar	t °C	data points
p_{CO_2}	0.1	0.3 - 2.8	0.02 - 0.74	40 - 120	20
	0.4	0.1 - 2.7	0.02 - 0.81	40 - 120	31
	0.1	2.1 - 6.2	5.1 - 73.2	40 - 120	22
	0.4	1.2 - 3.7	1.5 - 88.3	40 - 120	29
pK	0.01	0.0	amb	20 - 80	36
pH	0.001 - 0.4	0.0	*n.a.*	25 - 120	36
	0.1	0.3 - 2.6	*n.a.*	20 - 100	24
	0.4	0.3 - 2.6	*n.a.*	20 - 100	25
$\tilde{\alpha}_i$	0.1	0.2 - 3.1	*n.a.*	20 - 80	31
	0.4	0.1 - 3.3	*n.a.*	20 - 120	56

Table 9: continued from previous page

property	$\tilde{w}^0_{EvA34}$ g/g	$\tilde{\alpha}_{CO_2}$ mol/mol	p bar	t °C	data points
	0.1 - 1.0	0.0	amb	20 - 80	105
ρ	0.1	0.9 - 2.8	amb	20 - 80	25
	0.4	0.1 - 2.0	amb	20 - 90	59
	0.1 - 1.0	0.0	amb	20 - 80	105
η	0.1	0.9 - 2.8	amb	20 - 80	25
	0.4	0.1 - 2.0	amb	20 - 90	59
c_p	0.1 - 1.0	0.0	$^{n.a.}$	25 - 75	48
p^s	1.0	0.0	0.02 - 0.05	200 - 213	4

$\tilde{w}^0_{EvA34}$: mass fraction of EvA34 in the unloaded solvent, $\tilde{\alpha}_{CO_2}$: CO$_2$-loading, p: pressure, t: temperature, p_{CO_2}: partial pressure of CO$_2$, pK: pK-value, pH: pH-value, $\tilde{\alpha}_i$: quantification of CO$_2$-containing species, ρ: density, η: dynamic viscosity, c_p: liquid heat capacity, p^s: vapor pressure, amb: ambient pressure, $^{n.a.}$the pressure was not measured.

About 750 experimental data points are reported in the present section. The new data were compared to corresponding data for the widely used reference solvents for CO$_2$-absorption: MEA and MDEA/PZ. The aim of this comparison was to reevaluate the potential of EvA34 in aqueous solution for the reactive absorption of CO$_2$ in accordance with the results of the screening (cf. Section 3).

4.2 Experimental results

4.2.1 Gas solubility

The solubility of CO$_2$ in aqueous solutions of EvA34 from head space gas chromatography and from high pressure view cell experiments are presented in Figure 9. In the diagrams the partial pressure of CO$_2$ p_{CO_2} in the system (EvA34 + H$_2$O + CO$_2$) at $t = 40$ °C, $t = 80$ °C, and $t = 120$ °C with $\tilde{w}^0_{EvA34} = 0.1$ g/g and $\tilde{w}^0_{EvA34} = 0.4$ g/g is shown as a function of the CO$_2$-loading $\tilde{\alpha}_{CO_2}$ and mass fraction of CO$_2$ $\tilde{w}_{CO_2}$. The corresponding numerical experimental data are given in Appendix E. The partial pressure of CO$_2$ from head space gas chromatography experiments were used directly in the diagrams. The partial pressure of CO$_2$ from high pressure view cell experiments were calculated from the measured bubble point pressure in the same way as described in a previous work of our group [48].

The isotherms in Figure 9 show a parallel shape in most regions of both diagrams. The isotherms for $\tilde{w}^0_{EvA34} = 0.4$ g/g below a partial pressure of CO$_2$ of about $p_{CO_2} \leq 5$ bar,
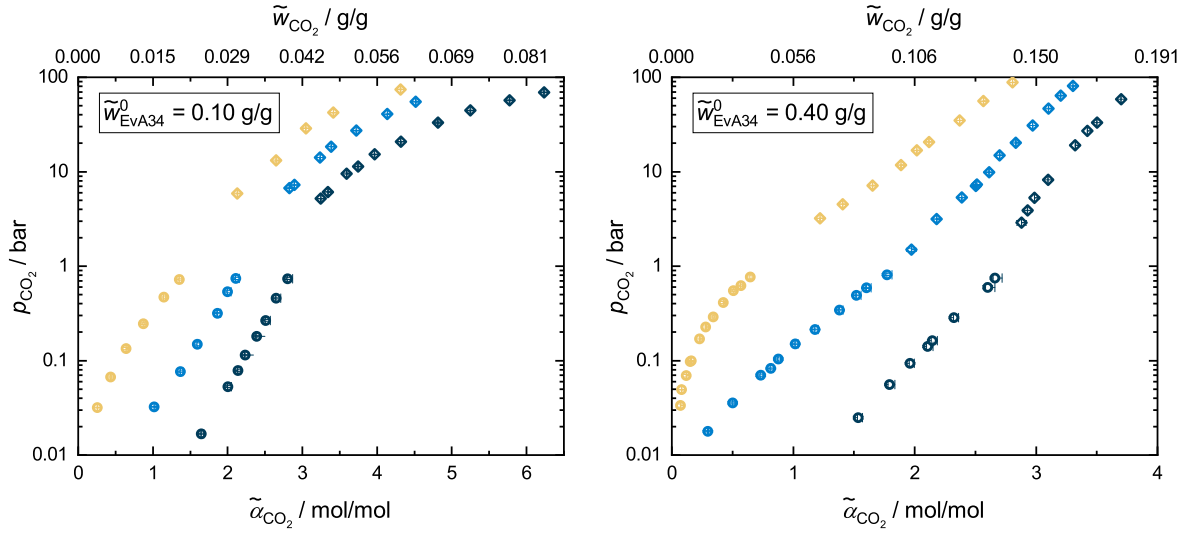
Figure 9: CO_2-solubility in the system $(EvA34 + H_2O + CO_2)$ with $\tilde{w}^0_{EvA34} = 0.1$ g/g and $\tilde{w}^0_{EvA34} = 0.4$ g/g. Experimental results from the present work. ○: from head space gas chromatography, ◇: from high pressure view cell. Black: $t = 40$ ℃, blue: $t = 80$ ℃, yellow: $t = 120$ ℃.

however, differ in their shape. The isotherm at $t = 40$ ℃ shows a slight convex bulge towards higher CO_2-loadings, whereas the isotherm at $t = 120$ ℃ does not. The difference between the two isotherms in this pressure region increases, which is generally beneficial for CO_2-absorption processes (cf. Section 3).

4.2.2 Chemical equilibrium

4.2.2.1 pK-values

Figure 10 (left) shows an exemplary result from a titration experiment of EvA34 highly diluted in H_2O at $t = 40$ ℃. The measured pH-value of the titration curve and its first derivative are shown as a function of the added volume of 1M NaOH titrant $V_{1M\ NaOH}$. The equivalent points EP1, EP2, EP3, and EP5 are taken at the turning points of the first derivative. EP4 can not be determined directly from the first derivative. It is calculated by assuming equivalent volumes of titrant between every equivalent point. The pK-values are determined at the mean added volumes of titrant between two adjacent equivalent points [114]. The true pK-values between EP3 and EP4, as well as between EP4 and EP5 might differ from the values, determined with this method.

Figure 10 (right) shows the pK-values of EvA34 highly diluted in H_2O, which were extracted from the resulting curves of the titration experiments at four temperatures between $t = 20$ ℃ and $t = 80$ ℃. The corresponding numerical experimental data are

given in Appendix E. The pK-values are designated using the amino group labeling from Figure 1. The assignment between the pK-values and the amino groups was taken from the considerations given in the screening (cf. Section 3.2.3).
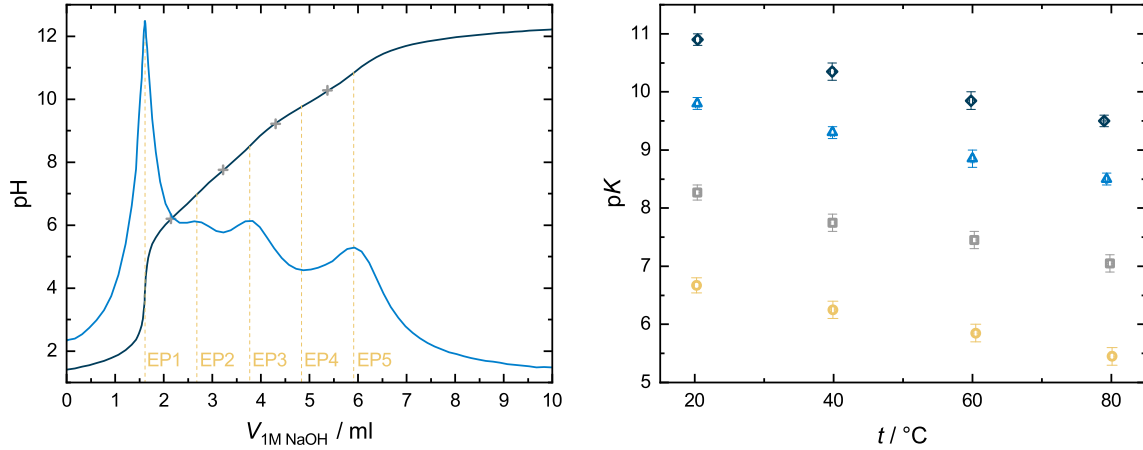
Figure 10: Left: Exemplary result of a titration experiment with EvA34 highly diluted in H$_2$O at $t = 40\,$°C. black solid line: pH-value, blue solid line: first derivative of the pH-value, yellow dashed line: EP (equivalent point), $+$: pK-value. Right: pK-values of the four amino groups of EvA34 (cf. Figure 1). Experimental results from the present work. ◇: α-amino group, △: δ-amino group, □: β-amino group, ○: γ-amino group.

4.2.2.2 pH-value

Figure 11 shows the pH-value of the system (EvA34 + H$_2$O) as a function of the mass fraction of EvA34 in the unloaded solvent $\tilde{w}^0_{\text{EvA34}}$ for four temperatures between $t = 25$ °C and $t = 120$ °C. The corresponding numerical experimental data are given in Appendix E. Compared to other solvents that are often used for CO$_2$-absorption [6, 48, 115], the obtained pH-values of the system (EvA34 + H$_2$O) are remarkably high. As expected, the pH-values increase with increasing mass fraction of EvA34 and decrease with increasing temperature.

Figure 12 shows the pH-value of the system (EvA34 + H$_2$O + CO$_2$) with $\tilde{w}^0_{\text{EvA34}} = 0.1$ g/g and $\tilde{w}^0_{\text{EvA34}} = 0.4$ g/g at $t = 20$ °C, $t = 60$ °C, and $t = 100$ °C as a function of the CO$_2$-loading $\tilde{\alpha}_{\text{CO}_2}$ and mass fraction of CO$_2$ $\tilde{w}_{\text{CO}_2}$. The corresponding numerical experimental data are given in Appendix E. The pH-value decreases almost linearly with increasing CO$_2$-loading except for very low loadings. The change in the pH-value as a function of the temperature slightly decreases with increasing CO$_2$-loading.
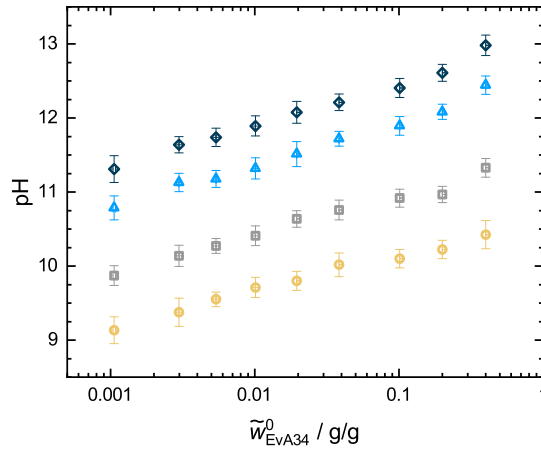
Figure 11: pH-value of the system (EvA34 + H$_2$O). Experimental results from the present work. ◇: $t = 25$ ℃, △: $t = 40$ ℃, □: $t = 80$ ℃, ○: $t = 120$ ℃.
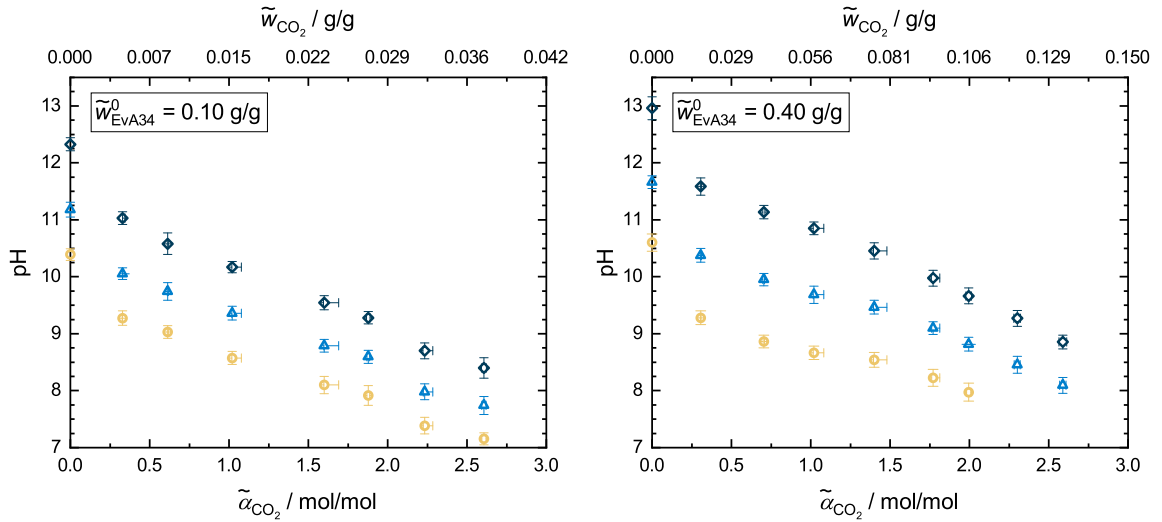
Figure 12: pH-value of the system (EvA34 + H$_2$O + CO$_2$) with $\tilde{w}^0_{\mathrm{EvA34}} = 0.1$ g/g and $\tilde{w}^0_{\mathrm{EvA34}} = 0.4$ g/g. Experimental results from the present work. ◇: $t = 20$ ℃, △: $t = 60$ ℃, ○: $t = 100$ ℃.

4.2.2.3 Elucidation of CO$_2$-containing species

Figure 13 shows the CO$_2$-containing species in the system (EvA34 + H$_2$O + CO$_2$) that were identified by NMR spectroscopy in the present work. The elucidation is described in detail in Appendix D. CO$_2$ reacts with both, the β- and γ-amino group of EvA34 to form β-carbamate, γ-carbamate and β-γ-dicarbamate with the greek letter giving information about the carbamate position (cf. Figure 1). Also (bi)carbonate is formed. Protonated and unprotonated species cannot be distinguished in NMR spectra. Depending on the pH-value, differently protonated species of the carbamates and carbonates arise. The results from NMR experiments include all protonation-states of the corresponding species.
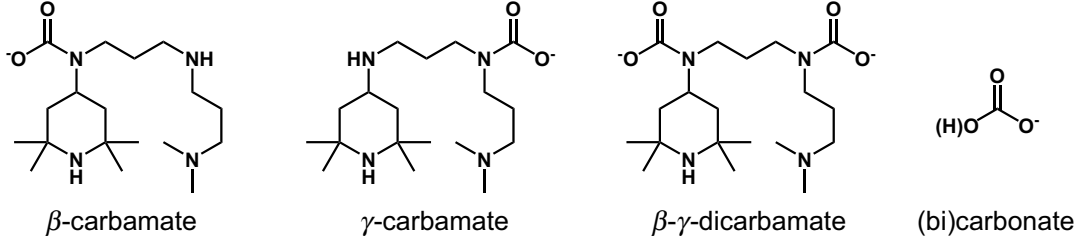
Figure 13: CO$_2$-containing species in the system (EvA34 + H$_2$O + CO$_2$). Experimental results from the present work. Greek letters indicate the position of the carbamate group corresponding to the designation in Figure 1.

4.2.2.4 Quantification of CO$_2$-containing species

Figure 14 shows the concentrations $\tilde{\alpha}_i$ of the CO$_2$-containing species (cf. Figure 13) in the system (EvA34 + H$_2$O + CO$_2$) for $\tilde{w}^0_{\text{EvA34}} = 0.1$ g/g and $\tilde{w}^0_{\text{EvA34}} = 0.4$ g/g at $t = 20$ ℃ as a function of the CO$_2$-loading $\tilde{\alpha}_{\text{CO}_2}$ and mass fraction of CO$_2$ $\tilde{w}_{\text{CO}_2}$. The corresponding numerical experimental data are given in Appendix E.

The major carbamate species is γ-carbamate. The concentrations of β-carbamate and β-γ-dicarbamate are low. The concentrations of β-carbamate and γ-carbamate increase with increasing CO$_2$-loading until they reach a maximum value which does not change significantly upon a further increase of the CO$_2$-loading. For $\tilde{w}^0_{\text{EvA34}} = 0.4$ g/g, this maximum is reached at a lower CO$_2$-loading than for $\tilde{w}^0_{\text{EvA34}} = 0.1$ g/g. For $\tilde{w}^0_{\text{EvA34}} = 0.4$ g/g, β-γ-dicarbamate is only observed at high CO$_2$-loadings. The loading of β-γ-dicarbamate as a function of the CO$_2$-loading shows a maximum. No β-γ-dicarbamate was found for $\tilde{w}^0_{\text{EvA34}} = 0.1$ g/g.
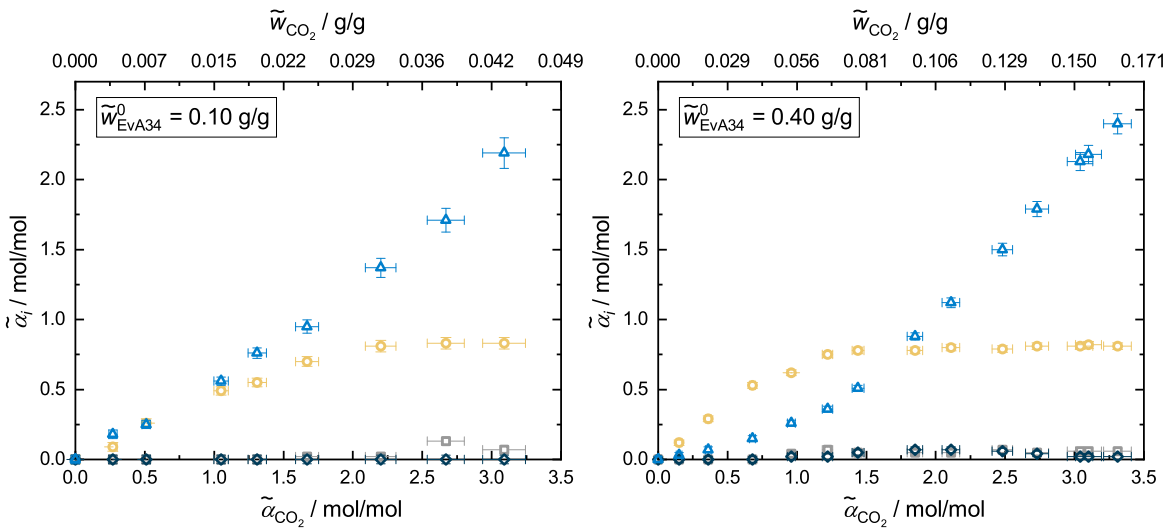
Figure 14: Concentration of the CO$_2$-containing species in the system (EvA34 + H$_2$O + CO$_2$) with $\tilde{w}^0_{\text{EvA34}} = 0.1$ g/g and $\tilde{w}^0_{\text{EvA34}} = 0.4$ g/g at $t = 20$ ℃. Experimental results from the present work. $\triangle$: (bi)carbonate, $\circ$: γ-carbamate, $\square$: β-carbamate, $\diamond$: β-γ-dicarbamate.

With increasing temperature, the concentration of carbamates decrease. This is demonstrated for γ-carbamate in Figure 15, where the speciation of γ-carbamate $\tilde{\alpha}_{\gamma-\text{carbamate}}$ in the system (EvA34 + H_2O + CO_2) for $\tilde{w}^0_{\text{EvA34}} = 0.1$ g/g and $\tilde{w}^0_{\text{EvA34}} = 0.4$ g/g at six temperatures between $t = 20\,°C$ and $t = 120\,°C$ is shown as a function of the CO_2-loading $\tilde{\alpha}_{CO_2}$ and mass fraction of CO_2 $\tilde{w}_{CO_2}$. The corresponding numerical experimental data are given in Appendix E. The decrease of the concentration of γ-carbamate with increasing temperature is stronger for $\tilde{w}^0_{\text{EvA34}} = 0.1$ g/g than for $\tilde{w}^0_{\text{EvA34}} = 0.4$ g/g. For $\tilde{w}^0_{\text{EvA34}} = 0.4$ g/g, a significant decrease is only observable above $t > 80\,°C$. The same observations were made for the concentrations of β-carbamate and β-γ-dicarbamate.
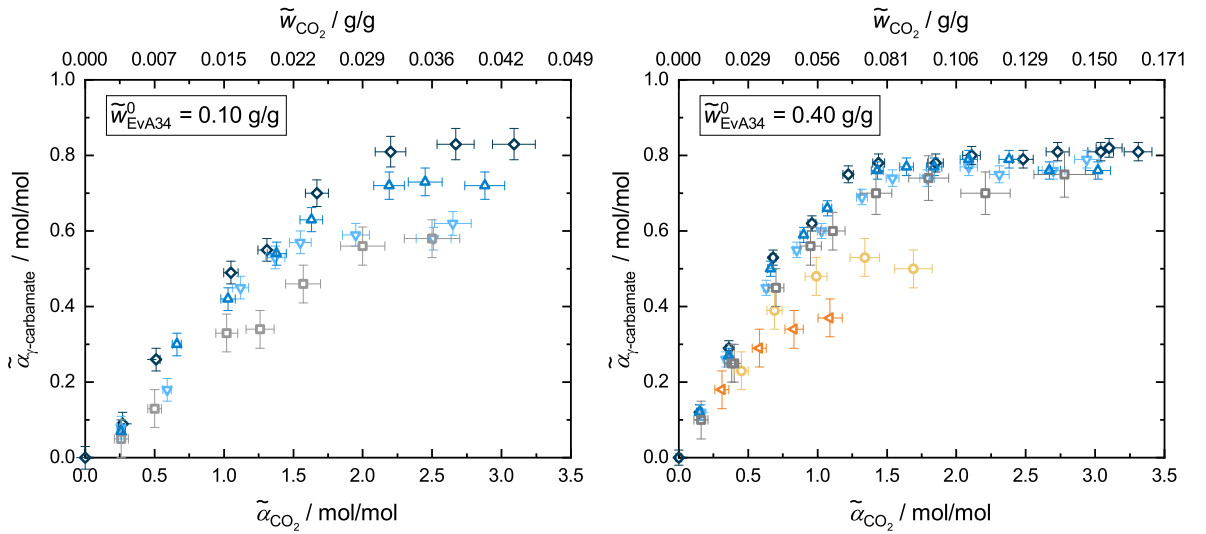
Figure 15: Temperature dependence of the concentration of γ-carbamate in the system (EvA34 + H_2O + CO_2) with $\tilde{w}^0_{\text{EvA34}} = 0.1$ g/g and $\tilde{w}^0_{\text{EvA34}} = 0.4$ g/g. Experimental results from the present work. $\diamond$: $t = 20\,°C$, $\triangle$: $t = 40\,°C$, $\triangledown$: $t = 60\,°C$, $\square$: $t = 80\,°C$, $\circ$: $t = 100\,°C$. $\triangleleft$: $t = 120\,°C$.

4.2.3 Density and dynamic viscosity

Figure 16 shows the density ρ and dynamic viscosity η of the system (EvA34 + H_2O) at seven temperatures between $t = 20\,°C$ and $t = 80\,°C$ as a function of the mass fraction of EvA34 in the unloaded solvent $\tilde{w}^0_{\text{EvA34}}$. The corresponding numerical experimental data are given in Appendix E.

The density of pure EvA34 is $\rho = 907$ g/cm³ at $t = 20\,°C$ and $\rho = 863$ g/cm³ at $t = 80\,°C$. For H_2O-rich mixtures, the density depends only weakly on the EvA34 concentration. For the lowest studied temperatures, a maximum in the density at about $\tilde{w}^0_{\text{EvA34}} = 0.4$ g/g is observable. The maximum relative increase of the density is 0.7 % compared to pure H_2O and is found for $t = 20\,°C$. It seems, that in H_2O-rich mixtures, the formation of an electrolyte system compensates the influence of the lower density
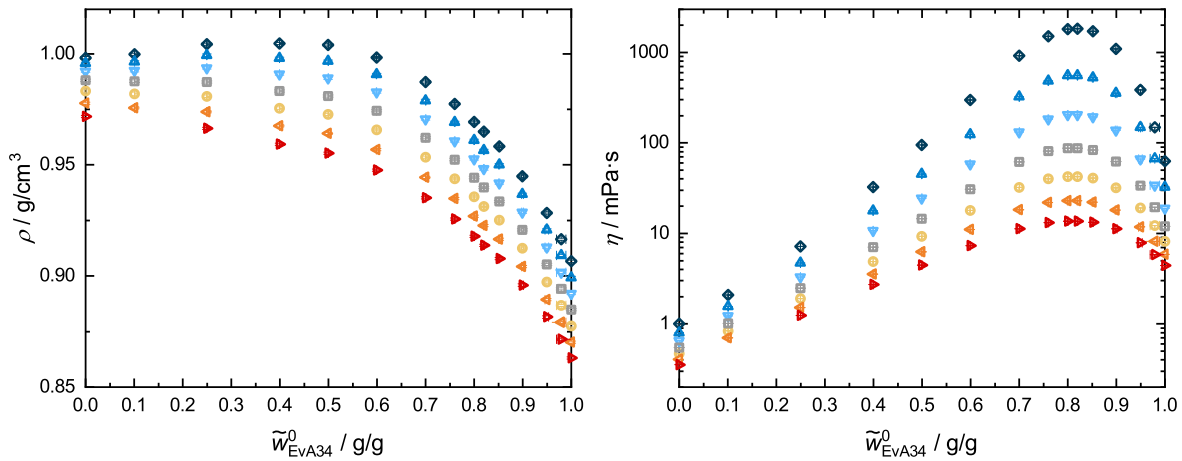
Figure 16: Density and dynamic viscosity of the system (EvA34 + H$_2$O). Experimental results from the present work. $\diamondsuit$: $t = 20$ ℃, $\triangle$: $t = 30$ ℃, $\triangledown$: $t = 40$ ℃, $\square$: $t = 50$ ℃, $\circ$: $t = 60$ ℃. $\triangleleft$: $t = 70$ ℃, $\triangleright$: $t = 80$ ℃.

of EvA34. At $\tilde{w}^0_{\mathrm{EvA34}} > 0.4$ g/g, the density decreases with increasing concentration of EvA34 and increasing temperature.

The dynamic viscosity of pure EvA34 is between $\eta = 63$ mPa·s at $t = 20$ ℃ and $\eta = 5$ mPa·s at $t = 80$ ℃. There is a maximum of the dynamic viscosity at about $\tilde{w}^0_{\mathrm{EvA34}} = 0.8$ g/g. This value equals a ratio between H$_2$O molecules and amino groups of 1/1. The maximum values are $\eta = 1829$ mPa·s at $t = 20$ ℃ and $\eta = 13.7$ mPa·s at $t = 80$ ℃. It can be assumed that H-bond-stabilized clusters are formed between EvA34 and H$_2$O that cause this strong increase in the dynamic viscosity.

The dynamic viscosity is very sensitive to the mass fraction of H$_2$O. One of the impurities of EvA34 is H$_2$O (cf. Section 2.1). Even though the amount of H$_2$O as an impurity in pure EvA34 is low (less than 0.01 g/g), it might have an influence on the measured dynamic viscosity. This should be kept in mind when the absolute values of the dynamic viscosity are regarded. The general interpretation and conclusions made from the results, however, retain their validity.

Figure 17 shows the density ρ and dynamic viscosity η of the system (EvA34 + H$_2$O + CO$_2$) at eight temperatures between $t = 20$ ℃ and $t = 90$ ℃ with $\tilde{w}^0_{\mathrm{EvA34}} = 0.1$ g/g and $\tilde{w}^0_{\mathrm{EvA34}} = 0.4$ g/g as a function of the CO$_2$-loading $\tilde{\alpha}_{\mathrm{CO_2}}$ and mass fraction of CO$_2$ $\tilde{w}_{\mathrm{CO_2}}$. The corresponding numerical experimental data are given in Appendix E. The density increases almost linearly with increasing CO$_2$-loading. The influence of the CO$_2$-loading on the dynamic viscosity is small for $\tilde{w}^0_{\mathrm{EvA34}} = 0.1$ g/g. However, for $\tilde{w}^0_{\mathrm{EvA34}} = 0.4$ g/g an increase of the dynamic viscosity is observable with increasing CO$_2$-loading. The slope of the increase changes at a CO$_2$-loading of about $\tilde{\alpha}_{\mathrm{CO_2}} = 1.5$ mol/mol. A comparison of the results that are shown in Figure 14 and Figure 17 indicates that this change of the slope could be related to the influence of the carbamates.
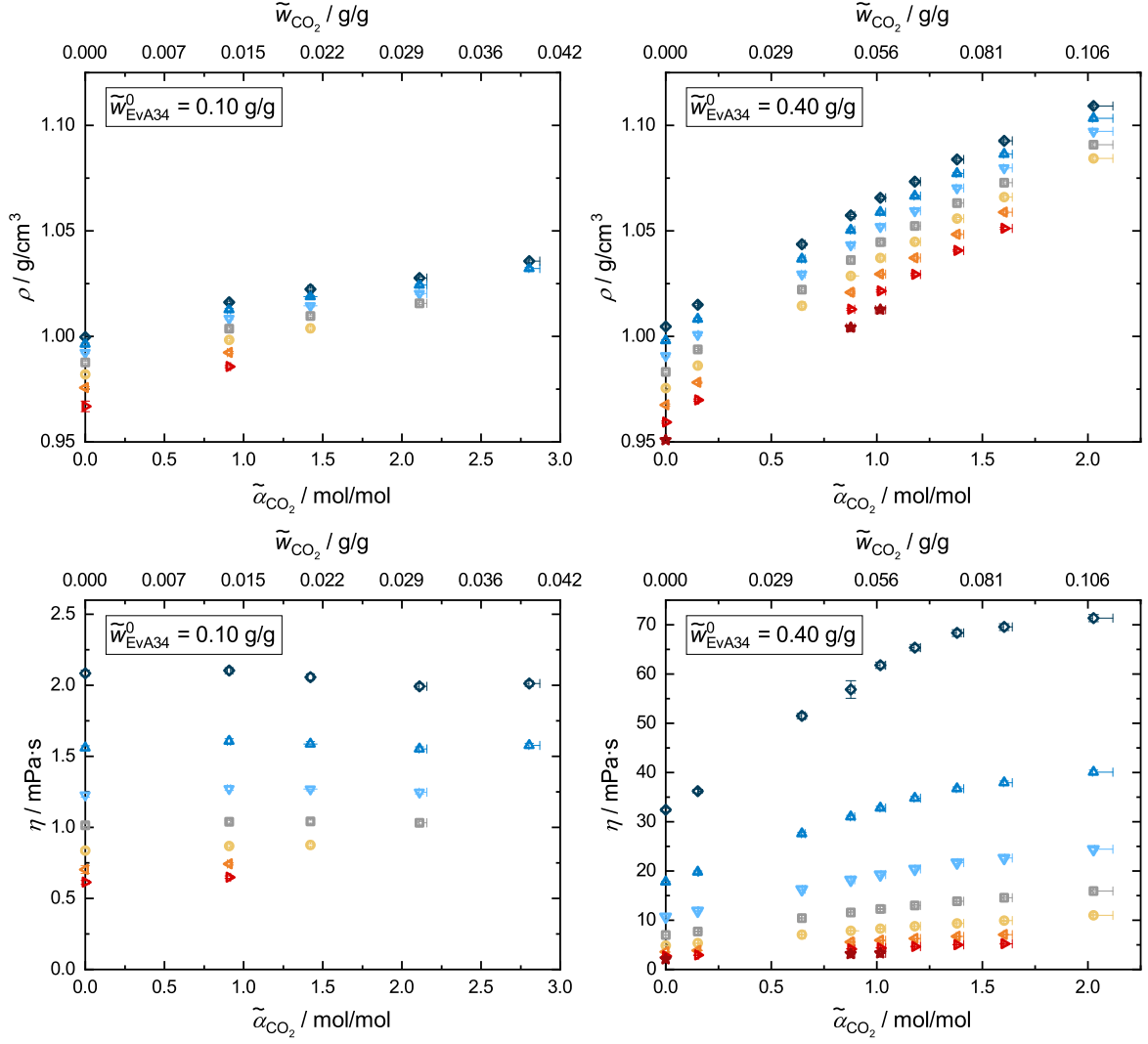
Figure 17: Density and dynamic viscosity of the system $(EvA34 + H_2O + CO_2)$ with $\tilde{w}^0_{EvA34} = 0.1$ g/g and $\tilde{w}^0_{EvA34} = 0.4$ g/g. Experimental results from the present work. $\diamond$: $t = 20$ ℃, $\triangle$: $t = 30$ ℃, $\triangledown$: $t = 40$ ℃, $\square$: $t = 50$ ℃, $\circ$: $t = 60$ ℃, $\triangleleft$: $t = 70$ ℃, $\triangleright$: $t = 80$ ℃, $\star$: $t = 90$ ℃.

4.2.4 Liquid heat capacity

In Figure 18 the liquid heat capacity c_p of the system $(EvA34 + H_2O)$ is presented as a function of the mass fraction of EvA34 in the unloaded solvent $\tilde{w}^0_{EvA34}$ for six temperatures between $t = 25$ ℃ and $t = 75$ ℃. The corresponding numerical experimental data are given in Appendix E. A maximum of the liquid heat capacity is observable at about $\tilde{w}^0_{EvA34} = 0.1$ g/g. However, the increase of the heat capacity in that maximum compared to that of water is small and does not exceed the experimental standard uncertainty. The liquid heat capacity of pure EvA34 is between 2.05 kJ/(kg·K) at $t = 25$ ℃ and 2.25 kJ/(kg·K) at $t = 75$ ℃.
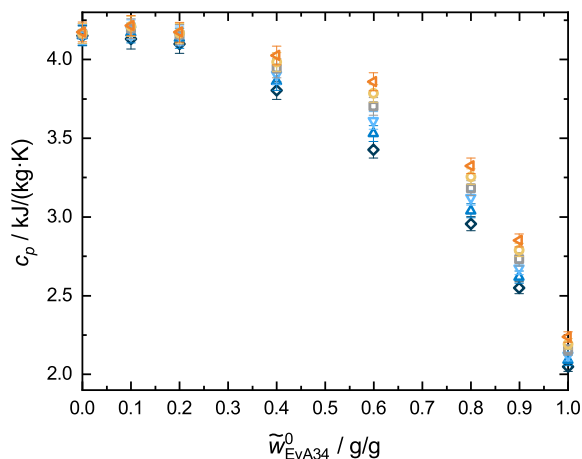
Figure 18: Liquid heat capacity of the system (EvA34 + H$_2$O). Experimental results from the present work. $\diamond$: $t = 25\,°C$, $\triangle$: $t = 35\,°C$, $\triangledown$: $t = 45\,°C$, $\square$: $t = 55\,°C$, $\circ$: $t = 65\,°C$, $\triangleleft$: $t = 75\,°C$.

4.2.5 Vapor pressure

The vapor pressure p^s of pure EvA34 is about $p^s = 20$ mbar at $t = 201\,°C$ and $p^s = 50$ mbar at $t = 213\,°C$. The corresponding numerical experimental data are given in Appendix E. Due to the onset of carbonization at high temperatures, only low pressures could be studied. Compared to other amines that are used for CO$_2$-absorption [6], EvA34 has a very low vapor pressure.

4.3 Comparison of EvA34 with MEA and MDEA/PZ

A comparison of the experimental results for EvA34 with literature data for MEA and a mixture of MDEA and PZ with a mass ratio of 7/1 (MDEA/PZ) is presented in this section. MEA is a common primary amine and often used as a reference in studies of solvents for CO$_2$-absorption. Mixtures of MDEA and PZ are commonly used for the CO$_2$-absorption from synthesis gas and can be seen as a benchmark in that field [6, 10]. In the following comparison, pure component data and data for aqueous solutions of amines with $\tilde{w}^0_{\text{amine}} = 0.4$ g/g are discussed. Two temperatures are considered: $t = 40\,°C$ and $t = 120\,°C$. These conditions are chosen because of their relevance for the industrial application.

A comparison of the pure component vapor pressure p^s, as well as of the liquid heat capacity c_p and dynamic viscosity η of EvA34, MEA, MDEA/PZ, and its mixtures

with H_2O is shown in Table 10. The vapor pressure of EvA34 is extrapolated from the measured data.

Table 10: Properties of EvA34, MEA, MDEA/PZ and their mixtures with H_2O.

	t °C	$\tilde{w}^0_{amine}$ g/g	EvA34	MEA	MDEA/PZ
c_p / kJ/(kg·K)	40	0.4	3.86^a	3.63 [116]	3.55 [117]
		1.0	2.11^a	2.78 [118]	2.35 [117]
η / mPa·s	40	0.4	10.7^a	2.3 [119]	3.5^a
		1.0	18.9^a	9.6 [119]	45.1^a
p^s / mbar	120	1.0	$\leq 0.02^b$	163.3 [120]	9.8 [120] / 162.8 [121]

t: temperature, $\tilde{w}^0_{amine}$: mass fraction of amine in the unloaded solvent, c_p: liquid heat capacity, η: dynamic viscosity, p^s: vapor pressure, ^{a}this work, ^{b}extrapolated from data of this work

The low vapor pressure of EvA34 compared to that of MEA and MDEA/PZ minimizes amine losses in CO_2-absorption processes. The viscosity of aqueous solutions of EvA34 is significantly higher than those of MEA and MDEA/PZ. The addition of CO_2 further increases the viscosity (cf. Figure 17) [122, 123]. Higher viscosities typically have negative influence on the mass transfer and reduce the rate of absorption [124]. The slightly higher liquid heat capacity of aqueous solutions of EvA34 is not relevant for the energy demand of CO_2-absorption processes.

Figure 19 shows a comparison of the CO_2-solubility and the chemical equilibrium of the three considered solvents. The data for MEA and MDEA/PZ is generated from the model of Wagner et al. [48] and Ermatchkov et al. [115], respectively. The upper row of the diagrams shows the partial pressure of CO_2 p_{CO_2}. The middle row shows the amount of CO_2 chemically bound as carbamates in relation to the summed amounts of CO_2 that is chemically bound as carbamates or carbonates; the carbamate ratio ξ_{CARB}. The bottom row shows the pH-value of the solvents. The pH-values for EvA34 were linearly inter- and extrapolated from the measured pH-values at $t = 20$ °C, $t = 60$ °C, and $t = 100$ °C (cf. Section 4.2.2.2). All values are depicted as a function of the mass-related CO_2-loading $\tilde{X}_{CO_2}$.

The CO_2-solubility in aqueous solutions of EvA34 and MEA at $t = 40$ °C is significantly higher than in aqueous solutions of MDEA/PZ. This is beneficial since the absorption rate increases and the amount of solvent needed for a given purification task decreases. At low partial pressure of CO_2, the high CO_2-solubility is favorable to achieve low residual amounts of CO_2 in the gas streams. This is important, e.g., in synthesis gas purification, where partial pressures of CO_2 down to few ppm are targeted. In this region, EvA34 fails MEA but exceeds MDEA/PZ by far. At $t = 120$ °C, the CO_2-
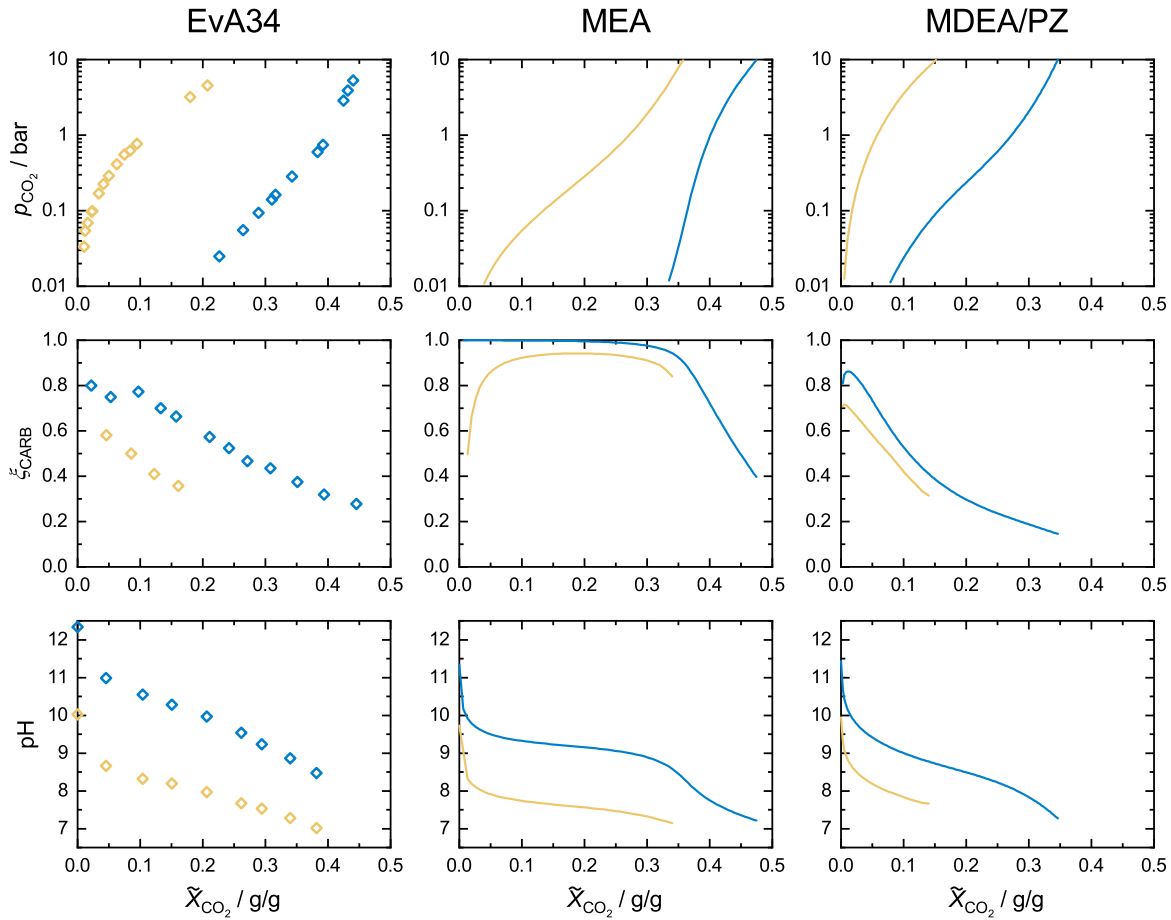
Figure 19: Comparison of the CO$_2$-solubility (top row) carbamate ratio in the liquid phase (middle row) and pH-value (bottom row) in aqueous solutions of amines with $\tilde{w}^0_{\mathrm{amine}} = 0.4$ g/g. Blue: $t = 40$ °C, yellow: $t = 120$ °C. ◇: Experimental results from the present work, solid lines: results generated from a model for MEA [48] and MDEA/PZ [115].

solubility in aqueous solutions of EvA34 and MDEA/PZ is much lower than in aqueous solutions of MEA. EvA34 and MDEA/PZ differ slightly in the higher pressure region, where the CO$_2$-solubility in MDEA/PZ is lower than in EvA34. A low CO$_2$-solubility reduces the amount of stripping steam required for the regeneration as more CO$_2$ flashes from the solvent just because of the pressure drop and temperature increase between absorber and desorber. The reduction of stripping steam lowers the energy demand for the regeneration of the solvent.

The ratio of CO$_2$ that is chemically bound as carbamates at $t = 40$ °C and $t = 120$ °C is much higher for aqueous solutions of MEA than for aqueous solutions of EvA34 and MDEA/PZ. At $t = 40$ °C, EvA34 forms more carbamates than MDEA/PZ. At $t = 120$ °C the ratios of EvA34 and MDEA/PZ are similar. The formation of carbamates is faster than the formation of carbonates [125]. Fast reactions are favorable for the absorption.

However, the regeneration of carbamates demands more energy than the regeneration of carbonates [8, 11, 126–128].

The pH-value in aqueous solutions of EvA34 at $t = 40$ ℃ is significantly higher than that in aqueous solutions of MEA and MDEA/PZ. High pH-values are favorable for the absorption as they increase the capacity of CO_2 of the solvent and increase the rate of absorption of CO_2 (cf. Section 3). At $t = 120$ ℃, the differences between the three solvents are small and the pH-value is low. Low pH-values are favorable for desorption as the equilibrium of the CO_2-hydrolysis reaction is shifted towards molecular CO_2, which can more easily be desorbed than chemically bound CO_2 [129, 130]. Overall, the larger difference between the pH-values at $t = 40$ ℃ and $t = 120$ ℃ of EvA34, compared to MEA and MDEA/PZ is advantageous.

For a CO_2-absorption process, EvA34 combines the favorable properties of MEA and MDEA/PZ in one molecule. EvA34 shows both, high CO_2-solubility at absorption conditions and low CO_2-solubility at desorption conditions. The large difference between the CO_2-solubility of EvA34 at $t = 40$ ℃ and $t = 120$ ℃ compared to MEA and MDEA/PZ allows to reduce the amount of solvent needed for a given purification task. Furthermore, it gives the opportunity to operate EvA34 at higher equilibrium loadings in both, absorber and desorber to reduce the amount of stripping steam needed for the regeneration. Furthermore, the wide operation window gives flexibility for adjusting process conditions. For example, the temperature could be increased, which would lead to a lower viscosity and improved mass transfer kinetics.

4.4 Conclusion

Results from a comprehensive study of physico-chemical properties of the system (EvA34 + H_2O + CO_2) are presented. CO_2-solubility, chemical equilibrium, density, dynamic viscosity, vapor pressure, and liquid heat capacity were measured. The data of the present section confirm the conclusions made for EvA34 in the screening. A detailed comparison to literature data for MEA and MDEA/PZ shows that aqueous solutions of EvA34 are interesting solvents for reactive CO_2-absorption processes, as EvA34 combines favorable properties of MEA and MDEA/PZ in one molecule. For further evaluation of this potential, pilot plant experiments and a reliable thermodynamic equilibrium model are required. The experimental data presented in this section provide the information to build such a model.

5 Phase equilibria in the system (EvA25 + H$_2$O + CO$_2$)

5.1 Introduction

A promising approach to reduce the energy demand of CO_2-absorption processes is the use of solvent systems that lead to solid-liquid or liquid-liquid phase split in the process and to take advantage of the distribution of CO_2 between the coexisting phases. The few available studies on using solid-liquid phase splits for improved CO_2-absorption have not yielded encouraging results [111–113]. Using liquid-liquid phase splits has been studied more broadly [37–43, 45, 110, 131–139], and some of the results indicate that the effect might be useful for designing CO_2-absorption processes with lower energy demand. Zhuang et al. [26] have given a review of work in this field. However, the discussions of such processes suffer from a lack of reliable thermodynamic data on the phase behavior of the investigated systems.

The present Section aims to fill this gap. It provides a comprehensive study of the system (EvA25 + H$_2$O + CO$_2$). EvA25 (cf. Figure 1) did not only turned out to be one of the best-performing solvents in the screening (cf. Section 3), but also showed a liquid-liquid phase split in a temperature range that is interesting for the design of an adapted new CO_2-absorption process. The liquid-liquid equilibrium (LLE) of the system (EvA25 + H$_2$O+ CO$_2$) has a lower critical temperature above about $t \geq 60$ °C. As a consequence, a liquid-liquid phase split can be avoided at the low absorption temperatures, whereas at the high desorption temperatures, the liquid-liquid phase split occurs.

For the investigation of the LLE in the system (EvA25 + H$_2$O + CO$_2$), a new analytical apparatus was built (cf. Section 2.5). The CO$_2$-solubility (VLE) was studied the same way as in the previous sections. Also, solid-liquid phase splits were observed in the system, so that also the compositions and conditions, where a solid phase occurs (SLE) were included in the study. The results of the LLE, VLE, and SLE were linked to determine the solid-liquid-liquid-vapor equilibrium in the system (EvA25 + H$_2$O + CO$_2$). This approach yields an overview of the phase behavior of the studied system, which, in turn, is the basis for a sound discussion of benefits that could be drawn from the formation of new phases in the design of advanced CO_2-absorption processes.

In addition to the phase equilibrium measurements, some further measurements were performed: pK-values of EvA25 highly diluted in H$_2$O (pK), pH-values (pH) in the system (EvA25 + H$_2$O) and (EvA25 + H$_2$O + CO$_2$), chemical speciation ($\tilde{\alpha}_i$) in the

system (EvA25 + H_2O + CO_2), liquid heat capacity (c_p) of pure EvA25 and in the system (EvA25 + H_2O), density (ρ) and dynamic viscosity (η) of pure EvA25 as well as in the system (EvA25 + H_2O) and (EvA25 + H_2O + CO_2), and vapor pressure of pure EvA25 (p^s). The focus of the present section is on the LLE, SLE, and VLE. To keep it concise, these additional measured data is presented in Appendix C. Table 11 gives an overview of all experiments that were made for the present study. The Table also includes the Section where the results are presented. In total, more than 750 data points were measured.

Table 11: Overview of the detailed experiments for the system (EvA25 + H_2O + CO_2).

property	$\tilde{w}^0_{\text{EvA25}}$ g/g	$\tilde{\alpha}_{CO_2}$ mol/mol	p bar	t °C	data points	presented in
SLE	0.35 - 1.0	0.0 - 2.2	*n.a.*	10 - 95	115	this section
LLE	0.35	0.0	*n.a.*	69 - 130	26	this section
	0.35 - 0.65	0.1 - 0.8	*n.a.*	65 - 120	118	
VLE	0.15	0.1 - 2.1	0.02 - 1.10	40 - 120	29	this section
	0.35	0.03 - 2.1	0.02 - 0.71	40 - 120	28	
	0.15	1.5 - 4.3	4.6 - 76.5	40 - 120	31	
	0.35	0.5 - 3.2	2.7 - 73.8	40 - 120	25	
pK	0.01	0.0	amb	20 - 80	12	Appendix C
pH	0.001 - 0.35	0.0	*n.a.*	25 - 120	28	Appendix C
	0.1	0.4 - 2.2	*n.a.*	20 - 100	19	
	0.15	0.3 - 2.2	*n.a.*	20 - 100	23	
	0.35	0.1 - 2.4	*n.a.*	20 - 100	26	
$\tilde{\alpha}_i$	0.15	0.4 - 2.5	*n.a.*	20 - 100	32	Appendix C
	0.35	0.3 - 2.7	*n.a.*	20 - 100	25	
ρ	0.15 - 1.0	0.0	amb	20 - 90	56	Appendix C
	0.15	0.5 - 1.9	amb	20 - 60	22	
	0.35	0.2 - 1.9	amb	20 - 70	29	
η	0.15 - 1.0	0.0	amb	20 - 90	56	Appendix C
	0.15	0.5 - 1.9	amb	20 - 60	22	Appendix C
	0.35	0.2 - 1.9	amb	20 - 60	29	
c_p	0.1 - 1.0	0.0	*n.a.*	25 - 75	27	Appendix C
p^s	1.0	0.0	0.01 - 0.05	164 - 190	8	Appendix C

SLE: solid-liquid equilibrium (liquidus temperature), LLE: liquid-liquid equilibrium, VLE: vapor-liquid equilibrium (CO_2-solubility), $\tilde{w}^0_{\text{EvA25}}$: mass fraction of EvA25 in the unloaded solvent of the feed solution, $\tilde{\alpha}_{CO_2}$: CO_2-loading, p: pressure, t: temperature, pK: pK-value, pH: pH-value, $\tilde{\alpha}_i$: quantification of CO_2-containing species, c_p: liquid heat capacity, ρ: density, η: dynamic viscosity, p^s: vapor pressure, amb: ambient pressure, *n.a.* the pressure was not measured.

5.2 Experimental results

5.2.1 Solid-liquid equilibrium

Figure 20 gives an overview of the results of the measurements of the liquidus tempera-
ture in the system ($EvA25 + H_2O + CO_2$). The corresponding numerical experimental
data are given in Appendix E. The studied temperature range was between $t = 10\,°C$
and $t = 80\,°C$. The following discussion refers only to this temperature range. The
composition of the individual experiments can be read from the diagram in Figure 20.
In the ternary diagrams that are used in the present section, the bottom axis shows
the binary system ($EvA25 + H_2O$) with pure EvA25 on the left corner of the ternary
diagram and pure H_2O on the right corner of the ternary diagram. Pure CO_2 would
be found in the top corner of the diagram, but is not shown as only mixtures with
comparatively low mass fractions of CO_2 were investigated in the present work and are
shown in the diagrams. The mass fraction of CO_2 can be read from the right axis of
the ternary diagram. The liquidus temperatures, which are subject to large uncertainty,
were binned in order to improve the clarity of the representation. The bins are mostly
about 5 °C to 7 °C wide, except for temperatures below $t = 43\,°C$, which were all put
into a single bin. A color code indicates the temperature. Experiments for which no
formation of solid was observed are marked by a gray square. As can be seen from Fig-
ure 20, no solids were observed in unloaded mixtures of EvA25 and H_2O in the studied
temperature range. Adding CO_2 leads to the formation of solids for mass fractions of
EvA25 in the unloaded solvent above about $\tilde{w}^0_{EvA25} = 0.35$ g/g. The amount of CO_2 that
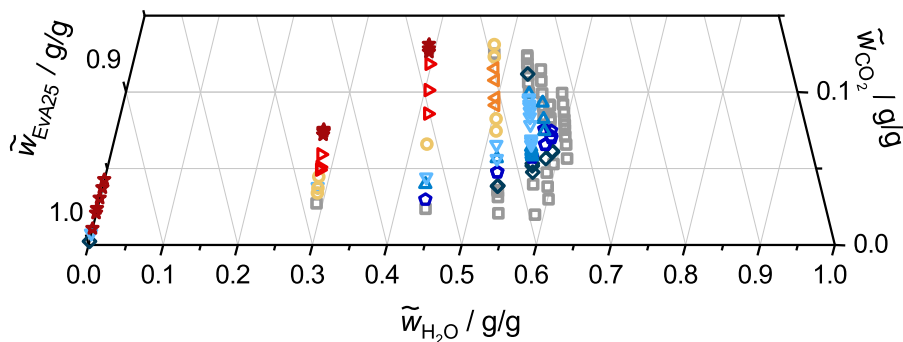
Figure 20: Overview of liquidus temperatures of the system ($EvA25 + H_2O + CO_2$).
Experimental results of the present work. Position of the symbols indicate
the composition. The color indicates the liquidus temperature, which is
presented in bins to get a clearer picture: ◇: $t = 10$ - 43 °C, ⬠: $t = 43$ -
48 °C, △: $t = 48$ - 55 °C, ▽: $t = 55$ - 60 °C, ○: $t = 60$ - 66 °C, ◁: $t = 66$ - 70 °C,
▷: $t = 70$ - 77 °C, ☆: 77 - 82 °C, □: no solid precipitation in the investigated
temperature range.

has to be added for solid formation at a given temperature decreases with increasing mass fraction of EvA25 in the solvent. However, with increasing mass fraction of CO$_2$, at constant mass fraction of EvA25 in the unloaded solvent and at a given temperature, the solid disappears again, if the mass fraction of CO$_2$ surpasses a certain value. For example, at a mass fraction of EvA25 in the unloaded solvent of $\tilde{w}^0_{EvA25} = 0.4$ g/g at about $t = 50$ ℃, solid formation can be observed at mass fractions of CO$_2$ between $\tilde{w}_{CO_2} = 0.05$ g/g and $\tilde{w}_{CO_2} = 0.1$ g/g, whereas at both, higher and lower mass fraction of CO$_2$, there is no solid.

5.2.2 Liquid-liquid equilibrium

Figure 21 shows the measured mass fraction of H$_2$O $\tilde{w}_{H_2O}$ in the two liquid phases of the system (EvA25 + H$_2$O) as a function of the temperature t between $t = 69$ ℃ and $t = 130$ ℃. The corresponding numerical experimental data are given in Appendix E. A wide miscibility gap was found at high temperatures, which narrows at lower temperatures and disappears in a critical point at $t = 68.5 \pm 0.5$ ℃. The mass fraction of EvA25 in the aqueous phase is always lower than that of H$_2$O in the organic phase. The critical composition can only be estimated from the results and is expected to be at a mass fraction of H$_2$O of $\tilde{w}_{H_2O} = 0.7 \pm 0.05$ g/g.

Figure 22 shows the results for the measured liquid-liquid equilibrium in the system (EvA25 + H$_2$O + CO$_2$) for six temperatures between $t = 65$ ℃ and $t = 120$ ℃. Error bars that indicate the uncertainty of the measured composition are not shown for clarity but are about twice the size of the symbols. The corresponding numerical experimental data are given in Appendix E. In the ternary system (EvA25 + H$_2$O + CO$_2$), a miscibility gap stretches out from the binary subsystem (EvA25 + H$_2$O). In the studied composition
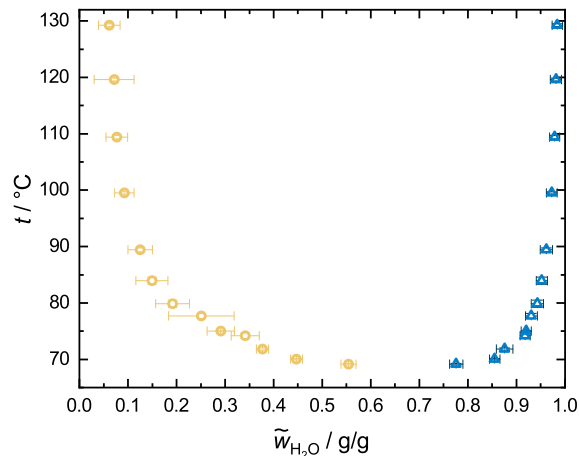
Figure 21: Liquid-liquid equilibrium in the system (EvA25 + H$_2$O). Experimental results from the present work. ○: organic phase, △: aqueous phase.
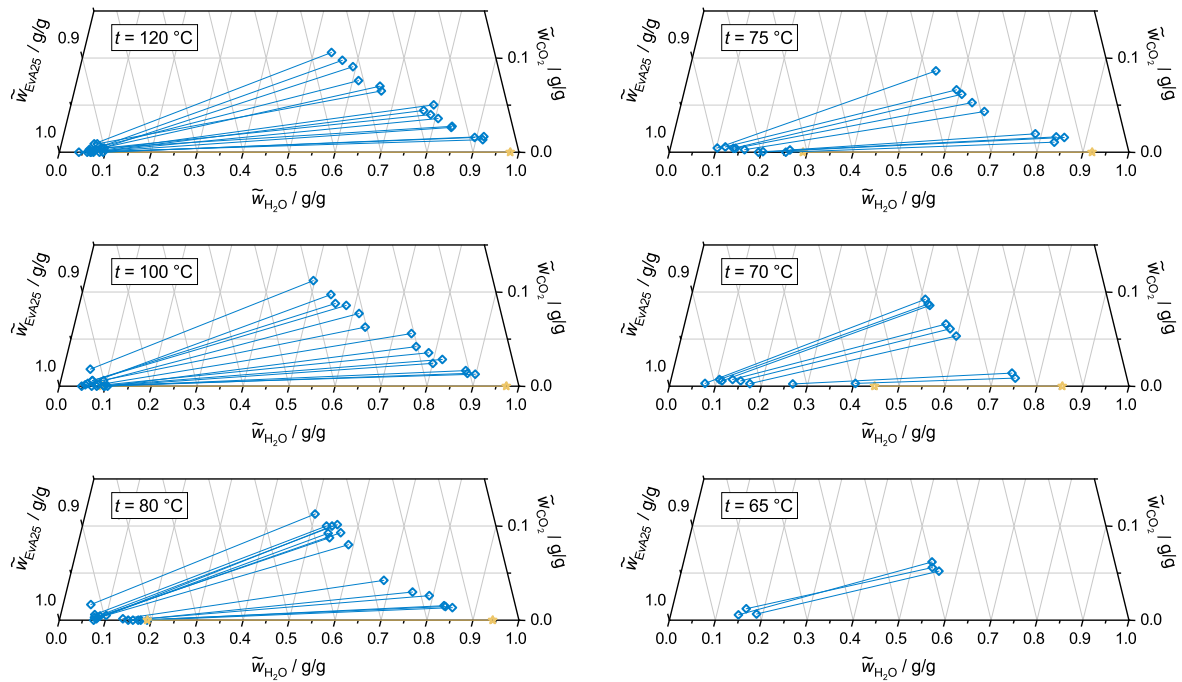
Figure 22: Liquid-liquid equilibria in the system (EvA25 + H_2O + CO_2). Experimental results from the present work. $\diamond$: tie-lines for the ternary system (EvA25 + H_2O + CO_2), $\star$: tie-lines for the binary system (EvA25 + H_2O) (cf. Figure 21). Error bars are not depicted but are about twice the symbol size.

range, the miscibility gap does not narrow significantly upon approaching the binary subsystem (EvA25 + CO_2) so that there is no indication of a critical point at the studied temperatures. Solid precipitates from the organic phase, when its H_2O-content is too low (cf. Section 5.2.1). This limits the composition range that could be studied in the present work. The liquid-liquid miscibility gap in the ternary system (EvA25 + H_2O + CO_2) gets wider with increasing temperature, which is related to the corresponding behavior of the binary subsystem (EvA25 + H_2O).

Adding CO_2 has a strong effect on the miscibility gap. The addition of CO_2 leads to a decrease of the H_2O-content in both, the organic and the aqueous phase. For EvA25-rich homogeneous aqueous solutions of EvA25, adding even small amounts of CO_2, quickly leads to a liquid-liquid phase split. This effect is less prominent for higher temperatures, where already the miscibility gap in the binary subsystem (EvA25 + H_2O) is wide, but is important at lower temperatures. At the lowest studied temperature ($t = 65$ ℃), there is no miscibility gap in the binary subsystem (EvA25 + H_2O), but there is still a miscibility gap in the ternary system (EvA25 + H_2O + CO_2). This demonstrates that the liquid-liquid phase split is enhanced by CO_2. Even though not visible in the diagram for $t = 65$ ℃ in Figure 22, there must be a LLE critical point in the gap between the last tie-line that was measured in the ternary system (EvA25 + H_2O + CO_2) and the

binary subsystem (EvA25 + H₂O). However, CO_2 only favors the phase split as long as it is added in moderate amounts. When added in large amounts, it acts as a phase mediator, especially if the H₂O-content in the reunited homogeneous phase is high.

In the ternary LLE, the organic phase contains only small amounts of CO_2, which leads to a high partition coefficient of CO_2 between the aqueous and the organic phase K_{CO_2} for all studied tie-lines, with

$$K_{CO_2} = \frac{\tilde{w}_{CO_2}^{aq}}{\tilde{w}_{CO_2}^{org}} \tag{9}$$

where $\tilde{w}_{CO_2}^{aq}$ is the mass fraction of CO_2 in the aqueous phase and $\tilde{w}_{CO_2}^{org}$ is the mass fraction of CO_2 in the organic phase. The measured values of the partition coefficient are in the range of $5 \leq K_{CO_2} \leq 80$. Due to the low CO_2 content in the organic phase, the results for K_{CO_2} are subject to large experimental uncertainties. As a result of the widening miscibility gap, K_{CO_2} tends to increase slightly with increasing temperature and increasing mass fraction of CO_2.

5.2.3 CO₂-solubility

The CO_2-solubility in the system (EvA25 + H₂O + CO₂) was measured at $t = 40\ °C$, $t = 80\ °C$, and $t = 120\ °C$ and partial pressures of CO_2 between $0.02\ \text{bar} \leq p_{CO_2} \leq 80\ \text{bar}$. Two series of experiments were carried out, which differ in the mass fractions of EvA25 in the unloaded solvent: $\tilde{w}_{EvA25}^0 = 0.15\ \text{g/g}$ and $\tilde{w}_{EvA25}^0 = 0.35\ \text{g/g}$. The results are shown in Figure 23. The corresponding numerical experimental data are given in Appendix E.

In Figure 23, the partial pressure of CO_2 p_{CO_2} is shown as a function of the mole-related CO_2-loading $\tilde{\alpha}_{CO_2}$, as well as of the mass fraction of CO_2 $\tilde{w}_{CO_2}$. The CO_2-loading and mass fraction of CO_2 refers to the total composition without regard to a phase split. However, the experimental data comprise results for which the liquid is homogenous and results for which two liquid phases coexist. The boundary that separates results with a homogeneous liquid phase and results with two coexisting liquid phases is indicated by triangles in Figure 23. The information needed to locate the position of the triangles in Figure 23 was obtained by using the information on the LLE from Figure 22 and is found from the intersection between the CO_2-solubility isotherm and the aqueous binodal of the LLE at a given temperature. A liquid-liquid phase split occurred only for the isotherms at $t = 80\ °C$ and $t = 120\ °C$, but not at $t = 40\ °C$, and only below a maximal CO_2-loading, which depends on both, the temperature and the mass fraction of EvA25 in the unloaded solvent. The positions of the boundaries that are shown in
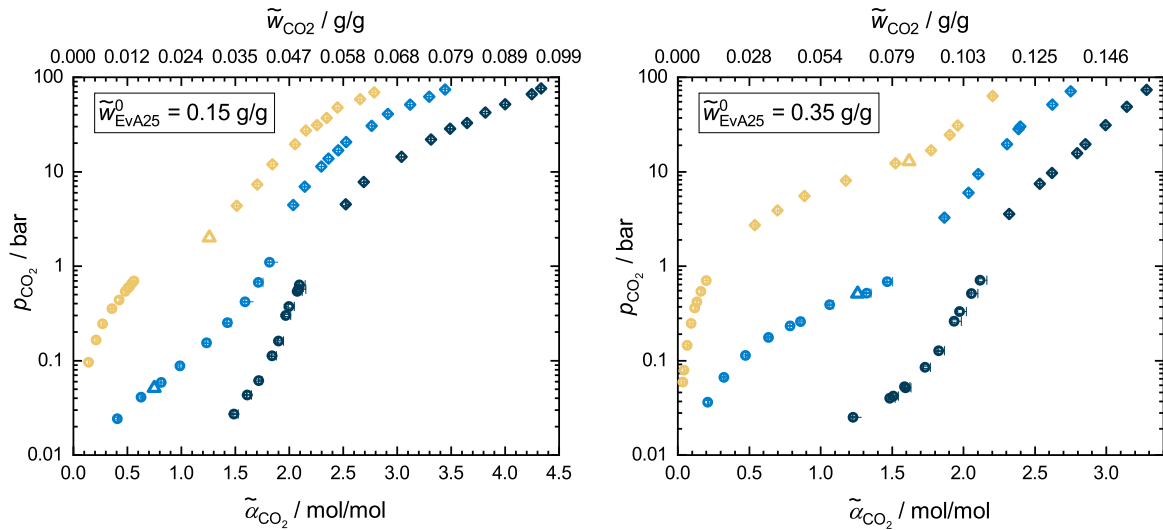
Figure 23: CO_2-solubility in the system (EvA25 + H_2O + CO_2). Experimental results from the present work. Black: $t = 40\,°C$, blue: $t = 80\,°C$, yellow: $t = 120\,°C$. ○: head space gas chromatography, ◇: high pressure view cell. For the isotherms at $t = 80\,°C$ and $t = 120\,°C$, a liquid-liquid phase split occurs at low CO_2-loadings. The boundary of that region is indicated by triangles (△), which were obtained from the information presented in Figure 22. The CO_2-loading refers to the weighed amounts from sample preparation where the liquid phase was homogeneous.

Figure 23 coincide with visual observations, which were possible in the high pressure experiments (cf. Section 2.7.2).

In Figure 23, in the high pressure region, where the liquid phase is always homogeneous, all studied isotherms follow a similar trend. In the mid and low pressure regions, different trends are found, depending on whether the liquid is homogeneous or split into two phases. If the liquid phase is homogeneous, the resulting shape of the isotherm is convex (the slope of the isotherm increases with increasing CO_2-loading) and the CO_2-solubility is increased. However, if the liquid phase splits, the shape of the isotherm becomes concave (the slope of the isotherm decreases with increasing CO_2-loading) and the CO_2-solubility is reduced. In a two-phase liquid, the amount of CO_2 in the organic phase is small and has only negligible contribution to the overall CO_2-solubility. Furthermore, the amount of EvA25 in the aqueous phase decreases compared to that in a homogeneous liquid phase, which reduces the solubility of CO_2 further. As a result of the lever rule, applied to the tie-lines (cf. Figure 22), the effect of the phase split is stronger for $\tilde{w}_{EvA25}^0 = 0.35$ g/g than for $\tilde{w}_{EvA25}^0 = 0.15$ g/g. This is in accordance with the results from Figure 23. Very high differences between the CO_2-loadings at $t = 40\,°C$ and $t = 120\,°C$ are observed in the mid and lower pressure regions, especially for $\tilde{w}_{EvA25}^0 = 0.35$ g/g. This is very favorable for CO_2-absorption processes (cf. Section 3).

5.3 Obtaining information for conceptual process design from the data

The experimental data presented in the previous sections are relevant for the design of CO$_2$-absorption processes with aqueous solutions of EvA25 that take advantage of the liquid-liquid phase split. For designing such processes, the LLE data and the CO$_2$-solubility data must be linked. Furthermore, they must be set in relation to the information on the SLE, as the formation of solids in the process is unwanted.

Ideally, the design of reactive CO$_2$-absorption processes should be based on a physico-chemical model of the system. Such a model for the present system (EvA25 + H$_2$O + CO$_2$) could, e.g., be set up in the spirit of Wagner et al. [48], based on the true speciation and accounting for physical non-idealities, e.g., using Pitzer-type equations [140]. For modeling the system (EvA25 + H$_2$O + CO$_2$), this approach would have to be extended to include the presence of a second liquid phase as well as the presence of a solid phase. The experimental results of the present work are a good basis for developing such a model. However, developing such a model would require information on the nature of the solid, which is presently not known. And even if that information was available (or the model was restricted to fluid phases), the parametrization of such a detailed physico-chemical model would remain highly challenging. In particular, it would require fitting a large number of parameters to different types of phase equilibrium data as well as data on the true speciation in both liquid phases. The development of such a physico-chemical model was outside the scope of the present work. Instead, a different approach was taken, which is based on interpolations of the experimental data and is, hence, much less elaborate. The interpolations were established for the liquidus lines, the binodals and corresponding tie-lines of the LLE, and the CO$_2$-solubility isotherms, each as a function of composition and temperature. In a few cases, when needed for the understanding of the phase behavior, some data were extrapolated. In the following, the extrapolated data are explicitly mentioned. They should be interpreted only in a qualitative manner. Details on the establishment of the inter- and extrapolations are given in Appendix B.

The combined results for liquidus lines and binodals with corresponding tie-lines of the LLE are depicted in Figure 24 in ternary diagrams of the system (EvA25 + H$_2$O + CO$_2$). The pressure is not specified as it has only little influence on the curves that are shown in Figure 24, but is assumed to be high enough such that no gas phase occurs in the region of interest. In the area between the liquidus line and the binary subsystem (EvA25 + CO$_2$), a solid phase exists (SL). Upon increasing the temperature, somewhere between $t = 50\,°C$ and $t = 60\,°C$, a LLE region appears in the phase diagram as the liquidus line retracts. This indicates that in the region where solid phases occur, also
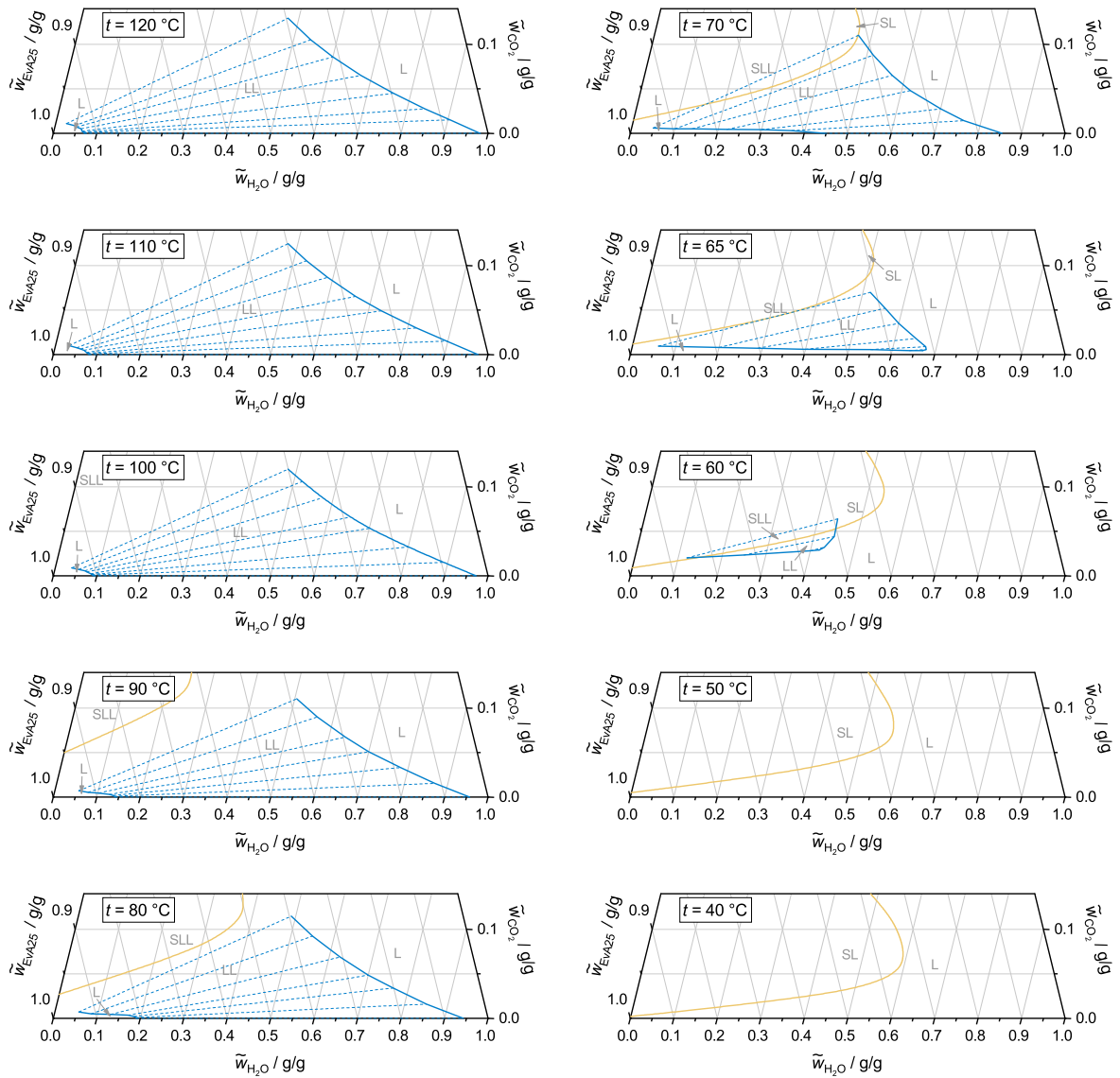
Figure 24: Interpolated solid-liquid-liquid equilibrium in the system ($EvA25$ + H_2O + CO_2). Yellow solid line: liquidus line, blue solid lines: binodals, blue dashed lines: tie-lines. Gray characters indicate the phases in the different regions: S: solid, L: liquid.

solid-liquid-liquid equilibria (SLLE) are present. Such SLLE were also observed in some of the SLE experiments (cf. Section 5.2.1). However, no detailed information on this region was obtained in the present study, as the study has a different focus. The binodals at $t = 60\,°C$ and $t = 65\,°C$ are partly extrapolated and, hence, provide only qualitative information on the SLE and SLLE in this region. Up to a temperature of $t = 68\,°C$, the LLE region ends in a ternary critical point. From $t = 68\,°C$ onwards, the ternary critical point of the LLE disappears in the lower critical point of the LLE of the binary subsystem ($EvA25$ + H_2O). Above that temperature, the LLE region of the ternary

system (EvA25 + H$_2$O + CO$_2$) is connected to the LLE of the binary subsystem (EvA25 + H$_2$O) and changes with temperature as described in Section 5.2.2.

The combined results for binodals and corresponding tie-lines of the LLE and CO$_2$-solubility are shown in Figure 25 in the same type of plot as shown in Figure 23. The isotherms comprise compositions for which the liquid is homogenous (VLE) and compositions for which two liquid phases coexist (VLLE). The line that separates these regions was determined using the interpolation for the LLE (cf. Figure 24). At CO$_2$-loadings higher than those of the intersection line, the liquid phase is homogeneous (VLE). At CO$_2$-loadings below those of the intersection line, a liquid-liquid phase split occurs (VLLE). For the VLLE, the compositions in the two liquid phases can be obtained from the LLE data (cf. Figure 24).

The relation between the LLE diagram in Figure 24 and the CO$_2$-solubility diagram in Figure 25 is illustrated using the qualitative sketch of a ternary phase diagram of the system (EvA25 + H$_2$O + CO$_2$) at constant temperature in Figure 26. Figure 26 serves only for illustration and is not quantitative. The positions of the phases were chosen only to make it well readable. In Figure 26, the binodals and two representative tie-lines of the LLE are shown together with a line of constant solvent composition $\tilde{w}^0_{\text{EvA25}}$. Three
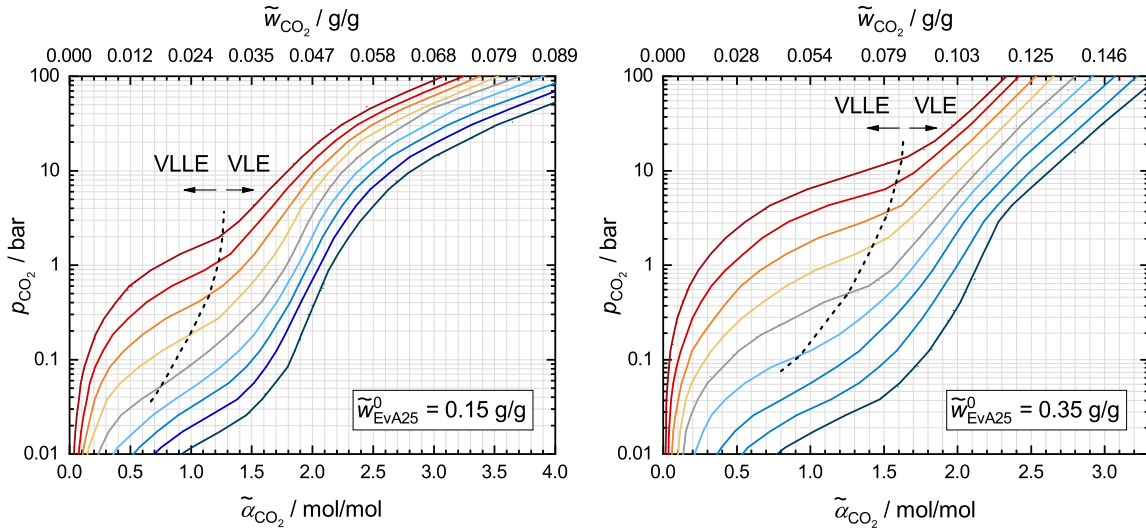
Figure 25: Interpolated CO$_2$-solubility isotherms in the system (EvA25 + H$_2$O + CO$_2$). Solid lines: CO$_2$-solubility isotherms. Dashed line: intersection between the interpolated CO$_2$-solubility isotherms and the interpolated aqueous binodals of the LLE (cf. Figure 24). At CO$_2$-loadings above the intersection line, the liquid phase is homogeneous (VLE). At CO$_2$-loadings below the intersection line, liquid-liquid phase split occurs (VLLE). The CO$_2$-loading given on the x-axis refers to the total amount of components without taking liquid-liquid phase split into account. Black: $t = 40$ ℃, dark blue: $t = 50$ ℃, blue: $t = 60$ ℃, light blue: $t = 70$ ℃, gray: $t = 80$ ℃, yellow: $t = 90$ ℃, orange: $t = 100$ ℃, red: $t = 110$ ℃, dark red: $t = 120$ ℃.
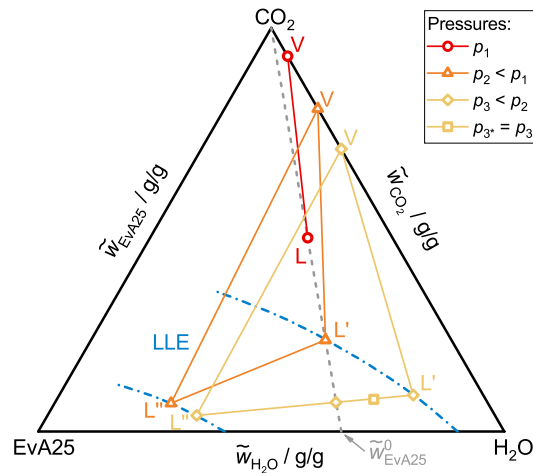
Figure 26: Qualitative illustration of the phase equilibria of the three different cases (see text) in a ternary diagram at a constant temperature. Blue dash-dotted line: binodals of the liquid-liquid equilibrium (LLE), gray dashed line: constant solvent composition ($\tilde{w}^0_{EvA25}$ = const.). L: composition of the liquid phase (L': aqueous phase, L": organic phase), V: composition of the vapor phase. ○: equilibrium compositions for case 1) at p_1 in the VLE, △: equilibrium compositions for case 2) at $p_2 < p_1$ at the edge of the VLLE, ◇: equilibrium compositions for case 3) at $p_3 < p_2$ in the VLLE, □: different solvent composition on the same tie-line as in case 3) at $p_{3*} = p_3$ resulting in the same VLLE as for case 3).

cases of phase equilibria that involve a vapor phase (V) are distinguished. They belong to different pressures.

1) At high partial pressure of CO_2 (p_1 in Figure 26), the concentration of CO_2 in the liquid is so high that no liquid-liquid phase split occurs. Hence, there is a simple VLE at pressure p_1. The liquid phase L lies on the line of constant $\tilde{w}^0_{EvA25}$.

2) Upon lowering the partial pressure of CO_2, the concentration of CO_2 in the liquid phase decreases until, at a certain pressure (p_2 in Figure 26), the LLE region is reached. This point is determined by the intersection between the line of constant $\tilde{w}^0_{EvA25}$ and the LLE binodal. This construction was used to obtain the composition and pressure of the intersection line separating the VLE and VLLE region in Figure 25.

3) Upon lowering the partial pressure of CO_2 further (p_3 in Figure 26), the concentration of CO_2 in the liquid phase further decreases and the liquid splits into two coexisting phases along the tie-lines of the LLE. The feed composition of the split continues to lie on the line of constant $\tilde{w}^0_{EvA25}$. The composition in the coexisting liquid phases of the VLLE as well as the split ratio depend on the chosen pressure.

The construction shown in Figure 26 can be carried out for any mass fraction of EvA25 in the unloaded solvent. If two different mass fractions of EvA25 in the unloaded solvent

are chosen, but the temperature and partial pressure of CO_2 are kept constant, then the same VLLE is formed (p_3* in Figure 26). The only difference is the split ratio between the liquid phases. This fact enables checking the consistency of the interpolated CO_2-solubility and LLE data, which passes this test well, as shown in the Appendix B.

In all cases, the gas phase is rich in CO_2 and contains practically no EvA25, due to the very low vapor pressure of EvA25 (cf. Appendix C). As the fugacity of H_2O in the gas phase does not change significantly for the three cases, the amount of H_2O in the gas phase increases with decreasing pressure.

5.4 Discussion of a CO_2-absorption process with liquid-liquid phase split

Aqueous solutions of EvA25 have performed best in the assessment with the NoVa short-cut method [35] in the screening (cf. Section 3.3). However, in the NoVa method, only a conventional process flow sheet is considered, and the assessment is carried out basically by using only the CO_2-solubility isotherms as presented in Figure 25. The liquid-liquid phase split in the system ($EvA25 + H_2O + CO_2$) was, hence, only considered implicitly in the ranking. The question remained open, whether additional benefits can be expected from using the liquid-liquid phase split in a suitably modified process.

Figure 27 shows a simplified scheme of such a process, which contains only the essential units. The absorber operates at low temperature to achieve high CO_2-loading and low residue amount of CO_2 in the purified gas. A common absorber inlet temperature for solvents is $t = 40\,°C$ [6]. However, aqueous solutions of EvA25 show solid precipitation in a wide part of the phase diagram at $t = 40\,°C$ (cf. Figure 24). To avoid solid precipitation in the absorber, either the mass fraction of EvA25 in the unloaded solvent should not exceed $\tilde{w}_{EvA25}^0 = 0.4\,g/g$, or, if higher mass fractions of EvA25 in the absorber are desired, the temperature of the solvent must be increased.

The liquid phase in the absorber is homogenous, due to the low temperature and high CO_2-loading. To induce a liquid-liquid phase split in the CO_2-rich solvent, two steps are required. Firstly, the CO_2-rich solvent needs to be heated up. Heating alone, however, is in most cases not sufficient to induce a liquid-liquid phase split. High CO_2-loadings prevent the solvent from splitting into two liquid phases. Hence, secondly, the amount of CO_2 in the solvent has to be reduced. Even if a phase split can be induced by simple heating, this second step is still favorable to obtain a sufficient amount of the organic phase. A convenient way to achieve lower CO_2-loadings is flashing. Such a flash of the CO_2-rich solvent is a well-established process option in CO_2-absorption processes [6].
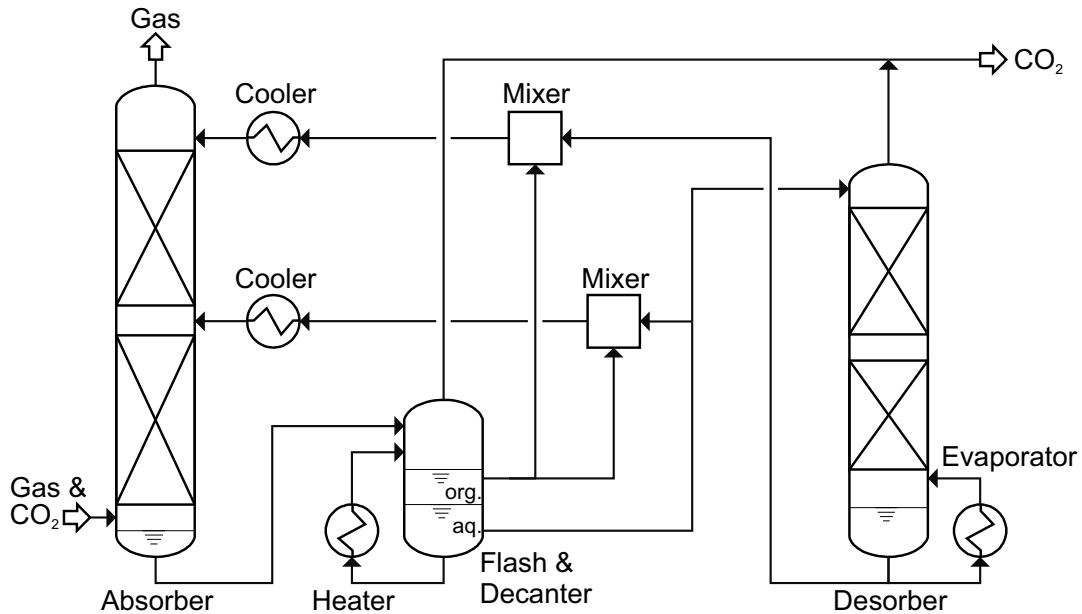
Figure 27: Simplified process scheme of a process that takes advantage of the liquid-liquid phase split in the system (EvA25 + H$_2$O + CO$_2$). The units that are not shown include pumps, valves, internal heat exchangers, etc.

Both steps can be performed in a single unit, a heated flash (Heater + Flash & Decanter in Figure 27). The CO$_2$-loading that is achieved in the heated flash unit depends on the temperature and pressure and can be obtained from the CO$_2$-absorption isotherms (cf. Figure 25). The lower the CO$_2$-loading, the more favorable is the split into the organic and aqueous phase (cf. Figures 24 and Figure 26). The organic phase obtained in that split contains almost no CO$_2$ and is recycled without being regenerated in the desorber. Only the aqueous phase is regenerated. The amount of aqueous phase that is regenerated can be reduced by a split stream configuration [6], in which, after the flash unit, parts of the aqueous phase are recycled to the lower part of the absorber column without further regeneration. An advantage of the phase split is that the amount of organic phase that is mixed with the recycled aqueous phases from the flash and from the desorber, as well as their inlet temperatures into the absorber can be adjusted individually.

To benefit from the opportunities of the liquid-liquid phase split, it is desirable to have a high split ratio between the organic and the aqueous phase. To obtain high split ratios, the following demands have to be met: I) high EvA25 concentration in the solvent, II) high temperature in the heated flash, III) low pressure in the heated flash. However, for each of these demands, there are counteracting factors that need to be considered. Demand I) is in conflict with the onset of solid precipitation in the absorber as well as with the limitation of the mass transfer in the absorber due to the increasing viscosity of the solvent with increasing concentration of EvA25 (cf. Appendix C). The pressure and/or temperature in the heated flash unit must be different from those in the desorber to benefit from the process scheme in Figure 27. Demands II) and III), hence, have to

be adapted in combination with the pressure and temperature in the desorber for each purification task individually. The chosen temperatures in the heated flash unit and the desorber have high impact on the design of the internal heat exchange of the process (not shown in Figure 27). It should be mentioned, that in most cases there will also be a small phase split in the desorber due to the reduced CO$_2$-loading, compared to the heated flash unit. Finally, demand III) is in conflict with the demand to supply H$_2$O-free CO$_2$ at high pressures.

It was not in the scope of the present study to carry out a more detailed conceptual design of the new process considering all these (and other) trade-offs. However, the present discussion shows that the essential information needed for such a design is now available. Such a design was up to now not possible based on thermo-physical data of a real solvent and is a highly interesting task to be tackled in future work.

5.5 Conclusion

The investigation of the system (EvA25 + H$_2$O + CO$_2$) provides a wealth of thermodynamic data for an interesting solvent for CO$_2$-absorption. There has been a discussion in the literature on whether a liquid-liquid phase split in CO$_2$-loaded solvents can be used beneficially in the CO$_2$-absorption process design. This discussion has suffered so far from the lack of appropriate thermodynamic data on systems that show such a liquid-liquid phase split. The present work supplies such data. Only the most important data for discussing concepts of how to use the phase split in adapted CO$_2$-absorption processes are reported in this Section: liquid-liquid equilibria, CO$_2$-solubility data, and liquidus lines. However, the present study provides further data in Appendix C: elucidation and quantification of CO$_2$-containing species in CO$_2$-loaded aqueous solutions of EvA25, which were carried out by NMR spectroscopy, pH-values of unloaded and CO$_2$-loaded aqueous solutions of EvA25, pK-values of EvA25 highly diluted in H$_2$O, density and dynamic viscosity of unloaded and CO$_2$-loaded aqueous solutions of EvA25, liquid heat capacity of unloaded aqueous solutions of EvA25, and vapor pressure of pure EvA25.

The evaluation of the data shows that even without an adapted process design for using the liquid-liquid phase split, the system (EvA25 + H$_2$O + CO$_2$) is highly interesting for CO$_2$ absorption, as the phase split leads to a lowering of the overall CO$_2$-capacity, compared to a homogeneous solvent at desorption. Further improvements seem possible by an adapted process design. At the low temperatures in the absorber, the solvent is homogeneous and has a high CO$_2$-absorption capacity. Solid formation is a potential problem at low temperatures, but can be mitigated as shown by the results for the liq-

uidus lines. At higher temperatures, the solvent splits into two liquid phases, an organic phase which contains only very little amount of CO_2 and which does not have to be regenerated, and an aqueous phase that can be regenerated by desorption. Furthermore, the study revealed that an adapted process design would benefit from a high split ratio between the organic and aqueous phase. To achieve high split ratios, a high mass fraction of EvA25 in the unloaded solvent and a heated flash unit at elevated temperature and reduced pressure, which is situated between the absorber and desorber, is required.

The information provided in the present work forms an excellent basis for developing a sound physico-chemical model of the thermodynamic properties of the system (EvA25 + H_2O + CO_2), which could be used for a simulation-based process design. This step, however, is very elaborate and was outside the scope of the present Section, in which the focus was on providing the experimental data and assessing the data with regards to potential benefits and pitfalls for a conceptual process design. As the results are very promising, the next step would be to develop the physico-chemical model. That model could be build on previous work [48, 115, 125], that would have to be extended to include the liquid-liquid phase split. It would be highly interesting to tackle this task in future work, not only to have such a model for a detailed process design, but also as it would allow a full elucidation of the very complex and interesting phase behavior of the studied ternary system (EvA25 + H_2O + CO_2), of which even the present extensive study has only revealed some aspects. With the model, the conceptual process design that was discussed in the present work could be evaluated and optimized. Then, the optimized design would have to be tested in a pilot plant. From all we know, the ternary system (EvA25 + H_2O + CO_2) is an excellent candidate to pursue on this path.

6 Elucidation of structure-property relationships

6.1 Introduction

The performance of CO_2-absorption processes depends crucially on the amine that is used in the aqueous solvent. Understanding the relationship between the chemical structure of the amine and the application properties of the solvent (e.g., CO_2-solubility, rate of absorption of CO_2, enthalpy of absorption of CO_2, and others) is therefore important, especially when the task is to search for new solvents with superior performance. Establishing such relationships is a challenge, as they must be based on comprehensive studies that need to be carried out at the same conditions with many different amines to enable a comparison. This has been tried in previous studies [57, 58, 88–91, 93, 141], but establishing links between the chemical structure of the amine and its properties as lead-component in the solvent has turned out to be difficult on the direct empirical route. Therefore, in the present section, a physico-chemical route was tried out. Figure 28 illustrates the route that is followed in the present Section. The speciation in the reactive solvents plays a key role in it. In a first step, the relationships between the chemical structure of the amine and the speciation in unloaded and CO_2-loaded aqueous solutions of amines at relevant conditions are elucidated. In a second step, the information on the speciation is related to the application properties of the solvent that are relevant for the CO_2-absorption process.

Determining the speciation of CO_2-loaded aqueous solutions of amines means quantifying the amounts of protonated/unprotonated amine, bicarbonate and carbonate, carbamates, alkylcarbonates, molecular CO_2, and eventually other compounds. The state of the art method for determining the speciation of CO_2-loaded aqueous solutions of amines is ^1H and ^{13}C NMR spectroscopy [60, 63, 64, 94, 108, 125, 142–152]. Other spectroscopic
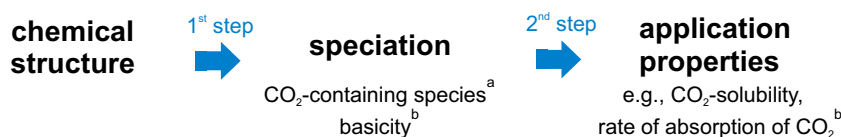
Figure 28: Scheme of the route that is followed in the present study for establishing structure-property relationships. 1st step: establishing relationships between the chemical structure and the speciation. 2nd step: relate the studied speciation to measured application properties of the solvent. [a]from experiments of the present section, [b]from experiments of Section 3.

methods, such as Infrared or Raman spectroscopy, have also been applied [153–156]. Complementary information on the protonated/unprotonated amine can be obtained from measurements of the pK-values of the amines [66, 80, 84, 86, 87, 98, 157, 158] or from measurements of the pH-value in unloaded and CO_2-loaded aqueous solutions of amines [159].

The EvAs are a particularly interesting class of amines for a systematic study on the speciation, as many different EvAs have been synthesized and investigated (cf. Section 3-5). They are ideal candidates to establish structure-property relationships that link information of the chemical structure of the amine with their speciation in aqueous solution. 20 of the 26 synthesized EvAs were considered. Their chemical structures are presented in Figure 1, where they are marked with an S. EvA29/30 and EvA41 were not considered for this study as no reliable information on the pK-values could be obtained from the titration curves (cf. Section 3). EvA22 and EvA33 were not considered as they contain large amounts of impurities, which would adulterate the findings of their investigation. EvA19, which also contains large amount of impurities serves only as an example for an aromatic structure according to findings from literature.

For 16 out of the 20 EvAs shown in Figure 1, the concentrations of CO_2-containing species was determined with ^{13}C NMR spectroscopy. The 16 selected EvAs are marked with an N in Figure 1. The remaining EvAs were not investigated as the corresponding variation of the substituent would have added only little information to the study. The concentrations were measured in CO_2-loaded aqueous solutions of EvAs with a mass fraction of EvA in the unloaded solvent of $\tilde{w}_{EvA}^0 = 0.1$ g/g. This concentration was chosen based on previous experience to avoid problems with solid precipitation (cf. Section 3). CO_2-loading $\tilde{\alpha}_{CO_2}$ and temperature t were varied systematically between 0.1 mol/mol $\leq \tilde{\alpha}_{CO_2} \leq$ 3 mol/mol and 20 ℃ $\leq t \leq$ 100 ℃. All in all, more than 350 NMR experiments were carried out. The results of this NMR study are presented in Section 6.2.

The NMR data were combined with results for the pK-values from the screening (cf. Table 7 in Section 3) and relationships between the chemical structure of the amine and the basicity and concentrations of CO_2-containing species were established. This corresponds to the first step of the route that is illustrated in Figure 28; its results are presented in the Sections 6.3.2-6.3.5.

In a second step, the knowledge on the speciation was related to application properties that are relevant for a CO_2-absorption process: CO_2-solubility and rate of absorption of CO_2 (c.f. Figure 28). The application property data were taken from the screening as well (cf. Section 3). From combining the information from both steps, some guidelines for the design of new amines were derived. These are presented in Section 6.4.

Finally, the guidelines were used for the design of new amines. Three basic structures as well as several promising derivatives of these compounds that can be customized with regard to the requirements of the purification task are proposed in Section 6.5. Testing these new amines was not in the scope of the present study.

6.2 Experimental results

6.2.1 Elucidation of CO_2-containing species

Five different types of CO_2-containing species i were observed in the investigation: primary carbamates, secondary carbamates, alkylcarbonates, (bi)carbonate, and molecular CO_2. The chemical structure of the five types of CO_2-containing species are shown in Figure 29. Protonated and unprotonated species cannot be distinguished in NMR spectra. Therefore, the given concentrations of CO_2-containing species include protonated and unprotonated forms. For brevity, carbonate and bicarbonate are lumped together and named (bi)carbonate. Any amino group stabilizes (bi)carbonate. The amino group where the carbamate is formed is given with a Greek letter that corresponds to the amino group labeling of Figure 1.

In the recorded ^{13}C NMR spectra of the EvAs, the signal of molecular CO_2 can be identified easily, as it is the only signal that appears at about 124 ppm. The signal of molecular CO_2 shows no correlations to any of the ^{1}H NMR signals in HMBC NMR spectra. The signals of (bi)carbonate, carbamate and alkylcarbonate appear between 155 and 168 ppm. The signal of the carbon atom of (bi)carbonate does not show correlations to any of the proton signals of the EvAs, whereas those of carbamate and alkylcarbonate do. Based on these correlations, the type and position of the carbamate or alkylcarbonate can be assigned unambiguously. Exemplary elucidations are shown in detail in Appendix D.

None of the investigated EvAs showed carbamate formation at the α-amino group. In contrast, it was found that all EvAs form carbamate at the β-amino group. EvA34 and EvA36 also form carbamate at the γ-amino group. EvA21, EvA27, and EvA31, which contain hydroxy groups, form also alkylcarbonates. No dicarbamates or combinations of a carbamate with an alkylcarbonate at a single EvA were observed in the present work, as they only occur at higher mass fraction of amine or higher CO_2-loadings (cf. Section 4 and [147, 160]). (Bi)carbonate was found in all investigated solutions. Molecular CO_2 was observed at high CO_2-loadings for all EvAs except for EvA01, EvA34, and EvA36, where it is probably only observable at higher CO_2-loadings than the ones investigated in the present work.
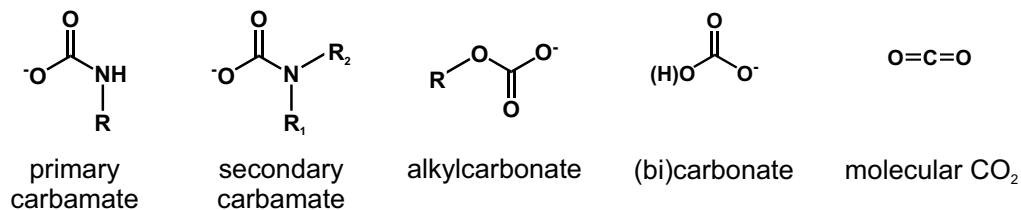
Figure 29: Chemical structures of the observed CO_2-containing species. Results of the present work.

6.2.2 Quantification of CO_2-containing species

A set of data for a given EvA usually consists of quantitative NMR results for temperatures between $t = 20$ ℃ and $t = 100$ ℃ in steps of $\Delta t = 20$ ℃ and CO_2-loadings up to the one that corresponds to an equilibrium partial pressure of CO_2 of about $p_{CO_2} = 2$ bar at $t = 25$ ℃. This results in a range of maximal CO_2-loadings of the EvAs between $\tilde{\alpha}_{CO_2} = 0.9$ mol/mol (EvA32) and $\tilde{\alpha}_{CO_2} = 3.1$ mol/mol (EvA34). The number of experimental data points was varied between the different EvAs, as it was adapted pragmatically, e.g., accounting for the availability of a given EvA or an occurring liquid-liquid phase split at elevated temperature.

For a better overview, the 16 EvAs that were investigated with NMR spectroscopy in the present work are divided into six groups. The classification depends on the substituent of the basic triacetoneamine ring structure of the EvAs and is as follows: the substituent contains a primary amino group (Group A), one secondary amino group but no hydroxy group (Group B), at least one hydroxy group (Group C), one secondary amino group and one tertiary amino group (Group D), at least two secondary amino groups (Group E), an ether or carboxylate group (Group F). Although some EvAs fit into more than one group, each EvA was assigned to only one group.

The discussion of the speciation of CO_2-containing species of the EvAs is done group by group in the following Subsections 6.2.2.1 to 6.2.2.6. The results of all NMR experiments are presented in diagrams that show the concentration $\tilde{\alpha}_i$ of the observed CO_2-containing species i = carbamates, alkylcarbonates, and molecular CO_2, as a function of the CO_2-loading, for which numbers for both, $\tilde{X}_{CO_2}$ and $\tilde{\alpha}_{CO_2}$, are shown (cf. Equation (5) and (6)). For clarity, the concentration of (bi)carbonate is not shown in the diagrams but can be derived from the difference between the CO_2-loading and the sum of the concentrations of the CO_2-containing species that are shown. The corresponding numerical experimental data are given in Appendix E.

6.2.2.1 Group A: substituent contains a primary amino group

Group A consists only of EvA01, as this is the only EvA with a primary amino group. The observed CO_2-containing species are β-carbamate and (bi)carbonate. The concentration of β-carbamate is presented in Figure 30. At $t = 20$ ℃, up to a CO_2-loading of about $\tilde{X}_{CO_2} = 0.3$ g/g, more CO_2 is chemically bound as β-carbamate than as (bi)carbonate. At higher CO_2-loading, (bi)carbonate dominates. The concentration of β-carbamate as a function of the CO_2-loading shows a maximum, which is $\tilde{\alpha}_i = 0.7$ mol/mol at $t = 20$ ℃. With increasing temperature, the maximum decreases and shifts towards lower CO_2-loadings.

Figure 30: Group A: speciation in CO_2-loaded aqueous solutions of EvA01. Results from NMR experiments of the present work. $\diamond$: β-carbamate, black: $t = 20$ ℃, blue: $t = 40$ ℃, gray: $t = 60$ ℃, yellow: $t = 80$ ℃, orange: $t = 100$ ℃. Lines are guides to the eye.

6.2.2.2 Group B: substituent contains one secondary amino group

EvA02, EvA04, and EvA05 form Group B in which the substituents are alkane amines with one secondary amino group. The observed CO_2-containing species are β-carbamate, (bi)carbonate, and molecular CO_2. The concentration of β-carbamate and molecular CO_2 of the three EvAs are shown in Figure 31. They form very low concentrations of β-carbamate, which are all below about $\tilde{\alpha}_i = 0.03$ mol/mol. Almost all CO_2 is chemically bound as (bi)carbonate. With increasing temperature, the concentration of β-carbamate decreases. Small amounts of molecular CO_2 are observed at high CO_2-loading. The concentration of molecular CO_2 increases with increasing temperature.
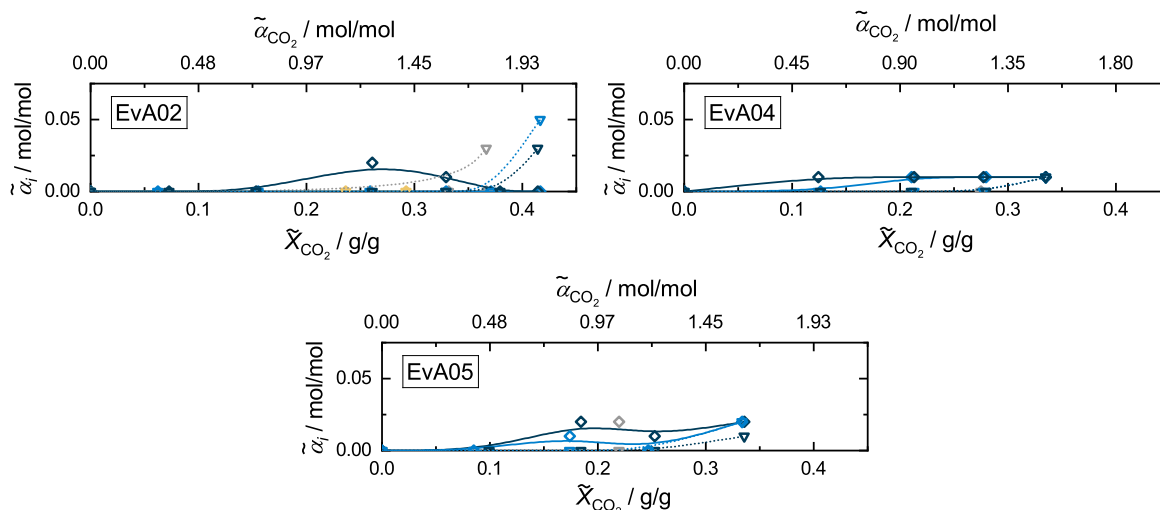
Figure 31: Group B: speciation in CO_2-loaded aqueous solutions of EvA02, EvA04, and EvA05. Results from NMR experiments of the present work. $\diamond$: β-carbamate, $\triangledown$: molecular CO_2, black: $t = 20$ °C, blue: $t = 40$ °C, gray: $t = 60$ °C, yellow: $t = 80$ °C. Lines are guides to the eye.

6.2.2.3 Group C: substituent contains at least one hydroxy group

EvA21, EvA27, and EvA31 form Group C in which the substituents contain at least one hydroxy group. The observed CO_2-containing species are β-carbamate, alkylcarbonate, (bi)carbonate, and molecular CO_2. The concentration of β-carbamate, alkylcarbonate, and molecular CO_2 of the three EvAs are shown in Figure 32. The concentration of β-carbamate as a function of the CO_2-loading shows a maximum while the concentration of alkylcarbonate continuously increases. For EvA21, the concentration of β-carbamate and alkylcarbonate are similar whereas for EvA27 and EvA31, the concentration of β-carbamate is higher than that of alkylcarbonate. Molecular CO_2 was observed at high CO_2-loadings for all three EvAs. The concentration of β-carbamate and alkylcarbonate decreases with increasing temperature, that of molecular CO_2 increases.

6.2.2.4 Group D: substituent contains one secondary and one tertiary amino group

EvA03, EvA07, EvA24, EvA25, and EvA26 form Group D, in which the substituents contain one secondary amino group and one tertiary amino group. The observed CO_2-containing species are β-carbamate, (bi)carbonate, and molecular CO_2. The concentration of β-carbamate and molecular CO_2 of the five EvAs are shown in Figure 33. For EvA03 and EvA25, the concentration of β-carbamate as a function of the CO_2-loading shows a maximum, which is about $\tilde{\alpha}_i = 0.2$ mol/mol. For EvA07, EvA24, and

EvA26 the concentration of β-carbamate continuously increases with increasing CO_2-loading. The maximum concentration of β-carbamate is $\tilde{\alpha}_i = 0.3$ mol/mol for EvA07, $\tilde{\alpha}_i = 0.06$ mol/mol for EvA24, and $\tilde{\alpha}_i = 0.53$ mol/mol for EvA26. Molecular CO_2 was observed at high CO_2-loadings, for all EvAs of this group. The concentration of β-carbamate decreases with increasing temperature, that of molecular CO_2 increases.
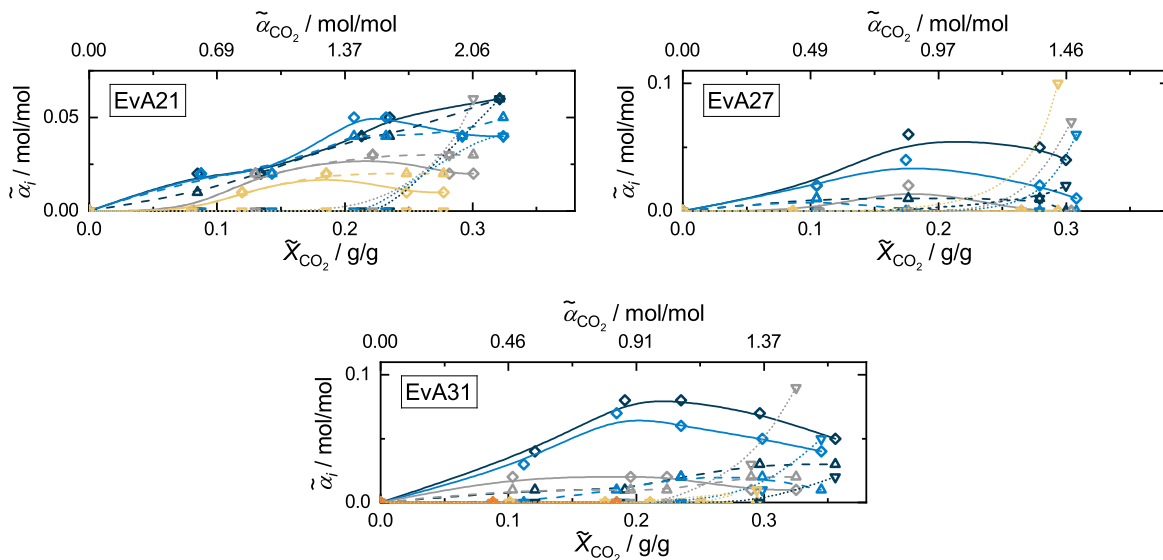
Figure 32: Group C: speciation in CO_2-loaded aqueous solutions of EvA21, EvA27, and EvA31. Results from NMR experiments of the present work. $\diamond$: β-carbamate, $\triangle$: alkylcarbonate, $\triangledown$: molecular CO_2, black: $t = 20\,°C$, blue: $t = 40\,°C$, gray: $t = 60\,°C$, yellow: $t = 80\,°C$, orange: $t = 100\,°C$. Lines are guides to the eye.

6.2.2.5 Group E: substituent contains at least two secondary amino groups

EvA34 and EvA36 form Group E, in which the substituents contain at least two secondary amino groups. The observed CO_2-containing species are β-carbamate, γ-carbamate, and (bi)carbonate. The concentration of β-carbamate and γ-carbamate of the two EvAs are shown in Figure 34. The concentration of γ-carbamate of EvA34 is up to $\tilde{\alpha}_i = 0.8$ mol/mol at $t = 20\,°C$. This is the highest carbamate concentration of all EvAs in the investigation. The concentration of γ-carbamate increases with increasing CO_2-loading until it reaches a maximum where the concentration does not change significantly upon a further increase of the CO_2-loading. Only small amounts of β-carbamate of around $\tilde{\alpha}_i = 0.07$ mol/mol are observed for EvA34. For EvA36, the concentration of β-carbamate and γ-carbamate show a maximum as a function of the CO_2-loading, which is $\tilde{\alpha}_i = 0.46$ mol/mol for γ-carbamate and $\tilde{\alpha}_i = 0.15$ mol/mol for β-carbamate at $t = 20\,°C$. The maximum of γ-carbamate is found at lower CO_2-loadings than that

of β-carbamate. For both EvAs of Group E, the concentration of β-carbamate and γ-carbamate decreases with increasing temperature.
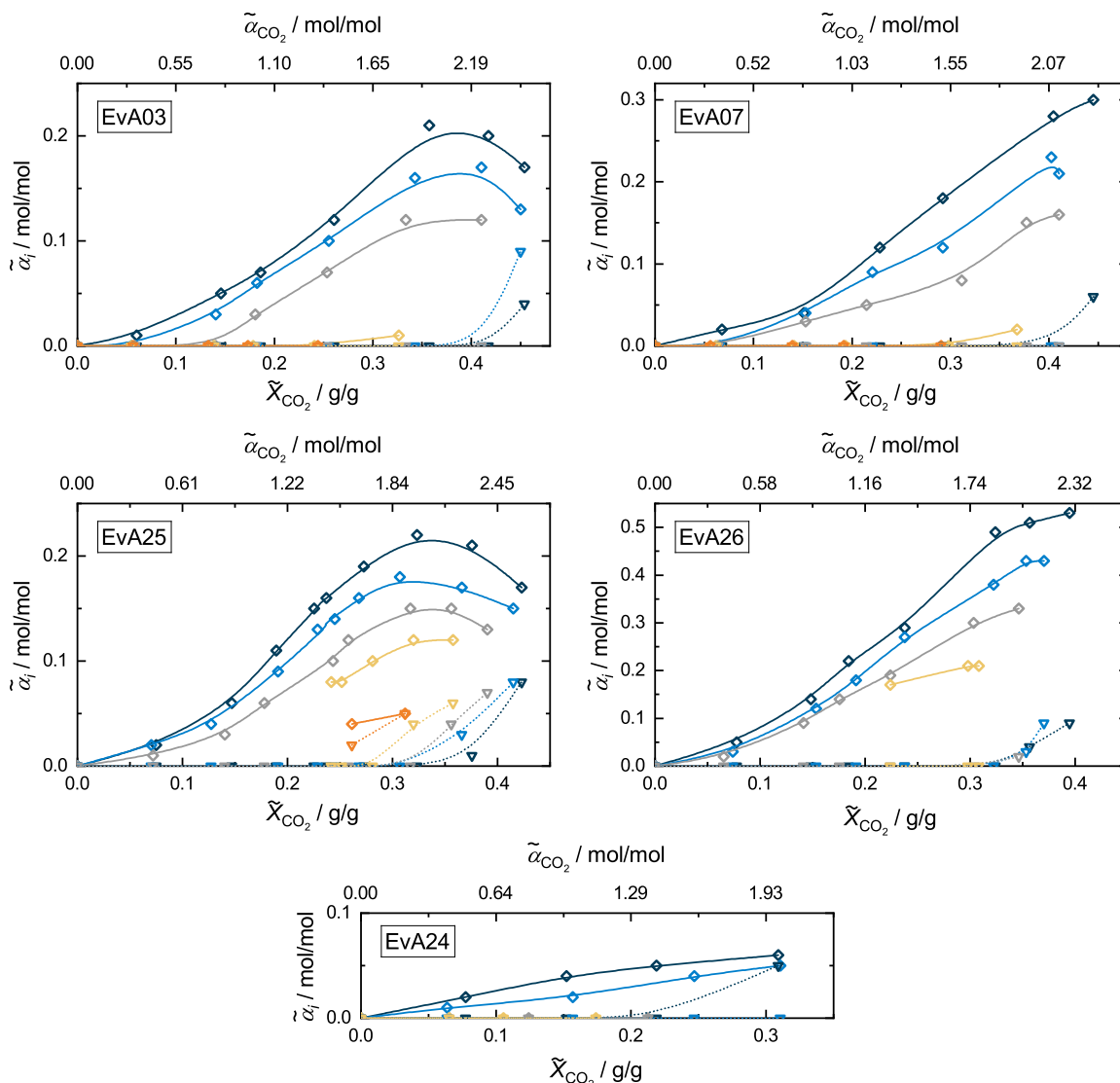
Figure 33: Group D: speciation in CO_2-loaded aqueous solutions of EvA03, EvA07, EvA24, EvA25, and EvA26. Results from NMR experiments of the present work. $\diamond$: β-carbamate, $\triangledown$: molecular CO_2, black: $t = 20\,°C$, blue: $t = 40\,°C$, gray: $t = 60\,°C$, yellow: $t = 80\,°C$, orange: $t = 100\,°C$. Lines are guides to the eye.

6.2.2.6 Group F: substituent contains an ether group or a carboxylate group

EvA06 and EvA32 form Group F. The substituent of EvA06 contains an ether group, that of EvA32 an carboxylate group. The observed CO_2-containing species are β-carbamate, (bi)carbonate, and molecular CO_2. The concentration of β-carbamate and molecular CO_2 of the two EvAs are shown in Figure 35. Both EvAs show particularly

high concentrations of molecular CO_2. The maximal concentration of molecular CO_2 for EvA06 was $\tilde{\alpha}_i = 0.25$ mol/mol at $t = 80$ ℃, which was the highest concentration of molecular CO_2 of all studied EvAs. The maximal concentration of molecular CO_2 for EvA32 was $\tilde{\alpha}_i = 0.13$ mol/mol and was found at $t = 60$ ℃. For both EvAs, the concentration of β-carbamate as a function of the CO_2-loading shows a maximum at $t = 20$ ℃, which is about $\tilde{\alpha}_i = 0.07$ mol/mol for EvA06 and $\tilde{\alpha}_i = 0.03$ mol/mol for EvA32. With increasing temperature, the concentration of β-carbamate decreases and that of molecular CO_2 increases. The maximum CO_2-loading of EvA32 which was obtained due to the loading process (cf. Section 2.3.2) was the lowest of all EvAs. It was below $\tilde{\alpha}_{CO_2} < 1$ mol/mol.
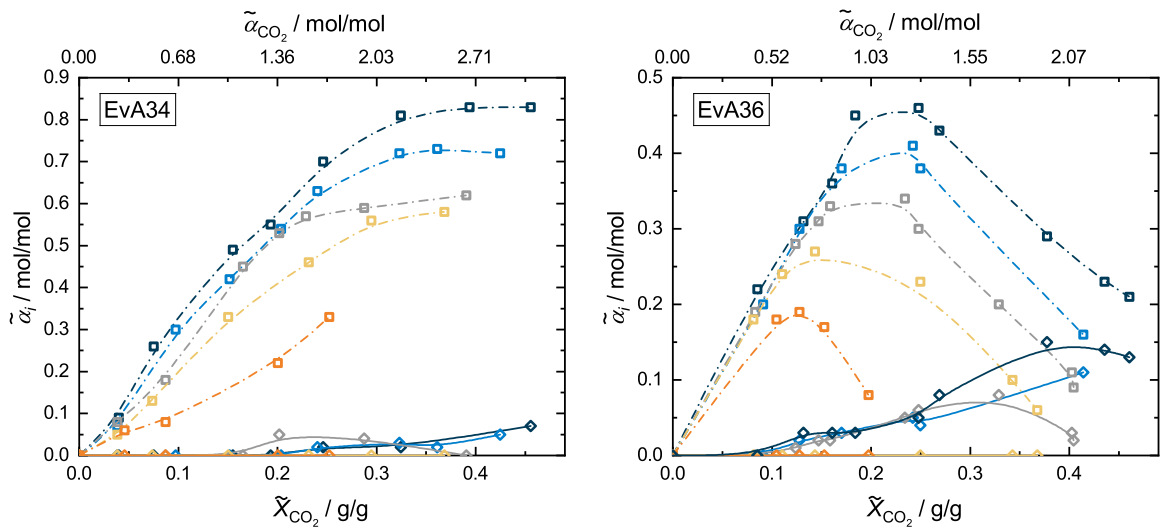
Figure 34: Group E: speciation in CO_2-loaded aqueous solutions of EvA34 and EvA36. Results from NMR experiments of the present work. $\diamondsuit$: β-carbamate, $\square$: γ-carbamate, black: $t = 20$ ℃, blue: $t = 40$ ℃, gray: $t = 60$ ℃, yellow: $t = 80$ ℃, orange: $t = 100$ ℃. Lines are guides to the eye.
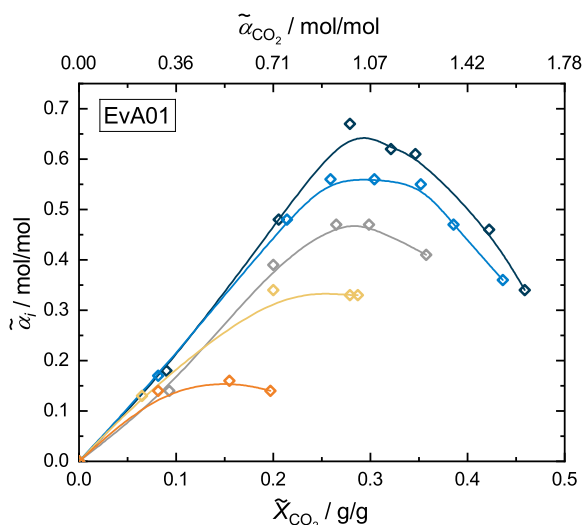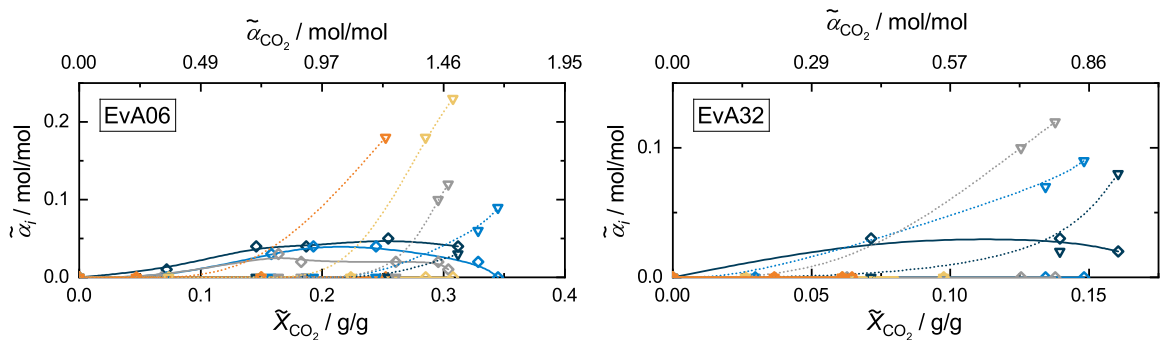

Figure 35: Group F: speciation in CO_2-loaded aqueous solutions of EvA06 and EvA32. Results from NMR experiments of the present work. $\diamondsuit$: β-carbamate, $\triangledown$: molecular CO_2, black: $t = 20$ ℃, blue: $t = 40$ ℃, gray: $t = 60$ ℃, yellow: $t = 80$ ℃, orange: $t = 100$ ℃. Lines are guides to the eye.

6.3 Structure-property relationships

6.3.1 Overview

In this section, the first step of the route that was followed in the present work to establish structure-property relationships is presented (cf. Figure 28). The first step was to establish relationships between the chemical structure of the EvAs and their basicity as well as between the chemical structure of the EvAs and their concentration of CO_2-containing species. These relationships base on the pK-values which were measured in the screening (cf. Section 3) and the results from NMR measurements which were presented in the previous section (cf. Section 6.2). Some of the relationships lead to counteracting trends. This has to be taken into account when trying to verify a given relationship by comparing different amines. Each relationship is introduced in the following using results for an EvA in which the effect described by the relationship is dominant.

6.3.2 Basicity: pK-value and BM-value

pK-values are valuable indicators for a comparison of the basicity of single amino groups. However, for a quantitative comparison of the basicity of amines, especially if the amines have different number of amino groups, the pK-values are insufficient. Therefore, a dimensionless number that enables a quantitative comparison of the basicity of the EvAs, independent of the number of amino groups in the EvAs, is introduced. The dimensionless number is named BM-value (BM stands for basicity per mass) and is calculated from Equation (10) by dividing the sum of all pK-values of a given EvA pK_{EvA} by the molar mass of the EvA M_{EvA}. The BM-value at 40 °C of the investigated EvAs are given in Table 12. Both, the BM-value and the pK-values are considered in the following discussion.

$$BM = \frac{\sum pK_{\mathrm{EvA}}}{M_{\mathrm{EvA}}} \cdot 100 \tag{10}$$

The addition of oxygen atoms to the substituents of the EvAs (EvA06, EvA09, EvA19, EvA21, EvA24, EvA27, EvA31, EvA32) lowers the pK-values of the amino groups (cf. Figure 1). This has already been reported in Section 3.2.3 and was found for other classes of amines as well [86, 98, 147, 157, 158]. The decrease of the pK-values is caused by the positive inductive effect of oxygen atoms. Further, the oxygen atoms add molar mass to the EvAs which, in combination with the lowered pK-values, lowers the BM-

value (cf. Table 12). This leads to the fact that the eight oxygen-containing EvAs are among the nine EvAs with the lowest BM-value in the comparison.

Table 12: *BM-values of the EvAs calculated from Equation (10) with pK-values at 40 ℃ (cf. Section 3.2.3).*

BM-value for EvAs that do not contain oxygen atoms		BM-value for EvAs that contain oxygen atoms	
EvA01	11.5	EvA06	7.9
EvA02	8.5	EvA09	6.8
EvA03	10.6	EvA19	6.9
EvA04	9.1	EvA21	8.1
EvA05	8.5	EvA24	8.3
EvA07	10.1	EvA27	8.0
EvA10	8.3	EvA31	8.5
EvA14	9.5	EvA32	6.9
EvA17	9.2		
EvA25	9.7		
EvA26	9.2		
EvA34	11.2		
EvA36	11.6		

EvA19 contains a furane ring (cf. Figure 1). The aromatic structure lowers the basicity and increases the molar mass such that EvA19 has one of the lowest BM-values in the study (cf. Table 12). Similar results for other amines that contain aromatic ring structures were reported in literature [89].

In contrast to expectations, the negative inductive effect of the carboxylate group of EvA32 does not show an exceptional influence on the pK-value of the β-amino group (cf. Section 3.2.3). However, the oxygen atoms and the potassium atom add much molar mass such that the BM-value of EvA32 is one of the lowest in the study (cf. Table 12).

By replacing an ethyl group between the β- and the γ-amino group (EvA07 and EvA26) with a propyl group (EvA03 and EvA25), the pK-values of both amino groups and the BM-value increases (cf. Figure 1, Section 3.2.3, and Table 12). A decrease of the BM-value as a result of the increasing molar mass due to the addition of one CH_2 group is overcompensated by an increase in the pK-values of the β- and the γ-amino group, resulting from the positive inductive effect of the added group. *n*-Butyl groups may also lead to higher BM-values [161] but were not investigated in this study.

The substitution of two methyl groups at the γ-amino group (EvA03 and EvA07) by two ethyl groups (EvA25 and EvA26) increases the pK-values of the γ-amino groups (cf. Figure 1 and Section 3.2.3), but lowers the BM-value (cf. Table 12). The increase

of molar mass by the two added carbon atoms exceeds their positive inductive effect. A combination of a methyl and an ethyl group might lead to higher BM-values compared to two methyl groups but was not investigated in this study.

The addition of one methyl group at the end of the alkyl chain of isopropylamine (EvA04) to sec-butyl amine (EvA05) does not have a significant influence on the pK-value of the β-amino group (cf. Figure 1 and Section 3.2.3), but lowers the BM-value as a result of the increased molar mass (cf. Table 12). Alkyl chains of terminating ligands with less than three carbon atoms might further increase the BM-value but were not investigated in this study.

Tertiary amino groups in ring structures have much lower pK-values than tertiary amino groups in chains. A good example for this effect is given by the comparison of the pK-values of the γ-amino groups of EvA24 and EvA21 (cf. Figure 1 and Section 3.2.3). Despite the larger positive inductive effect of the morpholine group of EvA24, compared to that of the two ethanol groups of EvA21, the pK-value of the γ-amino group of EvA24 is significantly lower than that of EvA21. A further example is the lower pK-value of the γ-amino group of EvA14 compared to that of EvA03, which is also contrary to the expected inductive effect of the surrounding alkyl groups. The same trend can be found by comparing pK-values of other amines than the EvAs [98, 157]. It is conceivable that the higher rigidity of a ring structure compared to that of a chain-structure causes the observed differences in the pK-values.

The pK-values of secondary amino groups are higher than those of similar tertiary amino groups. This is well-known in literature [157, 158, 162]. An example from the present work is given by the comparison of the pK-values of the γ-amino group of EvA36 and EvA03 (cf. Figure 1 and Section 3.2.3). Despite the higher positive inductive effect of two methyl groups on the γ-amino group of EvA03, compared to that of one methyl group for EvA36, the pK-value of the γ-amino group of EvA03 is lower than that of EvA36. Also the BM-value increases as the removal of one methyl group reduces the molar mass while simultaneously the pK-value of the amino group increases. The effect is enhanced if the tertiary amino group is part of a ring structure (cf. EvA06 compared to EvA09 in Figure 1 and Section 3.2.3). The reason for this observation is probably the better spatial accessibility of the free electron pair of secondary amino groups, compared to that of tertiary amino groups. The better spatial accessibility predominates the stronger positive inductive effect of a third alkyl group.

6.3.3 Formation of ring structures

6.3.3.1 Approach

The results of the present work indicate that carbamates and alkylcarbonates are stabilized by the formation of H-bond and zwitterionic stabilized ring structures. Even though no direct evidence for the existence of such ring structure was found, the obtained results strongly indicate that they can be formed. By postulating their existence, simple and plausible explanations for the observed results can be given that would otherwise be contradictory, namely regarding the carbamate and alkylcarbonate formation.

Ring formations in aqueous solutions of amines have been postulated previously; mainly between hydroxy- and amino groups [87, 88, 163–165], but also between carbamates and amino groups [94]. However, to the best of the authors knowledge, the present work is the first in which a systematic experimental study gives not only indications for the existence of such H-bond and zwitterionic stabilized ring structures, but also provides information on the conditions, under which they are formed and the consequences they have on the properties of the aqueous solvent.

6.3.3.2 Carbamate and amino group

The formation of a zwitterion with a ring structure between a carbamate and an amino group is schematically shown in Figure 36, using EvA07 as an example. For clarity, the reaction scheme focuses only on the steps which are directly relevant for the formation of the zwitterion. Other information such as that on protonation states of the amino groups that are not involved is not included. The reaction scheme starts with the components EvA07, H_2O, and CO_2 on the left side. R_I is the protonation of the β-amino group as well as the formation of bicarbonate. R_{II} is the formation of β-carbamate and R_{III} is the conversion between the CO_2-containing species bicarbonate and carbamate. These reactions are basically known [166]. R_{IV} is the formation of the carbamate zwitterion. This step has, to the best of the authors knowledge, not been described before in the literature, and is assumed to exist not only for EvAs but also for other amines. The protonated positively charged γ-amino group orients itself towards the negatively charged oxygen atom of the β-carbamate and forms a zwitterion with a stabilizing ring structure. The ring structure is stabilized by ionic and H-bond interactions between the amino group and the carbamate. Due to the stabilizing effect, larger concentrations of carbamate were found for EvAs that form a zwitterion with a ring structure, than for those who do not. This is illustrated by the comparison of the concentrations of β-carbamate of EvA02 (cf. Figure 31) with those of EvA03, EvA07, EvA24, EvA25, and EvA26 (cf. Figure 33). EvA02 can only form a zwitterion with the α-amino group of the
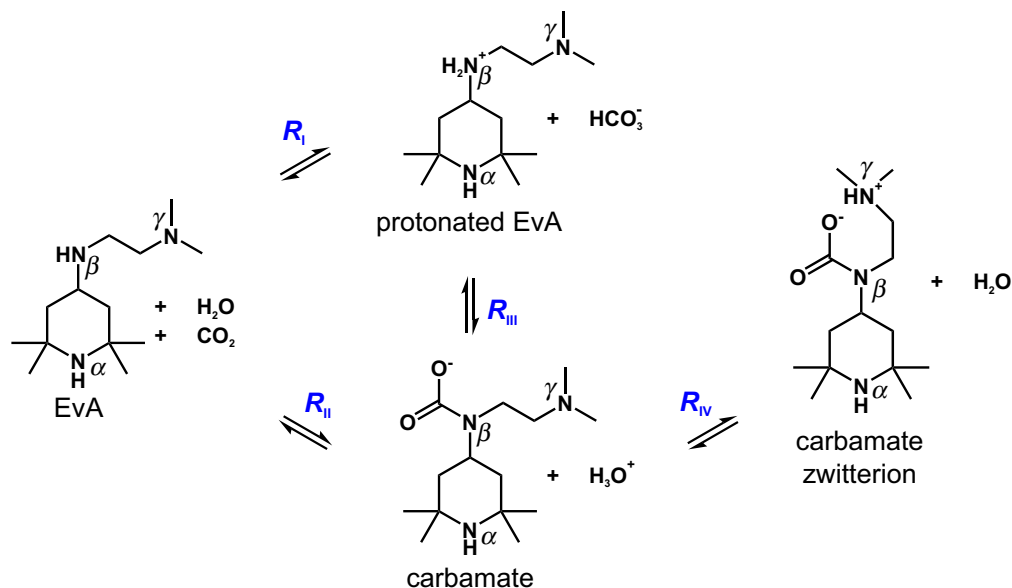
Figure 36: Reaction scheme for the formation of a carbamate zwitterion between β-carbamate and γ-amino group in aqueous solutions of EvA, exemplarily shown for EvA07. See text for description.

boat-conformation of the 2,2,6,6,tetramethylpiperidine ring. This confirmation is unstable and thus plays a minor roll in this study. The resulting concentration of β-carbamate of EvA02 is low. The other amines can form a zwitterion also with the γ-amino group. This ring structure is much more stable, which results in much higher concentrations of β-carbamate. The differences between the concentrations of β-carbamate of the EvAs that form the stable zwitterion result from the different stability of the zwitterions. Two parameters that influence the stability of the zwitterions were found in the study.

A high pK-value of the amino group that is involved in the zwitterionic structure enhances the stability of the carbamate zwitterion. For instance, this can be seen from the results for EvA07 and EvA26 shown in Figure 33. Both EvAs form a seven-membered zwitterionic stabilized ring (counting the carbon (#1) and the negatively charged oxygen atom of the β-carbamate (#2), the β-amino group (#3), the two carbons between the β- and γ-amino group (#4, #5), the γ-amino group (#6), and the proton that is attached to the protonated γ-amino group (#7)). The basicity of the γ-amino group of EvA26 is higher than that of the γ-amino group of EvA07 (cf. Figure 1 and Section 3.2.3). This results in a higher concentration of β-carbamate for EvA26 than for EvA07. The same trend is observable for EvA03, EvA24, and EvA25. EvA03, EvA24, and EvA25 form eight-membered zwitterionic stabilized rings (counting the carbon (#1) and the negatively charged oxygen atom of the β-carbamate (#2), the β-amino group (#3), the three carbons between the β- and γ-amino group (#4, #5, #6), the γ-amino group (#7), and the proton that is attached to the protonated γ-amino group (#8)). The concentration of β-carbamate of these EvAs decreases with decreasing pK-value of

the γ-amino group. It can be assumed that the higher pK-values of the γ-amino group leads to a higher concentration of the protonated species, which consequently leads to higher concentrations of stabilized β-carbamate.

Zwitterions with seven-membered rings are more stable than zwitterions with eight-membered rings. This can be seen from the results for EvA25 and EvA26 shown in Figure 33. Even though the pK-value of the γ-amino group of EvA25 is higher than that of EvA26 (cf. Figure 1 and Section 3.2.3), the concentration of γ-carbamate of EvA25 is lower than that of EvA26. The same trend is found for EvA03 and EvA07 (cf. Figure 33).

6.3.3.3 Carbamate and hydroxy group

The β-carbamate of the hydroxy group containing EvA27 and EvA31 (cf. Figure 32) are stabilized by H-bond interaction with the proton of their respective hydroxy group. This stabilizing interaction between carbamate and hydroxy group is schematically shown in the left part of Figure 37 and resembles the carbamate zwitterion shown in Figure 36. The stabilizing effect can be seen from a comparison of the results of EvA31 (cf. Figure 32), with the results of EvA02 and EvA06 (cf. Figure 31 and Figure 35) as well as with EvA03, EvA07, EvA25, and EvA26 (cf. Figure 33). The concentration of the H-bond stabilized β-carbamate of EvA31 is significantly higher than that of EvA06 and EvA02, which are not stabilized. However, it is also lower than that of EvA03, EvA07, EvA25, and EvA26, which are stabilized by a zwitterion. This indicates that the stabilizing effect of the H-bond is weaker than that of the zwitterion, but strong enough to increase the concentration of β-carbamate compared to the EvAs with no stabilizing effect.

6.3.3.4 Alkylcarbonate and amino group

Alkylcarbonates are formed between CO_2 and hydroxy groups at alkaline conditions. Accordingly, alkylcarbonates were found for EvA21, EvA27, and EvA31. The alkylcarbonates of EvA21, EvA27, and EvA31 are additionally stabilized by a zwitterion with a ring structure that is formed between the negatively charged alkylcarbonate and the positively charged β-amino group for EvA27 and EvA31 and the γ-amino group for EvA21, respectively. Such an alkylcarbonate zwitterion is schematically shown in the right part of Figure 37. Same as the carbamate zwitterion, it is stabilized by ionic and H-bond interactions. EvA21 shows a significantly higher concentration of alkyl-carbonate than EvA27 and EvA31. This is probably due to the higher basicity of the interacting γ-amino group of EvA21 compared to that of the β-amino group of EvA27

and EvA31. It can be assumed that the alkylcarbonate species, that were found in CO_2-loaded aqueous solutions of mono-ethanolamine and methyl-diethanolamine in previous works of our group [152, 160] are also stabilized by the formation of zwitterions with a ring structure. A study of CO_2-loaded aqueous solutions of ethanol proved that alkylcarbonates are formed also without being stabilized in a ring structure, as long as the CO_2-loaded aqueous solution is at alkaline conditions. For more details see Appendix A.
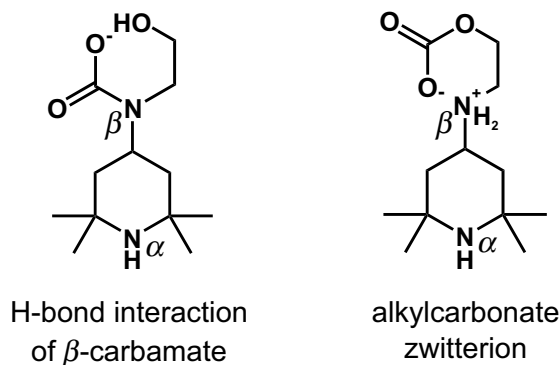
Figure 37: Chemical structures of the stabilizing ring structures in hydroxy group-containing EvAs, exemplarily shown for EvA31.

6.3.4 Steric hindrance

The substituents of carbon atoms that are adjacent to primary and secondary amino groups have a strong influence on the speciation of CO_2-containing species. This influence is often labeled as steric effect or steric hindrance. The influence of the differently hindered amino groups on the speciation of CO_2-containing species is discussed in the following text. In this discussion it is refered to different degrees of steric hindrance. These degrees are defined according to Figure 38. The degree depends on the number of hydrogen atoms (H) that are covalently bound to carbon atoms, which are adjacent to the amino group (R, R_l, R_r in Figure 38). A distinction of the hindrance is made between unhindered, single-hindered, double-hindered, triple-hindered, and quadruple-hindered amino groups (cf. Figure 38).

Unhindered and single-hindered primary amino groups show high concentrations of carbamate [48, 60, 94, 149]. EvA01 is the only amine in this study that contains a primary amino group (cf. Figure 1). The β-amino group of EvA01 is single-hindered and shows high concentrations of β-carbamate (cf. Figure 30). The good spatial accessibility of unhindered and single-hindered primary amino groups promotes the formation of carbamate.
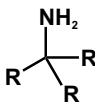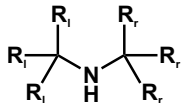
steric hindrance	primary amine	secondary amine		
unhindered	3 R = H	3 R_l = H & 3 R_r = H		
	2 R = H	2 R_l = H & 3 R_r = H		
		2 R_l = H & 2 R_r = H		
single	1 R = H	1 R_l = H & 3 R_r = H		
		1 R_l = H & 2 R_r = H		
double	0 R = H	1 R_l = H & 1 R_r = H		
		0 R_l = H & 3 R_r = H		
		0 R_l = H & 2 R_r = H		
triple	-	0 R_l = H & 1 R_r = H		
quadruple	-	0 R_l = H & 0 R_r = H		

Figure 38: Definition of the degrees of steric hindrance used in the present work.

Unhindered secondary amino groups show high concentrations of carbamate [60, 94, 149, 167]. In the present work, EvA34 and EvA36 were the only EvAs that contain an unhindered secondary amino group (cf. Figure 1). Both EvAs show high concentrations of γ-carbamate at the unhindered secondary γ-amino group (cf. Figure 34). However, for EvA34 and EvA36, the γ-carbamate formation is additionally promoted by the formation of a zwitterion with a ring structure.

Increased steric hindrance lowers the stability of zwitterionic stabilized ring structures between carbamates and protonated amino groups. This is demonstrated by the concentration of EvA36 which forms two carbamate species that are stabilized by the formation of eight-membered carbamate zitterion rings: β-carbamate and γ-carbamate (cf. Figure 34). β-carbamate is formed at the single-hindered secondary β-amino group and is stabilized by the γ-amino group which has a high pK-value, whereas γ-carbamate is formed at the unhindered secondary γ-amino group and is stabilized by the β-amino group, which has a lower pK-value. Regarding only the basicity, the concentration of β-carbamate should exceed the concentration of γ-carbamate due to the more stable zwitterionic ring structure. However, the observed concentrations show the opposite trend (cf. Figure 34), which can be interpreted as a result of the increased hindrance of the β-amino group compared to that of the γ-amino group. For EvA34 the influences of the steric hindrance and that of the basicity on the zwitterions are superimposed (cf. Figure 34). The γ-carbamate of EvA34 is less hindered than the β-carbamate and additionally forms a strong zwitterion with the δ-amino group. Therefore, the concentration of γ-carbamate of EvA34 exceeds that of the β-carbamate by far.

Single and double-hindered amino groups only show very low concentrations of carbamate if the carbamate is not stabilized by a zwitterion with a ring structure. This can be seen from the concentration of β-carbamate of EvA02 (cf. Figure 31), which is single-hindered, and EvA04 and EvA05 (cf. Figure 31), which are double-hindered and which all three are not stabilized. A difference between single-hindered and double-hindered secondary amino groups concerning the concentration of β-carbamate was not found in the study. If the carbamate at single hindered secondary amino groups is stabilized by a zwitterion with a ring structure, however, high concentrations of carbamate are observable (cf. Figure 33).

Increased steric hindrance of hydroxy groups lowers the stability of alkylcarbonate zwitterions and H-bond interaction stabilized carbamates in which the hydroxy group is involved. By applying the same definition of steric hindrance of primary amines from Figure 38 to hydroxy groups, the hydroxy group of EvA27 is defined as single-hindered, and the hydroxy group of EvA31 is defined as unhindered (cf. Figure 1). The concentration of β-carbamate and alkylcarbonate of the unhindered EvA31 exceeds the respective concentrations of the single-hindered EvA27 (cf. Figure 32). As the basicity and ring size are similar, this is most likely caused by the hindrance of the interacting hydroxy group. It is likely, that the same observations could be made for all stabilizing ring structures, which, however, was not investigated in the study.

For none of the EvAs a formation of carbamate at the quadruple-hindered secondary α-amino group was observed. Even though no triple-hindered secondary amino groups were investigated in the present work, it can be assumed that also triple-hindered secondary amino groups do not form significant amounts of carbamate.

Steric hindrance influences the amount of (bi)carbonate that can be captured in the aqueous solution of EvA. EvA02 and EvA05 have the same molar mass and similar pK-values of all amino groups, but they differ in the hindrance of the β-amino group, which is single-hindered for EvA02 and double-hindered for EvA05 (cf. Figure 1). Even though they also have a similar speciation of CO_2-containing species, i.e., CO_2 is mainly bound as (bi)carbonate (cf. Figure 31), they reveal strong differences in the equilibrium CO_2-loadings at low temperature. This is shown in Table 13 where the equilibrium CO_2-loading $\tilde{X}_{CO_2}$ of EvA02 and EvA05 at three different conditions (C1 to C3) are given. The conditions vary in the temperature t, in the mass fraction of EvA in the unloaded solvent $\tilde{w}^0_{EvA}$, and in the equilibrium partial pressure of CO_2 p_{CO_2}. At low temperature (C1 and C2 in Table 13), the equilibrium CO_2-loading of EvA02 is much higher than that of EvA05. As almost all CO_2 is bound as (bi)carbonate, this means that single-hindered secondary amino groups enhance the solubility of (bi)carbonate in the solvent, compared to double-hindered amino groups. It can be assumed that the better accessibility of less hindered amino groups promotes a short-range coordination

between (bi)carbonate and the amino group which stabilizes the (bi)carbonate. This effect was not observed at high temperature (cf. C3 in Table 13).

Table 13: Equilibrium CO_2-loadings of EvA02 and EvA05 at three selected conditions C1, C2, and C3.

	t	p_{CO_2}	$\tilde{w}^0_{EvA}$	$\tilde{X}_{CO_2}$	
	°C	bar	g/g	g/g	
				EvA02	EvA05
C1[a]	20	2.00	0.10	0.41	0.32
C2[b]	40	0.14	0.05	0.39	0.32
C3[b]	100	0.14	0.05	0.16	0.17

t: temperature with the expanded uncertainty $U(t) = 1$ °C, p_{CO_2}: partial pressure of CO_2 with the relative standard uncertainty $u_r(p_{CO_2}) = 0.035$, $\tilde{w}^0_{EvA}$: mass fraction of EvA in the unloaded solvent with the relative expanded uncertainty $U_r(\tilde{w}^0_{EvA}) = 0.001$ (0.99 level of confidence), $\tilde{X}_{CO_2}$: equilibrium CO_2-loading with the relative standard uncertainty $u_r(\tilde{X}_{CO_2}) = 0.05$. [a]results for the present section, [b]results from Section 3.

6.3.5 Ether groups

Ether groups enhance the solubility of molecular CO_2. Therefore, physical solvents for CO_2-absorption often contain ether groups [6, 168]. This is in line with the findings for the ether group containing EvA06, for which the highest concentrations of molecular CO_2 in the present study were found (cf. Figure 35). For EvA24 in contrast, where the oxygen atom is placed in a ring, the concentration of molecular CO_2 is low (cf. Figure 33). This unexpected low concentration of molecular CO_2 for EvA24 is probably due to a superposition with other effects, like the differing basicity, the formation of zwitterions with a ring structure, or the less flexible placement of the oxygen atom inside a ring structure.

The concentration of β-carbamate of the ether group containing EvA06 (cf. Figure 35) is higher than that of EvA02 (cf. Figure 31). A reason for this may be the lower pK-value of the β-amino group of EvA06 compared to that of EvA02 (cf. Figure 1 and Section 3.2.3). Low pK-values are suspected to favor the formation of carbamate [169, 170]. However, the influence of the ether group or the high concentration of molecular CO_2 on the concentration of β-carbamate are superimposed for EvA06, which complicates a final explanation of the observed higher concentration of β-carbamate.

6.4 Application properties and guidelines

In this section, the second step of the route that was followed in the present work to
establish structure-property relationships is presented (cf. Figure 28). The second step
was to link the established relationships from Section 6.3 with application properties
of the solvent, which are directly relevant for a CO_2-absorption process. This includes
quantitative relationships to measured data for the equilibrium CO_2-loading and rate
of absorption of CO_2, which were established in the screening (cf. Section 3), as well as
general considerations regarding the mass transfer, solubility and volatility of the amine,
and energy demand of a CO_2-absorption process. From this findings, some guidelines
for the design of new amines were derived.

Figure 39 (left) shows the equilibrium CO_2-loading $\tilde{X}_{CO_2}$ of aqueous solutions of EvAs
at $t = 40\,°C$ and $t = 100\,°C$ and Figure 39 (right) the initial rate of absorption of CO_2
RA at $t = 40\,°C$ as a function of the BM-value (cf. Section 6.3.2), respectively. Both,
equilibrium CO_2-loading and rate of absorption of CO_2, stem from the results of the
screening in Section 3 and were measured at a mass fraction of amine in the unloaded
solvent of $\tilde{w}^0_{amine} = 0.05$ g/g and a partial pressure of CO_2 of $p_{CO_2} = 140$ mbar.

In average, the equilibrium CO_2-loading increases with increasing BM-value. This is
observable for both temperatures. The slope however differs between the two temper-
atures, which leads to an average increase of the difference between the equilibrium
CO_2-loadings at the two temperatures with increasing BM-value. Also the rate of ab-
sorption of CO_2 increases with increasing BM-value. The equilibrium CO_2-loading can
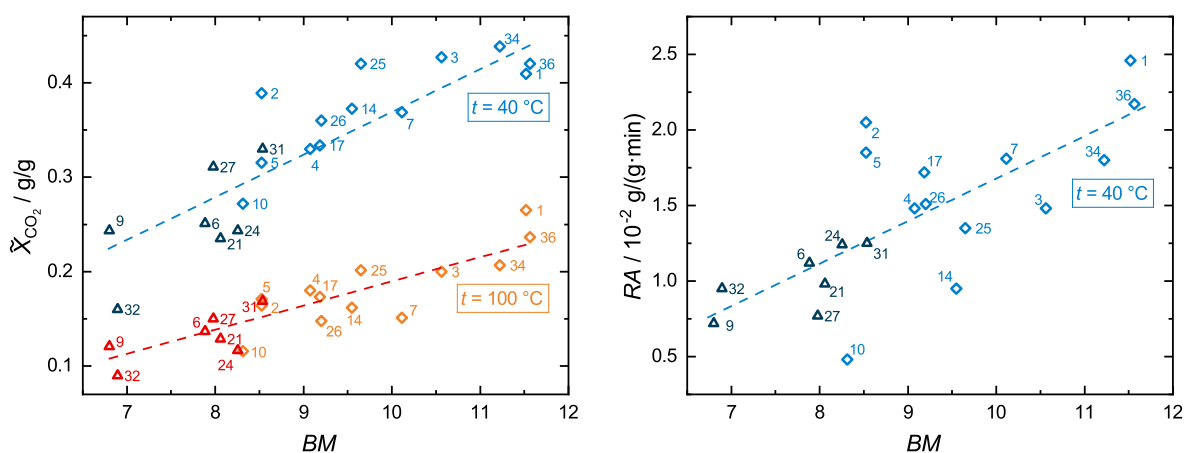
Figure 39: Equilibrium CO_2-loading and initial rate of absorption of CO_2 from Sec-
tion 3 respectively, as a function of the mass-related basicity (see text in
Section 6.3.2). Numbers indicate the EvA-number. black/blue: $t = 40\,°C$,
red/orange: $t = 100\,°C$, △: EvAs that contain oxygen atoms, ◇: EvAs that
do not contain oxygen atoms, dashed lines: linear trend of all isothermal
data.

be seen as the driving force for the absorption which is why the rate of absorption of CO_2 correlates with the equilibrium CO_2-loading and, hence, also with the BM-value. For the absorption of CO_2, high CO_2-loading and high rate of absorption of CO_2 at $t = 40\,°C$ are desired. For the desorption, a low energy demand for the regeneration of the solvent is preferred, for which to achieve a large difference between the equilibrium CO_2-loadings at $t = 40\,°C$ and $t = 100\,°C$, low equilibrium CO_2-loading at $t = 100\,°C$, and low enthalpy of absorption of CO_2 contribute in varying degrees, depending on the purification task that is performed (cf. Section 3.3). The enthalpy of absorption of CO_2 is strongly influenced by the speciation. Broadly generalized, it is small for solvents where CO_2 is captured as molecular CO_2, medium for solvents that mainly form (bi)carbonate and high for solvents where significant concentrations of carbamate are formed [6, 10, 82, 109, 127, 171, 172].

As expected, amines that contain carboxylate groups show low equilibrium CO_2-loadings, low differences between the equilibrium CO_2-loadings, and low rates of absorption of CO_2 and should be avoided in the design of good performing amines. The same was found for aromatic structures [63, 89, 111, 112].

Oxygen atoms have a negative effect on the BM-value which is rather undesired regarding equilibrium CO_2-loading and rate of absorption of CO_2 (cf. Figure 39). Oxygen atoms that are part of a ring structure should generally be avoided. Ether groups which are not part of a ring structure however significantly improve the solubility of molecular CO_2 in the solvent. This usually lowers the energy demand for the regeneration of the solvent and is advantageous in purification tasks where properties of a physical solvent are wanted, e.g., in tasks where the partial pressure of CO_2 in the feed gas is high and the purification requirement is low.

The addition of hydroxy groups significantly increases the water-solubility and decreases the volatility of the amine (cf. Section 3 and [66, 173]). Due to the lower volatility, the molecule size of the amine can be reduced which lowers the dynamic viscosity and enhances the mass transfer of CO_2. Additionally, hydroxy groups form alkylcarbonates which is an additional reaction pathway for the absorption of CO_2 that should increase the rate of reaction of CO_2 compared to similar systems without that reaction [125]. If high mass transfer and low volatility is absolutely essential in the purification task, the addition of hydroxy groups may be considered. Otherwise hydroxy groups should be avoided and di- or triamines should be favored as they lower the volatility due to their molar mass without generating disadvantageous ratios between alkyl and amino groups.

The optimal distance between two amino groups is three to four carbon atoms. A ring structure between the amino groups is advantageous as its steric influence impedes the formation of zwitterions which reduces the equilibrium CO_2-loadings and probably

increases the enthalpy of absorption of CO_2. The length of terminating alkyl ligands of secondary amino groups should have not more than three carbon atoms.

Tertiary amino groups that are part of a ring structure should be avoided due to their low BM-value compared to tertiary amino groups that are not part of a ring structure, resulting in low equilibrium CO_2-loading and low rate of absorption of CO_2. Secondary amino groups should be preferred over tertiary amino groups due to the increased BM-value and enabled reaction pathway of the formation of carbamate, from which the equilibrium CO_2-loading and the rate of absorption of CO_2 benefits.

Unhindered secondary amino groups form stable carbamates. Stable carbamates increase the CO_2-solubility at low partial pressure of CO_2 (cf. Section 3, Section 4, and [10, 167]), which is advantageous if the requirement for the residual amount of CO_2 in the purified gas stream is very low, but increase the energy demand for the regeneration of the solvent. Single-hindered secondary amino groups show stable carbamates only if the carbamate is stabilized by a zwitterion with a ring structure. By avoiding the stabilization, the carbamate constitutes as an intermediate (cf. Figure 36), which is advantageous for the rate of reaction of CO_2, the amount of CO_2 that can be captured, and the energy demand for the regeneration of the solvent. A higher degree of steric hindrance than single hindered is disadvantageous as it reduces the amount of bi(carbonate) that is captured.

From the investigated amino groups, single-hindered secondary amino groups emerge as advantageous in many aspects and seem to be especially favorable to reduce the energy demand for the regeneration without showing obvious deficiencies in other properties, e.g., the rate of absorption of CO_2. Also other amines than the EvAs that contain a single hindered secondary amino group were evaluated positively in literature [58, 60, 89, 147, 165].

A low ratio of polar groups (hydroxy, ether, ketone, amino) to unpolar groups (hydrocarbons) in the molecule can cause a liquid-liquid phase split of the solvent (cf. Section 3). The liquid-liquid phase split can reduce the solubility of CO_2 in the solvent, and if this is used beneficial in an advanced CO_2-absorption process design, it may lead to a reduction of the energy demand and recirculation rate of that process (cf. Section 5). The temperature, where the liquid-liquid phase split occurs is of high importance, as the split should be avoided at absorber conditions but be evoked at desorber conditions. The split temperature can roughly be estimated as described in Appendix B. If a liquid-liquid phase split is desired, primary amino groups, hydroxy groups, and carboxylate groups should generally be avoided. Ether groups, as well as secondary and tertiary amino groups should be used with a sufficient amount of surrounding hydrocarbon groups (cf. Appendix B).

6.5 Design of new amines

In this section, the structure-property relationships and guidelines from Section 6.3 and Section 6.4 are used for the design of new amines. This is a backward run through the steps that were taken to elucidate the structure-property relationships (cf. Figure 28), which means that desired application properties are selected and the corresponding optimized chemical structure is designed. Thereby, different purification tasks lead to different chemical structures. There is no single best design for all purification requirements. Nevertheless, some general rules can be applied for the design of basic structures which can then be tailored to fit best for a given purification task.

Three of such basic structures are proposed in the present work. These amines are abbreviated by the acronym ADAM which stands for **A**dvanced **D**esigned **Am**ines with a consecutive capital letter, designating the structure. The chemical structure of the ADAMs are shown in the upper part of Figure 40. Intermediates that can be used as starting materials for the synthesis of the proposed ADAMs are commercially available (CAS No.: 71322-99-1, 1245698-19-4, 59663-72-8, 183591-49-3, 3114-70-3, 637-88-7, 3385-21-5, 504-02-9) and routes for the synthesis of the ADAMs are known [46]. All ADAMs contain two amino groups which slightly differ in their position.
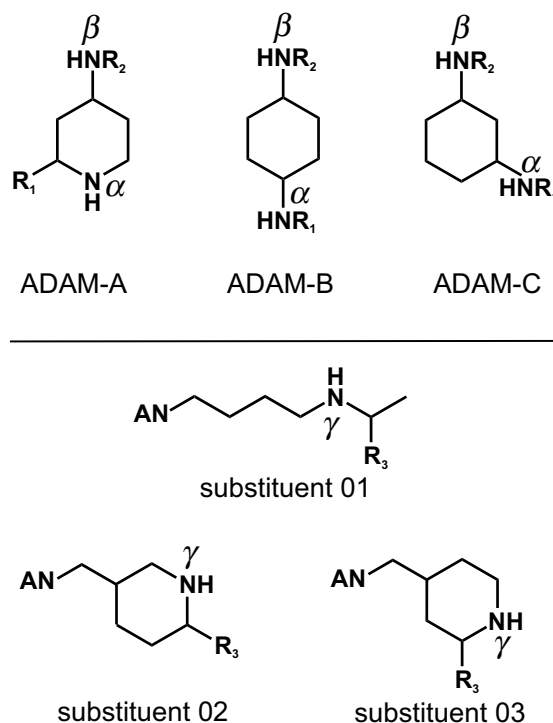
Figure 40: Basic chemical structures of the **A**dvanced **D**esigned **Am**ines (ADAMs) and a selection of substituents. The positions marked with R_1, R_2, and R_3 are intended for modifications with varying substituents (see text). AN is where the shown substituents are covalently bound to the β-amino group (R_2) of the ADAM.

In the ADAMs shown in the upper part of Figure 40, R_1 and R_2 mark the positions where modifications are intended, and by which the application properties of the molecules can be adjusted to the requirements of the purification task. To lower the energy demand, R_1 and R_2 may be methyl, ethyl, or propyl groups, as well as dimethyl-, ethyl methyl-, diethyl-, propyl methyl-, propyl ethyl-, or n-butyl methyl-ethers. To increase the CO_2-solubility at low partial pressure of CO_2, R_1 and/or R_2 may be a proton so that the ADAMs contain primary and/or unhindered secondary amino groups. To lower the volatility of the ADAMs, the substituents which are shown in the lower part of Figure 40 may be added at R_2. They were also designed based on the structure-property relationships of this work. The substituents or at least intermediates of them are commercially available (CAS No.: 42042-71-7, 110-60-1, 78-93-3, 107-87-9, 278789-37-0, 1550959-11-9, 1785070-11-2, 1236121-42-8, 2167461-04-1) and the routes for their synthesis and addition to the ADAMs are known [46]. R_3 is intended for further modifications. Due to the already high molar mass, only methyl or ethyl groups should be considered as substituents here. In case that the ADAMs are insufficiently soluble in water or show too high volatility, methanol, ethanol, propanol or n-butanol groups could also be considered for the positions R_1 or R_2. To induce a liquid-liquid phase split in the temperature range between 60 °C $\leq t \leq$ 100 °C, according to Appendix B, in total 3 to 5 additional hydrocarbon groups must be added to each ADAM.

6.6 Conclusion

The concentration of CO_2-containing species in 16 aqueous solutions of EvAs was measured between 20 °C $\leq t \leq$ 100 °C in the present work using NMR spectroscopy. The observed CO_2-containing species were carbamates of primary and secondary amino groups, alkylcarbonates, (bi)carbonate, and molecular CO_2. The data on the speciation were combined with data on the pK-values of the EvAs and relationships between their chemical structure and the observed speciation and basicity were established. Many of the results, that were obtained here for the EvAs can be generalized and applied to other amines. Some relationships, that had been described previously in literature for other amines were confirmed. Others were stated in the present work for the first time. Regarding these new relationships, some conclusions made in literature need to be reconsidered, e.g., in [80, 87, 90, 94, 148].

The established relationships were summarized and compared to application properties of the solvents, which are relevant for a CO_2-absorption process. From this comparison, some general guidelines for the design of new amines were derived. These guidelines were applied and three new basic chemical structures, called ADAMs, as well as a selection of substituents for the ADAMs were proposed. The ADAMs and their derivatives provide

a modular kit for the design of tailor-made amines for a variety of purification tasks for which, dependent on the substituent, the application properties of the amine can be adapted to the requirements of the purification task. The new amines can be synthesized from intermediates which are commercially available.

The next step on the pathway towards tailor-made amines would be to synthesize some ADAMs and investigate them in a thorough manner as it was done for the EvAs. This will show if they meet the expectations, drawn from the relationships of the present work. Furthermore, there are still many influencing parameters which are unknown and which need to be studied, e.g., the effect chemical groups which were not part of the present work, or the influence of interactions between functional groups which are not part of the same molecule [143, 149], which may lead to additional new chemical structures or substituents of the ADAMs. If the ADAMs meet the expectations, still the complexity of their synthesis, the price of the molecules, their thermal and chemical stability, toxicity as well as further physico-chemical properties namely solid precipitation, the dynamic viscosity of the aqueous solutions, or the vapor pressure of the ADAMs have to be evaluated. It is worthwhile to invest this effort and to pursue on this path towards tailor-made amines. More generally, the present work shows that understanding the influence of the structure of an amine on the speciation of CO_2-containing species is the key step in establishing relationships between the structure and the application properties of the aqueous solutions of amines.

7 Conclusions

An interesting new class of amines for reactive CO_2-absorption has been studied thoroughly in the present thesis. The amines are derivatives of triacetoneamine that share the triacetoneamine ring structure but differ in one substituent. The derivatives are abbreviated by the acronym EvA with a consecutive number that designates the derivative. About 50 EvAs were considered for the study, from which 26 were actually synthesized and investigated experimentally as aqueous solvents. In total, more than 2400 data points were measured in the present work. The mass fractions of amine in the unloaded solvent in the experiments were mostly $\tilde{w}^0_{\mathrm{amine}} \leq 0.4$ g/g, temperatures were between $20\,°C \leq t \leq 130\,°C$, and the partial pressures of CO_2 was between 0.02 bar $\leq p_{CO_2} \leq 100$ bar, which resulted in CO_2-loadings of up to $\tilde{\alpha}_{CO_2} \leq 6.2$ mol/mol. The investigated properties were: solubility of CO_2, rate of absorption of CO_2, liquid-liquid and solid-liquid equilibrium, elucidation and quantification of CO_2-containing species, pK-values, pH-values, foaming behavior, density, dynamic viscosity, vapor pressure, and liquid heat capacity. The aim of the study was to identify EvAs that show superior performance in CO_2-absorption processes and to understand the structure-property relationships that are behind that superior performance. Hence, not all EvAs were investigated with the full range of experiments.

The solvents were initially assessed in a broad experimental screening and compared to results for two reference solvents that are widely used for CO_2-absorption: aqueous solutions of monoethanolamine (MEA) and of a blend of methyl-diethanolamine (MDEA) and piperazine (PZ) with a mass ratio of 7:1 (MDEA/PZ). The investigation included qualitative assessments, e.g., foaming behavior or the occurrence of solid precipitation, as well as quantitative results, e.g., CO_2-solubility and rate of absorption of CO_2, with the target to identify solvent candidates for an industrial application. With this wide-ranging and target-oriented experimental assessment, the selection of promising solvents was reduced down to four promising candidates, which surpassed the performance of MEA and MDEA/PZ in many properties. The candidates were EvA02, EvA03, EvA25, and EvA34, and were hence investigated more in detail.

EvA02 revealed solid precipitation already at moderate mass fractions of amine in the unloaded solvent, which made the solvent unattractive to be applied in industrial CO_2-absorption processes [29]. EvA03 in opposite has already proven its commercial applicability as part of an amine-blend [36]. EvA25 reveals a liquid-liquid phase split at temperatures above about $t \geq 60\,°C$. The detailed investigation of EvA25 revealed that the liquid-liquid phase split leads to a lowering of the overall CO_2-capacity, compared to a homogeneous solvent, and that further improvements of the performance of the solvent

in a CO_2-absorption process seem possible, if the process design is adapted such that the liquid-liquid phase split is used beneficially. Such adapted process design would contain a heated flash unit between the absorber and desorber. Solid precipitation, which was also found for CO_2-loaded aqueous solutions of EvA25 at low temperatures and high mass fractions of EvA25 might become an issue in the design of that new process that had to be tackled. The data that was measured for EvA25 provide all information that is required for this task. The next step for a detailed process design would be to develop a sound physico-chemical model. With the model, the conceptual process design that was discussed in the present work could be evaluated and optimized. The detailed study of EvA34 has validated the excellent performance that was found from the screening. EvA34 combines favorable properties of MEA and MDEA/PZ in one molecule. The relatively high viscosity of aqueous solutions of EvA34 might become an issue for the mass transfer in an absorber column, which, however, might be compensated by higher temperature or more mass transfer area in the absorber column. For both solvents, EvA25 and EvA34, a final evaluation can only be provided after further investigations in a pilot plant. A special focus in the pilot plant experiments should be given to the mass transfer and reaction kinetics, as well as to the enthalpy of absorption of CO_2. Both, mass transfer and enthalpies were investigated only indirectly in the present studies (viscosity, rate of absorption of CO_2, CO_2-solubility isotherms, chemical speciation, and pK-values), which allowed only assumptions on these properties. As the assumptions were mostly promising, it is highly recommended to carry out pilot plant experiments in future work.

The data was furthermore used to understand the interaction between the chemical structure of the amine and the thereof induced concentrations of CO_2-containing species in the solvent. The concentrations of CO_2-containing species were measured with NMR spectroscopy for 16 different aqueous solutions of EvAs in a broad range of temperature and CO_2-loading. The NMR data were combined with data on the pK-values of the EvAs and a large number of relationships between the chemical structure of the EvAs and the observed speciation and basicity were established. The relationships were summarized and compared to application properties of the solvents, which are relevant for a CO_2-absorption process. From this comparison, some general guidelines for the design of new amines were derived. The present work shows that understanding the influence of the structure of an amine on the concentration of CO_2-containing species is the key step in establishing relationships between the structure and the application properties of the aqueous solutions of amines. By understanding these relationships, the development of advanced amines can be lifted from a mainly empirical approach towards a more knowledge based approach. The guidelines that were derived in the present work were then applied and three new basic chemical structures, called ADAMs, as well as a selection of

substituents for the ADAMs were proposed. The ADAMs and their derivatives provide a modular kit for the design of knowledge based tailor-made amines for a variety of purification tasks for which, dependent on the substituent, the application properties of the amine can be adapted to the requirements of the purification task. The new amines can be synthesized from intermediates which are commercially available. The next step on the pathway towards tailor-made amines would be to synthesize some ADAMs and investigate them in a thorough manner as it was done for the EvAs. It is worthwhile to invest this effort and to pursue on this path towards tailor-made amines.

References

[1] B. Metz, O. Davidson, H. d. Coninck, M. Loos, L. Meyer: IPCC special report on carbon dioxide capture and storage, IPCC, Cambridge, 2005.

[2] V. Masson-Delmotte, P. Zhai, A. Pirani, S. L. Connors, C. Péan, S. Berger, N. Caud, Y. Chen, L. Goldfarb, M. I. Gomis, M. Huang, K. Leitzell, E. Lonnoy, J. B. R. Matthews, T. K. Maycock, T. Waterfield, O. Yelekçi, R. Yu, B. Zhou: IPCC 2021 climate change 2021: the physical science basis. Contribution of working group I to the sixth assessment report of the intergovermental panel on climate change, IPCC, Cambridge, 2021.

[3] European academies science advisory council: Carbon capture and storage in Europe, volume 20 of *EASAC policy report*, German national acadamy of sciences Leopoldina, Halle, 2013.

[4] O. Edenhofer (Ed.): Climate change 2014. Mitigation of climate change working group III contribution to the fifth assessment report of the intergovernmental panel on climate change, Cambridge University Press, New York NY, 2014.

[5] International Energy Agency: Technology roadmap carbon capture and storage, OECD Publishing, Paris, 2009.

[6] A. L. Kohl, R. B. Nielsen: Gas Purification, 5 ed., Gulf Publishing Company, Houston, 1997. DOI:`10.1016/B978-0-88415-220-0.X5000-9`.

[7] Hydrocarbon Processing Industry: 2012 Gas Processes Handbook, Gulf Publishing Company, Houston, 2012.

[8] Ö. Yildirim, A. A. Kiss, N. Hüser, K. Leßmann, E. Y. Kenig: Reactive absorption in chemical process industry: A review on current activities, Chem. Eng. J. 213 (2012) 371–391. DOI:`10.1016/j.cej.2012.09.121`.

[9] B. Suresh, R. Gubler, H. Xiaoxiong, Y. Yamaguchi: Chemical economics handbook hydrogen, IHS Markit, Englewood, 2015.

[10] J. Rolker, M. Seiler: New energy-efficient absorbents for the co2 separation from natural gas, syngas and flue gas, Adv. Chem. Eng. Sci. 1 (2011) 280–288. DOI:`10.4236/aces.2011.14039`.

[11] T. E. Rufford, S. Smart, G. Watson, B. F. Graham, J. Boxall, J. C. Diniz da Costa, E. F. May: The removal of co2 and n2 from natural gas. a review of

conventional and emerging process technologies, J. Pet. Sci. Eng. 94-95 (2012) 123–154. DOI:`10.1016/j.petrol.2012.06.016`.

[12] Hydrocarbon Processing Industry: HPI market data, Gulf Publishing Company, Houston, 2021.

[13] T. Kuramochi, A. Ramírez, W. Turkenburg, A. Faaij: Comparative assessment of co2 capture technologies for carbon-intensive industrial processes, Prog. Energy Combust. Sci. 38 (2012) 87–112. DOI:`10.1016/j.pecs.2011.05.001`.

[14] M. K. Mondal, H. K. Balsora, P. Varshney: Progress and trends in co2 capture/separation technologies: A review, Energy 46 (2012) 431–441. DOI:`10.1016/j.energy.2012.08.006`.

[15] B. Li, Y. Duan, D. Luebke, B. Morreale: Advances in co2 capture technology: A patent review, Applied Energy 102 (2013) 1439–1447. DOI:`10.1016/j.apenergy.2012.09.009`.

[16] I. M. Bernhardsen, H. K. Knuutila: A review of potential amine solvents for co 2 absorption process. absorption capacity, cyclic capacity and pka, Int. J. Greenhouse Gas Control 61 (2017) 27–48. DOI:`10.1016/j.ijggc.2017.03.021`.

[17] B. A. Oyenekan, G. T. Rochelle: Alternative stripper configurations for co2 capture by aqueous amines, AIChE J. 53 (2007) 3144–3154. DOI:`10.1002/aic.11316`.

[18] D. Bhattacharyya, D. C. Miller: Post-combustion co2 capture technologies - a review of processes for solvent-based and sorbent-based co2 capture, Curr. Opin. Chem. Eng. 17 (2017) 78–92. DOI:`10.1016/j.coche.2017.06.005`.

[19] T. N. G. Borhani, A. Azarpour, V. Akbari, S. R. W. Alwi, Z. A. Manan: Co2 capture with potassium carbonate solutions: A state-of-the-art review, Int. J. Greenhouse Gas Control 41 (2015) 142–162. DOI:`10.1016/j.ijggc.2015.06.026`.

[20] M. Wang, A. Lawal, P. Stephenson, J. Sidders, C. Ramshaw: Post-combustion co2 capture with chemical absorption. a state-of-the-art review, Chem. Eng. Res. Des. 89 (2011) 1609–1624. DOI:`10.1016/j.cherd.2010.11.005`.

[21] K. Damen, M. van Troost, A. Faaij, W. Turkenburg: A comparison of electricity and hydrogen production systems with co2 capture and storage. part a: Review and selection of promising conversion and capture technologies, Prog. Energy Combust. Sci. 32 (2006) 215–246. DOI:`10.1016/j.pecs.2005.11.005`.

[22] R. Notz, I. Tönnies, H. Mangalapally, S. Hoch, H. Hasse: A short-cut method for assessing absorbents for post-combustion carbon dioxide capture, Int. J. Greenhouse Gas Control 5 (2011) 413–421. DOI:`10.1016/j.ijggc.2010.03.008`.

[23] Y.-J. Lin, G. T. Rochelle: Optimum heat of absorption for co 2 capture using the advanced flash stripper, Int. J. Greenhouse Gas Control 53 (2016) 169–177. DOI:`10.1016/j.ijggc.2016.08.002`.

[24] C. M. Quintella, S. A. Hatimondi, A. P. S. Musse, S. F. Miyazaki, G. S. Cerqueira, A. d. A. Moreira: Co2 capture technologies: An overview with technology assessment based on patents and articles, Energy Procedia 4 (2011) 2050–2057. DOI:`10.1016/j.egypro.2011.02.087`.

[25] Z. Liang, W. Rongwong, H. Liu, K. Fu, H. Gao, F. Cao, R. Zhang, T. Sema, A. Henni, K. Sumon, D. Nath, D. Gelowitz, W. Srisang, C. Saiwan, A. Benamor, M. Al-Marri, H. Shi, T. Supap, C. Chan, Q. Zhou, M. Abu-Zahra, M. Wilson, W. Olson, R. Idem, P. Tontiwachwuthikul: Recent progress and new developments in post-combustion carbon-capture technology with amine based solvents, Int. J. Greenhouse Gas Control 40 (2015) 26–54. DOI:`10.1016/j.ijggc.2015.06.017`.

[26] Q. Zhuang, B. Clements, J. Dai, L. Carrigan: Ten years of research on phase separation absorbents for carbon capture: Achievements and next steps, Int. J. Greenhouse Gas Control 52 (2016) 449–460. DOI:`10.1016/j.ijggc.2016.04.022`.

[27] M. Seiler, J. Rolker, R. Schneider, B. Glöckler, A. Kobus, W. Benesch, T. Riethmann, H. Winkler, J. Reich, H. Brüggemann: Patent wo2010089257: Co2 absorption from gas mixtures using an aqueous solution of 4-amino-2,2,6,6-tetramethylpiperidine, 2010.

[28] B. Willy, R. Schneider, J. Rolker, M. Neumann, R. Steglich, H. Hasse, E. von Harbou, E. Kessler, D. Vasiliu, L. Ninni Schäfer: Patent de102016204929: Absorptionsmedium, verfahren und vorrichtung zur absorption saurer gase aus gasmischungen, 2017.

[29] D. Vasiliu, A. Yazdani, N. McCann, M. Irfan, R. Schneider, J. Rolker, G. Maurer, E. v. Harbou, H. Hasse: Thermodynamic study of a complex system for carbon capture: Butyltriacetonediamine + water + carbon dioxide, J. Chem. Eng. Data 61 (2016) 3814–3826. DOI:`10.1021/acs.jced.6b00451`.

[30] E. Kessler, L. Ninni, B. Willy, R. Schneider, M. Irfan, J. Rolker, E. v. Harbou, H. Hasse: Structure-property relationships for new amines for reactive co2 absorption, Chem. Eng. Trans. 69 (2018) 109–114. DOI:`10.3303/CET1869019`.

[31] E. Kessler, L. Ninni, T. Breug-Nissen, B. Willy, R. Schneider, M. Irfan, J. Rolker, E. von Harbou, H. Hasse: Physicochemical properties of the system n,n-dimethyl-dipropylene-diamino-triacetonediamine (eva34), water, and carbon dioxide for reactive absorption, J. Chem. Eng. Data 64 (2019) 2368–2379. DOI:`10.1021/acs.jced.8b01174`.

[32] E. Kessler, L. Ninni, D. Vasiliu, A. Yazdani, B. Willy, R. Schneider, M. Irfan, J. Rolker, E. von Harbou, H. Hasse: Triacetone-amine derivatives (evas) for co2-absorption from process gases, Int. J. Greenhouse Gas Control 95 (2020) 102932. DOI:`10.1016/j.ijggc.2019.102932`.

[33] E. Kessler, L. Ninni, T. Breug-Nissen, B. Willy, R. Schneider, M. Irfan, J. Rolker, W. R. Thiel, E. v. Harbou, H. Hasse: Speciation in co2-loaded aqueous solutions of sixteen triacetoneamine-derivates (evas) and elucidation of structure-property relationships, Chem. Eng. Sci. 229 (2021) 115999. DOI:`10.1016/j.ces.2020.115999`.

[34] E. Kessler, L. Ninni, T. Breug-Nissen, B. Willy, R. Schneider, M. Irfan, J. Rolker, E. v. Harbou, H. Hasse: Thermodynamic properties of a system for co2 absorption with liquid-liquid phase split: Eva25 + h2o + co2, Ind. Eng. Chem. Res. 61 (2022) 15289–15300. DOI:`10.1021/acs.iecr.2c02701`.

[35] D. Vasiliu, E. Kessler, E. v. Harbou, H. Hasse: Short-cut method for assessing solvents for gas cleaning by reactive absorption, Chem. Eng. Res. Des. 153 (2020) 757–767. DOI:`10.1016/j.cherd.2019.10.015`.

[36] J. Rolker, J. Lally: Alkanolamines - what is next? conference proceeding on laurence reid gas conditioning conference (2022).

[37] D. D. Pinto, H. Knuutila, G. Fytianos, G. Haugen, T. Mejdell, H. F. Svendsen: Co 2 post combustion capture with a phase change solvent. pilot plant campaign, Int. J. Greenhouse Gas Control 31 (2014) 153–164. DOI:`10.1016/j.ijggc.2014.10.007`.

[38] Q. Ye, X. Wang, Y. Lu: Screening and evaluation of novel biphasic solvents for energy-efficient post-combustion co2 capture, Int. J. Greenhouse Gas Control 39 (2015) 205–214. DOI:`10.1016/j.ijggc.2015.05.025`.

[39] P. Broutin, H. Kvamsdal, C. La Marca, P. van Os, N. Booth: A new fp7 project demonstrating co2 capture technologies, Energy Procedia 37 (2013) 6365–6373. DOI:`10.1016/j.egypro.2013.06.566`.

[40] L. Raynal, P. Alix, P.-A. Bouillon, A. Gomez, M. F. de Le Nailly, M. Jacquin, J. Kittel, A. Di Lella, P. Mougin, J. Trapy: The dmx™ process. an original solution for lowering the cost of post-combustion carbon capture, Energy Procedia 4 (2011) 779–786. DOI:`10.1016/j.egypro.2011.01.119`.

[41] L. Raynal, P. Briot, M. Dreillard, P. Broutin, A. Mangiaracina, B. S. Drioli, M. Politi, C. La Marca, J. Mertens, M.-L. Thielens, G. Laborie, L. Normand: Evaluation of the dmx process for industrial pilot demonstration – methodology and results, Energy Procedia 63 (2014) 6298–6309. DOI:`10.1016/j.egypro.2014.11.662`.

[42] Y. Coulier, A. R. Lowe, A. Moreau, K. Ballerat-Busserolles, J.-Y. Coxam: Liquid-liquid phase separation of amine – H 2 O – CO 2 systems: New methods for key data, Fluid Phase Equilib. 431 (2017) 1–7. DOI:`10.1016/j.fluid.2016.10.010`.

[43] J. Zhang, D. W. Agar, X. Zhang, F. Geuzebroek: Co2 absorption in biphasic solvents with enhanced low temperature solvent regeneration, Energy Procedia 4 (2011) 67–74. DOI:`10.1016/j.egypro.2011.01.024`.

[44] F. Yang, X. Jin, J. Fang, W. Tu, Y. Yang, C. Cui, W. Zhang: Development of co 2 phase change absorbents by means of the cosolvent effect, Green Chemistry 20 (2018) 2328–2336. DOI:`10.1039/C8GC00283E`.

[45] U. Liebenthal, D. D. Di Pinto, J. G. M.-S. Monteiro, H. F. Svendsen, A. Kather: Overall process analysis and optimisation for co2 capture from coal fired power plants based on phase change solvents forming two liquid phases, Energy Procedia 37 (2013) 1844–1854. DOI:`10.1016/j.egypro.2013.06.064`.

[46] S. G. Warren, P. Wyatt: Organic synthesis. The disconnection approach / Stuart Warren and Paul Wyatt, 2nd ed. ed., Wiley-Blackwell, Oxford, 2008.

[47] K. Minke, B. Willy: Patent us20180009734: An n-substituted triacetonediamine compound is produced by reacting 4-amino-2,2,6,6-tetramethylpiperidine or a derivative thereof with a carbonyl compound in a reductive amination, 2018.

[48] M. Wagner, I. v. Harbou, J. Kim, I. Ermatchkova, G. Maurer, H. Hasse: Solubility of carbon dioxide in aqueous solutions of monoethanolamine in the low and high gas loading regions, J. Chem. Eng. Data 58 (2013) 883–895. DOI:`10.1021/je301030z`.

[49] B. Rumpf, G. Maurer: An experimental and theoretical investigation on the solubility of carbon dioxide in aqueous solutions of strong electrolytes, Berichte der Bunsengesellschaft für physikalische Chemie 97 (1993) 85–97. DOI:`10.1002/bbpc.19930970116`.

[50] M. Wendland, H. Hasse, G. Maurer: Multiphase high-pressure equilibria of carbon dioxide-water-isopropanol, The Journal of Supercritical Fluids 6 (1993) 211–222. DOI:`10.1016/0896-8446(93)90029-W`.

[51] T. Adrian, H. Hasse, G. Maurer: Multiphase high-pressure equilibria of carbon dioxide-water-propionic acid and carbon dioxide-water-isopropanol, The Journal of Supercritical Fluids 9 (1996) 19–25. DOI:`10.1016/S0896-8446(96)90040-6`.

[52] K. Rauscher, J. Voigt, I. Wilke, W. K. Th: Chemische Tabellen und Rechentafeln für die analytische Praxis, 7 ed., Deutsch Harri GmbH, Thun, 1983.

[53] M. Luckas, J. Krissmann: Thermodynamik der Elektrolytlösungen. Eine einheitliche Darstellung der Berechnung komplexer Gleichgewichte, Springer, Heidelberg, 2001.

[54] C. Ammann, P. Meier, A. Merbach: A simple multinuclear nmr thermometer, J. Magn. Reson. 46 (1982) 319–321. DOI:`10.1016/0022-2364(82)90147-0`.

[55] H. Rafflenbuel, L. Hartmann: Eine dynamische apparatur zur bestimmung von dampf-flüssigkeits-phasengleichgewichten, Chem. Tech. (Heidelberg, Ger.) 4 (1978) 145–148.

[56] H. Hasse: Dampf-Flüssigkeits-Gleichgewichte, Enthalpien und Reaktionskinetik in formaldehydhaltigen Mischungen, Phd, TU Kaiserslautern, Germany, 1990.

[57] F. A. Chowdhury, H. Okabe, S. Shimizu, M. Onoda, Y. Fujioka: Development of novel tertiary amine absorbents for co2 capture, Energy Procedia 1 (2009) 1241–1248. DOI:`10.1016/j.egypro.2009.01.163`.

[58] F. A. Chowdhury, H. Okabe, H. Yamada, M. Onoda, Y. Fujioka: Synthesis and selection of hindered new amine absorbents for co2 capture, Energy Procedia 4 (2011) 201–208. DOI:`10.1016/j.egypro.2011.01.042`.

[59] F. A. Chowdhury, H. Yamada, T. Higashii, Y. Matsuzaki, S. Kazama: Synthesis and characterization of new absorbents for co2 capture, Energy Procedia 37 (2013) 265–272. DOI:`10.1016/j.egypro.2013.05.111`.

[60] K. Goto, F. A. Chowdhury, H. Okabe, S. Shimizu, Y. Fujioka: Development of a low cost co2 capture system with a novel absorbent under the cocs project, Energy Procedia 4 (2011) 253–258. DOI:`10.1016/j.egypro.2011.01.049`.

[61] K. Goto, H. Okabe, F. A. Chowdhury, S. Shimizu, Y. Fujioka, M. Onoda: Development of novel absorbents for co2 capture from blast furnace gas, Int. J. Greenhouse Gas Control 5 (2011) 1214–1219. DOI:`10.1016/j.ijggc.2011.06.006`.

[62] W. Conway, Y. Beyad, P. Feron, G. Richner, G. Puxty: Co2 absorption into aqueous amine blends containing benzylamine (bza), monoethanolamine (mea), and sterically hindered/tertiary amines, Energy Procedia 63 (2014) 1835–1841. DOI:`10.1016/j.egypro.2014.11.191`.

[63] Q. Yang, G. Puxty, S. James, M. Bown, P. Feron, W. Conway: Toward intelligent co2 capture solvent design through experimental solvent development and amine synthesis, Energy Fuels 30 (2016) 7503–7510. DOI:`10.1021/acs.energyfuels.6b00875`.

[64] R. J. Hook: An investigation of some sterically hindered amines as potential carbon dioxide scrubbing compounds, Ind. Eng. Chem. Res. 36 (1997) 1779–1790. DOI:`10.1021/ie9605589`.

[65] K. Maneeintr, R. O. Idem, P. Tontiwachwuthikul, A. G. H. Wee: Synthesis, solubilities, and cyclic capacities of amino alcohols for co2 capture from flue gas streams, Energy Procedia 1 (2009) 1327–1334. DOI:`10.1016/j.egypro.2009.01.174`.

[66] S. Singto, T. Supap, R. Idem, P. Tontiwachwuthikul, S. Tantayanon, M. J. Al-Marri, A. Benamor: Synthesis of new amines for enhanced carbon dioxide (co2) capture performance. the effect of chemical structure on equilibrium solubility, cyclic capacity, kinetics of absorption and regeneration, and heats of absorption and regeneration, Sep. Purif. Technol. 167 (2016) 97–107. DOI:`10.1016/j.seppur.2016.05.002`.

[67] J. Salazar, U. Diwekar, K. Joback, A. H. Berger, A. S. Bhown: Solvent selection for post-combustion co2 capture, Energy Procedia 37 (2013) 257–264. DOI:`10.1016/j.egypro.2013.05.110`.

[68] T. Zarogiannis, A. I. Papadopoulos, P. Seferlis: Systematic selection of amine mixtures as post-combustion co2 capture solvent candidates, Journal of Cleaner Production 136 (2016) 159–175. DOI:`10.1016/j.jclepro.2016.04.110`.

[69] A. Adeosun, Z. Abbas, M. R. Abu-Zahra: Screening and characterization of advanced amine based solvent systems for co2 post-combustion capture, Energy Procedia 37 (2013) 300–305. DOI:`10.1016/j.egypro.2013.05.115`.

[70] U. E. Aronu, H. F. Svendsen, K. A. Hoff: Investigation of amine amino acid salts for carbon dioxide absorption, Int. J. Greenhouse Gas Control 4 (2010) 771–775. DOI:`10.1016/j.ijggc.2010.04.003`.

[71] U. E. Aronu, K. A. Hoff, H. F. Svendsen: Co2 capture solvent selection by combined absorption–desorption analysis, Chem. Eng. Res. Des. 89 (2011) 1197–1203. DOI:`10.1016/j.cherd.2011.01.007`.

[72] U. E. Aronu, A. F. Ciftja, I. Kim, A. Hartono: Understanding precipitation in amino acid salt systems at process conditions, Energy Procedia 37 (2013) 233–240. DOI:`10.1016/j.egypro.2013.05.107`.

[73] P. Brœder, H. F. Svendsen: Capacity and kinetics of solvents for post-combustion co2 capture, Energy Procedia 23 (2012) 45–54. DOI:`10.1016/j.egypro.2012.06.028`.

[74] X. Chen, G. T. Rochelle: Aqueous piperazine derivatives for co2 capture: Accurate screening by a wetted wall column, Chem. Eng. Res. Des. 89 (2011) 1693–1710. DOI:`10.1016/j.cherd.2011.04.002`.

[75] X. Chen, F. Closmann, G. T. Rochelle: Accurate screening of amines by the wetted wall column, Energy Procedia 4 (2011) 101–108. DOI:`10.1016/j.egypro.2011.01.029`.

[76] S. Y. Choi, S. C. Nam, Y. I. Yoon, K. T. Park, S.-J. Park: Carbon dioxide absorption into aqueous blends of methyldiethanolamine (mdea) and alkyl amines containing multiple amino groups, Ind. Eng. Chem. Res. 53 (2014) 14451–14461. DOI:`10.1021/ie502434m`.

[77] W. Conway, Q. Yang, S. James, C.-C. Wei, M. Bown, P. Feron, G. Puxty: Designer amines for post combustion co2 capture processes, Energy Procedia 63 (2014) 1827–1834. DOI:`10.1016/j.egypro.2014.11.190`.

[78] Y. Du, Y. Yuan, G. T. Rochelle: Capacity and absorption rate of tertiary and hindered amines blended with piperazine for co 2 capture, Chem. Eng. Sci. 155 (2016) 397–404. DOI:`10.1016/j.ces.2016.08.017`.

[79] L. Dubois, D. Thomas: Postcombustion co2 capture by chemical absorption: Screening of aqueous amine(s)-based solvents, Energy Procedia 37 (2013) 1648–1657. DOI:`10.1016/j.egypro.2013.06.040`.

[80] N. El Hadri, D. V. Quang, E. L. V. Goetheer, M. R. M. A. Zahra: Aqueous amine solution characterization for post-combustion co2 capture process, Appl. Energy 185 (2017) 1433–1449. DOI:10.1016/j.apenergy.2016.03.043.

[81] A. Hartono, S. J. Vevelstad, A. Ciftja, H. K. Knuutila: Screening of strong bicarbonate forming solvents for co 2 capture, Int. J. Greenhouse Gas Control 58 (2017) 201–211. DOI:10.1016/j.ijggc.2016.12.018.

[82] Y. E. Kim, S. J. Moon, Y. I. Yoon, S. K. Jeong, K. T. Park, S. T. Bae, S. C. Nam: Heat of absorption and absorption capacity of co2 in aqueous solutions of amine containing multiple amino groups, Sep. Purif. Technol. 122 (2014) 112–118. DOI:10.1016/j.seppur.2013.10.030.

[83] X. Luo, S. Liu, H. Gao, H. Liao, P. Tontiwachwuthikul, Z. Liang: An improved fast screening method for single and blended amine-based solvents for post-combustion co2 capture, Sep. Purif. Technol. 169 (2016) 279–288. DOI:10.1016/j.seppur.2016.06.018.

[84] Y. Mergler, R. R.-v. Gurp, P. Brasser, M. d. Koning, E. Goetheer: Solvents for co2 capture. structure-activity relationships combined with vapour-liquid-equilibrium measurements, Energy Procedia 4 (2011) 259–266. DOI:10.1016/j.egypro.2011.01.050.

[85] P. Muchan, J. Narku-Tetteh, C. Saiwan, R. Idem, T. Supap, P. Tontiwachwuthikul: Effect of number of hydroxyl group in sterically hindered alkanolamine on co 2 capture activity, Energy Procedia 114 (2017) 1966–1972. DOI:10.1016/j.egypro.2017.03.1328.

[86] P. Muchan, C. Saiwan, J. Narku-Tetteh, R. Idem, T. Supap, P. Tontiwachwuthikul: Screening tests of aqueous alkanolamine solutions based on primary, secondary, and tertiary structure for blended aqueous amine solution selection in post combustion co2 capture, Chem. Eng. Sci. 170 (2017) 574–582. DOI:10.1016/j.ces.2017.02.031.

[87] G. Puxty, R. Rowland, A. Allport, Q. Yang, M. Bown, R. Burns, M. Maeder, M. Attalla: Carbon dioxide postcombustion capture. a novel screening study of the carbon dioxide absorption performance of 76 amines, Environ. Sci. Technol. 43 (2009) 6427–6433. DOI:10.1021/es901376a.

[88] P. Singh, J. P. M. Niederer, G. F. Versteeg: Structure and activity relationships for amine based co2 absorbents i, Int. J. Greenhouse Gas Control 1 (2007) 5–10. DOI:10.1016/S1750-5836(07)00015-1.

[89] P. Singh, D. Brilman, M. Groeneveld: Solubility of co2 in aqueous solution of newly developed absorbents, Energy Procedia 1 (2009) 1257–1264. DOI:`10.1016/j.egypro.2009.01.165`.

[90] P. Singh, J. P. M. Niederer, G. F. Versteeg: Structure and activity relationships for amine-based co2 absorbents ii, Chem. Eng. Res. Des. 87 (2009) 135–144. DOI:`10.1016/j.cherd.2008.07.014`.

[91] P. Singh, D. W. F. Brilman, M. J. Groeneveld: Evaluation of co2 solubility in potential aqueous amine-based solvents at low co2 partial pressure, Int. J. Greenhouse Gas Control 5 (2011) 61–68. DOI:`10.1016/j.ijggc.2010.06.009`.

[92] Z. Wang, M. Fang, Y. Pan, S. Yan, Z. Luo: Comparison and selection of amine-based absorbents in membrane vacuum regeneration process for co2 capture with low energy cost, Energy Procedia 37 (2013) 1085–1092. DOI:`10.1016/j.egypro.2013.05.205`.

[93] Z. Wang, M. Fang, Y. Pan, S. Yan, Z. Luo: Amine-based absorbents selection for co2 membrane vacuum regeneration technology by combined absorption–desorption analysis, Chem. Eng. Sci. 93 (2013) 238–249. DOI:`10.1016/j.ces.2013.01.057`.

[94] R. Zhang, Q. Yang, Z. Liang, G. Puxty, R. J. Mulder, J. E. Cosgriff, H. Yu, X. Yang, Y. Xue: Toward efficient co2 capture solvent design by analyzing the effect of chain lengths and amino types to the absorption capacity, bicarbonate/carbamate, and cyclic capacity, Energy Fuels 31 (2017) 11099–11108. DOI:`10.1021/acs.energyfuels.7b01951`.

[95] A. T. Zoghi, F. Feyzi, S. Zarrinpashneh: Experimental investigation on the effect of addition of amine activators to aqueous solutions of n-methyldiethanolamine on the rate of carbon dioxide absorption, Int. J. Greenhouse Gas Control 7 (2012) 12–19. DOI:`10.1016/j.ijggc.2011.12.001`.

[96] H. K. Hall: Correlation of the base strengths of amines, J. Am. Chem. Soc. 79 (1957) 5441–5444. DOI:`10.1021/ja01577a030`.

[97] E. A. Braude, F. C. Nachod (Eds.): Determination of Organic Structures by Physical Methods, Academic Press, New York, 1955.

[98] A. V. Rayer, K. Z. Sumon, L. Jaffari, A. Henni: Dissociation constants (pka) of tertiary and cyclic amines. structural and temperature dependences, J. Chem. Eng. Data 59 (2014) 3805–3813. DOI:`10.1021/je500680q`.

[99] H. K. Hall: Sterically hindered phenolic buffers. application to determination of rates of amidation of ethyl chloroformate1, J. Am. Chem. Soc. 79 (1957) 5439–5441. DOI:`10.1021/ja01577a029`.

[100] P. W. Jencks, J. Regenstein: Handbook of Biochemistry and Molecular Biology: Ionization Constants of Acids and Bases, 4 ed., CRC Press, Boca Raton, 2010.

[101] M. Smith, J. March: March's advanced organic chemistry: Reactions, mechanisms, and structure, 6 ed., Wiley, Hoboken, 2007.

[102] A. S. N. Murthy, K. G. Rao, C. N. R. Rao: Molecular orbital study of the configuration protonation, and hydrogen bonding of secondary amides, J. Am. Chem. Soc. 92 (1970) 3544–3548. DOI:`10.1021/ja00715a003`.

[103] U. E. Aronu, S. Gondal, E. T. Hessen, T. Haug-Warberg, A. Hartono, K. A. Hoff, H. F. Svendsen: Solubility of co2 in 15, 30, 45 and 60 mass% mea from 40 to 120°c and model representation using the extended uniquac framework, Chem. Eng. Sci. 66 (2011) 6393–6406. DOI:`10.1016/j.ces.2011.08.042`.

[104] V. Ermatchkov, G. Maurer: Solubility of carbon dioxide in aqueous solutions of n-methyldiethanolamine and piperazine: Prediction and correlation, Fluid Phase Equilib. 302 (2011) 338–346. DOI:`10.1016/j.fluid.2010.06.001`.

[105] R. Notz, N. Asprion, I. Clausen, H. Hasse: Selection and pilot plant tests of new absorbents for post-combustion carbon dioxide capture, Chem. Eng. Res. Des. 85 (2007) 510–515. DOI:`10.1205/cherd06085`.

[106] O. Spuhl, H. Garcia, G. Sieder, R. Notz: Comparison and limitation of different evaluation methods for novel pcc solvents, Energy Procedia 4 (2011) 51–58. DOI:`10.1016/j.egypro.2011.01.022`.

[107] P. M. Mathias, J. P. O'Connell: The gibbs–helmholtz equation and the thermodynamic consistency of chemical absorption data, Ind. Eng. Chem. Res. 51 (2012) 5090–5097. DOI:`10.1021/ie202668k`.

[108] I. Kim, K. A. Hoff, T. Mejdell: Heat of absorption of co2 with aqueous solutions of mea: New experimental data, Energy Procedia 63 (2014) 1446–1455. DOI:`10.1016/j.egypro.2014.11.154`.

[109] H. Svensson, C. Hulteberg, H. T. Karlsson: Heat of absorption of co2 in aqueous solutions of n-methyldiethanolamine and piperazine, Int. J. Greenhouse Gas Control 17 (2013) 89–98. DOI:`10.1016/j.ijggc.2013.04.021`.

[110] D. D. Pinto, S. A. Zaidy, A. Hartono, H. F. Svendsen: Evaluation of a phase change solvent for co2 capture. absorption and desorption tests, Int. J. Greenhouse Gas Control 28 (2014) 318–327. DOI:`10.1016/j.ijggc.2014.07.002`.

[111] S. Ma'mun, I. Kim: Selection and characterization of phase-change solvent for carbon dioxide capture: precipitating system, Energy Procedia 37 (2013) 331–339. DOI:`10.1016/j.egypro.2013.05.119`.

[112] E. Sanchez-Fernandez, F. d. M. Mercader, K. Misiak, L. van der Ham, M. Linders, E. Goetheer: New process concepts for co2 capture based on precipitating amino acids, Energy Procedia 37 (2013) 1160–1171. DOI:`10.1016/j.egypro.2013.05.213`.

[113] S. Zheng, M. Tao, Q. Liu, L. Ning, Y. He, Y. Shi: Capturing co2 into the precipitate of a phase-changing solvent after absorption, Environ. Sci. Technol. 48 (2014) 8905–8910. DOI:`10.1021/es501554h`.

[114] J.-M. Mermet, M. Otto, M. Valcárcel Cases: Analytical Chemistry: A Modern Approach to Analytical Science, 2nd ed. ed., Wiley-VCH, Weinheim, 2004.

[115] V. Ermatchkov: Phasengleichgewichte in komplexen, chemisch reagierenden Systemen: NH3 + SO2 + H2O + Salze und CO2 + H2O + MDEA/Piperazin, Phd, TU Kaiserslautern, Germany, 2006.

[116] R. H. Weiland, J. C. Dingman, D. B. Cronin: Heat capacity of aqueous monoethanolamine, diethanolamine, n-methyldiethanolamine, and n-methyldiethanolamine-based blends with carbon dioxide, J. Chem. Eng. Data 42 (1997) 1004–1006. DOI:`10.1021/je960314v`.

[117] Y.-R. Chen, A. R. Caparanga, A. N. Soriano, M.-H. Li: Liquid heat capacity of the solvent system (piperazine + n-methyldiethanolamine + water), J. Chem. Thermodyn. 42 (2010) 54–59. DOI:`10.1016/j.jct.2009.07.005`.

[118] L.-F. Chiu, H.-F. Liu, M.-H. Li: Heat capacity of alkanolamines by differential scanning calorimetry, J. Chem. Eng. Data 44 (1999) 631–636. DOI:`10.1021/je980217x`.

[119] T. G. Amundsen, L. E. Øi, D. A. Eimer: Density and viscosity of monoethanolamine + water + carbon dioxide from (25 to 80) °c, J. Chem. Eng. Data 54 (2009) 3096–3100. DOI:`10.1021/je900188m`.

[120] I. Kim, H. F. Svendsen, E. Børresen: Ebulliometric determination of vapor–liquid equilibria for pure water, monoethanolamine, n-methyldiethanolamine, 3-

(methylamino)-propylamine, and their binary and ternary solutions, J. Chem. Eng. Data 53 (2008) 2521–2531. DOI:`10.1021/je800290k`.

[121] S. Bishnoi, G. T. Rochelle: Thermodynamics of piperazine/ methyldiethanolamine/ water/ carbon dioxide, Ind. Eng. Chem. Res. 41 (2002) 604–612. DOI:`10.1021/ie0103106`.

[122] R. H. Weiland, J. C. Dingman, D. B. Cronin, G. J. Browning: Density and viscosity of some partially carbonated aqueous alkanolamine solutions and their blends, J. Chem. Eng. Data 43 (1998) 378–382. DOI:`10.1021/je9702044`.

[123] S. A. Jayarathna, A. Weerasooriya, S. Dayarathna, D. A. Eimer, M. C. Melaaen: Densities and surface tensions of co2 loaded aqueous monoethanolamine solutions with r = (0.2 to 0.7) at t = (303.15 to 333.15) k, J. Chem. Eng. Data 58 (2013) 986–992. DOI:`10.1021/je301279x`.

[124] D. Fu, P. Zhang, L. Wang: Absorption performance of co2 in high concentrated [bmim][lys]-mdea aqueous solution, Energy 113 (2016) 1–8. DOI:`10.1016/j.energy.2016.07.049`.

[125] R. Behrens, M. Dyga, G. Sieder, Erik, H. Hasse: Nmr spectroscopic method for studying homogenous liquid phase reaction kinetics in systems used in reactive gas absorption and application to monoethanolamine–water–carbon dioxide, Chem. Eng. J. 374 (2019) 1127–1137. DOI:`10.1016/j.cej.2019.05.189`.

[126] N. McCann, M. Maeder, H. Hasse: Prediction of the overall enthalpy of co2 absorption in aqueous amine systems from experimentally determined reaction enthalpies, Energy Procedia 4 (2011) 1542–1549. DOI:`10.1016/j.egypro.2011.02.023`.

[127] N. McCann, M. Maeder, M. Attalla: Simulation of enthalpy and capacity of co2 absorption by aqueous amine systems, Ind. Eng. Chem. Res. 47 (2008) 2002–2009. DOI:`10.1021/ie070619a`.

[128] X. Yang, R. J. Rees, W. Conway, G. Puxty, Q. Yang, D. A. Winkler: Computational modeling and simulation of co2 capture by aqueous amines, Chem. Rev. 117 (2017) 9524–9593. DOI:`10.1021/acs.chemrev.6b00662`.

[129] C. Patterson, G. Slocum, R. Busey, R. Mesmer: Carbonate equilibria in hydrothermal systems: First ionization of carbonic acid in nacl media to 300°c, Geochimica et Cosmochimica Acta 46 (1982) 1653–1663. DOI:`10.1016/0016-7037(82)90320-9`.

[130] C. S. Patterson, R. H. Busey, R. E. Mesmer: Second ionization of carbonic acid in nacl media to 250°c, J Solution Chem 13 (1984) 647–661. DOI:`10.1007/bf00650372`.

[131] M. W. Arshad, N. von Solms, K. Thomsen: Thermodynamic modeling of liquid–liquid phase change solvents for co 2 capture, Int. J. Greenhouse Gas Control 53 (2016) 401–424. DOI:`10.1016/j.ijggc.2016.08.014`.

[132] Y. E. Kim, J. H. Park, S. H. Yun, S. C. Nam, S. K. Jeong, Y. I. Yoon: Carbon dioxide absorption using a phase transitional alkanolamine–alcohol mixture, J. Ind. Eng. Chem. 20 (2014) 1486–1492. DOI:`10.1016/j.jiec.2013.07.036`.

[133] H. Machida, T. Esaki, K. Oba, T. Tomikawa, T. Yamaguchi, H. Horizoe: Phase separation solvent for co2 capture, Energy Procedia 114 (2017) 823–826. DOI:`10.1016/j.egypro.2017.03.1224`.

[134] H. Machida, K. Oba, T. Tomikawa, T. Esaki, T. Yamaguchi, H. Horizoe: Development of phase separation solvent for co 2 capture by aqueous (amine + ether) solution, J. Chem. Thermodyn. 113 (2017) 64–70. DOI:`10.1016/j.jct.2017.05.043`.

[135] L. Raynal, P.-A. Bouillon, A. Gomez, P. Broutin: From mea to demixing solvents and future steps, a roadmap for lowering the cost of post-combustion carbon capture, Chem. Eng. J. 171 (2011) 742–752. DOI:`10.1016/j.cej.2011.01.008`.

[136] Z. Xu, S. Wang, C. Chen: Co2 absorption by biphasic solvents: Mixtures of 1,4-butanediamine and 2-(diethylamino)-ethanol, Int. J. Greenhouse Gas Control 16 (2013) 107–115. DOI:`10.1016/j.ijggc.2013.03.013`.

[137] J. K. You, W. Y. Lee, J. Y. Kim, J. Lee, Y. K. Hong: Screening of biphasic solvents for energy efficient co2 capture, Energy Procedia 114 (2017) 2096–2102. DOI:`10.1016/j.egypro.2017.03.1344`.

[138] W. Zhang, X. Jin, W. Tu, Q. Ma, M. Mao, C. Cui: Development of mea-based co 2 phase change absorbent, Applied Energy 195 (2017) 316–323. DOI:`10.1016/j.apenergy.2017.03.050`.

[139] X. Zhou, F. Liu, B. Lv, Z. Zhou, G. Jing: Evaluation of the novel biphasic solvents for co2 capture: Performance and mechanism, Int. J. Greenhouse Gas Control 60 (2017) 120–128. DOI:`10.1016/j.ijggc.2017.03.013`.

[140] K. S. Pitzer: Thermodynamics of electrolytes. i. theoretical basis and general equations, J. Phys. Chem. 77 (1973) 268–277. DOI:`10.1021/j100621a026`.

[141] P. Singh, G. F. Versteeg: Structure and activity relationships for co2 regeneration from aqueous amine-based absorbents, Process Saf. Environ. Prot. 86 (2008) 347–359. DOI:10.1016/j.psep.2008.03.005.

[142] C. Perinu, B. Arstad, K.-J. Jens: Nmr spectroscopy applied to amine–co2–h2o systems relevant for post-combustion co2 capture. a review, Int. J. Greenhouse Gas Control 20 (2014) 230–243. DOI:10.1016/j.ijggc.2013.10.029.

[143] C. Perinu, I. M. Bernhardsen, D. D. D. Pinto, H. K. Knuutila, K. J. Jens: Aqueous mapa, deea, and their blend as co2 absorbents. interrelationship between nmr speciation, ph, and heat of absorption data, Ind. Eng. Chem. Res. 58 (2019) 9781–9794. DOI:10.1021/acs.iecr.9b01437.

[144] D. Fernandes, W. Conway, X. Wang, R. Burns, G. Lawrance, M. Maeder, G. Puxty: Protonation constants and thermodynamic properties of amines for post combustion capture of co2, J. Chem. Thermodyn. 51 (2012) 97–102. DOI:10.1016/j.jct.2012.02.031.

[145] E. F. da Silva, H. F. Svendsen: Study of the carbamate stability of amines using ab initio methods and free-energy perturbations, Ind. Eng. Chem. Res. 45 (2006) 2497–2504. DOI:10.1021/ie050501z.

[146] G. Sartori, W. S. Ho, D. W. Savage, G. R. Chludzinski, S. Wlechert: Sterically-hindered amines for acid-gas absorption, Sep. Purif. Methods 16 (1987) 171–200. DOI:10.1080/03602548708058543.

[147] W. Conway, X. Wang, D. Fernandes, R. Burns, G. Lawrance, G. Puxty, M. Maeder: Toward the understanding of chemical absorption processes for post-combustion capture of carbon dioxide. electronic and steric considerations from the kinetics of reactions of co2(aq) with sterically hindered amines, Environ. Sci. Technol. 47 (2013) 1163–1169. DOI:10.1021/es3025885.

[148] N. McCann, D. Phan, D. Fernandes, M. Maeder: A systematic investigation of carbamate stability constants by 1h nmr, Int. J. Greenhouse Gas Control 5 (2011) 396–400. DOI:10.1016/j.ijggc.2010.01.008.

[149] C. Perinu, I. M. Bernhardsen, D. D. D. Pinto, H. K. Knuutila, K.-J. Jens: Nmr speciation of aqueous mapa, tertiary amines, and their blends in the presence of co2. influence of pka and reaction mechanisms, Ind. Eng. Chem. Res. 57 (2018) 1337–1349. DOI:10.1021/acs.iecr.7b03795.

[150] W. Böttinger, M. Maiwald, H. Hasse: Online nmr spectroscopic study of species distribution in mdea-h2o-co2 and mdea-pip-h2o-co2, Ind. Eng. Chem. Res. 47 (2008) 7917–7926. DOI:10.1021/ie800914m.

[151] W. Böttinger, M. Maiwald, H. Hasse: Online nmr spectroscopic study of species distribution in mea–h2o–co2 and dea–h2o–co2, Fluid Phase Equilib. 263 (2008) 131–143. DOI:`10.1016/j.fluid.2007.09.017`.

[152] R. Behrens, E. v. Harbou, W. R. Thiel, W. Böttinger, T. Ingram, G. Sieder, H. Hasse: Monoalkylcarbonate formation in methyldiethanolamine-h2o-co2, Ind. Eng. Chem. Res. 56 (2017) 9006–9015. DOI:`10.1021/acs.iecr.7b01937`.

[153] M. Vogt, C. Pasel, D. Bathen: Characterisation of co2 absorption in various solvents for pcc applications by raman spectroscopy, Energy Procedia 4 (2011) 1520–1525. DOI:`10.1016/j.egypro.2011.02.020`.

[154] P. G. L. Samarakoon, N. H. Andersen, C. Perinu, K.-J. Jens: Equilibria of mea, dea and amp with bicarbonate and carbamate. a raman study, Energy Procedia 37 (2013) 2002–2010. DOI:`10.1016/j.egypro.2013.06.080`.

[155] V. Souchon, M. d. O. Aleixo, O. Delpoux, C. Sagnard, P. Mougin, A. Wender, L. Raynal: In situ determination of species distribution in alkanolamine- h2o - co2 systems by raman spectroscopy, Energy Procedia 4 (2011) 554–561. DOI:`10.1016/j.egypro.2011.01.088`.

[156] P. Jackson, K. Robinson, G. Puxty, M. Attalla: In situ fourier transform-infrared (ft-ir) analysis of carbon dioxide absorption and desorption in amine solutions, Energy Procedia 1 (2009) 985–994. DOI:`10.1016/j.egypro.2009.01.131`.

[157] D. Fernandes, W. Conway, R. Burns, G. Lawrance, M. Maeder, G. Puxty: Investigations of primary and secondary amine carbamate stability by 1h nmr spectroscopy for post combustion capture of carbon dioxide, J. Chem. Thermodyn. 54 (2012) 183–191. DOI:`10.1016/j.jct.2012.03.030`.

[158] F. Khalili, A. Henni, A. L. L. East: pka values of some piperazines at (298, 303, 313, and 323 k), J. Chem. Eng. Data 54 (2009) 2914–2917. DOI:`10.1021/je900005c`.

[159] Á. Pérez-Salado Kamps, G. Maurer: Dissociation constant of n-methyldiethanolamine in aqueous solution at temperatures from 278 k to 368 k, J. Chem. Eng. Data 41 (1996) 1505–1513. DOI:`10.1021/je960141`.

[160] R. Behrens, E. Kessler, K. Münnemann, H. Hasse, E. v. Harbou: Monoalkylcarbonate formation in the system monoethanolamine–water–carbon dioxide, Fluid Phase Equilib. 486 (2019) 98–105. DOI:`10.1016/j.fluid.2018.12.031`.

[161] D. D. Perrin: Dissociation Constants of Organic Bases in Aqueous Solution, Butterworths, London, 1965.

[162] M. Nitta, M. Hirose, T. Abe, Y. Furukawa, H. Sato, Y. Yamanaka: 13c-nmr spectroscopic study on chemical species in piperazine–amine–co2–h2o system before and after heating, Energy Procedia 37 (2013) 869–876. DOI:`10.1016/j.egypro.2013.05.179`.

[163] M. M. Sharma: Kinetics of reactions of carbonyl sulphide and carbon dioxide with amines and catalysis by brönsted bases of the hydrolysis of cos, Trans. Faraday Soc. 61 (1965) 681–688. DOI:`10.1039/TF9656100681`.

[164] J. R. Lane, S. D. Schrøder, G. C. Saunders, H. G. Kjaergaard: Intramolecular hydrogen bonding in substituted aminoalcohols, J. Phys. Chem. A 120 (2016) 6371–6378. DOI:`10.1021/acs.jpca.6b05898`.

[165] D. L. Thomsen, J. L. Axson, S. D. Schrøder, J. R. Lane, V. Vaida, H. G. Kjaergaard: Intramolecular interactions in 2-aminoethanol and 3-aminopropanol, J. Phys. Chem. A 117 (2013) 10260–10273. DOI:`10.1021/jp405512y`.

[166] G. Sartori, D. W. Savage: Sterically hindered amines for carbon dioxide removal from gases, Ind. Eng. Chem. Fund. 22 (1983) 239–249. DOI:`10.1021/i100010a016`.

[167] Á. P.-S. Kamps, J. Xia, G. Maurer: Solubility of co2 in (h2o+piperazine) and in (h2o+mdea+piperazine), AIChE J. 49 (2003) 2662–2670. DOI:`10.1002/aic.690491019`.

[168] B. Burr, L. Lyddon: A comparison of physical solvents for acid gas removal, GPA Annu. Convention Proc. 1 (2008) 1–13.

[169] C. Perinu, B. Arstad, A. M. Bouzga, J. A. Svendsen, K. J. Jens: Nmr-based carbamate decomposition constants of linear primary alkanolamines for co2 capture, Ind. Eng. Chem. Res. 53 (2014) 14571–14578. DOI:`10.1021/ie5020603`.

[170] C. Perinu, B. Arstad, A. M. Bouzga, K.-J. Jens: 13c and 15n nmr characterization of amine reactivity and solvent effects in co2 capture, J. Phys. Chem. B 118 (2014) 10167–10174. DOI:`10.1021/jp503421x`.

[171] I. Kim, K. A. Hoff, E. T. Hessen, T. Haug-Warberg, H. F. Svendsen: Enthalpy of absorption of co2 with alkanolamine solutions predicted from reaction equilibrium constants, Chem. Eng. Sci. 64 (2009) 2027–2038. DOI:`10.1016/j.ces.2008.12.037`.

[172] I. v. Harbou: Post-combustion carbon capture by reactive absorption using aqueous amine solutions. Experiments, modeling, and simulation, Phd, TU Kaiserslautern, Germany, 2013.

[173] S. Yan, M. Fang, Z. Wang, Z. Luo: Regeneration performance of co2-rich solvents by using membrane vacuum regeneration technology. relationships between absorbent structure and regeneration efficiency, App. Energy 98 (2012) 357–367. DOI:`10.1016/j.apenergy.2012.03.055`.

A Supporting Information on measurements

A.1 Uncertainty of the gravimetric determination of the CO$_2$-loading

A comparison between CO$_2$-loadings that were determined gravimetrically and those determined from NMR spectroscopy revealed a systematic deviation. The CO$_2$-loadings from NMR measurements are higher than those obtained gravimetrically. It is assumed that these systematic deviations were caused by incomplete mixing of CO$_2$ and the solvent in the loading process. A scheme of the stainless steel cylinders that were used for loading the solvents with CO$_2$ is shown in Figure A1. The cylinder is equipped with two valves V1 and V2. V1 is connected to a riser pipe that ends 2 cm above the bottom of the cylinder. V2 is connected to an annular gap in the upper part of the cylinder. Aqueous amine solutions were filled into the evacuated stainless steel cylinders through V1. V2 was used afterwards to add CO$_2$. Before the solutions were used, they were mixed for four hours in a rotator and then placed upright for additional 24 hours to settle. The samples were taken through V1 by applying pressure to V2. The first 20 g were discarded.

The comparison with the NMR spectroscopic results indicate that the mixing was incomplete, despite the efforts. In the worst case, the aqueous solvent inside the riser pipe would be completely unloaded. The CO$_2$-loading of the solvent that is determined gravimetrically would then be lower than the loading determined by NMR spectroscopy.
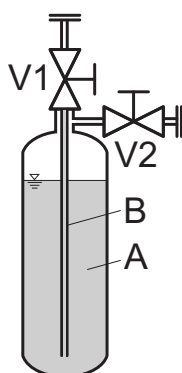
Figure A1: Scheme of the stainless steel cylinders used for the CO$_2$-loading procedure. A: aqueous amine solution, B: riser pipe, V1 and V2: valves.

The maximum possible deviation resulting from this incomplete mixing is stated as the expanded uncertainty with 0.99 level of confidence in this work.

A.2 Formation of alkylcarbonate in the system $(EtOH + H_2O + CO_2 / KHCO_3)$

Figure A3 shows $^{13}C\{^1H\}$ inverse gated NMR spectra of three aqueous solutions of ethanol (EtOH) at $t = 20$ °C with mass fractions of EtOH in the unloaded solvent of $\tilde{w}^0_{EtOH} = 0.3$ g/g, respectively. Figure A3 A (first row) shows the spectrum of an unloaded aqueous solution of EtOH, Figure A3 B (second row) shows the spectrum of an aqueous solution of EtOH which was saturated with CO_2 from a CO_2-cylinder at a partial pressure of CO_2 of about $p_{CO_2} = 2$ bar, and Figure A3 C (bottom row) shows the spectrum of an aqueous solution of EtOH which was saturated with $KHCO_3$. The NMR spectra were recorded the same way as described in Section 2.8.3. The signals are labeled with numbers that correspond to the carbon atoms as designated in Figure A2. Furthermore, the pH-value of the solutions was determined with indicator stripes. In Figure A3 A, two signals are observable (1, 2) which correspond to the two carbon atoms of EtOH. The pH-value of the solution was between $6 \leq pH \leq 7$. In Figure A3 B, the resulting signals correspond to EtOH (1, 2) and molecular CO_2 (3). The pH-value of the solution was between $4 \leq pH \leq 5$. In Figure A3 C, the observable NMR signals correspond to EtOH (1, 2), molecular CO_2 (3), (bi)carbonate (4), and ethylcarbonate (5, 6, 7). The corresponding ^1H-^{13}C heteronuclear multiple bond correlation NMR spectrum (HMBC) is given in Figure A4. The pH-value of the solution was between $8 \leq pH \leq 9$. Ethylcarbonate is the alkylcarbonate-species of EtOH. At alkaline conditions, the alkylcarbonate is observable (cf. Figure A3 C), whereas at acidic conditions (cf. Figure A3 B), it is not. In the present case, the alkylcarbonate is not stabilized by a zwitterionic ring structure (cf. Section 6.3.3).
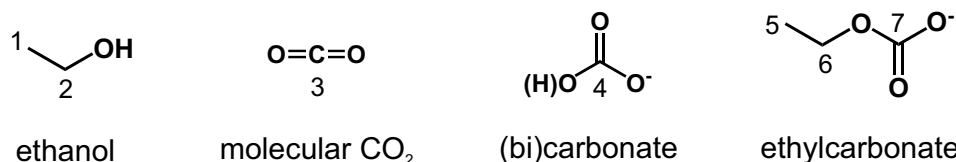
Figure A2: Chemical structures of the observed CO_2-containing species in the system $(EtOH + H_2O + CO_2)$ and $(EtOH + H_2O + KHCO_3)$ (cf. Figure A3).
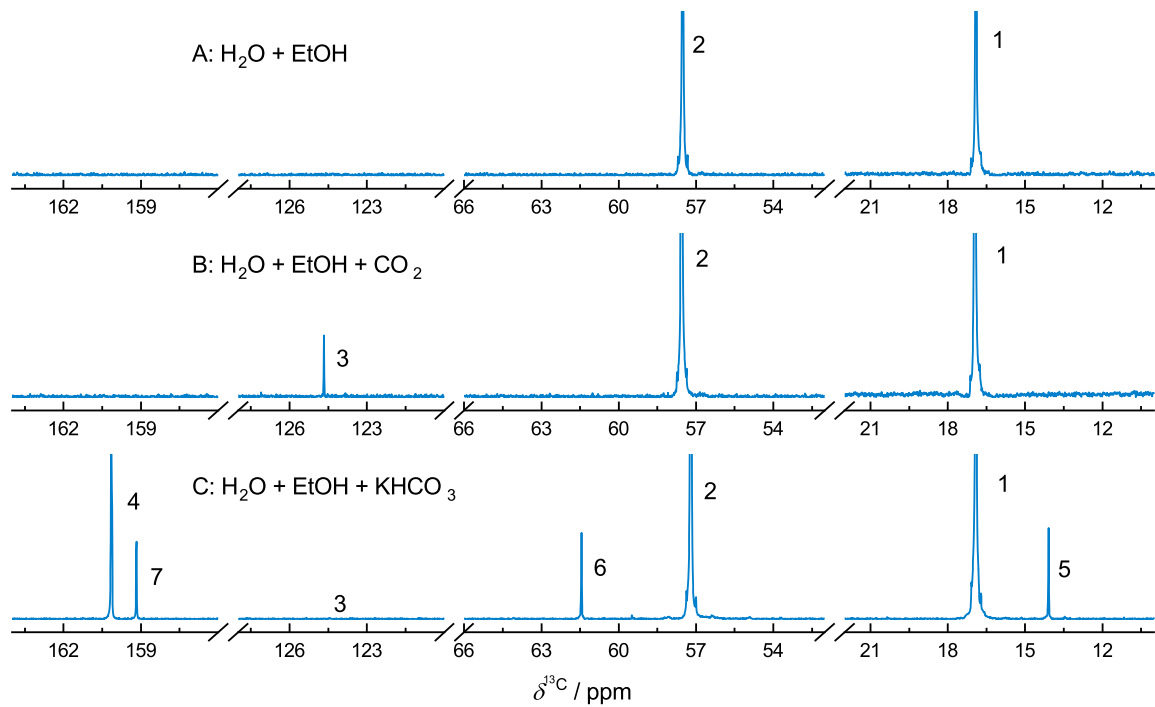
Figure A3: $^{13}C\{^1H\}$ inverse gated NMR spectra of aqueous solutions of EtOH with $\tilde{w}^0_{EtOH} = 0.3$ g/g at $t = 20$ °C. A: unloaded, B: loaded with CO_2 from a CO_2-cylinder (acid conditions), C: saturated with $KHCO_3$ (alkaline conditions). Peak numbers according to Figure A2.
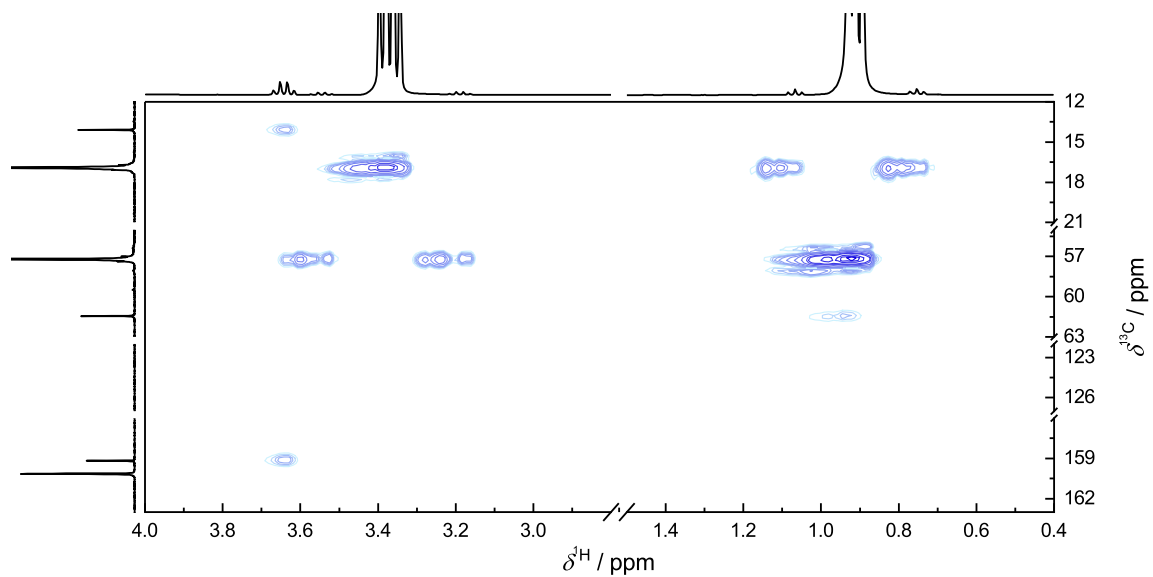
Figure A4: HMBC NMR spectrum of an aqueous solution of EtOH with $\tilde{w}^0_{EtOH} = 0.3$ g/g at $t = 20$ °C, saturated with $KHCO_3$.

A.3   Determination of the H$_2$O-content in LLE experiments with NMR spectroscopy in the system (EvA25 + H$_2$O + CO$_2$)

Standard ^{1}H NMR spectroscopy was used for the quantification of the mass fraction of H$_2$O in LLE experiments. The experimental setup for the NMR experiments was the same as described in Section 2.8.3. The main acquisition parameters for ^{1}H NMR spectroscopy were: pulse program: zg10, flip angle: 10°, relaxation delay: 10 s, acquired size of FID: 12k, sweep width: 22 ppm, excitation frequency offset: 8 ppm, acquisition time: 0.7 s, and 24 scans per spectra. T_1 measurements ($T_1 \leq 1$ sec) and variations of acquisition parameters proved the applicability of the parameters for the investigated system. The recorded spectra were post-processed manually. The processing steps were phase correction and polynomial baseline correction.

Figure A5 shows six ^{1}H NMR spectra of the system (EvA25 + H$_2$O) at different mass fractions of EvA25 in the unloaded solvent $\tilde{w}^0_{\text{EvA25}}$. The spectra stem from weighed samples that were used to proof the applicability of ^{1}H NMR spectroscopy for the determination of the mass fraction of H$_2$O in the systems (EvA25 + H$_2$O) and (EvA25
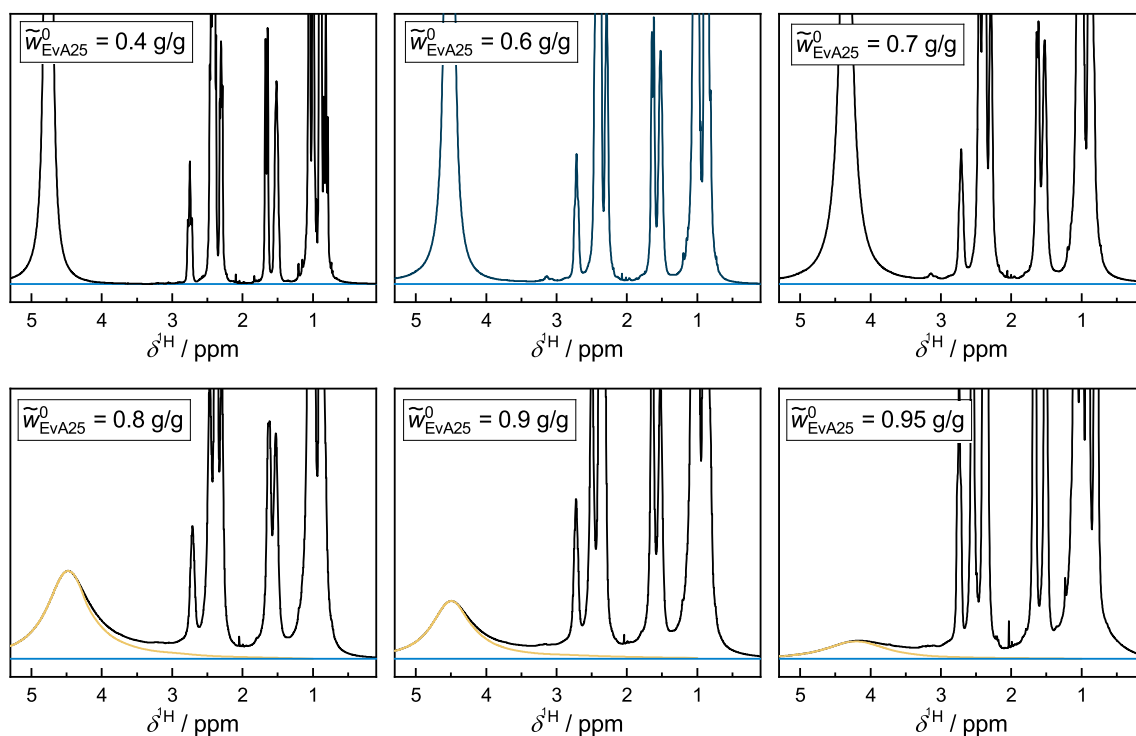
Figure A5: ^{1}H NMR spectra of the system (EvA25 + H$_2$O) with increasing mass fraction of EvA25 in the unloaded solvent at $t = 20\,$°C. Blue line: base line, black line: ^{1}H NMR spectrum, yellow line: deconvoluted water peak.

+ H_2O + CO_2). From the spectra, the mass fraction of H_2O $\tilde{w}_{H_2O}$ was determined by comparing the integral of the water peak (found at $\delta^{1H} \approx 4.6$ ppm) to that of all other peaks that belong to EvA25 (see also Appendix D.3). The mass fraction resulting from the evaluation of the spectra was compared to the weighed amount from sample preparation. Three observations were made in the analysis.

1) For mass fractions of EvA25 of $\tilde{w}_{EvA} \leq 0.65$ g/g, the peak areas can be determined by direct integration between 0 ppm $\leq \delta^{1H} \leq 3.5$ ppm (EvA25) and 3.5 ppm $\leq \delta^{1H} \leq 6$ ppm (H_2O). At these conditions, the protons of the amino groups of EvA25 are located in the water peak and, hence, have to be subtracted from the integral of the water peak for determining the mass fraction of H_2O in the sample. The standard uncertainty resulting from calibration for mass fractions of EvA25 $\tilde{w}_{EvA25} \leq 0.65$ g/g was $u(\tilde{w}_{H_2O}) = 0.010$ g/g, which was below that of Karl-Fischer titration.

2) At mass fractions of EvA25 of $\tilde{w}_{EvA25} \geq 0.65$ g/g, the water peak overlaps with those of EvA25, which makes direct integration an inappropriate and inaccurate method. To tackle this issue, the water peak was fitted with a Lorentzian-Gauss-peak-combination, which was provided by the software tool MestreNova, and which was used for processing the phase correction and integration of the water peak. The integral resulting from that fit was subtracted from the total integral of the spectrum to receive results for the integral of the water peak and the peaks that belong to EvA25. This method however was more elaborate and less accurate than Karl-Fischer titration. Hence, at mass fractions of EvA25 of $\tilde{w}_{EvA} \geq 0.65$ g/g, Karl-Fischer titration was the method of choice for determining the mass fraction of H_2O in the sample.

3) At mass fractions of EvA25 of $\tilde{w}_{EvA} \geq 0.8$ g/g (this is roughly when the ratio between amino groups and H_2O molecules becomes 1/1), the signals of the amino groups separate from the water peak and shift into the signals of EvA25. This separation is no hard cut, but proceeds with increasing mass fraction of EvA25 in the solvent. This also affects the calculation of the resulting mass fraction of H_2O and can only be quantified by two-dimensional calibration with varying amount of EvA25 and CO_2. At these compositions, NMR spectroscopy is not an appropriate method for determining the H_2O-content in the samples.

B Supporting information on modeling

B.1 SolSOFT equation and parameters for describing the CO$_2$-absorption isothermes in the screening

The SolSOFT equation, which was used in the screening (cf. Section 3) to describe gas solubility data, is given in Equation (11). For more information, see [29, 35].

$$\tilde{X}_{CO_2} = \frac{M_{CO_2}}{M_{amine}} \cdot \left[\left(\frac{p_{CO_2}}{K_p} \right)^m + n \cdot \frac{\left(\frac{p_{CO_2}}{K_c} \right)^n}{1 + \left(\frac{p_{CO_2}}{K_c} \right)^n} \right] \tag{11}$$

In Equation (11), $\tilde{X}_{CO_2}$ is the equilibrium CO$_2$-loading, p_{CO_2} is the partial pressure of CO$_2$, and M_{CO_2} and M_{amine} are the molar masses of CO$_2$ and the amine(mixture), respectively. K_p, K_c, m, and n are parameters. The parameters were determined from a fit to the CO$_2$-solubility data from the head space gas chromatography experiments (cf. Table E2). The resulting parameters are given in Table B1. The parameters for MEA and MDEA/PZ were determined from a fit to simulation data from [48, 104]. The mass fraction of amine in the unloaded solvent was always $\tilde{w}^0_{amine} = 0.4$ g/g.

Table B1: Parameters for the SolSOFT equation (Equation (11)) for describing the CO$_2$-solubility in the studied aqueous solutions of amines.

solvent	t / ℃	K_p	K_c	m	n
MEA	40	450	0.004	0.8	0.58
	100	1500	0.07	0.92	0.56
MDEA/PZ	40	71	0.082	0.35	0.62
	100	450	2.1	0.99	0.62
EvA03	40	0.1	0.052	0.082	0.97
	100	4	1.2	0.7	0.7
EvA06	40	9.3	0.032	0.17	0.63
	100	80	1.15	0.9	0.85
EvA09	40	184	0.031	2.74	1.02
	100	60	2.4	0.9	0.9

Table B1: continued from previous page

solvent	t / °C	K_p	K_c	m	n
EvA21	40	2.4	0.07	0.14	0.92
	100	10	0.45	0.7	0.7
EvA24	40	3	0.019	0.45	0.96
	100	7	0.8	0.8	0.62
EvA25	40	0.3	0.035	0.15	1.1
	100	2.9	8	0.7	0.6
EvA29/30	40	38	0.031	0.44	0.96
	100	6	0.6	0.7	0.5
EvA34	40	0.003	0.094	0.095	1.09
	100	1.5	0.4	0.6	0.8
EvA36	40	0.05	0.025	0.15	0.5
	100	5	0.12	0.47	0.75

t: temperature. K_p, K_c, m, n: Parameters for the SolSOFT equation (cf. Equation (11))

B.2 Interpolation of the VLE, LLE, and SLE data of the system (EvA25 + H$_2$O + CO$_2$)

The interpolation of the SLE, VLE, and LLE was performed by applying the same procedure for all systems. First, the available isothermal experimental data was plotted and extended by additional grid points in regions, where insufficient experimental data was available. The position of the grid points were calculated by interpolating between the experimental data. The grid points for the SLE (liquidus lines) and LLE (aqueous and organic binodals and tie-lines) were interpolated in the variables mass fraction of H$_2$O $\tilde{w}_{H_2O}$ and mass fraction of CO$_2$ $\tilde{w}_{CO_2}$. The grid points for the VLE (CO$_2$-solubility) were interpolated in the variables partial pressure of CO$_2$ p_{CO_2} and CO$_2$-loading $\tilde{\alpha}_{CO_2}$. The resulting isothermal curves were then smoothed to fit into the overall context of the SLLVE. The resulting interpolation of the SLE is presented in Figure B1, the resulting interpolation of the LLE is presented in Figure B2, and the resulting interpolation of the VLE is presented in Figure B4. In Figure B3, all interpolated binodals and some tie-lines are shown in one diagram. In few cases (the solidus line at 90 °C (cf. Figure B1), the low pressure region of the CO$_2$-absorption isotherms (cf. Figure B4), as well as the binodals and tie-lines of the LLE at 65 °C and 60 °C (cf. Figure B2)) the data was extrapolated. The extrapolated data should only be evaluated qualitatively. The data of the grid points are given in an EXCEL-file as Supplemental Material on the web site of its first publication [34].
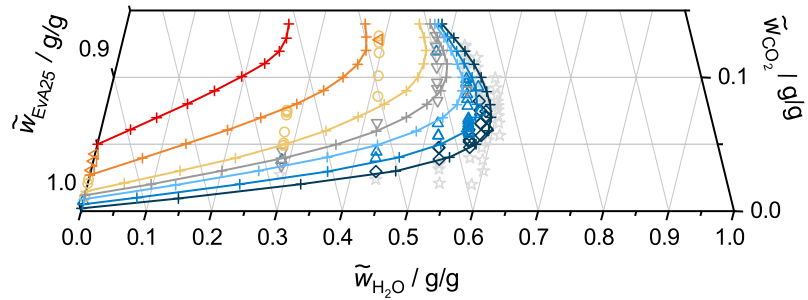
Figure B1: Interpolation of the solidus lines of the system (EvA25 + H_2O + CO_2). Solid lines: interpolated solidus lines, +: grid points of the interpolation, all other symbols: experimental results (cf. Section 5.2.1). Black: $t = 40$ °C, blue: $t = 50$ °C, light blue: $t = 60$ °C, gray: $t = 65$ °C, yellow: $t = 70$ °C, orange: $t = 80$ °C, red: $t = 90$ °C.
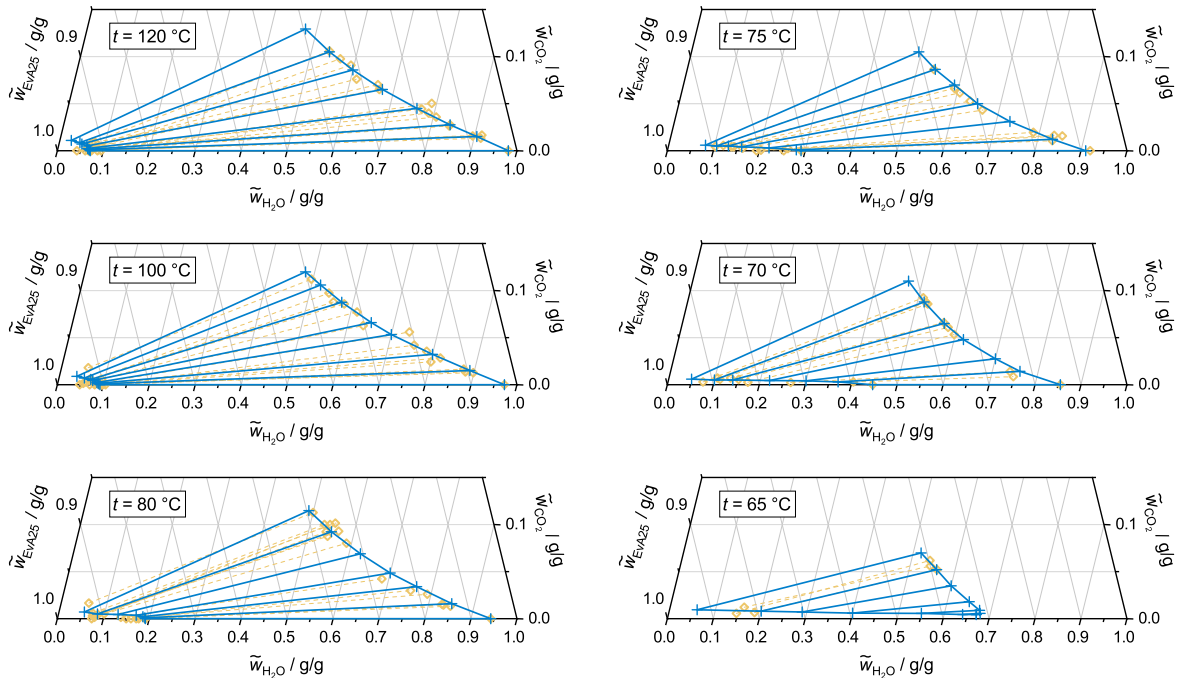
Figure B2: Interpolation of the liquid-liquid equilibrium of the system (EvA25 + H_2O + CO_2). Blue solid lines: interpolated binodals and tie-lines, +: grid points of the interpolation, ◇ with yellow dashed lines: experimental results (cf. Section 5.2.2).
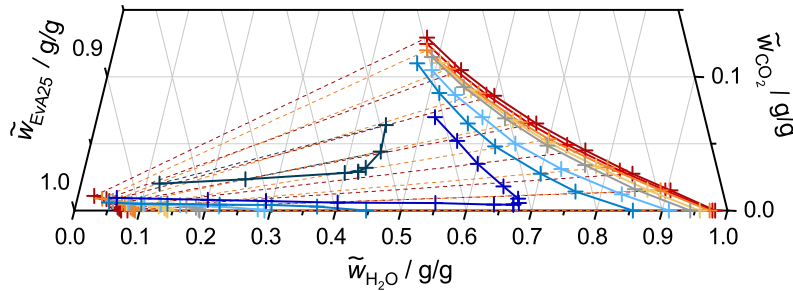
Figure B3: All interpolated binodals and some tie-lines of the liquid-liquid equilibrium of the system (EvA25 + H_2O + CO_2). Solid lines: interpolated binodals, dashed lines: interpolated tie-lines, +: grid points of the interpolation. Black: $t = 60$ ℃, dark blue: $t = 65$ ℃, blue: $t = 70$ ℃, light blue: $t = 75$ ℃, gray: $t = 80$ ℃, yellow: $t = 90$ ℃, orange: $t = 100$ ℃, red: $t = 110$ ℃, dark red: $t = 120$ ℃.
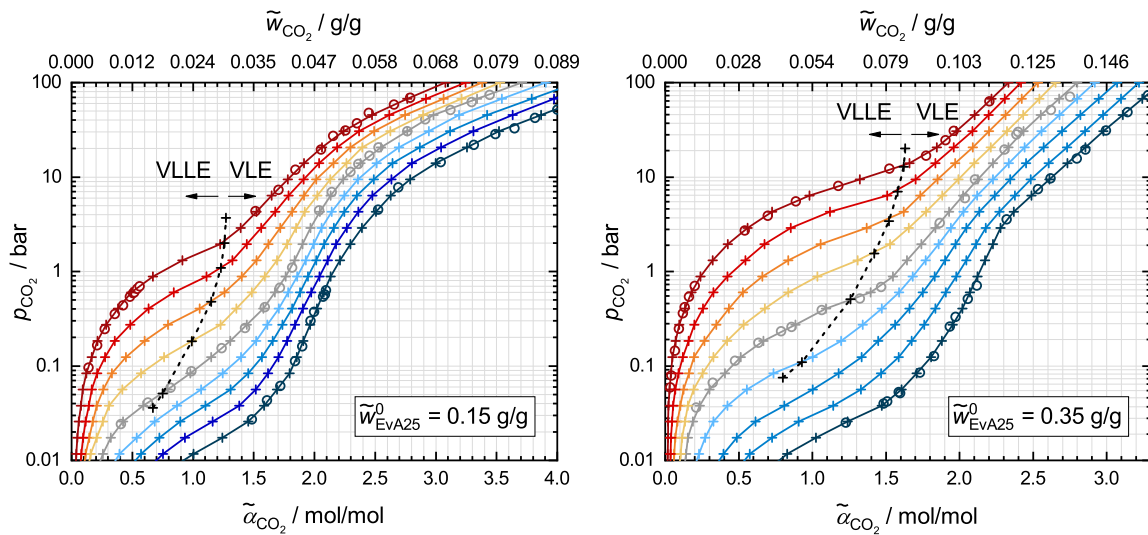
Figure B4: Interpolated CO_2-solubility isotherms of the system (EvA25 + H_2O + CO_2) for $\tilde{w}^0_{EvA25} = 0.15$ g/g and $\tilde{w}^0_{EvA25} = 0.35$ g/g. Solid lines: interpolated CO_2-solubility isotherms, dashed line: intersection between the interpolated CO_2-solubility isotherm and the interpolated aqueous binodals of the LLE, +: grid points of the interpolations, ○: experimental results (cf. Section 5.2.3). Black: $t = 40$ ℃, dark blue: $t = 50$ ℃, blue: $t = 60$ ℃, light blue: $t = 70$ ℃, gray: $t = 80$ ℃, yellow: $t = 90$ ℃, orange: $t = 100$ ℃, red: $t = 110$ ℃, dark red: $t = 120$ ℃.

B.3 Consistency test of the interpolation of the VLE and LLE data of the system ($EvA25 + H_2O + CO_2$)

Figure B5 shows the results of the consistency test between the interpolated VLE and LLE grid points. The LLE data in Figure B5 is plotted the same way as shown in Figure B2 and B3. For orientation, also the interpolated liquidus lines (cf. Figure B1) are shown in Figure B5. The VLE data was added to Figure B5 at four mass fractions of EvA25 in the unloaded solvent ($\tilde{w}^0_{EvA25} = 0.00$ g/g, $\tilde{w}^0_{EvA25} = 0.15$ g/g, $\tilde{w}^0_{EvA25} = 0.35$ g/g, and $\tilde{w}^0_{EvA25} = 0.40$ g/g) and five partial pressures of CO_2 ($p_{CO_2} = 5$ bar, $p_{CO_2} = 1.5$ bar, $p_{CO_2} = 0.5$ bar, $p_{CO_2} = 0.14$ bar, and $p_{CO_2} = 0.01$ bar) and are shown as symbols which are connected by lines as a guide for the eye. The VLE data do not consider a phase split and were extracted from the diagrams in Figure B4 as well as from literature data [32, 49].

The consistency between the VLE and LLE interpolations can only be tested in the LLE-region between the aqueous and organic binodal in Figure B5. In this LLE-region, different initial compositions must split into the same compositions in the aqueous and organic phase if they have the same temperature and same partial pressure of CO_2. To pass the consistency test, the lines that connect the initial compositions of the VLE data (yellow lines and symbols) must be congruent to the tie-lines of the LLE data (blue dashed lines). As can be seen in Figure B5, the consistency test is passed well for the developed interpolation of the VLE and LLE data. The compositions of the VLE data of the consistency test are given in an EXCEL-file as supplemental material on the web site of its first publication [34].
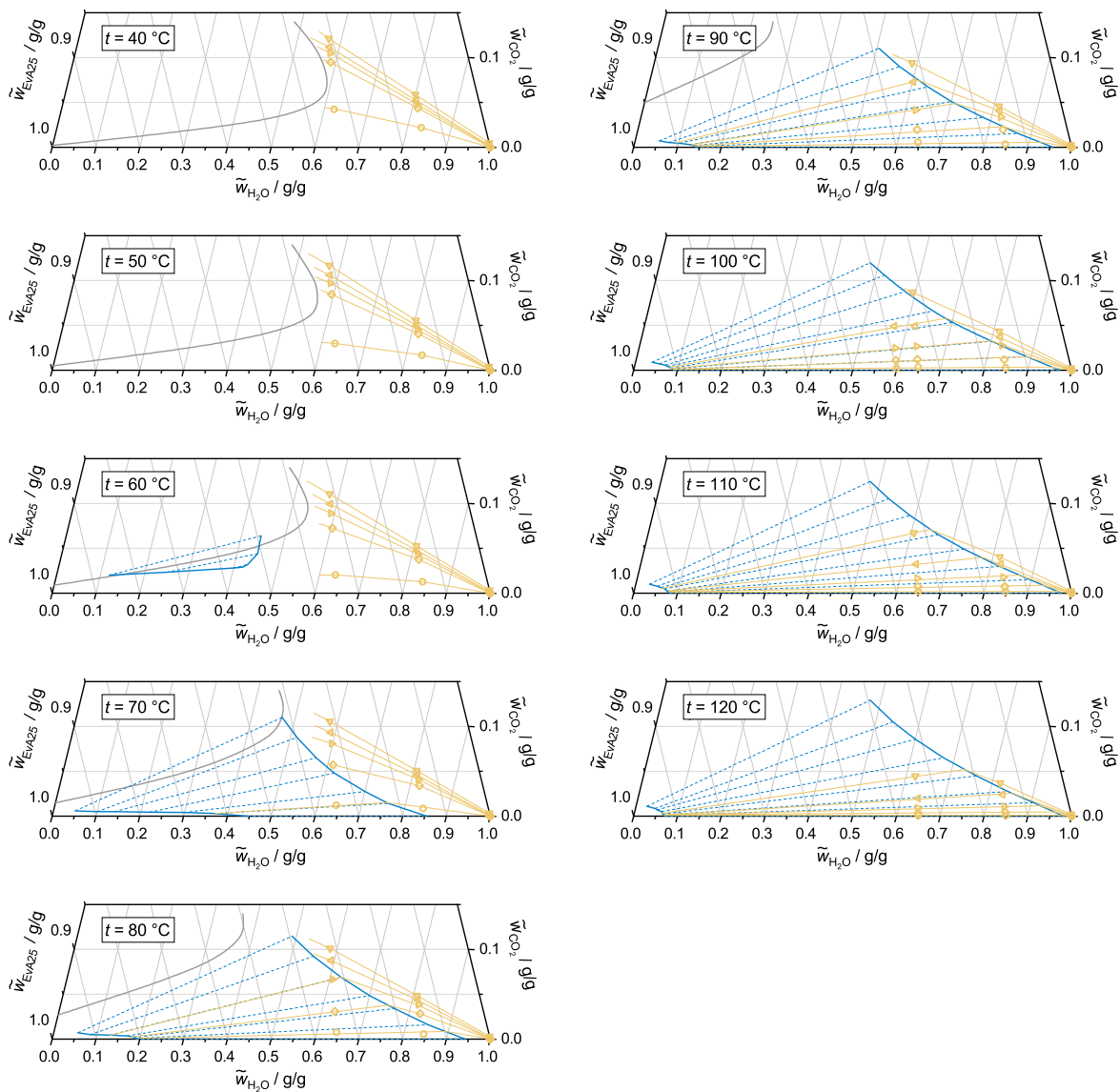
Figure B5: Consistency test between the interpolation of the LLE and VLE data of the system (EvA25 + H_2O + CO_2). Gray solid lines: liquidus line, blue solid lines: binodals, blue dashed lines: tie-lines, yellow solid lines: isobars of the partial pressure of CO_2 at $\triangledown$: $p_{CO_2} = 5$ bar, $\triangleleft$: $p_{CO_2} = 1.5$ bar, $\triangleright$: $p_{CO_2} = 0.5$ bar, $\diamondsuit$: $p_{CO_2} = 0.14$ bar, $\circ$: $p_{CO_2} = 0.01$ bar. Test is passed if within the LLE, the isobars are congruent to the tie-lines.

B.4 Correlating the demixing temperature of EvAs

Some of the aqueous solutions of EvAs show a liquid-liquid miscibility gap with a lower critical solution temperature (cf. Section 3). The liquid-liquid phase split lowers the solubility of CO_2 in the solvent and can be used beneficial in advanced CO_2 absorption process designs (cf. Section 5). The demixing temperature, where a liquid-liquid phase split occurs, is of high importance. The demixing temperature must be high enough to not affect the absorption of CO_2 but low enough to form two liquid phases below desorber conditions such that it can be used beneficially. According to the findings from Section 5, a good region for the demixing temperature is approximately between $60\,°C \leq t \leq 100\,°C$.

The demixing temperature correlates with the ratio of polar groups (hydroxy, ether, ketone, amino) to unpolar groups (hydrocarbons) in the amine. As some data for demixing temperatures of the EvAs at $\tilde{w}_{EvA}^0 = 0.4$ g/g are available from the screening (cf. Section 3), a dimensionless number that characterizes the ratio of polar and unpolar groups in the molecule is introduced. The dimensionless number is named PM-value (PM stands for polarity per mass) and was inspired by the BM-value (basicity per mass) that was introduced in Section 6.3.2. The PM-value is calculated from Equation (12) by dividing the sum of factors that characterize the polar groups in an amine F_i by the molar mass of the amine M_{amine}.

$$PM = \frac{\sum F_i}{M_{amine}} \cdot 100 \tag{12}$$

The factors F_i differ depending on the type of the polar group (e.g., hydroxy, ether, ketone, amino). The more polar groups the amine contains, the higher becomes the sum in the numerator of Equation (12) and, hence, the higher becomes also the resulting PM-value. High PM-values mean high polarity and high demixing temperatures. The factors F_i were approximated with a least square regression of a linear correlation between the PM-values and the demixing temperatures of the EvAs, which were measured in the screening (cf. Section 3). This linear correlation, as well as the measured demixing temperatures t_{demix} as a function of the calculated PM-values are shown in Figure B6. The F_i that were calculated from the regression were $F_i = 10$ for i = secondary amino groups, $F_i = 9$ for i = tertiary amino groups, and $F_i = 7$ for i = ether groups and furan rings. Unfortunately, no F_i could be obtained for other polar functional groups from the study, as the EvAs that contained other polar groups either had their demixing temperature above the investigated temperature range of $t \leq 130\,°C$ (hydroxy group, primary amino group), or were insufficient miscible with H_2O (carboxylate group, amide group).
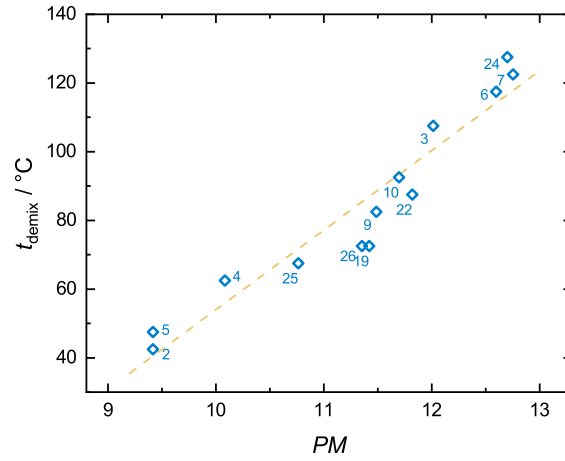
Figure B6: Demixing temperatures of EvAs with $\tilde{w}^0_{\text{EvA}} = 0.4$ g/g as a function of the polarity of the amine, expressed with the PM-value (see text). ◇: experimental results from Section 3. Numbers indicate the EvA-number. Yellow dashed line: correlation from Equation (13).

From the correlation that is shown in Figure B6, the demixing temperature t_{demix} can be estimated from Equation (13). To obtain a demixing temperature in the desired temperature range between 60 °C $\leq t \leq$ 100 °C, a PM-value between 10.5 $\leq PM \leq$ 12 should be targeted.

$$t_{\text{demix}} / \text{°C} = 23.2 \cdot PM - 178 \tag{13}$$

C Additional physico-chemical properties of the system ($EvA25 + H_2O + CO_2$)

C.1 pK-values

In Figure C1 (left), the molal activity based pH-value of the titration curve of EvA25 highly diluted in H_2O and its first derivative are shown as a function of the added volume of 1M NaOH titrant $V_{1M\ NaOH}$. The equivalent points EP1-4 are taken at the turning points of the first derivative. EP3 can not be determined directly from the first derivative. It is calculated by assuming equivalent volumes of titrant between every equivalent point. The pK-values are determined at the mean added volumes of titrant between two adjacent equivalent points.

Figure C1 (right) shows the results of the titration measurements. In the diagram, the molal activity based pK-values of EvA25 highly diluted in H_2O is shown as a function of the temperature t. The corresponding numerical experimental data are given in Appendix E. The designation of the amino groups refers to the amino group labeling of EvA25 as described in Figure 1. The assignment of the pK-values to the amino groups of EvA25 was taken from Section 3. The pK-values at $t = 20\,°C$, $t = 40\,°C$, and $t = 60\,°C$ were measured in the screening (cf. Section 3). These experiments were extended to $t = 80\,°C$ in the present section. The experiments at the already studied temperatures, were repeated. The results that were obtained here for $t = 20\,°C$, $t = 40\,°C$, and $t = 60\,°C$ agree well with the previous data from Section 3. With increasing temperature, the pK-values decrease linearly.

C.2 pH-values

Figure C2 shows the measured pH-value in the system ($EvA25 + H_2O$) as a function of the mass fraction of EvA25 in the unloaded solvent $\tilde{w}^0_{EvA25}$ at $t = 25\,°C$, $t = 40\,°C$, $t = 80\,°C$, and $t = 120\,°C$. The corresponding numerical experimental data are given in Appendix E. Only results for samples with a homogeneous liquid phase are reported.

The pH-values of the system ($EvA25 + H_2O$) are high compared to other solvents that are often used for CO_2-absorption [6, 48, 115], but slightly lower than those in the system
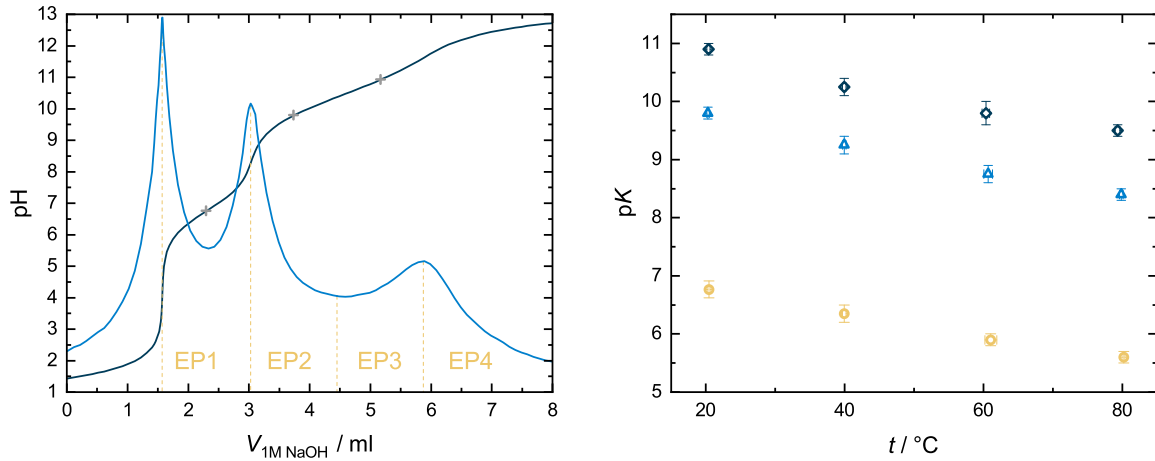
Figure C1: Left: Exemplary result of a titration experiment with EvA25 highly diluted in H_2O at $t = 20$ °C. Black solid line: pH-value, blue solid line: first derivative of the pH-value, yellow dashed line EP: equivalent point, $+$: pK-value. Right: pK-values of the three amino groups of EvA25 (cf. Figure 1). Experimental results from the present work. $\diamond$: α-amino group, $\triangle$: γ-amino group, $\circ$: β-amino group.

$(\text{EvA34} + \text{H}_2\text{O})$ (cf. Section 4). As expected, the pH-value increases with increasing mass fraction of EvA25 and decreases with increasing temperature.

Figure C3, shows the measured pH-value in the system $(\text{EvA25} + \text{H}_2\text{O} + \text{CO}_2)$ as a function of the mole-related CO_2-loading $\tilde{\alpha}_{\text{CO}_2}$, as well as of the mass fraction of CO_2 $\tilde{w}_{\text{CO}_2}$ at $t = 20$ °C, $t = 60$ °C, and $t = 100$ °C for a mass fractions of EvA25 in the unloaded solvent of $\tilde{w}^0_{\text{EvA25}} = 0.10$ g/g, $\tilde{w}^0_{\text{EvA25}} = 0.15$ g/g, and $\tilde{w}^0_{\text{EvA25}} = 0.35$ g/g. The corresponding numerical experimental data are given in Appendix E. Only results for samples with a homogeneous liquid phase are reported.

As can be seen in Figure C3, the pH-value of the solution decreases with increasing temperature. All isotherms can be divided into three sections, which differ in the slope of the decrease. The differences in the slopes decrease with decreasing mass fraction of EvA25 in the unloaded solvent and are best observable for $\tilde{w}^0_{\text{EvA25}} = 0.35$ g/g. The first section is at CO_2-loadings below about $\tilde{\alpha}_{\text{CO}_2} \leq 0.25$ mol/mol. The pH-value strongly decreases with increasing CO_2-loading even though only small amounts of CO_2 are added. Such strong decreases were observed for other aqueous solutions of amines as well [48]. The second section is between around 0.25 mol/mol $\leq \tilde{\alpha}_{\text{CO}_2} \leq 1.7$ mol/mol. In this section, the pH-value decreases almost linearly with increasing CO_2-loading. The range of the pH-value of this section matches the pK-values of the α- and γ-amino group (cf. Section 3.2.3). It is most likely, that the buffering effect of the α- and γ-amino group lead to the comparably small slope in this region. In the third section, at CO_2-loadings above around $\tilde{\alpha}_{\text{CO}_2} \geq 1.7$ mol/mol, the pH-value decreases more strongly and is most likely determined by the buffering effect of the β-amino group.
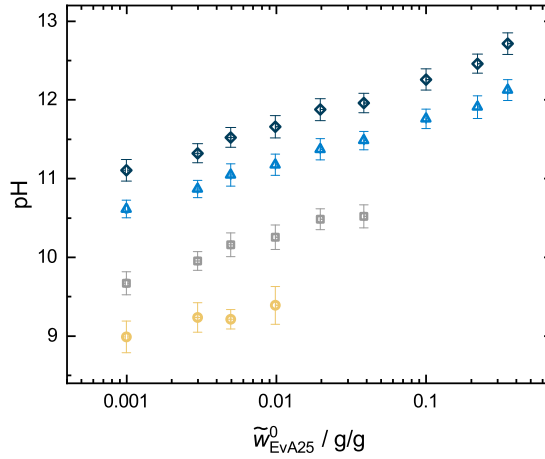
Figure C2: pH-value in the system (EvA25 + H$_2$O). Experimental results from the present work. $\diamond$: $t = 25$ ℃, $\triangle$: $t = 40$ ℃, $\square$: $t = 80$ ℃, $\circ$: $t = 120$ ℃.
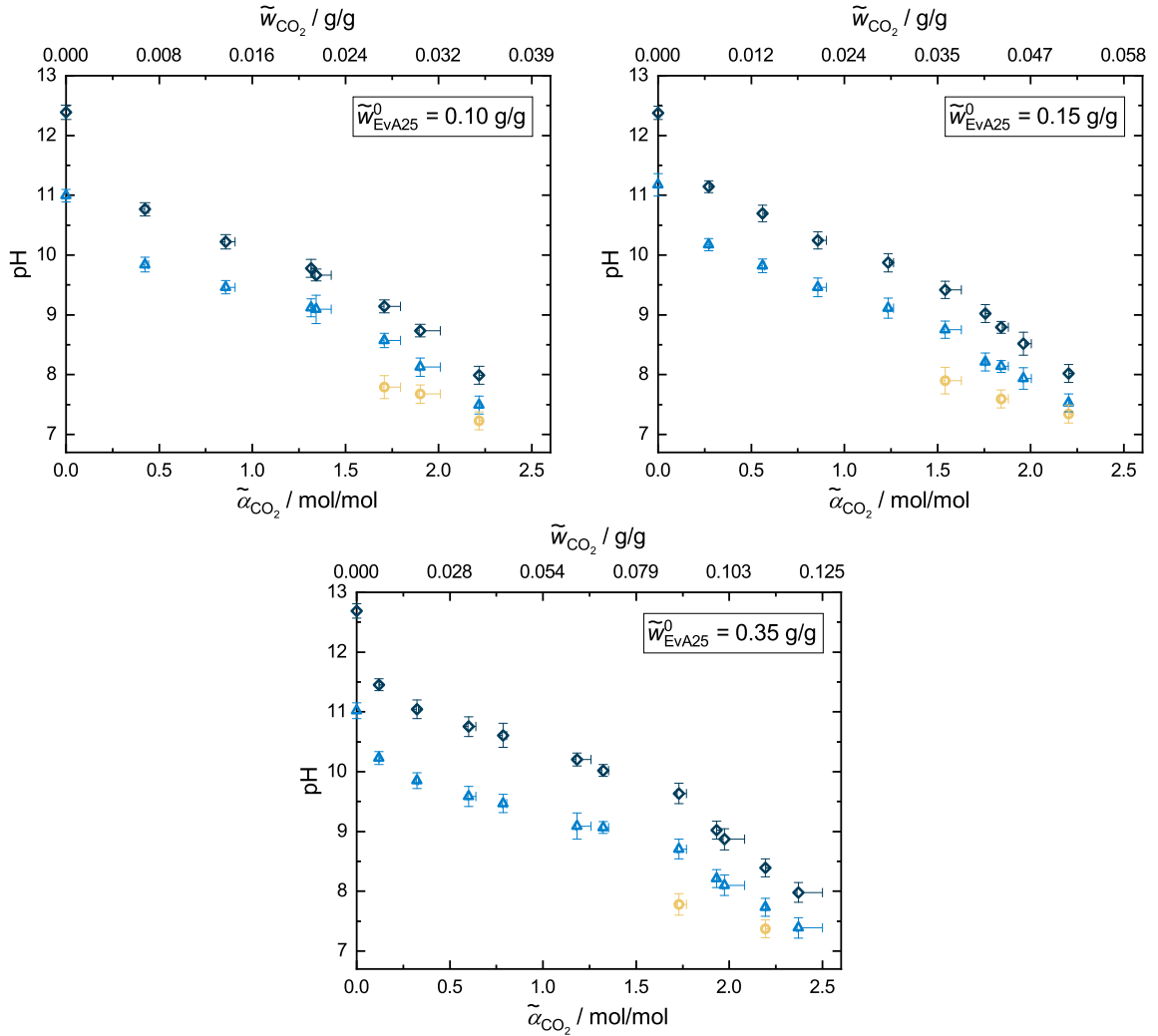
Figure C3: pH-value in the system (EvA25 + H$_2$O + CO$_2$) with $\tilde{w}_{EvA25}^0 = 0.10$ g/g, $\tilde{w}_{EvA25}^0 = 0.15$ g/g, and $\tilde{w}_{EvA25}^0 = 0.35$ g/g. Experimental results from the present work. $\diamond$: $t = 20$ ℃, $\triangle$: $t = 60$ ℃, $\circ$: $t = 100$ ℃.

C.3 NMR-spectroscopic quantification of CO$_2$-containing species

The CO$_2$-containing species in the system (EvA25 + H$_2$O + CO$_2$) for mass fractions of EvA25 in the unloaded solvent of $\tilde{w}^0_{\mathrm{EvA25}} = 0.1$ g/g is given in Section 6. In this Section, the presented NMR data is extended to mass fractions of EvA25 in the unloaded solvent of $\tilde{w}^0_{\mathrm{EvA25}} = 0.15$ g/g and $\tilde{w}^0_{\mathrm{EvA25}} = 0.35$ g/g. The same CO$_2$-containing species as in Section 6 were found: carbamate formed at the β-amino group (β-carbamate), (bi-)carbonate and molecular CO$_2$. For more details see Appendix D. The chemical structures of the species are shown in Figure C4. Depending on the pH-value of the CO$_2$-loaded aqueous solution of EvA25, differently protonated species of the carbamate and carbonate arise which cannot be distinguished by NMR spectroscopy. The concentrations of the CO$_2$-containing species given in the present work include all protonation-states of the corresponding species.
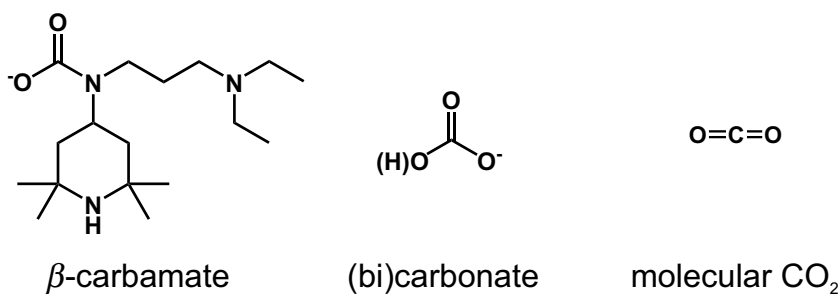
Figure C4: Chemical structures of the CO$_2$-containing species in CO$_2$-loaded aqueous solutions of EvA25. Results from the present work.

Figure C5 shows the concentration $\tilde{\alpha}_i$ of β-carbamate and (bi-)carbonate as a function of the mole-related CO$_2$-loading $\tilde{\alpha}_{\mathrm{CO}_2}$, as well as of the mass fraction of CO$_2$ $\tilde{w}_{\mathrm{CO}_2}$ in the system (EvA25 + H$_2$O + CO$_2$) with mass fractions of EvA25 in the unloaded solvent of $\tilde{w}^0_{\mathrm{EvA25}} = 0.15$ g/g and $\tilde{w}^0_{\mathrm{EvA25}} = 0.35$ g/g for five temperatures between 20 °C $\leq t \leq$ 100 °C. The corresponding numerical experimental data are given in Section E. Only results for samples with a homogeneous liquid phase are reported. Molecular CO$_2$ is not shown in Figure C5, as only very low concentrations ($\tilde{\alpha}_i <$ 0.01 mol/mol) were found at the investigated conditions.

Figure C5 shows that for both mass fractions of EvA25 in the unloaded solvent, the concentration of (bi-)carbonate is much higher than that of β-carbamate. This means that most CO$_2$ is bound as (bi-)carbonate. The concentration of β-carbamate as a function of the CO$_2$-loading shows a maximum. At $t = 20$ °C and $\tilde{w}^0_{\mathrm{EvA25}} = 0.35$ g/g, that maximum is about $\tilde{\alpha}_i = 0.4$ mol/mol and is found at a CO$_2$-loading of about $\tilde{\alpha}_{\mathrm{CO}_2} = 2$ mol/mol. As

reported in Section 6, it is assumed that the β-carbamate is stabilized by a zwitterionic ring structure. The maximum concentration of β-carbamate decreases with increasing temperature and decreasing mass fraction of EvA25 in the unloaded solvent, but the CO_2-loading, where the maximum is found, is roughly constant.
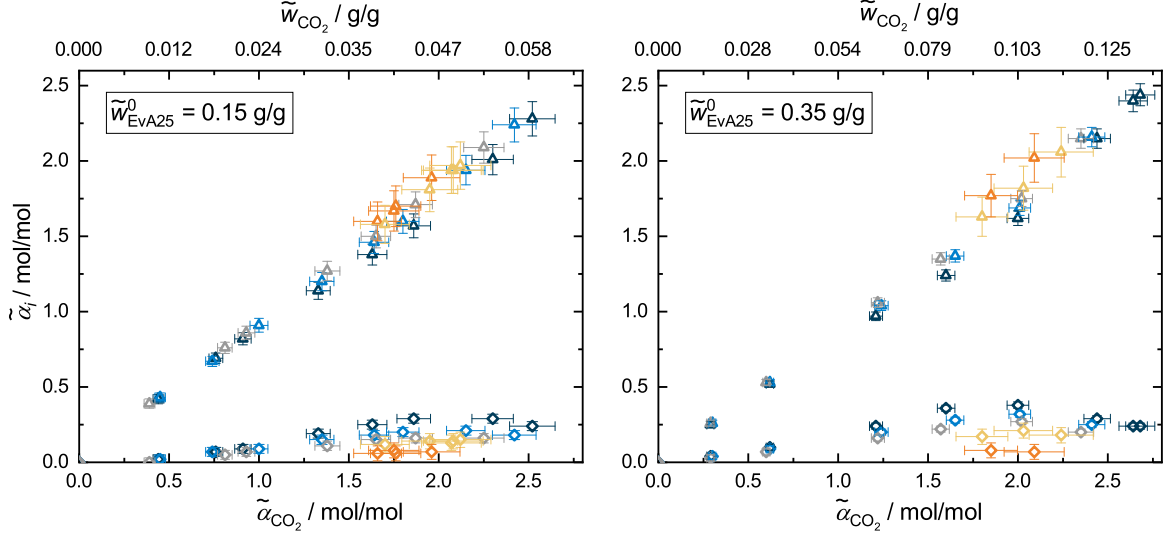
Figure C5: Concentration of CO_2-containing species in the system ($EvA25 + H_2O + CO_2$) with $\tilde{w}^0_{EvA25} = 0.15$ g/g and $\tilde{w}^0_{EvA25} = 0.35$ g/g. Experimental results from the present work. $\triangle$: (bi-)carbonate, $\diamond$: β-carbamate (cf. Figure C4). Molecular CO_2 is not shown, as only very low concentrations ($\tilde{\alpha}_i < 0.01$ mol/mol) were found. Black: $t = 20\,°C$, blue: $t = 40\,°C$, gray: $t = 60\,°C$, yellow: $t = 80\,°C$, orange: $t = 100\,°C$.

C.4 Density and dynamic viscosity

Figure C6 shows the measured density ρ and dynamic viscosity η of the system ($EvA25 + H_2O$) at eight temperatures between $20\,°C \leq t \leq 90\,°C$ as a function of the mass fraction of EvA25 in the unloaded solvent $\tilde{w}^0_{EvA25}$. The corresponding numerical experimental data are given in Appendix E. Only results for samples with a homogeneous liquid phase are reported.

The density of pure EvA25 is $\rho = 886$ g/cm³ at $t = 20\,°C$ and $\rho = 834$ g/cm³ at $t = 90\,°C$. For all temperatures, except for $t = 20\,°C$, the density of the mixture decreases with increasing mass fraction of EvA25. For H_2O-rich mixtures, the density depends only weakly on the mass fraction of EvA25. At $t = 20\,°C$, a very shallow maximum of the density was found. A similar behavior has been observed previously for EvA34 (cf. Section 4). It seems, that in H_2O-rich mixtures, the formation of an electrolyte system compensates the influence of the lower density of the EvA.
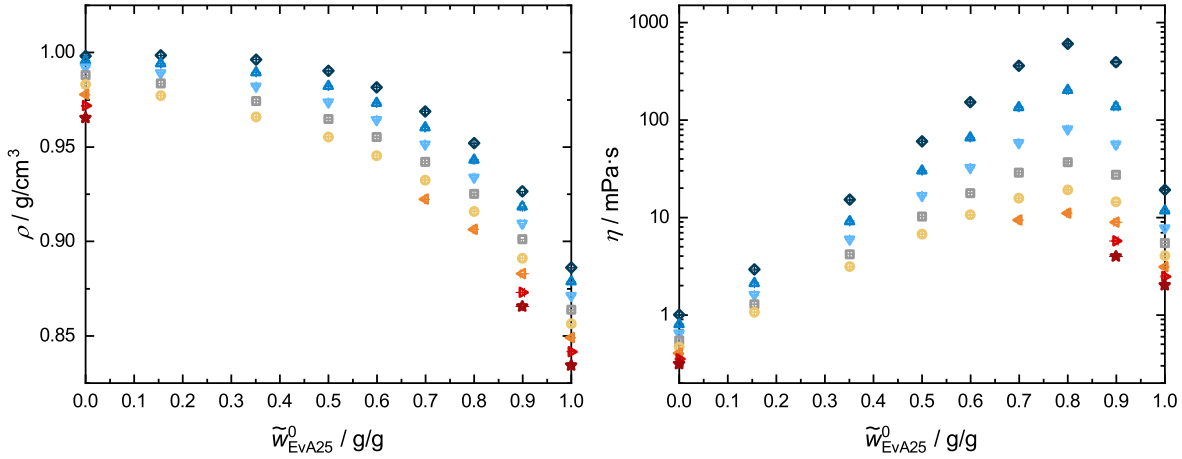
Figure C6: Density and dynamic viscosity of the system $(\text{EvA25} + \text{H}_2\text{O})$. Experimental results from the present work. $\diamondsuit$: $t = 20\,°\text{C}$, $\triangle$: $t = 30\,°\text{C}$, $\triangledown$: $t = 40\,°\text{C}$, $\square$: $t = 50\,°\text{C}$, $\circ$: $t = 60\,°\text{C}$, $\triangleleft$: $t = 70\,°\text{C}$, $\triangleright$: $t = 80\,°\text{C}$, $\star$: $t = 90\,°\text{C}$.

The dynamic viscosity of pure EvA25 decreases from $\eta = 19$ mPa·s at $t = 20\,°\text{C}$ to $\eta = 2$ mPa·s at $t = 90\,°\text{C}$. There is a maximum of the dynamic viscosity at a mass fraction of EvA25 in the unloaded solvent of about $\tilde{w}^0_{\text{EvA25}} = 0.8$ g/g, where the viscosity is about $\eta = 605$ mPa·s at $t = 20\,°\text{C}$ and $\eta = 11$ mPa·s at $t = 70\,°\text{C}$. Such a maximum was also found for EvA34 (cf. Section 4). For EvA34 it has been argued that this maximum results from H-bond stabilized clusters that are formed at a molar ratio of H_2O molecules and amino groups of about 1/1. For EvA25, this ratio is found at about $\tilde{w}^0_{\text{EvA25}} = 0.83$ g/g, which supports this theory. The dynamic viscosity is very sensitive to the mass fraction of H_2O. One of the impurities of EvA25 is H_2O (cf. Section 2). Even though the amount of H_2O as an impurity in pure EvA25 is low (less than 0.01 g/g), it might have an influence on the measured dynamic viscosity.

Figure C7 shows the measured density ρ and dynamic viscosity η of the system $(\text{EvA25} + \text{H}_2\text{O} + \text{CO}_2)$ with mass fractions of EvA25 in the unloaded solvent of $\tilde{w}^0_{\text{EvA25}} = 0.15$ g/g and $\tilde{w}^0_{\text{EvA25}} = 0.35$ g/g at five temperatures between $20\,°\text{C} \le t \le 60\,°\text{C}$ as a function of the mole-related CO_2-loading $\tilde{\alpha}_{\text{CO}_2}$, as well as of the mass fraction of CO_2 $\tilde{w}_{\text{CO}_2}$. The corresponding numerical experimental data are given in Appendix E. Only results for samples with a homogeneous liquid phase are reported.

At all temperatures, the density increases almost linearly with increasing CO_2-loading. For the aqueous solution of EvA25 with $\tilde{w}^0_{\text{EvA25}} = 0.35$ g/g, the relative increase of the density is about 5 % for an increase of the CO_2-loading $\tilde{\alpha}_{\text{CO}_2}$ of 1 mol/mol, whereas for $\tilde{w}^0_{\text{EvA25}} = 0.15$ g/g that number is only about 2.5 %. Regarding the amounts of EvA25 and CO_2 in the solution, the relative increase seems to correspond with the total amount of CO_2 in the solvent. Such behavior was observed for EvA34 as well (cf. Section 4). With increasing temperature, the density decreases.
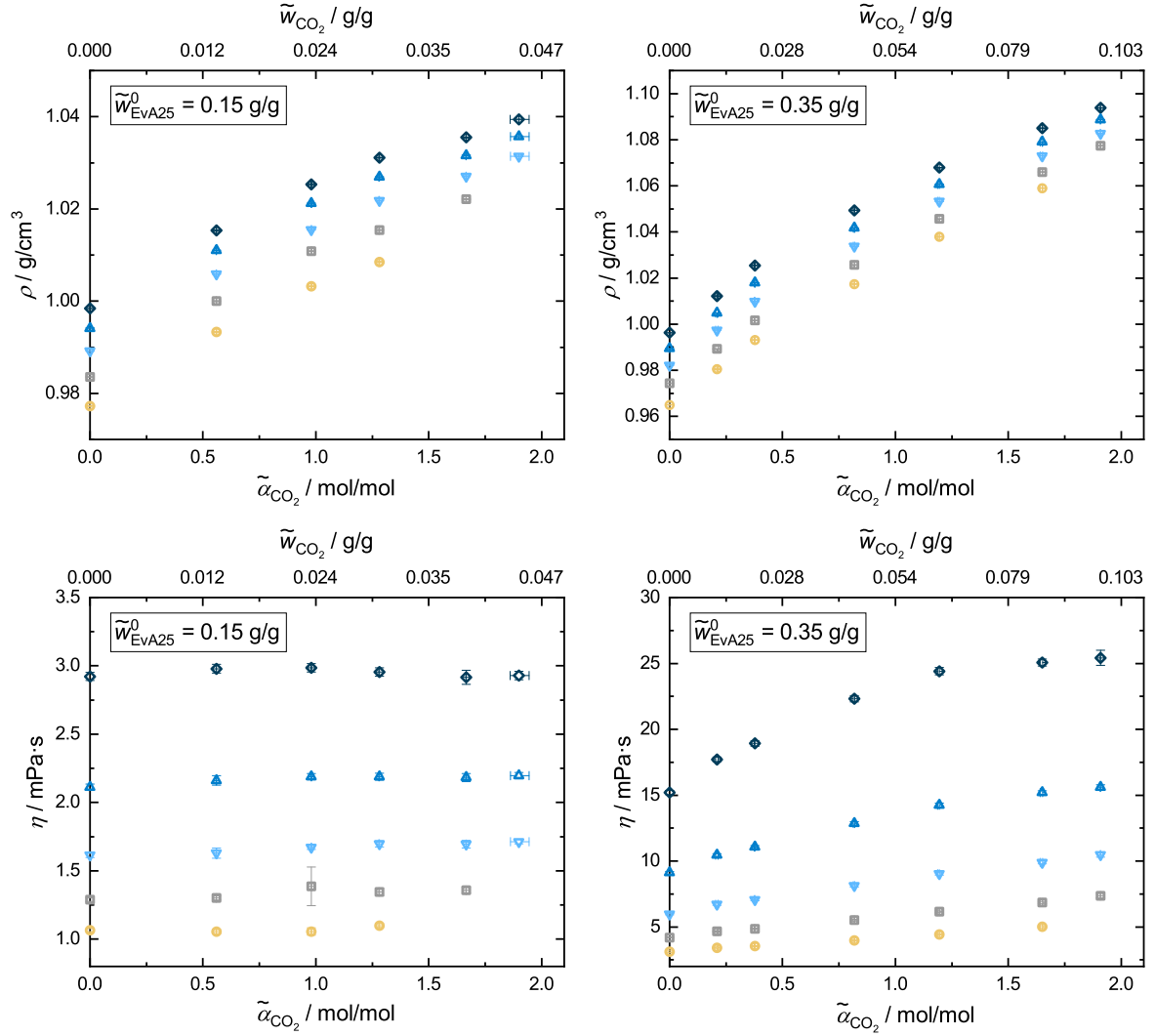
Figure C7: Density and dynamic viscosity in the system (EvA25 + H$_2$O + CO$_2$) with
$\tilde{w}^0_{\text{EvA25}} = 0.15$ g/g and $\tilde{w}^0_{\text{EvA25}} = 0.35$ g/g. Experimental results from the
present work. $\diamond$: $t = 20$ °C, $\triangle$: $t = 30$ °C, ∇: $t = 40$ °C, $\square$: $t = 50$ °C,
$\circ$: $t = 60$ °C.

The dynamic viscosity of aqueous solutions of EvA25 with $\tilde{w}^0_{\text{EvA25}} = 0.15$ g/g is not significantly influenced by the CO$_2$-loading. For $\tilde{w}^0_{\text{EvA25}} = 0.35$ g/g, however, the dynamic
viscosity increases with increasing CO$_2$-loading and the slope decreases with increasing
temperature. At $t = 20$ °C, a flattening of the curve is observed at high CO$_2$-loading.
For EvA34, the results for the viscosity were found to correlate with those of the carbamate concentration (cf. Section 4), which, however, is not the case for EvA25. The
viscosity decreases with increasing temperature.

C.5 Liquid heat capacity

Figure C8 shows the measured liquid heat capacity c_p of the system $(EvA25 + H_2O)$ for five temperatures between $25\,°C \leq t \leq 75\,°C$ as a function of the mass fraction of EvA25 in the unloaded solvent $\tilde{w}^0_{EvA25}$. The corresponding numerical experimental data are given in Appendix E. Only results for samples with a homogeneous liquid phase are reported. The liquid heat capacity of aqueous solutions of EvA25 decreases with increasing mass fraction of EvA25 and decreasing temperature. The liquid heat capacity of pure EvA25 is $c_p = 2.20$ kJ/(kg·K) at $t = 25\,°C$ and $c_p = 2.56$ kJ/(kg·K) at $t = 75\,°C$.
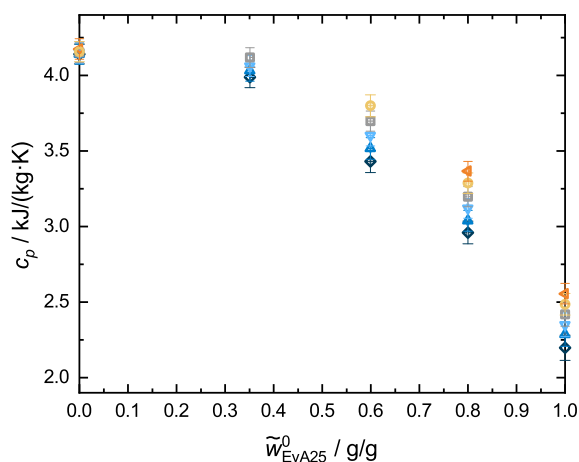
Figure C8: Liquid heat capacity in the system $(EvA25 + H_2O)$. Experimental results from the present work. $\diamond$: $t = 25\,°C$, $\triangle$: $t = 35\,°C$, $\triangledown$: $t = 45\,°C$, $\square$: $t = 55\,°C$, $\circ$: $t = 65\,°C$, $\triangleleft$: $t = 75\,°C$.

C.6 Vapor pressure

The vapor pressure p^s of pure EvA25 is about $p^s = 15$ mbar at $t = 164\,°C$ and $p^s = 50$ mbar at $t = 190\,°C$. The corresponding numerical experimental data is given in Appendix E. Due to the onset of carbonization at high temperatures, only low pressures could be studied. The vapor pressure of EvA25 is higher than that of EvA34 (cf. Section 4) but lower than that of EvA02 [29]. Compared to other amines that are used for CO_2-absorption [6], EvA25 has a very low vapor pressure.

D Species elucidation by NMR spectroscopy

The elucidation of CO_2-containing species in the systems (EvA + H_2O + CO_2) was done with ^{1}H and ^{13}C nuclear magnetic resonance (NMR) spectroscopy using one-dimensional ^{1}H and ^{13}C{^{1}H} inverse gated (^{13}Cig) as well as two-dimensional ^{1}H-^{13}C heteronuclear single quantum coherence (HSQC), ^{1}H-^{13}C heteronuclear multiple bond correlation (HMBC), and 135° distortionless enhanced polarization transfer ^{13}C (DEPT135) NMR techniques. Protonated and unprotonated species cannot be distinguished in NMR spectra. Therefore, in the present work, the given concentrations of all species include protonated and unprotonated forms.

The elucidation of CO_2-containing species was done for 16 EvAs in total: EvA01, EvA02, EvA03, EvA04, EvA05, EvA06, EvA07, EvA21, EvA24, EvA25, EvA26, EvA27, EvA31, EvA32, EvA34, and EvA36. The elucidation of four of these EvAs (EvA07, EvA21, EvA25, and EvA34) is shown in detail in the present section. Furthermore there is NMR data available for EvA02 [29]. The elucidations shown in the present section are blueprints for all EvAs, as the same procedures and techniques were applied. The elucidation of CO_2-containing species in CO_2-loaded aqueous solutions of EvA07 and EvA25 are excellent examples for demonstrating the procedure and unambiguity of the results. The elucidation of EvA21 and EvA34 are much more difficult and proves that also for such challenging systems, an unambiguous assignment of the CO_2-containing species is obtainable.

D.1 System (EvA07 + H_2O + CO_2)

Figure D2 shows the ^{1}H NMR spectrum of an unloaded aqueous solution of the system (EvA07 + H_2O) with a mass fraction of EvA07 in the unloaded solvent of $\tilde{w}^0_{\text{EvA07}} = 0.1\,\text{g/g}$. The corresponding ^{13}Cig NMR spectrum is given in Figure D3. In both spectra, the peaks are labeled with numbers that were assigned to the carbons/hydrogens as designated in Figure D1. The recorded DEPT135, HSQC, and HMBC NMR spectra that were used for the elucidation are shown in Figure D4 to D6, respectively.

The carbons 3,4 are clearly assignable as they show no signal in the DEPT135. In the HMBC NMR spectrum the carbons 3,4 correlate with the protons 6,8, 7,9 and 2,5. The ^{1}H NMR signals for 6,8 and 7,9 are singlets, respectively. The ^{1}H NMR signal of 2,5 consists of two double-doublets. One of the double-doublets overlaps such as it looks like

a triplet. The splitting pattern in combination with the peak integrals prove the shown assignment of 6,8, 7,9, and 2,5 in the ^{1}H NMR spectrum. The corresponding carbons 6,8, 7,9, and 2,5 are matched with the HSQC NMR spectrum. Peaks 1 and 12,13 are the remaining positively polarized peaks in the DEPT135. They are unambiguously assignable by comparing their peak integrals in the ^{13}Cig NMR spectrum. The corresponding protons are relatable with the HSQC NMR spectrum. The remaining peaks 10 and 11 are assignable by HMBC and HSQC NMR spectra.
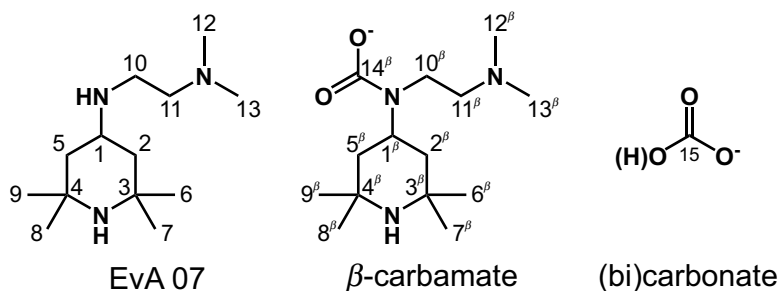
Figure D1: Chemical structures of the elucidated species in the system (EvA07 + H$_2$O + CO$_2$) with assignments of the carbon and hydrogen atoms.
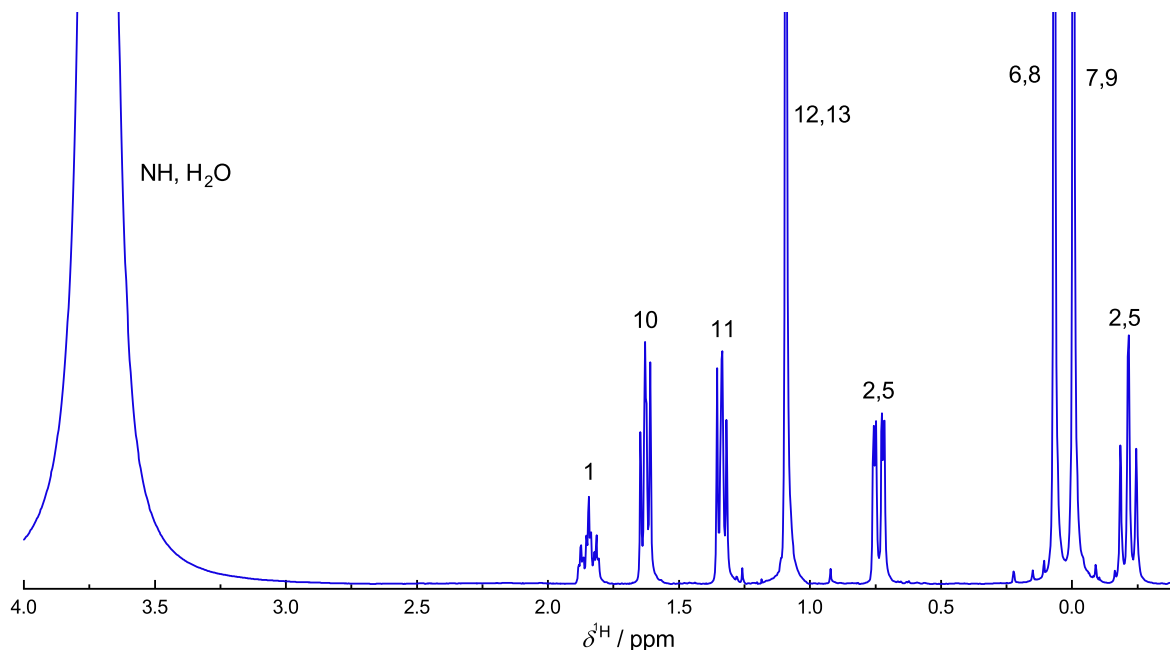
Figure D2: ^{1}H NMR spectrum of the system (EvA07 + H$_2$O) with $\tilde{w}^0_{\text{EvA07}} = 0.1$ g/g at $t = 20$ °C. Notation of the peaks according to Figure D1.
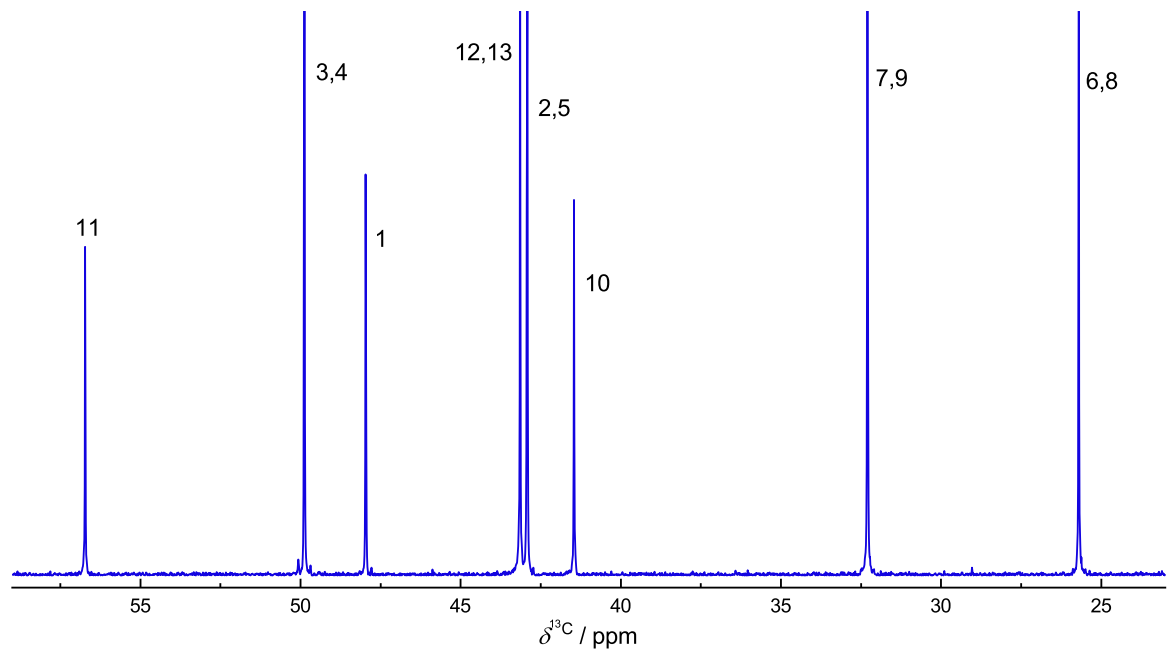
Figure D3: ^{13}Cig NMR spectrum of the system (EvA07 + H$_2$O) with $\tilde{w}^0_{\mathrm{EvA07}} = 0.1$ g/g at $t = 20$ ℃. Notation of the peaks according to Figure D1.
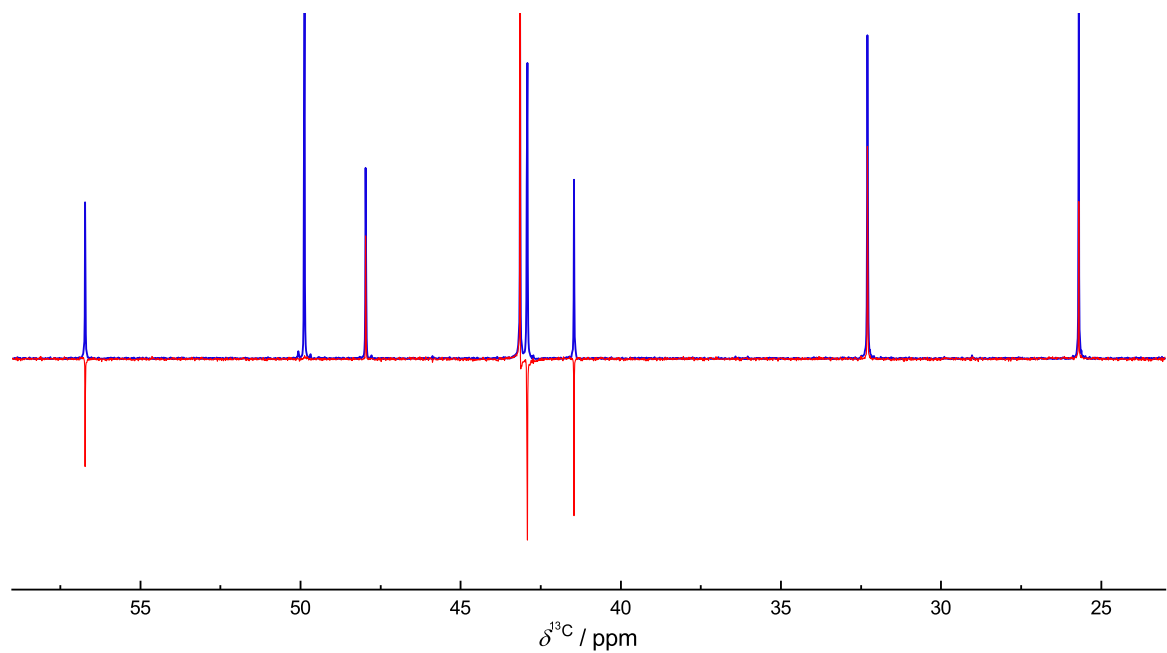
Figure D4: Superimposed DEPT135 ($-$) and ^{13}Cig ($-$) NMR spectrum of the system (EvA07 + H$_2$O) with $\tilde{w}^0_{\mathrm{EvA07}} = 0.1$ g/g at $t = 20$ ℃.
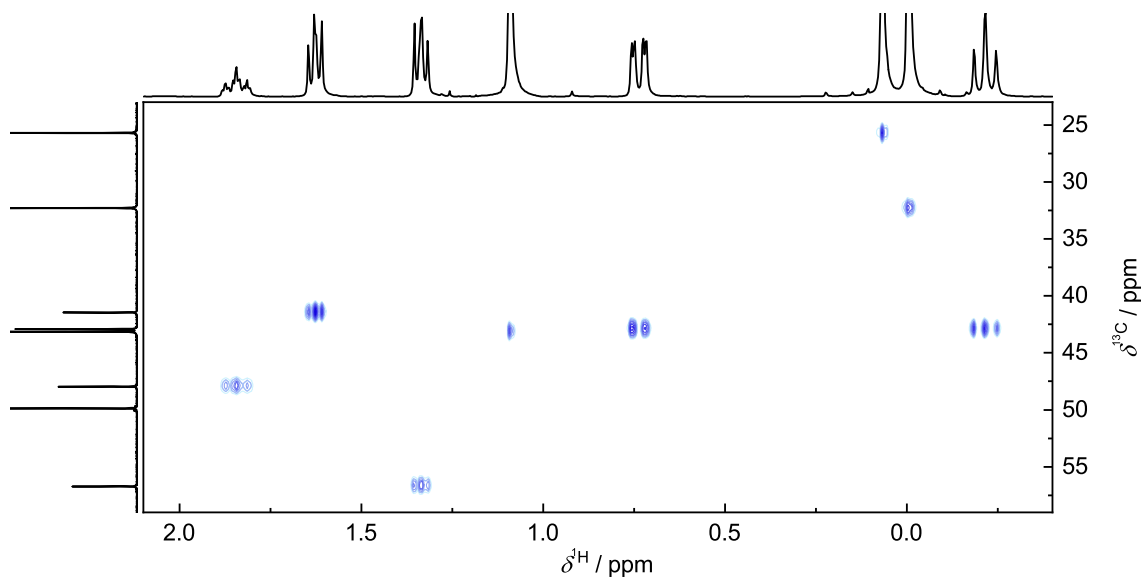
Figure D5: HSQC NMR spectrum of the system (EvA07 + H_2O) with $\tilde{w}_{EvA07}^0 = 0.1$ g/g at $t = 20$ ℃.
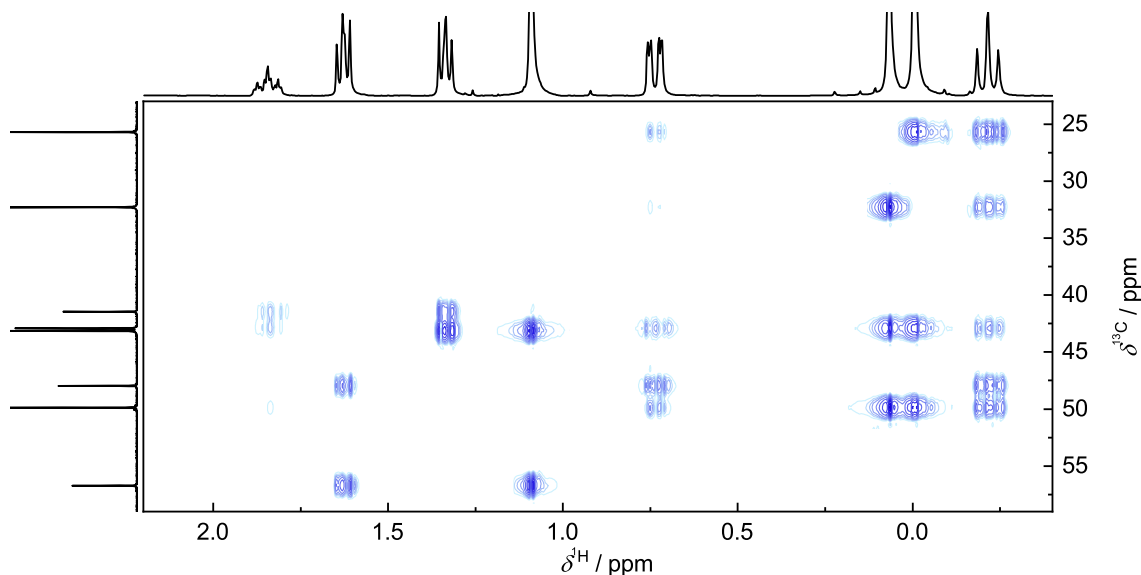
Figure D6: HMBC NMR spectrum of the system (EvA07 + H_2O) with $\tilde{w}_{EvA07}^0 = 0.1$ g/g at $t = 20$ ℃.

Figure D7 shows the ¹H NMR spectrum of the system (EvA07 + H_2O + CO_2) with a mass fraction of EvA07 in the unloaded solvent of $\tilde{w}_{EvA07}^0 = 0.1$ g/g and a CO_2-loading of $\tilde{\alpha}_{CO_2} = 1.51$ mol/mol. The corresponding ¹³Cig NMR spectrum is given in Figure D8. In both spectra, the peaks are labeled with numbers that were assigned to the carbons/hydrogens as designated in Figure D1. The recorded DEPT135, HSQC, and HMBC NMR spectra that were used for the elucidation are shown in Figures D9 to D11, respectively.

The carbons and protons 1 to 13 for EvA07 can be assigned as described for the system (EvA07 + H_2O) in the previous text. Due to the change of the pH-value as a result of the CO_2-loading, the peaks shift, compared to the unloaded aqueous solution. This is especially visible for the proton signals 10 and 11. They show separated signals in the ^1H NMR spectrum of the unloaded aqueous solution (cf. Figure D2), approximate with increasing CO_2-loading, and overlap at the CO_2-loading of $\tilde{\alpha}_{CO_2} = 1.51$ mol/mol which is shown in Figure D7. In Figure D7 the overlapping splitting pattern of 10 and 11 appears to be a singlet but actually consists of two overlapping triplets. Such strong shifts are also observable in the ^{13}Cig NMR spectrum and show the necessity of 2D NMR spectroscopy for the elucidation of the CO_2-containing species.

The assignment for the carbons and protons 1^β to 13^β was performed analogous to that of 1 to 13. In the ^{13}Cig NMR spectrum (cf. Figure D8), peak 15 represents the (bi)carbonate carbon. Its concentration rises to values of $\tilde{\alpha}_{CO_2} \geq 1$ mol/mol which excludes the possibility of being a carbamate. Also no correlation to any proton is observable in the HMBC NMR spectrum. Peak 14^β is assignable to the carbon of β-carbamate as it correlates to the adjacing protons 1^β and 10^β in the HMBC NMR spectrum.
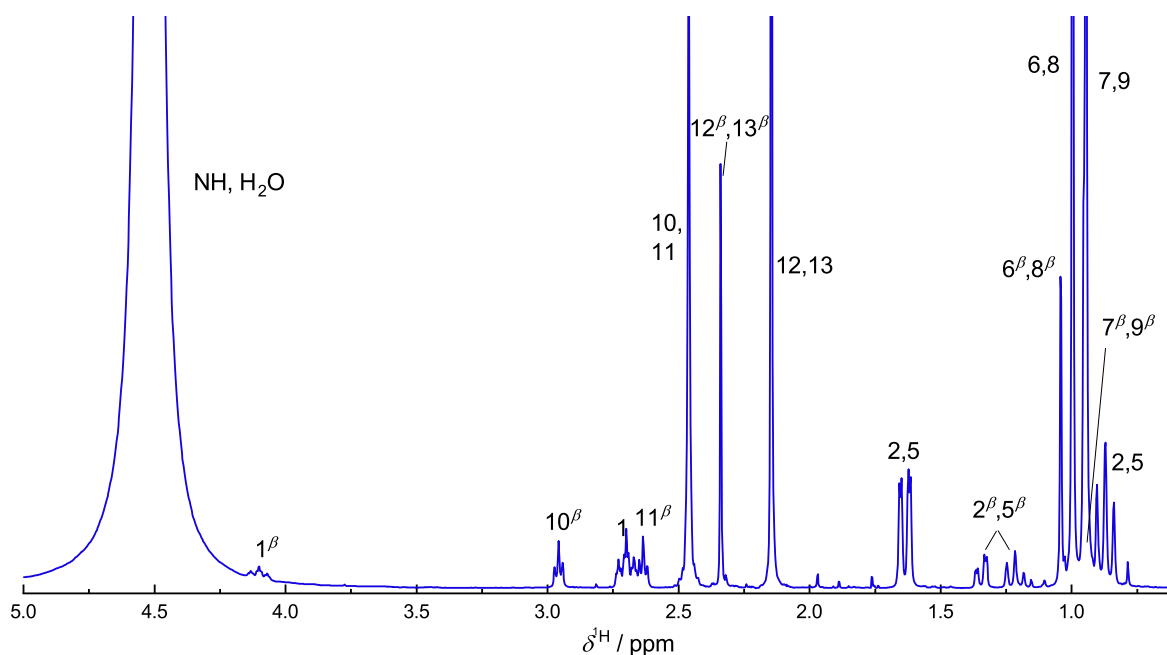
Figure D7: ^1H NMR spectrum of the system (EvA07 + H_2O + CO_2) with $\tilde{w}^0_{EvA07} = 0.1$ g/g and $\tilde{\alpha}_{CO_2} = 1.51$ mol/mol at $t = 20$ °C. Notation of the peaks according to Figure D1.
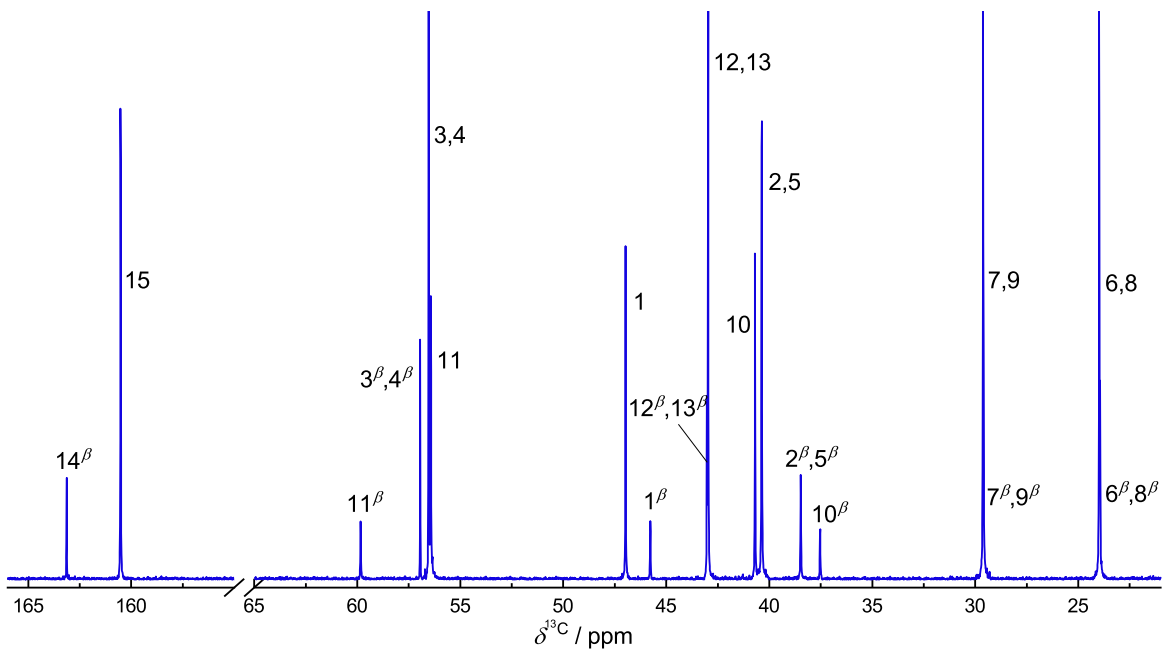
Figure D8: ^{13}Cig NMR spectrum of the system (EvA07 + H$_2$O + CO$_2$) with $\tilde{w}^0_{\text{EvA07}} = 0.1$ g/g and $\tilde{\alpha}_{\text{CO}_2} = 1.51$ mol/mol at $t = 20$ ℃. Notation of the peaks according to Figure D1.
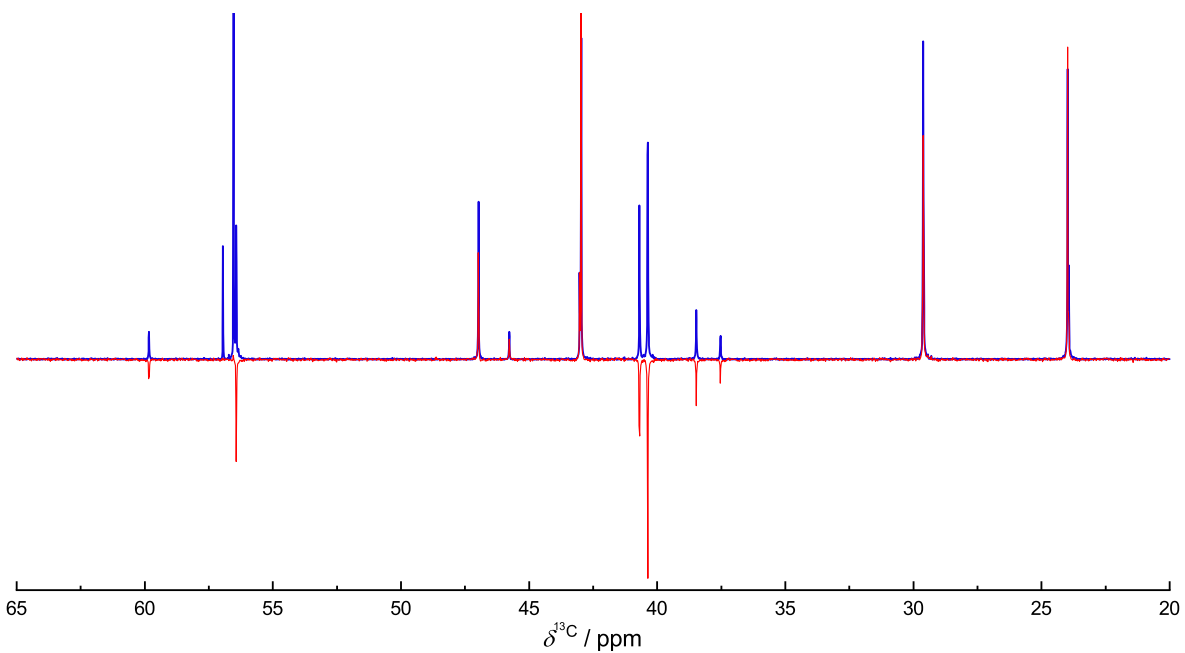
Figure D9: Superimposed DEPT135 (—) and ^{13}Cig (—) NMR spectrum of the system (EvA07 + H$_2$O + CO$_2$) with $\tilde{w}^0_{\text{EvA07}} = 0.1$ g/g and $\tilde{\alpha}_{\text{CO}_2} = 1.51$ mol/mol at $t = 20$ ℃.
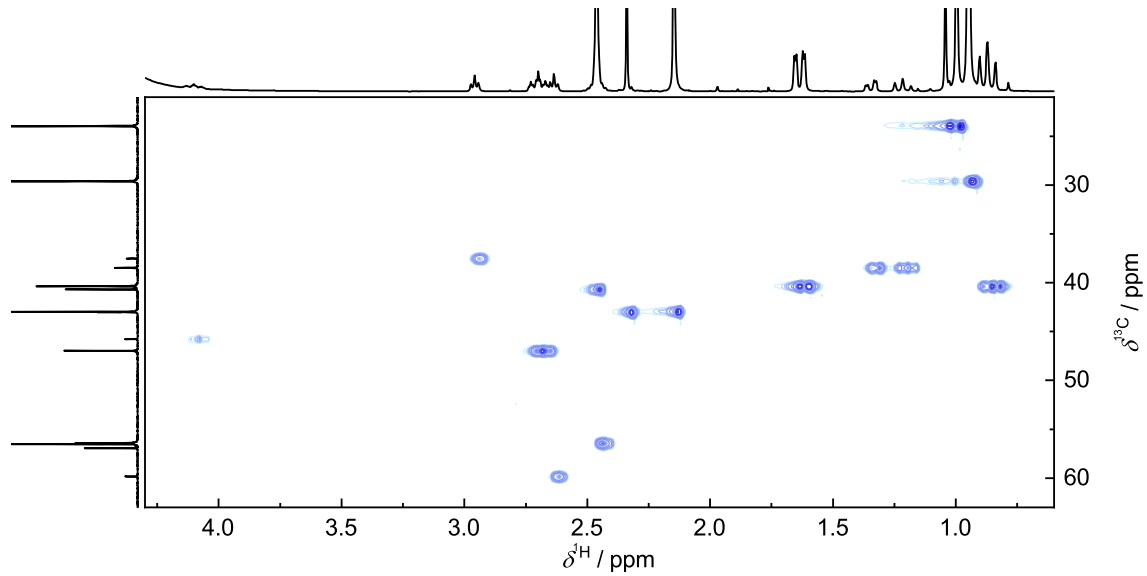
Figure D10: HSQC NMR spectrum of the system (EvA07 + H$_2$O + CO$_2$) with $\tilde{w}^0_{\text{EvA07}} = 0.1$ g/g and $\tilde{\alpha}_{\text{CO}_2} = 1.51$ mol/mol at $t = 20$ ℃.
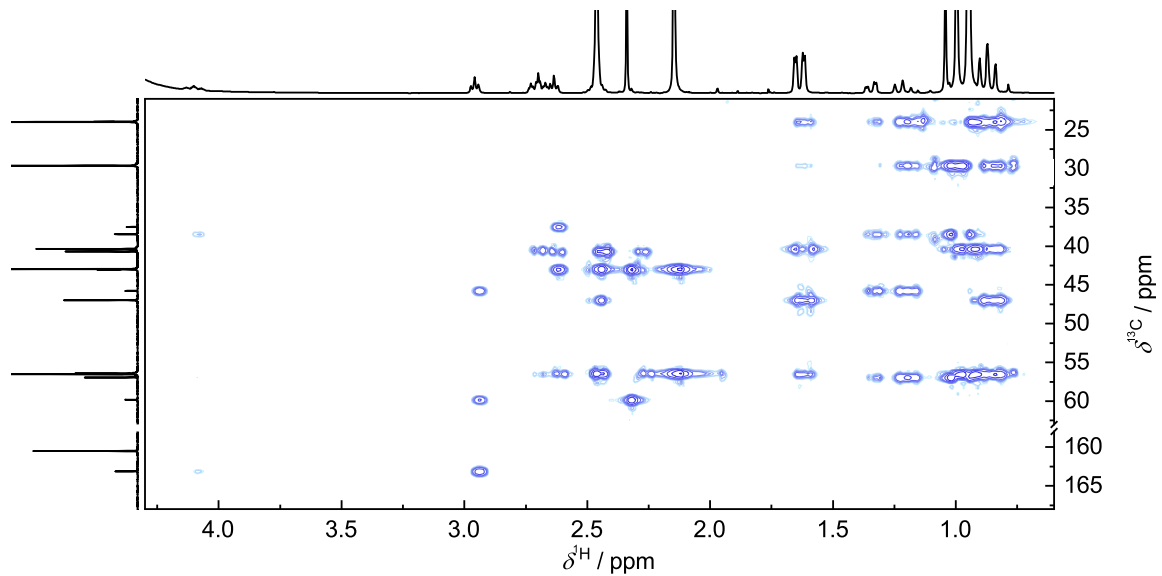
Figure D11: HMBC NMR spectrum of the system (EvA07 + H$_2$O + CO$_2$) with $\tilde{w}^0_{\text{EvA07}} = 0.1$ g/g and $\tilde{\alpha}_{\text{CO}_2} = 1.51$ mol/mol at $t = 20$ ℃.

D.2 System (EvA21 + H$_2$O + CO$_2$)

Figure D13 shows the ^{1}H NMR spectrum of the system (EvA21 + H$_2$O + CO$_2$) with a mass fraction of EvA21 in the unloaded solvent of $\tilde{w}^0_{\text{EvA21}} = 0.1$ g/g and a CO$_2$-loading of $\tilde{\alpha}_{\text{CO}_2} = 2.2$ mol/mol. The corresponding ^{13}Cig NMR spectrum is given in Figure D14. In both spectra, the peaks are labeled with numbers that were assigned to the carbons/hydrogens as designated in Figure D12. The recorded DEPT135, HSQC,

and HMBC NMR spectra that were used for the elucidation are shown in Figures D15 to D17, respectively.

The carbons and protons 1 to 9 of EvA21 were assigned as described for the unloaded aqueous solution of EvA07 (cf. Appendix D.1). The carbon signals 15,16 and 13,14 in the ^{13}Cig NMR spectrum are distinguishable from the signals of 10, 11, and 12 by comparing their integrals. The carbon signal of 15,16 is distinguishable from 13,14 as it correlates to the protons 13,14 in the HMBC NMR spectrum, whereas the carbon signal of 13,14 correlates to the proton signals of themselves, 15,16, and 12. The proton signals 12, 13,14, and 15,16 are matchable with their corresponding carbon signals by the HSQC NMR spectrum. The remaining proton signal 10 and 11 are assignable as the carbon signal 11 correlates with the carbon signal 10 and 12 and the carbon signal 10 correlates with the proton signals 1 and 11 in the HMBC NMR spectrum. The corresponding proton/carbon signals are relatable by the HSQC NMR spectrum, respectively.

The signals 1^β to 16^β and 1^{ac} to 9^{ac} were assigned the same way as described above for the signals 1 to 16. In the ^{13}Cig NMR spectrum, peak 18 represents the carbon signal of (bi)carbonate. Its concentration rises to values of $\tilde{\alpha}_{CO_2} \geq 1$ mol/mol which excludes the possibility of being a carbamate or alkylcarbonate. Also no correlation to any proton is observable in the HMBC NMR spectrum. Peak 19 represents the carbon atom of molecular CO_2 which only occurs at high CO_2-loadings and at a chemical shift of around 124 ppm. The signal shows no correlations to any proton in the HMBC NMR spectrum. Peak 17^β is assignable to the carbon signal of β-carbamate because of the correlation to the adjacing proton signal 10^β in the HMBC NMR spectrum. A correlation to the proton signal 1^β was not found in the HMBC spectrum, which is probably a result of the low concentration of β-carbamate. Peak 17^{ac} represents the carbon signal of alkylcarbonate. The carbon signal 17^{ac} correlates to the proton signal 16^{ac} in the HMBC NMR spectrum. Due to the formation of alkylcarbonate, the signals 13 and 14 as well as 15 and 16 separate from each other. With alternate application of HMBC and HSQC NMR spectra, the signals 12^{ac} to 15^{ac} are assignable. The proton and carbon signals 1^{ac} and 10^{ac} as well as the carbon signal 11^{ac}, remain unassigned. Their signals and correlations are superimposed by others and show too little intensity to be distinguishable from them and from noise. An unambiguous assignment of these peaks is hence impossible, but also not relevant for the unambiguous elucidation of CO_2-containing species for EvA21.
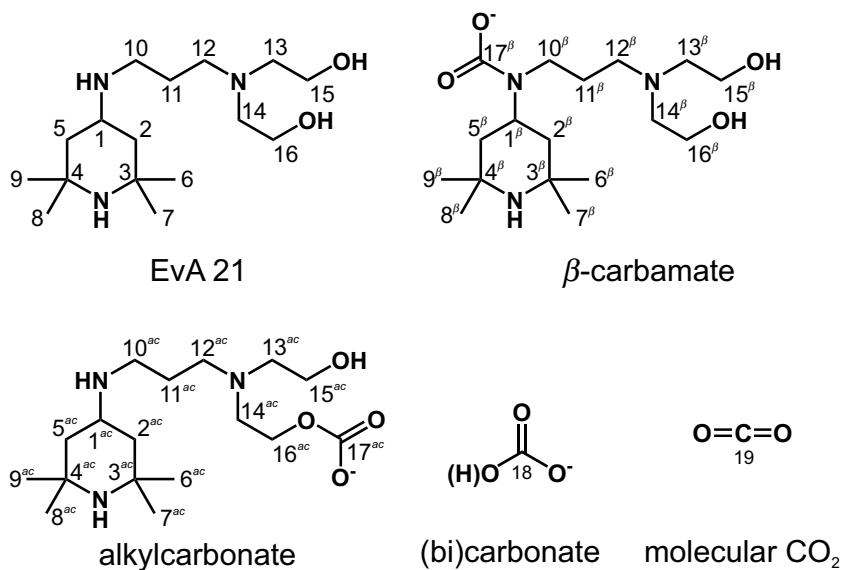
Figure D12: Chemical structures of the elucidated species in the system (EvA21 + H_2O + CO_2) with assignments of the carbon and hydrogen atoms.
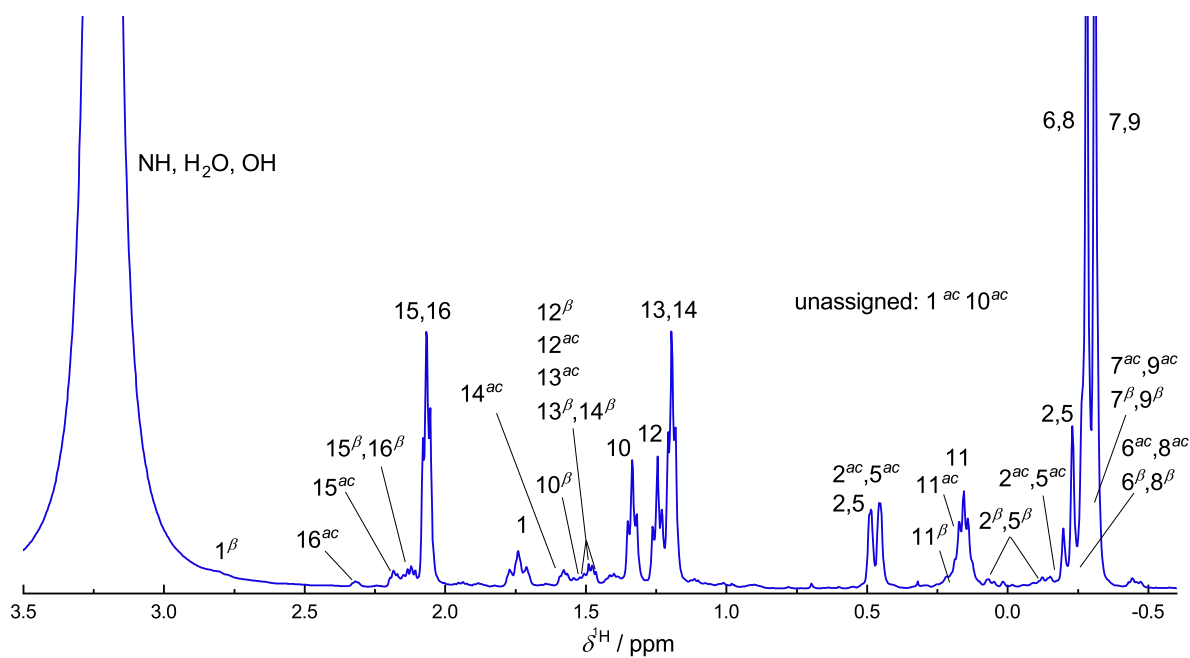
Figure D13: ^1H NMR spectrum of the system (EvA21 + H_2O + CO_2) with $\tilde{w}^0_{\text{EvA21}} = 0.1$ g/g and $\tilde{\alpha}_{CO_2} = 2.2$ mol/mol at $t = 20$ ℃. Notation of the peaks according to Figure D12.
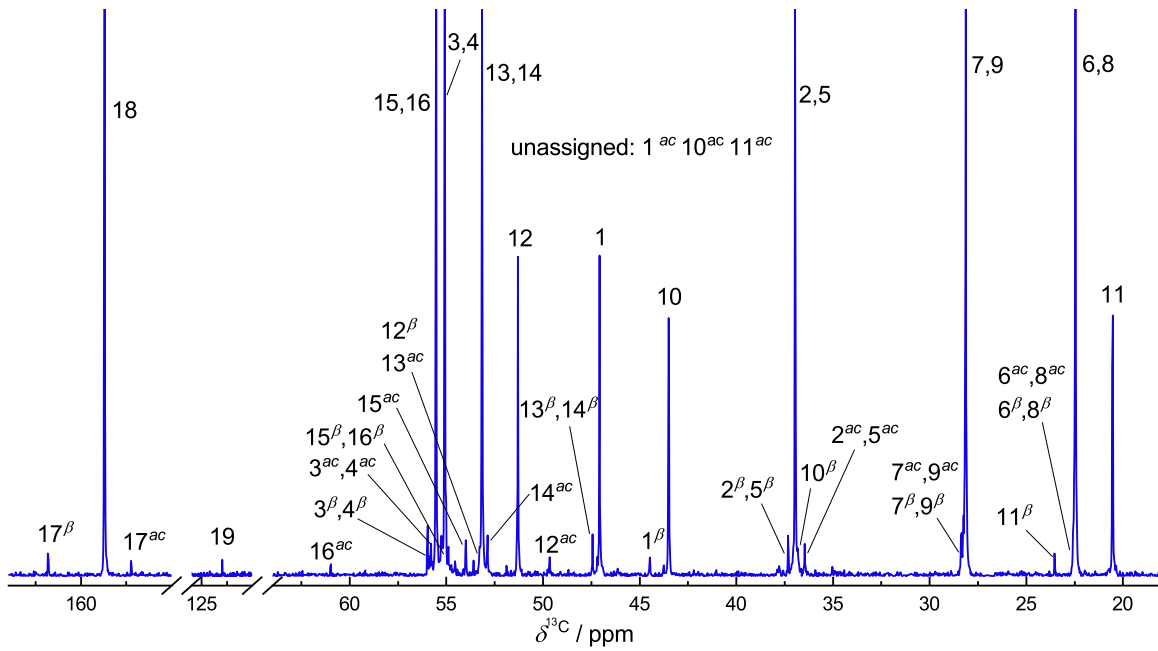
Figure D14: ^{13}Cig NMR spectrum of the system (EvA21 + H$_2$O + CO$_2$) with $\tilde{w}^0_{\mathrm{EvA21}} = 0.1$ g/g and $\tilde{\alpha}_{\mathrm{CO_2}} = 2.2$ mol/mol at $t = 20$ ℃. Notation of the peaks according to Figure D12.
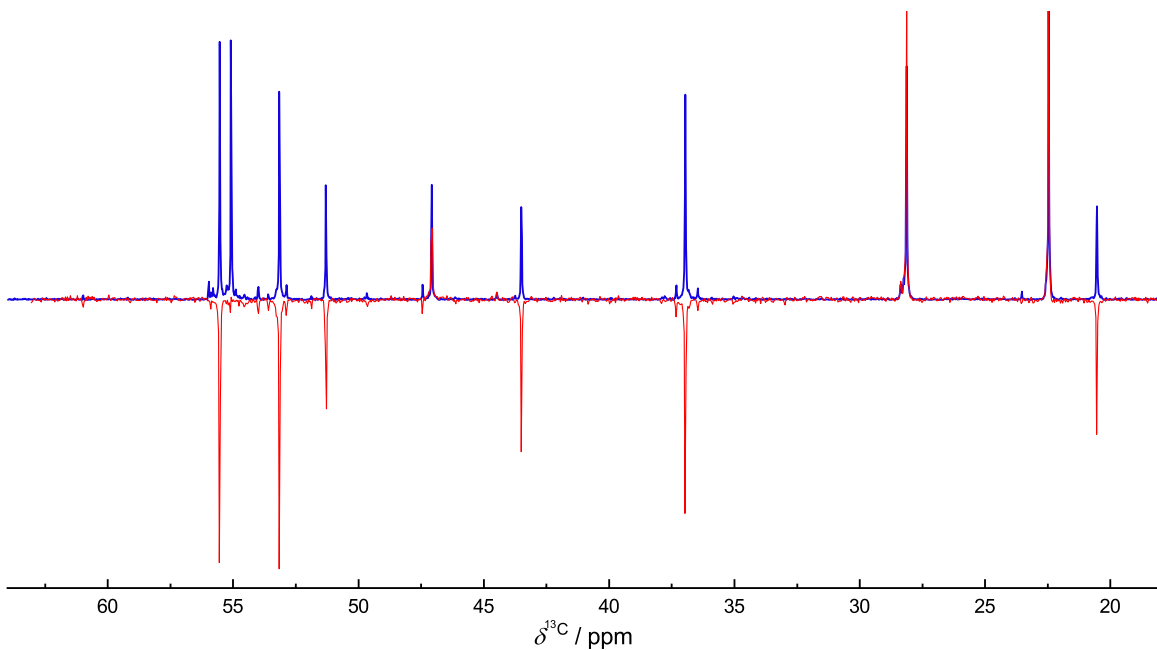
Figure D15: Superimposed DEPT135 (—) and ^{13}Cig (—) NMR spectrum of the system (EvA21 + H$_2$O + CO$_2$) with $\tilde{w}^0_{\mathrm{EvA21}} = 0.1$ g/g and $\tilde{\alpha}_{\mathrm{CO_2}} = 2.2$ mol/mol at $t = 20$ ℃.
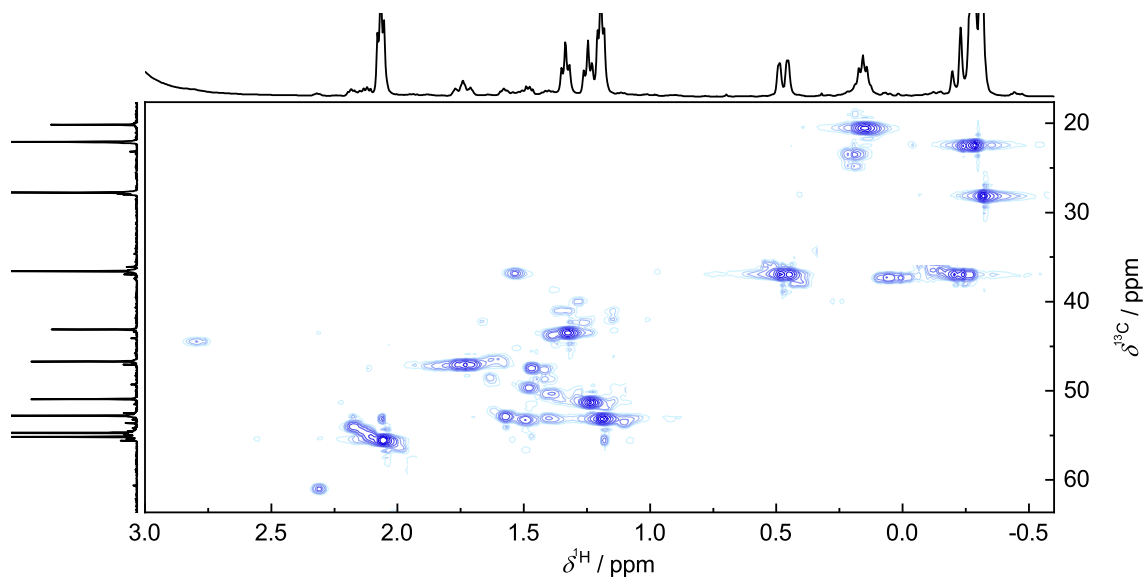
Figure D16: HSQC NMR spectrum of the system (EvA21 + H_2O + CO_2) with $\tilde{w}^0_{\text{EvA21}} = 0.1$ g/g and $\tilde{\alpha}_{CO_2} = 2.2$ mol/mol at $t = 20$ ℃.
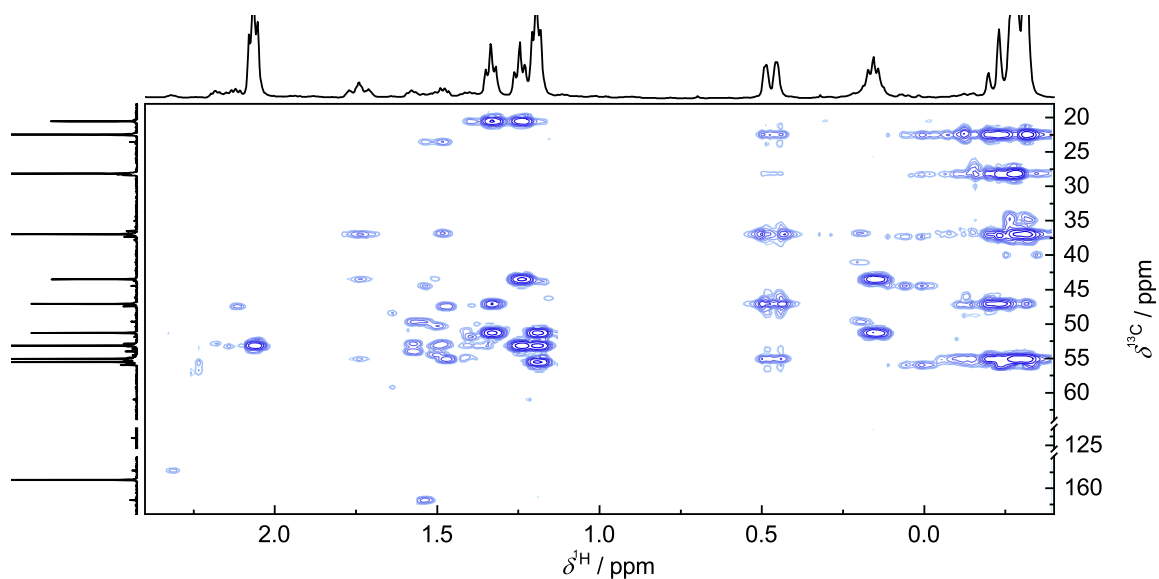
Figure D17: HMBC NMR spectrum of the system (EvA21 + H_2O + CO_2) with $\tilde{w}^0_{\text{EvA21}} = 0.1$ g/g and $\tilde{\alpha}_{CO_2} = 2.2$ mol/mol at $t = 20$ ℃.

D.3 System (EvA25 + H_2O + CO_2)

Figure D19 shows the ^{1}H NMR spectrum of the system (EvA25 + H_2O + CO_2) with mass fractions of EvA25 in the unloaded solvent of $\tilde{w}^0_{\text{EvA25}} = 0.35$ g/g and a CO_2-loading of $\tilde{\alpha}_{CO_2} = 1.85$ mol/mol. The corresponding ^{13}Cig NMR spectrum is given in Figure D20. In both spectra, the peaks are labeled with numbers that were assigned to the carbons/hydrogens as designated in Figure D18. The recorded DEPT135, HSQC,

and HMBC NMR spectra that were used for the elucidation are shown in Figures D21
to D23.

The carbons and protons 1 to 9 of EvA25 were assigned as described for the unloaded
aqueous solution of EvA07 (cf. Appendix D.1). Peaks 15,16 are the remaining positively
polarized peaks in the DEPT135 and are hence unambiguously assignable. The corre-
sponding protons are relatable with the HSQC NMR spectrum. The integrals of the
signals of 13,14 in the ^{13}Cig NMR spectrum are double as high as the remaining signals
of 10, 11, and 12 and are therefore unambiguously assignable. The corresponding signal
in the ^{1}H NMR spectrum is deducible from the HSQC NMR spectrum. The carbons
and protons 10, 11, and 12 are assignable from the combined application of the HMBC
and HSQC NMR Spectrum. Then the long range correlations from the HMBC NMR
Spectrum show that carbon signal 12 has long range correlations to the proton signals
of 13,14, and 11, the carbon signal of 11 shows long range correlations to the proton
signals of 10 and 12, and the carbon signal of 10 shows long range correlations to the
proton signals of 1, 11, and 12. This makes the assignments unambiguous. The proton
signals can be assigned to the corresponding carbon signals by using the HSQC NMR
Spectrum.

The carbons and protons 1^{β} to 16^{β} can be assigned as described for the carbons and pro-
tons of peak 1 to 16. Peak 18 of the ^{13}Cig NMR spectrum represents the (bi)carbonate
carbon. Its concentration rises to values of $\tilde{\alpha}_{CO_2} \geq 1$ mol/mol which excludes the pos-
sibility of being a carbamate. Also no correlation to any proton is observable in the
HMBC NMR spectrum. Peak 17^{β} is assigned to the carbamate carbon of β-carbamate
because of the long range correlation to the proton 1^{β} in the HMBC NMR spectrum.
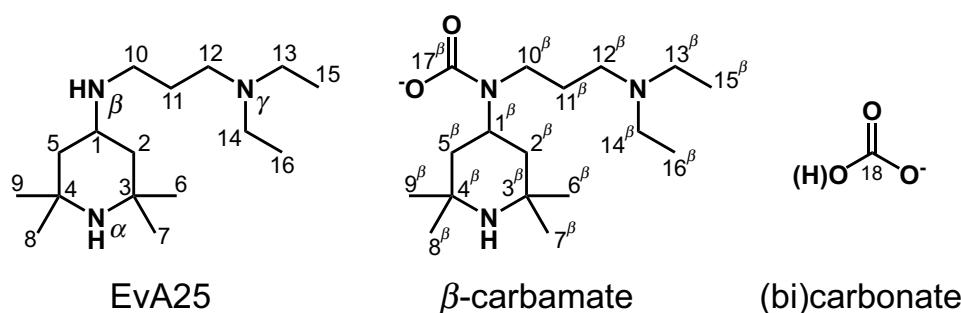
Figure D18: Chemical structures of the elucidated species in the system (EvA25 +
        H_2O + CO_2) with assignments of the carbon and hydrogen atoms.
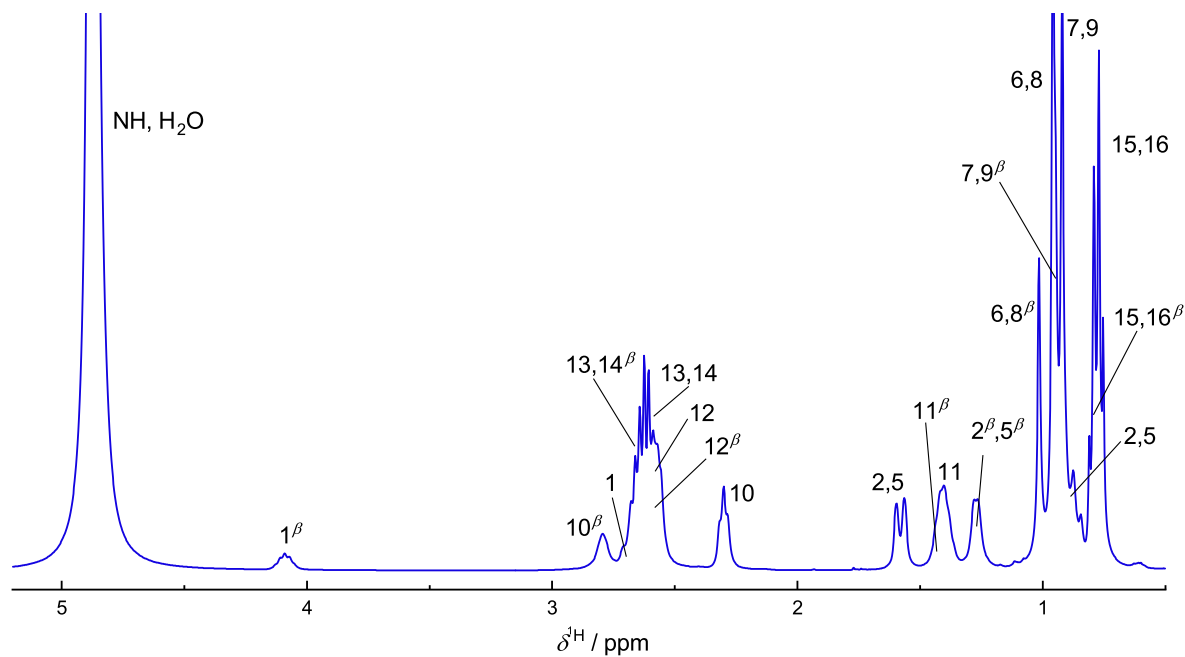
Figure D19: ^{1}H NMR spectrum of the system (EvA25 + H$_2$O + CO$_2$) with $\tilde{w}^0_{\mathrm{EvA25}} = 0.35$ g/g and $\tilde{\alpha}_{\mathrm{CO}_2} = 1.85$ mol/mol at $t = 20$ ℃. Notation of the peaks according to Figure D18.
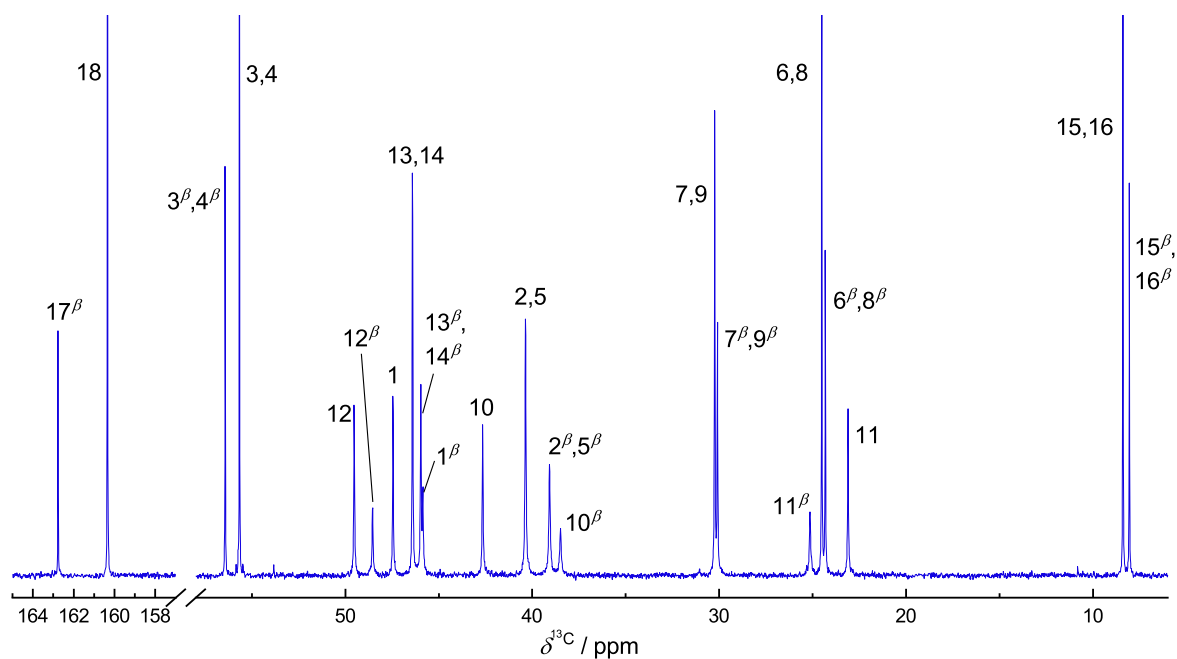
Figure D20: ^{13}Cig NMR spectrum of the system (EvA25 + H$_2$O + CO$_2$) with $\tilde{w}^0_{\mathrm{EvA25}} = 0.35$ g/g and $\tilde{\alpha}_{\mathrm{CO}_2} = 1.85$ mol/mol at $t = 20$ ℃. Notation of the peaks according to Figure D18.
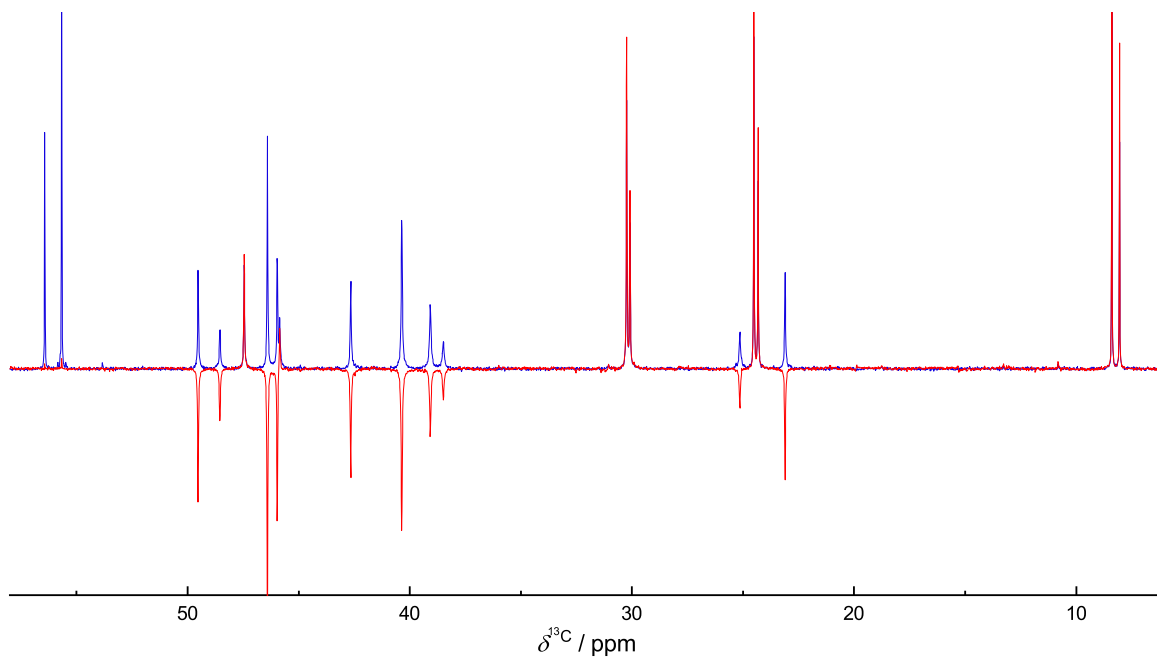
Figure D21: Superimposed DEPT135 (—) and ^{13}Cig (—) NMR spectrum of the system (EvA25 + H_2O + CO_2) with $\tilde{w}^0_{\mathrm{EvA25}} = 0.35$ g/g and $\tilde{\alpha}_{\mathrm{CO_2}} = 1.85$ mol/mol at $t = 20$ ℃.
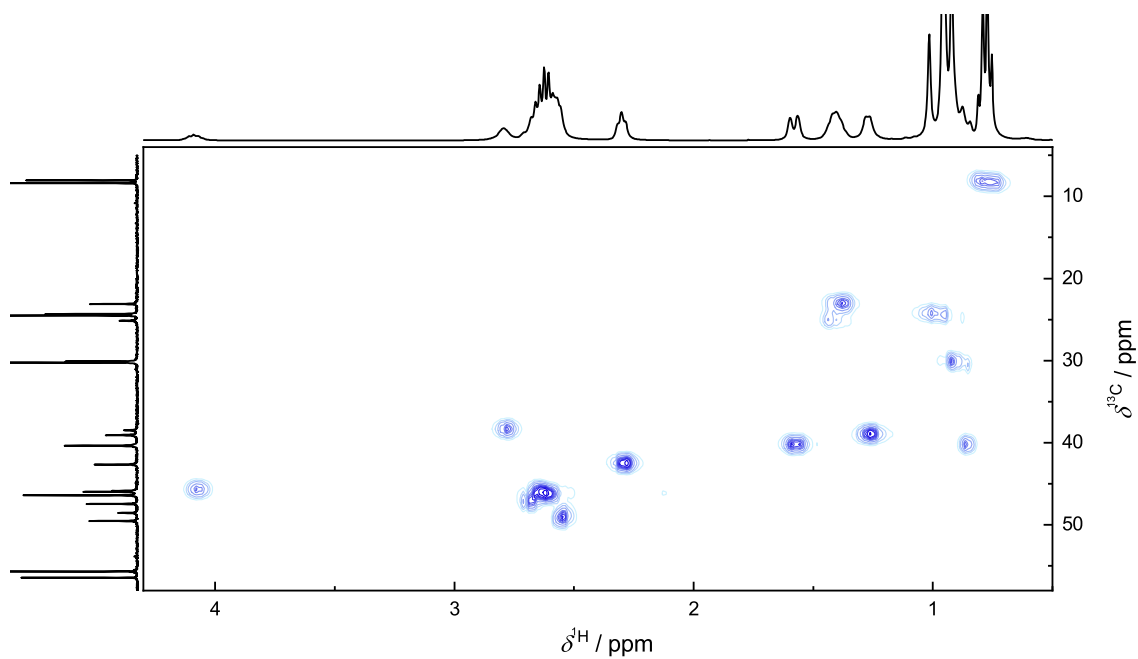
Figure D22: HSQC NMR spectrum of the system (EvA25 + H_2O + CO_2) with $\tilde{w}^0_{\mathrm{EvA25}} = 0.35$ g/g and $\tilde{\alpha}_{\mathrm{CO_2}} = 1.85$ mol/mol at $t = 20$ ℃.
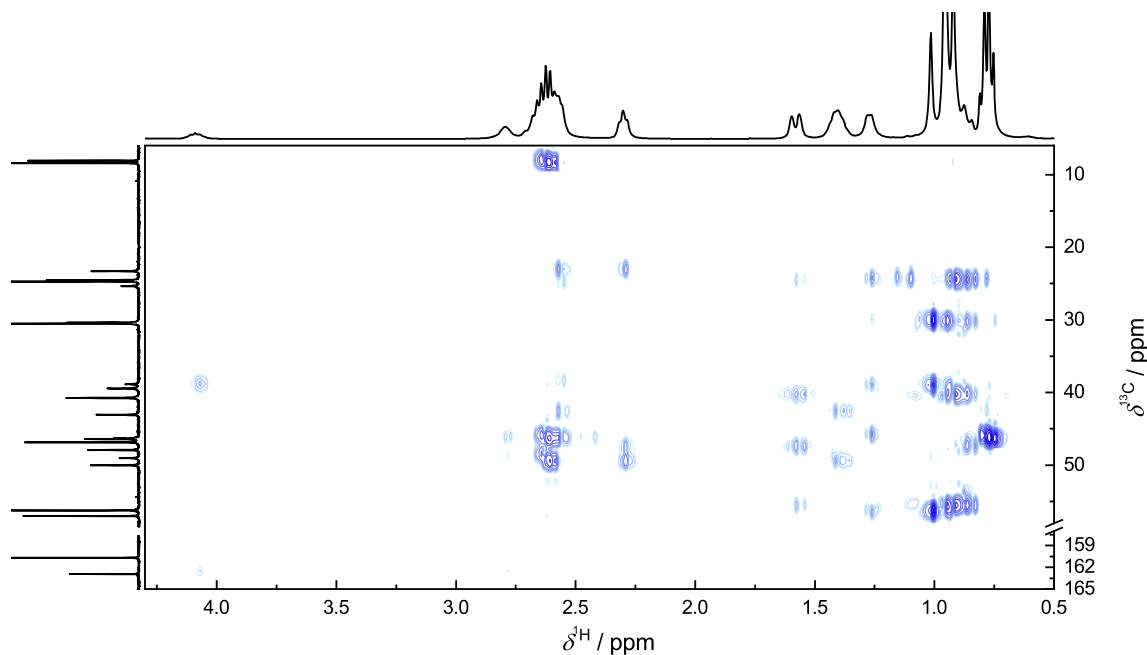
Figure D23: HMBC NMR spectrum of the system (EvA25 + H_2O + CO_2) with $\tilde{w}^0_{EvA25} = 0.35$ g/g and $\tilde{\alpha}_{CO_2} = 1.85$ mol/mol at $t = 20\,°C$.

D.4 System (EvA34 + H_2O + CO_2)

Figure D25 shows the ^1H NMR spectrum of the system (EvA34 + H_2O + CO_2) with mass fractions of EvA34 in the unloaded solvent of $\tilde{w}^0_{EvA34} = 0.4$ g/g and a CO_2-loading of $\tilde{\alpha}_{CO_2} = 2.35$ mol/mol. The corresponding ^{13}Cig NMR spectrum is given in Figure D26. In both spectra, the peaks are labeled with numbers that were assigned to the carbons/hydrogens as designated in Figure D24. The recorded DEPT135, HSQC, and HMBC NMR spectra that were used for the elucidation are shown in Figures D27 to D29, respectively.

The carbons and protons 1 to 9 of EvA34 were assigned as described for the unloaded aqueous solution of EvA07 (cf. Appendix D.1). Peaks 16,17 are the remaining positively polarized peaks in the DEPT135 and hence are unambiguously assignable. The corresponding protons are relatable with the HSQC NMR spectrum. The remaining peaks 10 to 15 are assignable by alternating application of the HMBC and HSQC NMR spectra, starting from the peaks 1 and 16,17, respectively.

The carbons and protons for β-carbamate, γ-carbamate, and β-γ-dicarbamate can be assigned the same way as described for EvA34. Peak 20 of the ^{13}Cig NMR spectrum represents the (bi)carbonate carbon. Its concentration rises to values of $\tilde{\alpha}_{CO_2} \geq 1$ mol/mol which excludes the possibility of being a carbamate. Also no correlation to any proton is observable in the HMBC NMR spectrum. Peak 19^γ is assignable to the carbamate

carbon of γ-carbamate because of the strong correlation to the protons 12^γ and 13^γ in the HMBC NMR spectrum. Peak 18^β is assignable to the carbamate carbon of β-carbamate as it shows a correlation to the proton of 1^β in the HMBC NMR spectrum. The carbon peaks $18^{\beta\gamma}$ and $19^{\beta\gamma}$ does not show any long range correlation. However, some arguments indicate the displayed assignment of the dicarbamate structure. Firstly, the carbamate formation at the β-amino group and γ-amino group was already proven. Secondly, with varying CO_2-loading, a synchronous increase and decrease of the $18^{\beta\gamma}$ and $19^{\beta\gamma}$ peak integrals is observable in the set of ^{13}Cig NMR spectra.
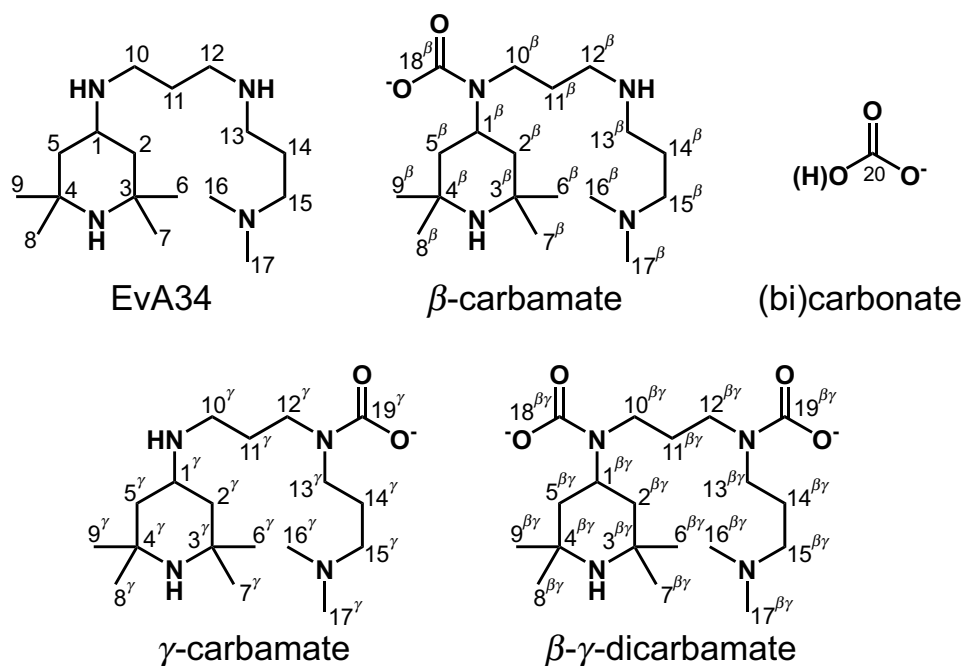
Figure D24: Chemical structures of the elucidated species in the system (EvA34 + H_2O + CO_2) with assignments of the carbon and hydrogen atoms.
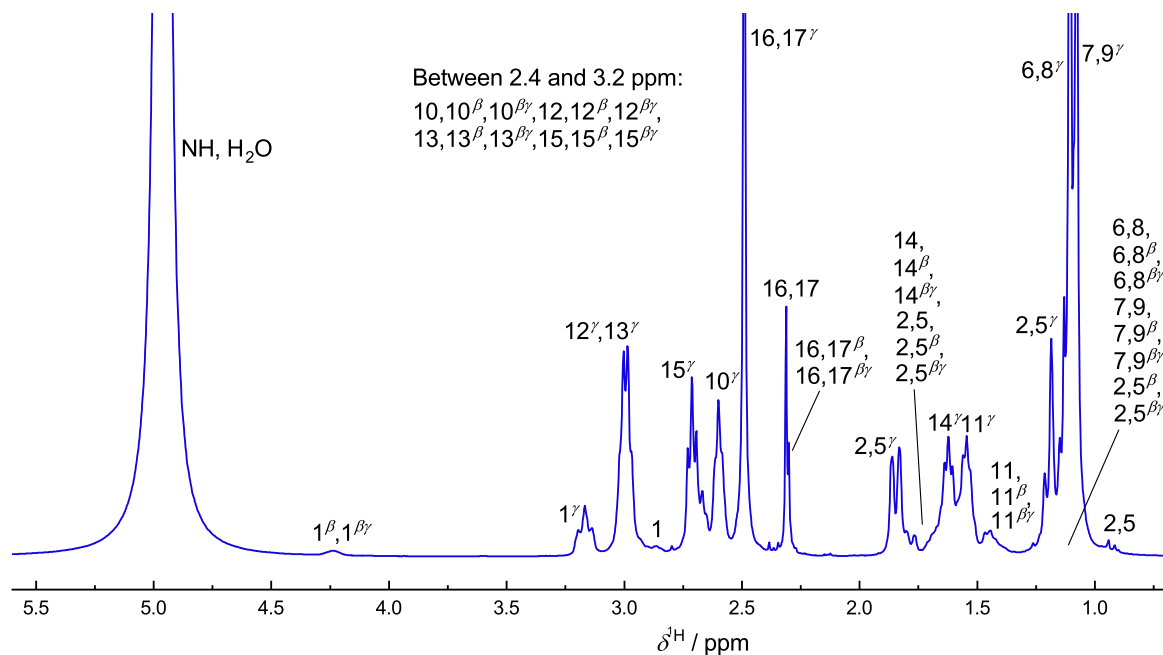
Figure D25: ^{1}H NMR spectrum of the system (EvA34 + H$_2$O + CO$_2$) with $\tilde{w}^0_{\mathrm{EvA34}} = 0.4$ g/g and $\tilde{\alpha}_{\mathrm{CO}_2} = 2.35$ mol/mol at $t = 20$ °C. Notation of the peaks according to Figure D24.
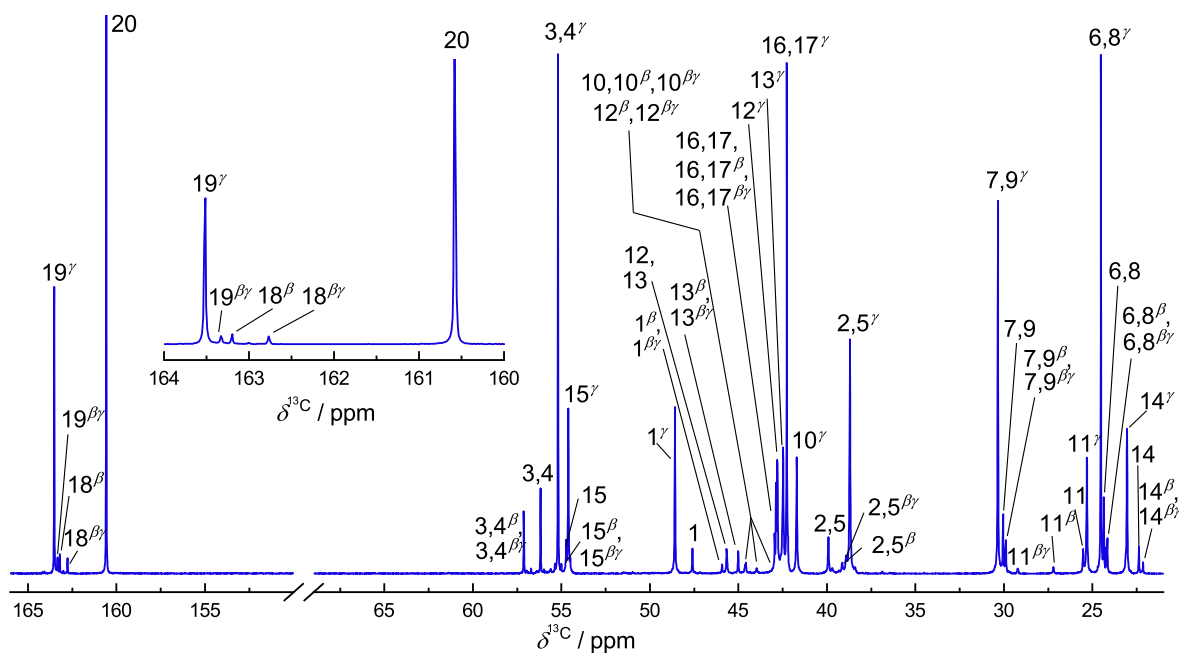
Figure D26: ^{13}Cig NMR spectrum of the system (EvA34 + H$_2$O + CO$_2$) with $\tilde{w}^0_{\mathrm{EvA34}} = 0.4$ g/g and $\tilde{\alpha}_{\mathrm{CO}_2} = 2.35$ mol/mol at $t = 20$ °C. Notation of the peaks according to Figure D24.
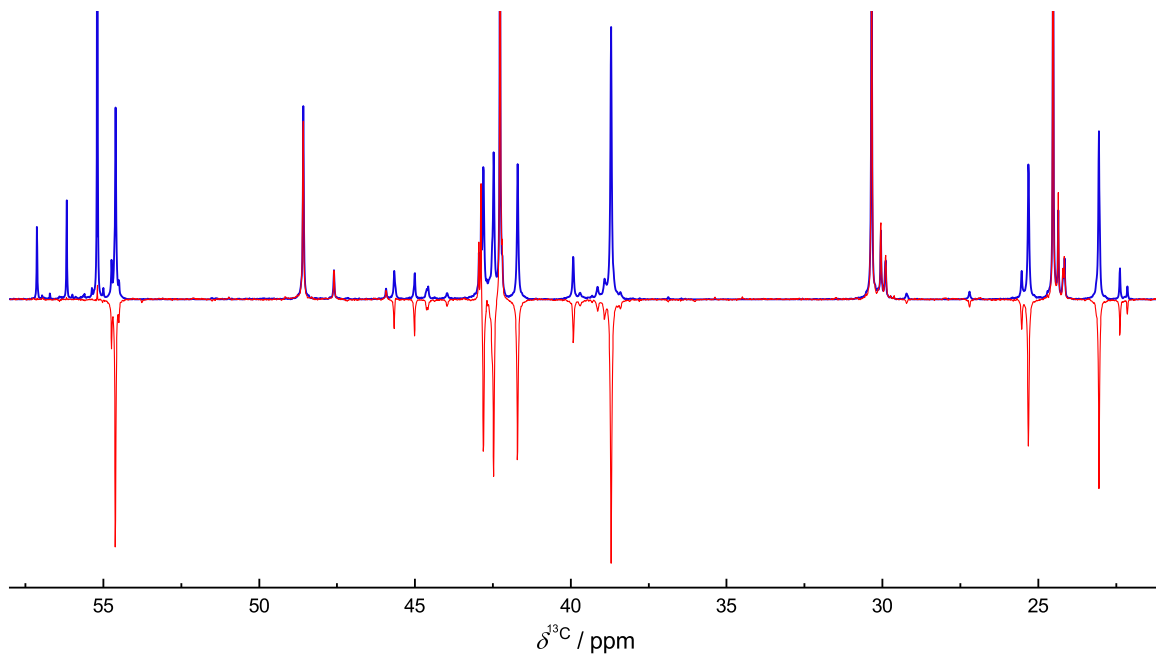
Figure D27: Superimposed DEPT135 (—) and ^{13}Cig (—) NMR spectrum of the system (EvA34 + H_2O + CO_2) with $\tilde{w}^0_{\text{EvA34}} = 0.4$ g/g and $\tilde{\alpha}_{CO_2} = 2.35$ mol/mol at $t = 20$ °C.
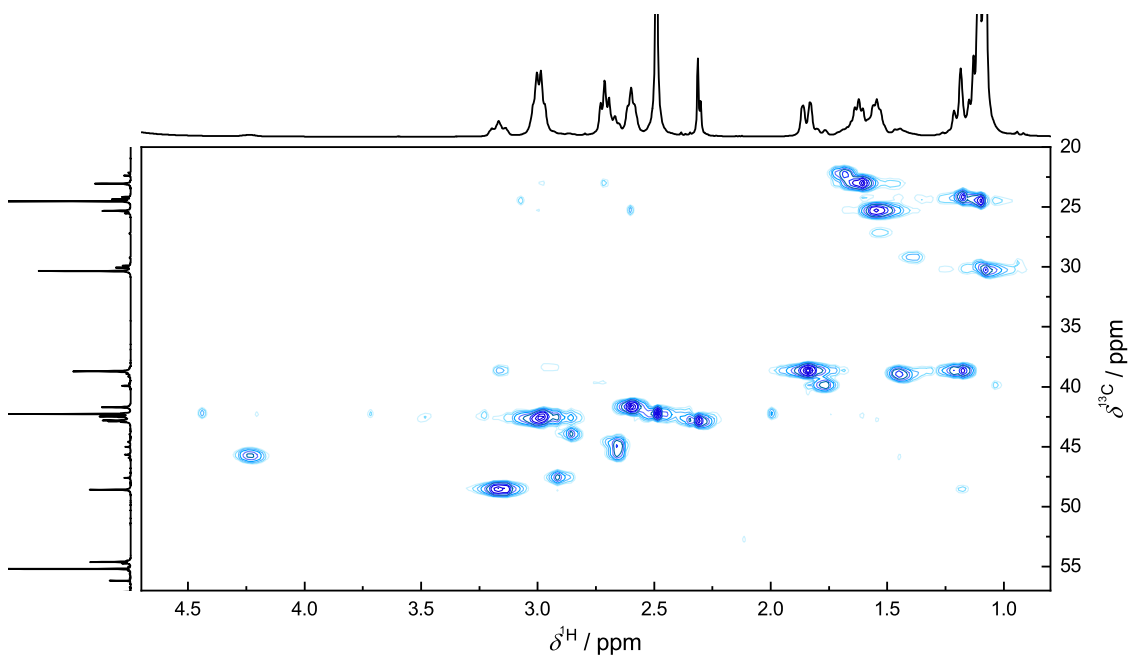
Figure D28: HSQC NMR spectrum of the system (EvA34 + H_2O + CO_2) with $\tilde{w}^0_{\text{EvA34}} = 0.4$ g/g and $\tilde{\alpha}_{CO_2} = 2.35$ mol/mol at $t = 20$ °C.
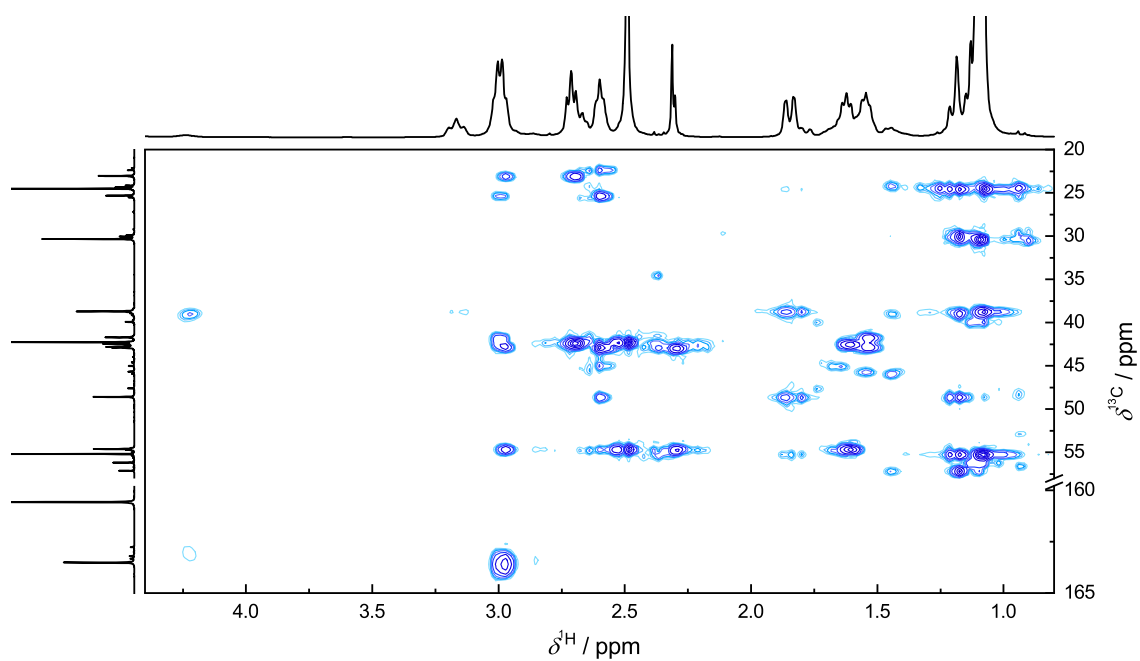
Figure D29: HMBC NMR spectrum of the system $(\text{EvA34} + \text{H}_2\text{O} + \text{CO}_2)$ with $\tilde{w}^0_{\text{EvA34}} = 0.4$ g/g and $\tilde{\alpha}_{\text{CO}_2} = 2.35$ mol/mol at $t = 20\,°\text{C}$.

E Numerical experimental data

E.1 Screening

The experimental numerical data from bubble cell experiments of the screening are given in Table E1. A preliminary report of the results has been given in a conference paper [30]. The data that were presented in that paper and the data from the present work are not identical, as the primary IR data was reevaluated. It is recommended to use the data reported in the present work. The trends and basic findings of both publications match perfectly. The experimental numerical data from head space gas chromatography experiments of the screening are given in Table E2.

Table E1: Initial rate of absorption of CO_2 and equilibrium CO_2-loading from bubble cell experiments in the systems (amine + H_2O + CO_2) with $\tilde{w}^0_{amine} = 0.05$ g/g and $p_{CO_2} = 140$ mbar.

	RA	$\tilde{X}_{CO_2}$	
	10^{-2} g/(g·min)	g/g	
T / K	313.15	313.15	373.15
MEA	1.97	0.47	0.27
MDEA/PZ	1.52	0.34	0.11
EvA01	2.46	0.41	0.27
EvA02	2.05	0.39	0.16
EvA03	1.48	0.43	0.20
EvA04	1.48	0.33	0.18
EvA05	1.85	0.32	0.17
EvA06	1.12	0.25	0.14
EvA07	1.81	0.37	0.15
EvA09	0.72	0.24	0.12
EvA10	0.48	0.27	0.12
EvA14	0.95	0.37	0.16
EvA17	1.72	0.33	0.17
EvA21	0.98	0.24	0.13
EvA22	1.70	0.33	0.16
EvA24	1.24	0.24	0.12
EvA25	1.35	0.42	0.20
EvA26	1.51	0.36	0.15
EvA27	0.77	0.31	0.15
EvA29/30	1.00	0.20	0.11
EvA31	1.25	0.33	0.17
EvA32	0.95	0.16	0.09

Table E1: continued from previous page

T / K	RA 10^{-2} g/(g·min) 313.15	$\tilde{X}_{CO_2}$ g/g 313.15	$\tilde{X}_{CO_2}$ g/g 373.15
EvA33	1.01	0.21	0.09
EvA34	1.80	0.44	0.21
EvA36	2.17	0.42	0.24
EvA41	0.84	0.19	0.08

$\tilde{w}_{amine}^0$: mass fraction of amine in the unloaded solvent with the relative expanded uncertainty $u_r(\tilde{w}_{amine}^0) = 0.001$ (0.99 level of confidence), p_{CO_2}: partial pressure of CO_2 with the standard uncertainty $u(p_{CO_2}) = 5$ mbar, RA: initial rate of absorption of CO_2 with the relative standard uncertainty $u_r(RA) = 0.05$, $\tilde{X}_{CO_2}$: equilibrium CO_2-loading with the relative standard uncertainty $u_r(\tilde{X}_{CO_2}) = 0.05$, T: temperature with the expanded uncertainty $U(T) = 1$ K (0.99 level of confidence).

Table E2: CO_2-solubility from head space gas chromatography experiments in the systems (amine + H_2O + CO_2) with $\tilde{w}_{EvA}^0 = 0.4$ g/g.

T / K	313.15		373.15		313.15		373.15	
	$\tilde{X}_{CO_2}$ g/g	p_{CO_2} bar	$\tilde{X}_{CO_2}$ g/g	p_{CO_2} bar	$\tilde{X}_{CO_2}$ g/g	p_{CO_2} bar	$\tilde{X}_{CO_2}$ g/g	p_{CO_2} bar
	EvA03				EvA06			
	0.281	0.073	0.038	0.129	0.172	0.076	0.029	0.161
	0.321	0.167	0.071	0.332	0.213	0.221	0.050	0.420
	0.348	0.275	0.095	0.495	0.233	0.474	0.075	0.804
	0.371	0.754	0.126	0.997	0.247	0.960	0.101	1.382
	0.377	0.746	0.149	1.225	0.276	1.586	0.105	1.447
	0.391	1.005	0.173	1.531				
	0.395	1.646						
	EvA09				EvA21			
	0.058	0.013	0.027	0.334	0.171	0.099	0.022	0.049
	0.128	0.054	0.052	0.807	0.216	0.304	0.037	0.123
	0.154	0.097	0.056	0.876	0.234	0.521	0.061	0.339
	0.192	1.059	0.076	1.569				
	EvA24				EvA25			
	0.086	0.017	0.024	0.076	0.168	0.020	0.025	0.121
	0.191	0.299	0.036	0.236	0.238	0.050	0.076	0.632
	0.217	0.621	0.049	0.375	0.303	0.179	0.136	1.605
	0.237	0.836	0.087	0.982	0.389	1.728	0.163	2.103
	EvA29/30				EvA34			
	0.046	0.010	0.009	0.005	0.203	0.021	0.025	0.028
	0.144	0.126	0.024	0.060	0.295	0.109	0.074	0.154
	0.172	0.365	0.051	0.269	0.298	0.113	0.076	0.144

Table E2: continued from previous page

T / K	313.15		373.15		313.15		373.15	
	$\tilde{X}_{CO_2}$	p_{CO_2}	$\tilde{X}_{CO_2}$	p_{CO_2}	$\tilde{X}_{CO_2}$	p_{CO_2}	$\tilde{X}_{CO_2}$	p_{CO_2}
	g/g	bar	g/g	bar	g/g	bar	g/g	bar
EvA29/30 continued					EvA34 continued			
	0.192	0.926	0.080	0.632	0.372	0.445	0.124	0.363
	0.202	1.566	0.103	1.130	0.391	0.694	0.134	0.439
					0.404	0.817	0.147	0.548
					0.412	1.312	0.221	1.326
EvA36								
	0.202	0.014	0.050	0.025				
	0.309	0.170	0.074	0.053				
	0.345	0.438	0.111	0.120				
	0.359	0.593	0.149	0.300				
	0.377	0.831	0.193	0.694				
	0.390	1.167	0.194	0.699				
	0.405	1.265	0.226	1.251				

$\tilde{w}^0_{EvA}$: mass fraction of EvA in the unloaded solvent with the relative expanded uncertainty $u_r(\tilde{w}^0_{EvA}) = 0.001$ (0.99 level of confidence), T: temperature with the expanded uncertainty $U(T) = 0.1$ K (0.99 level of confidence), $\tilde{X}_{CO_2}$: equilibrium CO_2-loading with the relative expanded uncertainty $U_r(\tilde{X}_{CO_2}) = 0.01$ (0.99 level of confidence), p_{CO_2}: partial pressure of CO_2 with the relative standard uncertainty $u_r(p_{CO_2}) = 0.08$.

E.2 System (EvA34 + H$_2$O + CO$_2$)

Table E3: CO_2-solubility in the system (EvA34 + H$_2$O + CO$_2$) in the low pressure region.

T	$\tilde{m}_{EvA34}$	$\tilde{m}_{CO_2}$	p_{CO_2}
K	mol_{EvA34}/kg_{H_2O}	mol_{CO_2}/kg_{H_2O}	mbar
313.15	0.380	$0.625\ ^{+0.013}_{-0.002}$	16.84 ± 0.18
313.21	0.374	$0.749\ ^{+0.018}_{-0.003}$	53.00 ± 1.15
313.18	0.374	$0.799\ ^{+0.014}_{-0.001}$	78.31 ± 1.93
313.17	0.380	$0.847\ ^{+0.020}_{-0.003}$	114.43 ± 1.60
313.18	0.380	$0.905\ ^{+0.021}_{-0.004}$	181.10 ± 3.25
313.19	0.380	$0.952\ ^{+0.023}_{-0.004}$	266.38 ± 6.11
313.14	0.380	$1.005\ ^{+0.022}_{-0.004}$	456.33 ± 7.47
313.21	0.374	$1.049\ ^{+0.025}_{-0.004}$	738.46 ± 14.61

Table E3: continued from previous page

T	$\tilde{m}_{\text{EvA34}}$	$\tilde{m}_{\text{CO}_2}$	p_{CO_2}
K	$\text{mol}_{\text{EvA34}}/\text{kg}_{\text{H}_2\text{O}}$	$\text{mol}_{\text{CO}_2}/\text{kg}_{\text{H}_2\text{O}}$	mbar
353.16	0.368	$0.374\ ^{+0.008}_{-0.001}$	32.45 ± 0.33
353.15	0.368	$0.504\ ^{+0.012}_{-0.002}$	76.44 ± 1.29
353.12	0.365	$0.582\ ^{+0.013}_{-0.002}$	149.37 ± 5.57
353.15	0.368	$0.685\ ^{+0.016}_{-0.003}$	317.44 ± 4.51
353.09	0.365	$0.730\ ^{+0.016}_{-0.002}$	537.21 ± 13.99
353.10	0.365	$0.771\ ^{+0.017}_{-0.003}$	740.47 ± 18.13
393.13	0.373	$0.095\ ^{+0.002}_{-0.000}$	31.83 ± 0.33
393.13	0.373	$0.161\ ^{+0.004}_{-0.001}$	67.32 ± 1.79
393.13	0.373	$0.239\ ^{+0.005}_{-0.001}$	134.16 ± 3.46
393.15	0.373	$0.324\ ^{+0.007}_{-0.001}$	246.14 ± 5.33
393.13	0.368	$0.421\ ^{+0.010}_{-0.001}$	471.02 ± 13.81
393.15	0.373	$0.504\ ^{+0.012}_{-0.002}$	724.89 ± 13.35
313.16	2.246	$3.450\ ^{+0.075}_{-0.017}$	24.95 ± 0.92
313.15	2.180	$3.909\ ^{+0.096}_{-0.027}$	55.70 ± 0.85
313.16	2.180	$4.274\ ^{+0.078}_{-0.010}$	93.44 ± 1.83
313.18	2.271	$4.785\ ^{+0.098}_{-0.019}$	141.01 ± 2.76
313.16	2.300	$4.930\ ^{+0.095}_{-0.016}$	162.92 ± 2.63
313.16	2.300	$5.340\ ^{+0.089}_{-0.006}$	284.03 ± 6.82
313.15	2.246	$5.840\ ^{+0.138}_{-0.036}$	598.55 ± 22.62
313.16	2.246	$5.974\ ^{+0.137}_{-0.034}$	746.69 ± 19.92
353.11	2.249	$0.665\ ^{+0.015}_{-0.004}$	17.81 ± 0.30
353.11	2.249	$1.124\ ^{+0.026}_{-0.006}$	35.62 ± 0.90
353.16	2.235	$1.635\ ^{+0.040}_{-0.010}$	70.05 ± 1.79
353.17	2.235	$1.821\ ^{+0.045}_{-0.011}$	82.60 ± 1.16
353.16	2.257	$1.976\ ^{+0.042}_{-0.008}$	103.97 ± 2.37
353.16	2.257	$2.296\ ^{+0.053}_{-0.012}$	150.64 ± 2.68
353.16	2.257	$2.661\ ^{+0.063}_{-0.015}$	213.75 ± 2.47
353.16	2.257	$3.113\ ^{+0.072}_{-0.016}$	344.11 ± 6.08
353.16	2.257	$3.432\ ^{+0.085}_{-0.022}$	493.08 ± 4.30
353.16	2.247	$3.603\ ^{+0.088}_{-0.022}$	588.71 ± 8.30
353.18	2.235	$3.961\ ^{+0.092}_{-0.021}$	813.66 ± 17.45
392.77	2.249	$0.162\ ^{+0.004}_{-0.001}$	33.48 ± 1.37
393.18	2.259	$0.183\ ^{+0.005}_{-0.001}$	49.14 ± 0.11
393.13	2.259	$0.271\ ^{+0.006}_{-0.001}$	69.49 ± 2.16
393.14	2.235	$0.340\ ^{+0.008}_{-0.002}$	97.69 ± 1.55
393.14	2.262	$0.360\ ^{+0.008}_{-0.002}$	99.15 ± 1.11
393.15	2.224	$0.509\ ^{+0.012}_{-0.002}$	169.34 ± 3.47
393.16	2.224	$0.621\ ^{+0.014}_{-0.003}$	226.63 ± 5.52
393.14	2.262	$0.769\ ^{+0.019}_{-0.004}$	290.20 ± 6.73
393.13	2.262	$0.961\ ^{+0.022}_{-0.004}$	411.64 ± 9.90
393.14	2.246	$1.136\ ^{+0.026}_{-0.005}$	552.97 ± 12.48

Table E3: continued from previous page

T	$\tilde{m}_{EvA34}$	$\tilde{m}_{CO_2}$	p_{CO_2}
K	mol_{EvA34}/kg_{H_2O}	mol_{CO_2}/kg_{H_2O}	mbar
393.13	2.224	1.264 $^{+0.029}_{-0.006}$	621.28 ± 15.05
393.15	2.246	1.449 $^{+0.035}_{-0.008}$	770.74 ± 32.79

T: temperature with the expanded uncertainty $U(T) = 0.1$ K (0.99 level of confidence), $\tilde{m}_{EvA34}$: molality of EvA34 with the relative expanded uncertainty $U_r(\tilde{m}_{EvA34}) = 0.001$ (0.99 level of confidence), $\tilde{m}_{CO_2}$: molality of CO_2 with the intervals representing the expanded uncertainty $U(\tilde{m}_{CO_2})$ (0.99 level of confidence). p_{CO_2}: partial pressure of CO_2 with the intervals representing the standard uncertainty $u(p_{CO_2})$.

Table E4: CO_2-solubility in the system (EvA34 + H_2O + CO_2) in the high pressure region.

T	$\tilde{m}_{EvA34}$	$\tilde{m}_{CO_2}$	p
K	mol_{EvA34}/kg_{H_2O}	mol_{CO_2}/kg_{H_2O}	bar
313.23		1.223	5.264 ± 0.023
313.16		1.260	6.168 ± 0.021
313.21		1.354	9.606 ± 0.109
313.23		1.410	11.426 ± 0.068
313.20	0.377	1.494	15.314 ± 0.068
313.16		1.626	20.847 ± 0.074
313.20		1.813	33.160 ± 0.505
313.23		1.978	44.512 ± 0.245
313.22		2.175	56.974 ± 0.545
313.19		2.348	69.020 ± 0.496
353.11		1.064	7.141 ± 0.061
353.24		1.090	7.673 ± 0.049
353.17		1.220	14.527 ± 0.022
353.27	0.377	1.275	18.869 ± 0.076
353.27		1.402	27.555 ± 0.113
353.32		1.559	41.078 ± 0.122
353.28		1.702	55.364 ± 0.467
393.13		0.803	7.822 ± 0.036
393.22		0.997	14.976 ± 0.170
393.27	0.377	1.148	30.410 ± 0.158
393.23		1.286	43.502 ± 0.194
393.19		1.625	75.221 ± 0.341
313.24		6.442	2.956 ± 0.168
313.21		6.553	3.959 ± 0.118
313.22	2.237	6.684	5.388 ± 0.149
313.22		6.931	8.277 ± 0.165
313.19		7.434	19.127 ± 0.150

Table E4: continued from previous page

T	$\tilde{m}_{\text{EvA34}}$	$\tilde{m}_{\text{CO}_2}$	p
K	$\text{mol}_{\text{EvA34}}/\text{kg}_{\text{H}_2\text{O}}$	$\text{mol}_{\text{CO}_2}/\text{kg}_{\text{H}_2\text{O}}$	bar
313.19		7.657	27.223 ± 0.196
313.20	2.237	7.833	33.290 ± 0.140
313.21		8.277	58.422 ± 0.551
353.21		4.418	1.983 ± 0.062
353.28		4.884	3.647 ± 0.014
353.21		5.346	5.815 ± 0.026
353.22		5.606	7.589 ± 0.030
353.24		5.623	7.788 ± 0.028
353.21	2.238	5.847	10.317 ± 0.099
353.12		6.046	15.437 ± 0.065
353.19		6.343	20.827 ± 0.212
353.07		6.651	31.286 ± 0.092
353.15		6.947	46.943 ± 0.458
353.22		7.168	64.476 ± 0.440
353.19		7.397	81.497 ± 0.401
393.05		2.735	5.233 ± 0.008
393.14		3.152	6.562 ± 0.037
392.96		3.703	9.157 ± 0.073
393.12		4.225	13.802 ± 0.043
393.06	2.238	4.515	18.804 ± 0.122
393.00		4.739	22.690 ± 0.103
393.04		5.305	36.861 ± 0.090
393.12		5.747	57.882 ± 0.148
393.06		6.282	90.292 ± 0.417

T: temperature with the expanded uncertainty $U(T) = 0.1$ K (0.99 level of confidence), $\tilde{m}_{\text{EvA34}}$: molality of EvA34 with the relative expanded uncertainty $U_r(\tilde{m}_{\text{EvA34}}) = 0.001$ (0.99 level of confidence), $\tilde{m}_{\text{CO}_2}$: molality of CO_2 with the relative expanded uncertainty $U_r(\tilde{m}_{\text{CO}_2}) = 0.001$ (0.99 level of confidence). p bubble point pressure with the intervals representing the standard uncertainty $u(p)$.

Table E5: pK-values of EvA34 highly diluted in H_2O

	T	$\tilde{m}_{\text{EvA34}}$	$\tilde{m}_{\text{HCl}}$	$\tilde{m}_{\text{NaOH}}$	pK
	K	$\text{mol}_{\text{EvA34}}/\text{kg}_{\text{H}_2\text{O}}$	$\text{mol}_{\text{HCl}}/\text{kg}_{\text{H}_2\text{O}}$	$\text{mol}_{\text{NaOH}}/\text{kg}_{\text{H}_2\text{O}}$	
	293.6	0.031 ± 0.001	0.141 ± 0.007	0.124 ± 0.007	10.90 ± 0.10
pK_α	313.0	0.028 ± 0.003	0.139 ± 0.005	0.123 ± 0.003	10.35 ± 0.15
	333.0	0.025 ± 0.001	0.144 ± 0.004	0.129 ± 0.004	9.85 ± 0.15
	352.2	0.025 ± 0.001	0.140 ± 0.007	0.125 ± 0.007	9.50 ± 0.10
	293.5	0.032 ± 0.001	0.145 ± 0.008	0.096 ± 0.008	9.80 ± 0.10
pK_δ	313.1	0.028 ± 0.003	0.143 ± 0.005	0.099 ± 0.001	9.30 ± 0.10
	333.2	0.025 ± 0.001	0.147 ± 0.004	0.108 ± 0.004	8.85 ± 0.15

Table E5: continued from previous page

	T	$\tilde{m}_{EvA34}$	$\tilde{m}_{HCl}$	$\tilde{m}_{NaOH}$	pK
	K	mol_{EvA34}/kg_{H_2O}	mol_{HCl}/kg_{H_2O}	mol_{NaOH}/kg_{H_2O}	
pK_δ	352.6	0.026 ± 0.001	0.144 ± 0.007	0.103 ± 0.008	8.50 ± 0.10
pK_β	293.5	0.033 ± 0.001	0.150 ± 0.008	0.067 ± 0.008	8.25 ± 0.13
	313.1	0.029 ± 0.003	0.147 ± 0.006	0.074 ± 0.002	7.75 ± 0.15
	333.5	0.026 ± 0.001	0.151 ± 0.004	0.086 ± 0.004	7.45 ± 0.15
	353.0	0.027 ± 0.001	0.147 ± 0.007	0.080 ± 0.009	7.05 ± 0.15
pK_γ	293.4	0.035 ± 0.001	0.155 ± 0.008	0.035 ± 0.009	6.65 ± 0.13
	313.1	0.030 ± 0.003	0.151 ± 0.007	0.047 ± 0.005	6.25 ± 0.15
	333.7	0.026 ± 0.001	0.155 ± 0.004	0.062 ± 0.004	5.85 ± 0.15
	353.3	0.027 ± 0.001	0.151 ± 0.007	0.056 ± 0.009	5.45 ± 0.15

T: temperature with the expanded uncertainty $U(T) = 0.1$ K (0.99 level of confidence) $\tilde{m}_{EvA34}$: molality of EvA34 with the intervals representing the standard uncertainty $u(\tilde{m}_{EvA34})$, $\tilde{m}_{HCl}$: molality of HCl with the intervals representing the standard uncertainty $u(\tilde{m}_{HCl})$, $\tilde{m}_{NaOH}$: molality of NaOH with the intervals representing the standard uncertainty $u(\tilde{m}_{NaOH})$, pK: molal activity based pK-value with the intervals representing the standard uncertainty $u(pK)$. The Greek letter indicates the corresponding amino group as shown in Figure 1. The experiments were performed at ambient pressure, which was $p = 977 ± 20$ mbar.

Table E6: pH-values of the system (EvA34 + H_2O).

T	$\tilde{m}_{EvA34}$	pH
K	mol_{EvA34}/kg_{H_2O}	
298.15	0.004	11.31 ± 0.18
	0.010	11.64 ± 0.11
	0.018	11.74 ± 0.12
	0.034	11.89 ± 0.13
	0.067	12.08 ± 0.15
	0.134	12.21 ± 0.11
	0.377	12.40 ± 0.13
	0.838	12.61 ± 0.11
	2.234	12.98 ± 0.14
313.15	0.004	10.79 ± 0.16
	0.010	11.13 ± 0.12
	0.018	11.18 ± 0.11
	0.034	11.32 ± 0.14
	0.067	11.51 ± 0.17
	0.134	11.72 ± 0.10
	0.377	11.89 ± 0.13
	0.838	12.08 ± 0.10
	2.234	12.44 ± 0.12
353.15	0.004	9.87 ± 0.13
	0.010	10.14 ± 0.14

Table E6: continued from previous page

T	$\tilde{m}_{EvA34}$	pH
K	mol_{EvA34}/kg_{H_2O}	
	0.018	10.27 ± 0.10
	0.034	10.41 ± 0.13
	0.067	10.64 ± 0.11
353.15	0.134	10.76 ± 0.13
	0.377	10.92 ± 0.12
	0.838	10.97 ± 0.11
	2.234	11.33 ± 0.13
	0.004	9.13 ± 0.18
	0.010	9.38 ± 0.19
	0.018	9.55 ± 0.10
	0.034	9.71 ± 0.14
393.15	0.067	9.80 ± 0.13
	0.134	10.02 ± 0.16
	0.377	10.10 ± 0.12
	0.838	10.22 ± 0.12
	2.234	10.42 ± 0.19

T: temperature with the expanded uncertainty $U(T) = 0.1$ K (0.99 level of confidence), $\tilde{m}_{EvA34}$: molality of EvA34 with the relative expanded uncertainty $U_r(\tilde{m}_{EvA34}) = 0.001$ (0.99 level of confidence), pH: molal activity based pH-value with the intervals representing the standard uncertainty $u(pH)$. The pressure was not measured as it has no significant influence on the measured pH-values.

Table E7: pH-values of the system (EvA34 + H_2O + CO_2).

T	$\tilde{m}_{EvA34}$	$\tilde{m}_{CO_2}$	pH
K	mol_{EvA34}/kg_{H_2O}	mol_{CO_2}/kg_{H_2O}	
	0.373	0	12.33 ± 0.12
	0.373	$0.123^{+0.006}_{-0.000}$	11.03 ± 0.11
	0.375	$0.230^{+0.001}_{-0.001}$	10.58 ± 0.19
293.15	0.373	$0.381^{+0.021}_{-0.001}$	10.17 ± 0.10
	0.371	$0.593^{+0.034}_{-0.002}$	9.55 ± 0.13
	0.375	$0.704^{+0.004}_{-0.004}$	9.28 ± 0.11
	0.380	$0.847^{+0.020}_{-0.004}$	8.70 ± 0.14
	0.374	$0.974^{+0.006}_{-0.006}$	8.40 ± 0.18
	0.373	0	11.18 ± 0.13
	0.373	$0.123^{+0.006}_{-0.000}$	10.06 ± 0.11
	0.375	$0.230^{+0.001}_{-0.001}$	9.75 ± 0.16
333.15	0.373	$0.381^{+0.021}_{-0.001}$	9.36 ± 0.12
	0.371	$0.593^{+0.034}_{-0.001}$	8.79 ± 0.11
	0.375	$0.704^{+0.004}_{-0.004}$	8.60 ± 0.12
	0.380	$0.847^{+0.020}_{-0.003}$	7.98 ± 0.14

Table E7: continued from previous page

T	$\tilde{m}_{\text{EvA34}}$	$\tilde{m}_{\text{CO}_2}$	pH
K	$\text{mol}_{\text{EvA34}}/\text{kg}_{\text{H}_2\text{O}}$	$\text{mol}_{\text{CO}_2}/\text{kg}_{\text{H}_2\text{O}}$	
333.15	0.374	$0.974^{+0.005}_{-0.005}$	7.74 ± 0.16
	0.372	0	10.39 ± 0.10
	0.373	$0.123^{+0.000}_{-0.000}$	9.28 ± 0.13
	0.375	$0.230^{+0.001}_{-0.001}$	9.03 ± 0.11
	0.373	$0.381^{+0.021}_{-0.001}$	8.58 ± 0.12
373.15	0.371	$0.593^{+0.034}_{-0.001}$	8.10 ± 0.15
	0.375	$0.704^{+0.003}_{-0.003}$	7.92 ± 0.18
	0.380	$0.847^{+0.020}_{-0.003}$	7.39 ± 0.15
	0.374	$0.974^{+0.005}_{-0.005}$	7.16 ± 0.11
	2.234	0	12.96 ± 0.20
	2.233	$0.687^{+0.006}_{-0.006}$	11.59 ± 0.15
	2.233	$1.573^{+0.014}_{-0.014}$	11.14 ± 0.12
	2.217	$2.263^{+0.138}_{-0.012}$	10.85 ± 0.11
293.15	2.237	$3.133^{+0.176}_{-0.013}$	10.46 ± 0.14
	2.235	$3.961^{+0.092}_{-0.025}$	9.98 ± 0.14
	2.233	$4.456^{+0.039}_{-0.039}$	9.67 ± 0.13
	2.233	$5.140^{+0.047}_{-0.047}$	9.27 ± 0.14
	2.233	$5.782^{+0.052}_{-0.052}$	8.86 ± 0.12
	2.231	0	11.66 ± 0.19
	2.233	$0.687^{+0.005}_{-0.005}$	10.38 ± 0.12
	2.233	$1.573^{+0.013}_{-0.013}$	9.95 ± 0.11
	2.217	$2.263^{+0.138}_{-0.011}$	9.69 ± 0.15
333.15	2.237	$3.133^{+0.176}_{-0.011}$	9.47 ± 0.12
	2.235	$3.961^{+0.092}_{-0.022}$	9.10 ± 0.11
	2.233	$4.456^{+0.034}_{-0.034}$	8.82 ± 0.12
	2.233	$5.140^{+0.041}_{-0.041}$	8.46 ± 0.15
	2.233	$5.782^{+0.046}_{-0.046}$	8.10 ± 0.14
	2.234	0	10.60 ± 0.15
	2.233	$0.687^{+0.005}_{-0.005}$	9.28 ± 0.12
	2.233	$1.573^{+0.011}_{-0.011}$	8.87 ± 0.11
373.15	2.217	$2.263^{+0.138}_{-0.010}$	8.67 ± 0.12
	2.237	$3.133^{+0.176}_{-0.010}$	8.54 ± 0.13
	2.235	$3.961^{+0.092}_{-0.020}$	8.23 ± 0.15
	2.233	$4.456^{+0.031}_{-0.031}$	7.98 ± 0.16

T: temperature with the expanded uncertainty $U(T) = 0.1$ K (0.99 level of confidence), $\tilde{m}_{\text{EvA34}}$: molality of EvA34 with the relative expanded uncertainty $U_r(\tilde{m}_{\text{EvA34}}) = 0.001$ (0.99 level of confidence), $\tilde{m}_{\text{CO}_2}$: molality of CO_2 with the intervals representing the expanded uncertainty $U(\tilde{m}_{\text{CO}_2})$ (0.99 level of confidence), pH: molal activity based pH-value with the intervals representing the standard uncertainty $u(\text{pH})$. The pressure was not measured as it has no significant influence on the measured pH-values.

Table E8: Loading of CO_2-containing species in the system (EvA34 + H_2O + CO_2).

T	$\tilde{m}_{EvA34}$	$\tilde{\alpha}_i$			
K	mol_{EvA34}/kg_{H_2O}	mol_i/mol_{EvA34}			
		β-carbamate	γ-carbamate	β-γ-dicarbamate	(bi)carbonate
	0.376	0.00 ± 0.03	0.09 ± 0.03	0.00 ± 0.03	0.18 ± 0.03
	0.381	0.00 ± 0.03	0.26 ± 0.03	0.00 ± 0.03	0.25 ± 0.03
	0.381	0.00 ± 0.03	0.49 ± 0.03	0.00 ± 0.03	0.56 ± 0.03
	0.376	0.00 ± 0.03	0.55 ± 0.03	0.00 ± 0.03	0.76 ± 0.04
293.15	0.378	0.02 ± 0.03	0.70 ± 0.04	0.00 ± 0.03	0.95 ± 0.05
	0.378	0.02 ± 0.03	0.81 ± 0.04	0.00 ± 0.03	1.37 ± 0.07
	0.378	0.13 ± 0.03	0.83 ± 0.04	0.00 ± 0.03	1.71 ± 0.09
	0.376	0.07 ± 0.03	0.83 ± 0.04	0.00 ± 0.03	2.19 ± 0.11
	0.376	0.00 ± 0.03	0.07 ± 0.03	0.00 ± 0.03	0.19 ± 0.03
	0.381	0.00 ± 0.03	0.30 ± 0.03	0.00 ± 0.03	0.36 ± 0.03
	0.381	0.00 ± 0.03	0.42 ± 0.03	0.00 ± 0.03	0.61 ± 0.03
	0.376	0.00 ± 0.03	0.54 ± 0.03	0.00 ± 0.03	0.84 ± 0.04
313.15	0.378	0.02 ± 0.03	0.63 ± 0.03	0.00 ± 0.03	0.98 ± 0.05
	0.378	0.03 ± 0.03	0.72 ± 0.04	0.00 ± 0.03	1.44 ± 0.07
	0.378	0.02 ± 0.03	0.73 ± 0.04	0.00 ± 0.03	1.70 ± 0.09
	0.376	0.05 ± 0.03	0.72 ± 0.04	0.00 ± 0.03	2.11 ± 0.11
	0.376	0.00 ± 0.03	0.08 ± 0.03	0.00 ± 0.03	0.18 ± 0.03
	0.381	0.00 ± 0.03	0.18 ± 0.03	0.00 ± 0.03	0.41 ± 0.03
	0.381	0.00 ± 0.03	0.45 ± 0.03	0.00 ± 0.03	0.67 ± 0.03
	0.376	0.05 ± 0.03	0.53 ± 0.03	0.00 ± 0.03	0.79 ± 0.04
333.15	0.378	0.00 ± 0.03	0.57 ± 0.03	0.00 ± 0.03	0.98 ± 0.05
	0.378	0.04 ± 0.03	0.59 ± 0.03	0.00 ± 0.03	1.32 ± 0.07
	0.378	0.05 ± 0.03	0.58 ± 0.03	0.00 ± 0.03	1.88 ± 0.09
	0.376	0.00 ± 0.03	0.62 ± 0.03	0.00 ± 0.03	2.03 ± 0.10
	0.376	0.00 ± 0.05	0.05 ± 0.05	0.00 ± 0.05	0.21 ± 0.05
	0.381	0.00 ± 0.05	0.13 ± 0.05	0.00 ± 0.05	0.37 ± 0.05
	0.381	0.00 ± 0.05	0.33 ± 0.05	0.00 ± 0.05	0.69 ± 0.06
353.15	0.376	0.00 ± 0.05	0.34 ± 0.05	0.00 ± 0.05	0.92 ± 0.07
	0.378	0.00 ± 0.05	0.46 ± 0.05	0.00 ± 0.05	1.11 ± 0.09
	0.378	0.00 ± 0.05	0.56 ± 0.05	0.00 ± 0.05	1.44 ± 0.12
	0.376	0.00 ± 0.05	0.58 ± 0.05	0.00 ± 0.05	1.92 ± 0.15
	2.242	0.00 ± 0.02	0.12 ± 0.02	0.00 ± 0.02	0.03 ± 0.02
	2.242	0.00 ± 0.02	0.29 ± 0.02	0.00 ± 0.02	0.07 ± 0.02
	2.243	0.00 ± 0.02	0.53 ± 0.02	0.00 ± 0.02	0.15 ± 0.02
293.15	2.234	0.04 ± 0.02	0.62 ± 0.02	0.02 ± 0.02	0.26 ± 0.02
	2.234	0.07 ± 0.02	0.75 ± 0.02	0.02 ± 0.02	0.36 ± 0.02
	2.243	0.05 ± 0.02	0.78 ± 0.02	0.05 ± 0.02	0.51 ± 0.02
	2.232	0.05 ± 0.02	0.78 ± 0.02	0.07 ± 0.02	0.88 ± 0.03

Table E8: continued from previous page

T	$\tilde{m}_{\text{EvA34}}$	$\tilde{\alpha}_i$			
K	$\text{mol}_{\text{EvA34}}/\text{kg}_{\text{H}_2\text{O}}$	$\text{mol}_i/\text{mol}_{\text{EvA34}}$			
		β-carbamate	γ-carbamate	β-γ-dicarbamate	(bi)carbonate
293.15	2.232	0.05 ± 0.02	0.80 ± 0.02	0.07 ± 0.02	1.12 ± 0.03
	2.232	0.07 ± 0.02	0.79 ± 0.02	0.06 ± 0.02	1.50 ± 0.05
	2.230	0.05 ± 0.02	0.81 ± 0.02	0.04 ± 0.02	1.79 ± 0.05
	2.230	0.06 ± 0.02	0.81 ± 0.02	0.02 ± 0.02	2.13 ± 0.06
	2.241	0.06 ± 0.02	0.82 ± 0.02	0.02 ± 0.02	2.18 ± 0.07
	2.241	0.06 ± 0.02	0.81 ± 0.02	0.02 ± 0.02	2.40 ± 0.07
313.15	2.242	0.00 ± 0.02	0.12 ± 0.02	0.00 ± 0.02	0.03 ± 0.02
	2.242	0.00 ± 0.02	0.27 ± 0.02	0.00 ± 0.02	0.09 ± 0.02
	2.243	0.01 ± 0.02	0.50 ± 0.02	0.00 ± 0.02	0.15 ± 0.02
	2.234	0.03 ± 0.02	0.59 ± 0.02	0.01 ± 0.02	0.26 ± 0.02
	2.243	0.04 ± 0.02	0.66 ± 0.02	0.01 ± 0.02	0.35 ± 0.02
	2.243	0.04 ± 0.02	0.76 ± 0.02	0.02 ± 0.02	0.59 ± 0.02
	2.234	0.04 ± 0.02	0.77 ± 0.02	0.05 ± 0.02	0.73 ± 0.02
	2.232	0.05 ± 0.02	0.77 ± 0.02	0.04 ± 0.02	0.94 ± 0.03
	2.232	0.05 ± 0.02	0.79 ± 0.02	0.07 ± 0.02	1.11 ± 0.03
	2.232	0.07 ± 0.02	0.79 ± 0.02	0.03 ± 0.02	1.46 ± 0.04
	2.230	0.07 ± 0.02	0.76 ± 0.02	0.02 ± 0.02	1.80 ± 0.05
	2.230	0.08 ± 0.02	0.76 ± 0.02	0.00 ± 0.02	2.18 ± 0.07
333.15	2.242	0.00 ± 0.02	0.12 ± 0.02	0.00 ± 0.02	0.04 ± 0.02
	2.242	0.00 ± 0.02	0.26 ± 0.02	0.00 ± 0.02	0.08 ± 0.02
	2.243	0.00 ± 0.02	0.45 ± 0.02	0.00 ± 0.02	0.18 ± 0.02
	2.234	0.02 ± 0.02	0.55 ± 0.02	0.00 ± 0.02	0.28 ± 0.02
	2.243	0.02 ± 0.02	0.60 ± 0.02	0.00 ± 0.02	0.41 ± 0.02
	2.243	0.03 ± 0.02	0.69 ± 0.02	0.00 ± 0.02	0.60 ± 0.02
	2.234	0.04 ± 0.02	0.74 ± 0.02	0.00 ± 0.02	0.76 ± 0.02
	2.232	0.03 ± 0.02	0.74 ± 0.02	0.03 ± 0.02	0.96 ± 0.03
	2.232	0.03 ± 0.02	0.77 ± 0.02	0.03 ± 0.02	1.23 ± 0.04
	2.232	0.03 ± 0.02	0.75 ± 0.02	0.02 ± 0.02	1.49 ± 0.04
	2.230	0.06 ± 0.02	0.76 ± 0.02	0.01 ± 0.02	1.86 ± 0.06
	2.230	0.04 ± 0.02	0.79 ± 0.02	0.00 ± 0.02	2.11 ± 0.06
353.15	2.242	0.00 ± 0.05	0.10 ± 0.05	0.00 ± 0.05	0.06 ± 0.05
	2.242	0.00 ± 0.05	0.25 ± 0.05	0.00 ± 0.05	0.13 ± 0.05
	2.217	0.00 ± 0.05	0.25 ± 0.05	0.00 ± 0.05	0.15 ± 0.05
	2.243	0.00 ± 0.05	0.45 ± 0.05	0.00 ± 0.05	0.25 ± 0.05
	2.234	0.04 ± 0.05	0.56 ± 0.05	0.00 ± 0.05	0.35 ± 0.05
	2.243	0.03 ± 0.05	0.60 ± 0.05	0.00 ± 0.05	0.48 ± 0.05
	2.243	0.03 ± 0.05	0.70 ± 0.06	0.00 ± 0.05	0.69 ± 0.06
	2.232	0.02 ± 0.05	0.74 ± 0.06	0.00 ± 0.05	1.04 ± 0.08
	2.232	0.03 ± 0.05	0.70 ± 0.06	0.00 ± 0.05	1.48 ± 0.12
	2.230	0.06 ± 0.05	0.75 ± 0.06	0.00 ± 0.05	1.97 ± 0.16

Table E8: continued from previous page

T	$\tilde{m}_{\text{EvA34}}$	$\tilde{\alpha}_i$			
K	$\text{mol}_{\text{EvA34}}/\text{kg}_{\text{H}_2\text{O}}$	$\text{mol}_i/\text{mol}_{\text{EvA34}}$			
		β-carbamate	γ-carbamate	β-γ-dicarbamate	(bi)carbonate
	2.217	0.00 ± 0.05	0.23 ± 0.05	0.00 ± 0.05	0.22 ± 0.05
	2.217	0.00 ± 0.05	0.39 ± 0.05	0.00 ± 0.05	0.30 ± 0.05
373.15	2.237	0.02 ± 0.05	0.48 ± 0.05	0.00 ± 0.05	0.49 ± 0.05
	2.237	0.02 ± 0.05	0.53 ± 0.05	0.00 ± 0.05	0.79 ± 0.06
	2.237	0.00 ± 0.05	0.50 ± 0.05	0.00 ± 0.05	1.19 ± 0.10
	2.217	0.00 ± 0.05	0.18 ± 0.05	0.00 ± 0.05	0.13 ± 0.05
393.15	2.217	0.00 ± 0.05	0.29 ± 0.05	0.00 ± 0.05	0.29 ± 0.05
	2.237	0.00 ± 0.05	0.34 ± 0.05	0.00 ± 0.05	0.49 ± 0.05
	2.237	0.02 ± 0.05	0.37 ± 0.05	0.00 ± 0.05	0.70 ± 0.06

T: temperature with the expanded uncertainty $U(T) = 1$ K (0.99 level of confidence), $\tilde{m}_{\text{EvA34}}$: molality of EvA34 with the relative expanded uncertainty $U_r(\tilde{m}_{\text{EvA34}}) = 0.001$ (0.99 level of confidence), $\tilde{\alpha}_i$: loading of CO_2-containing species (cf. Figure 13) with the intervals representing the standard uncertainty $u(\tilde{\alpha}_i)$. The pressure was not measured as it has no significant influence on the loadings of CO_2-containing species.

Table E9: Density and dynamic viscosity of the system (EvA34 + H_2O).

T	$\tilde{m}_{\text{EvA34}}$	ρ	η
K	$\text{mol}_{\text{EvA34}}/\text{kg}_{\text{H}_2\text{O}}$	g/cm^3	mPa·s
	0	0.998	1.00 ± 0.01
	0.374	1.000	2.09 ± 0.02
	1.114	1.004	7.19 ± 0.07
	2.224	1.005	32.43 ± 0.33
	3.344	1.004	94.59 ± 0.95
	5.008	0.998	298.44 ± 3.14
	7.823	0.987	921.53 ± 9.23
293.15	10.607	0.978	1515.70 ± 16.01
	13.403	0.969	1814.95 ± 18.79
	15.261	0.965	1828.85 ± 19.49
	19.206	0.958	1721.05 ± 17.42
	30.009	0.945	1091.75 ± 11.27
	63.476	0.928	384.81 ± 3.93
	159.133	0.917	148.94 ± 1.56
	pure EvA34	0.907	62.67 ± 0.64
	0	0.996	0.80 ± 0.01
	0.374	0.996	1.56 ± 0.03
303.15	1.114	0.999	4.70 ± 0.05
	2.224	0.998	17.75 ± 0.18
	3.344	0.997	45.43 ± 0.46

Table E9: continued from previous page

T	$\tilde{m}_{\text{EvA34}}$	ρ	η
K	$\text{mol}_{\text{EvA34}}/\text{kg}_{\text{H}_2\text{O}}$	g/cm^3	mPa·s
	5.008	0.991	123.53 ± 1.24
	7.823	0.979	323.15 ± 3.28
	10.607	0.969	483.96 ± 4.87
	13.403	0.961	556.15 ± 5.68
303.15	15.261	0.957	557.58 ± 5.66
	19.206	0.950	527.24 ± 5.28
	30.009	0.937	356.23 ± 3.60
	63.476	0.921	148.12 ± 1.57
	159.133	0.909	66.96 ± 0.71
	pure EvA34	0.899	32.61 ± 0.34
	0	0.992	0.65 ± 0.01
	0.374	0.992	1.23 ± 0.03
	1.114	0.994	3.31 ± 0.05
	2.224	0.991	10.74 ± 0.11
	3.344	0.989	24.52 ± 0.25
	5.008	0.983	58.50 ± 0.60
	7.823	0.971	132.42 ± 1.39
313.15	10.607	0.961	184.36 ± 1.85
	13.403	0.953	204.64 ± 2.15
	15.261	0.948	204.39 ± 2.04
	19.206	0.942	193.94 ± 1.98
	30.009	0.929	138.74 ± 1.42
	63.476	0.913	66.30 ± 0.67
	159.133	0.902	34.22 ± 0.36
	pure EvA34	0.892	18.93 ± 0.19
	0	0.988	0.55 ± 0.01
	0.374	0.988	1.01 ± 0.01
	1.114	0.987	2.48 ± 0.04
	2.224	0.983	7.02 ± 0.07
	3.344	0.981	14.52 ± 0.15
	5.008	0.974	30.91 ± 0.32
	7.823	0.962	61.78 ± 0.62
323.15	10.607	0.952	81.00 ± 0.83
	13.403	0.944	87.54 ± 0.92
	15.261	0.940	87.33 ± 0.88
	19.206	0.934	83.27 ± 0.85
	30.009	0.921	62.60 ± 0.64
	63.476	0.905	33.73 ± 0.34
	159.133	0.894	19.52 ± 0.20
	pure EvA34	0.885	12.02 ± 0.13
333.15	0	0.983	0.47 ± 0.01

Table E9: continued from previous page

T	$\tilde{m}_{\text{EvA34}}$	ρ	η
K	$\text{mol}_{\text{EvA34}}/\text{kg}_{\text{H}_2\text{O}}$	g/cm^3	mPa·s
	0.374	0.982	0.84 ± 0.02
	1.114	0.981	1.90 ± 0.02
	2.224	0.976	4.87 ± 0.05
	3.344	0.973	9.26 ± 0.09
	5.008	0.966	17.87 ± 0.19
	7.823	0.953	32.14 ± 0.33
333.15	10.606	0.944	40.11 ± 0.41
	13.403	0.936	42.56 ± 0.44
	15.261	0.931	42.47 ± 0.43
	19.206	0.925	40.73 ± 0.41
	30.009	0.913	31.98 ± 0.32
	63.476	0.897	19.11 ± 0.20
	159.133	0.887	12.17 ± 0.12
	pure EvA34	0.878	8.18 ± 0.09
	0	0.978	0.40 ± 0.01
	0.374	0.976	0.70 ± 0.03
	1.114	0.974	1.51 ± 0.02
	2.224	0.968	3.54 ± 0.04
	3.344	0.964	6.26 ± 0.06
	5.008	0.957	11.09 ± 0.12
	7.823	0.944	18.29 ± 0.19
343.15	10.607	0.935	22.01 ± 0.23
	13.403	0.927	23.08 ± 0.24
	15.261	0.923	23.01 ± 0.24
	19.206	0.917	22.22 ± 0.23
	30.009	0.904	18.13 ± 0.18
	63.476	0.889	11.83 ± 0.12
	159.133	0.879	8.16 ± 0.09
	pure EvA34	0.870	5.89 ± 0.06
	0	0.972	0.35 ± 0.01
	0.374	0.967	0.61 ± 0.02
	2.224	0.959	2.72 ± 0.09
	3.344	0.955	4.45 ± 0.05
	5.008	0.948	7.32 ± 0.08
	7.823	0.935	11.22 ± 0.12
353.15	10.607	0.926	13.14 ± 0.13
	13.403	0.918	13.67 ± 0.14
	15.261	0.914	13.63 ± 0.14
	19.206	0.908	13.25 ± 0.14
	30.009	0.896	11.20 ± 0.11
	63.476	0.882	7.87 ± 0.08

Table E9: continued from previous page

T	$\tilde{m}_{EvA34}$	ρ	η
K	mol_{EvA34}/kg_{H_2O}	g/cm^3	mPa·s
353.15	159.133	0.872	5.80 ± 0.06
	pure EvA34	0.863	4.43 ± 0.04

T: temperature with the expanded uncertainty $U(T) = 0.1$ K (0.99 level of confidence), $\tilde{m}_{EvA34}$: molality of EvA34 with the relative expanded uncertainty $U_r(\tilde{m}_{EvA34}) = 0.001$ (0.99 level of confidence), ρ: density with the standard uncertainty $u(\rho) = 0.001$ g/cm^3, η: dynamic viscosity with the intervals representing the standard uncertainty $u(\eta)$. The experiments were performed at ambient pressure, which was $p = 977 \pm 20$ mbar.

Table E10: Density and dynamic viscosity of the system (EvA34 + H$_2$O + CO$_2$).

T	$\tilde{m}_{EvA34}$	$\tilde{m}_{CO_2}$	ρ	η
K	mol_{EvA34}/kg_{H_2O}	mol_{CO_2}/kg_{H_2O}	g/cm^3	mPa·s
293.15	0.372	$0.338\ ^{+0.004}_{-0.004}$	1.016	2.10 ± 0.02
	0.372	$0.529\ ^{+0.005}_{-0.005}$	1.022	2.06 ± 0.02
	0.365	$0.771\ ^{+0.017}_{-0.001}$	1.028	1.99 ± 0.02
	0.374	$1.049\ ^{+0.025}_{-0.001}$	1.036	2.01 ± 0.02
303.15	0.372	$0.338\ ^{+0.004}_{-0.004}$	1.013	1.61 ± 0.02
	0.372	$0.529\ ^{+0.005}_{-0.005}$	1.019	1.59 ± 0.02
	0.365	$0.771\ ^{+0.017}_{-0.001}$	1.024	1.55 ± 0.02
	0.374	$1.049\ ^{+0.025}_{-0.001}$	1.032	1.58 ± 0.02
313.15	0.372	$0.338\ ^{+0.004}_{-0.004}$	1.009	1.27 ± 0.01
	0.372	$0.529\ ^{+0.005}_{-0.005}$	1.015	1.27 ± 0.01
	0.365	$0.771\ ^{+0.017}_{-0.001}$	1.020	1.25 ± 0.01
323.15	0.372	$0.338\ ^{+0.004}_{-0.004}$	1.004	1.04 ± 0.01
	0.372	$0.529\ ^{+0.005}_{-0.005}$	1.010	1.04 ± 0.01
	0.365	$0.771\ ^{+0.017}_{-0.001}$	1.016	1.03 ± 0.01
333.15	0.372	$0.338\ ^{+0.004}_{-0.004}$	0.998	0.87 ± 0.01
	0.372	$0.529\ ^{+0.005}_{-0.005}$	1.004	0.88 ± 0.01
343.15	0.372	$0.338\ ^{+0.004}_{-0.004}$	0.992	0.74 ± 0.01
353.15	0.372	$0.338\ ^{+0.004}_{-0.004}$	0.986	0.65 ± 0.02
293.15	2.235	$0.340\ ^{+0.008}_{-0.001}$	1.015	36.22 ± 0.39
	2.246	$1.449\ ^{+0.035}_{-0.003}$	1.044	51.47 ± 0.91
	2.257	$1.976\ ^{+0.042}_{-0.003}$	1.057	56.85 ± 2.35
	2.257	$2.296\ ^{+0.053}_{-0.004}$	1.066	61.79 ± 0.64
	2.257	$2.661\ ^{+0.063}_{-0.005}$	1.073	65.36 ± 0.74
	2.257	$3.113\ ^{+0.072}_{-0.005}$	1.084	68.34 ± 0.72
	2.247	$3.603\ ^{+0.088}_{-0.006}$	1.093	69.55 ± 0.71
	2.239	$4.537\ ^{+0.205}_{-0.011}$	1.109	71.38 ± 0.79
303.15	2.235	$0.340\ ^{+0.008}_{-0.001}$	1.008	19.77 ± 0.21
	2.246	$1.449\ ^{+0.035}_{-0.003}$	1.037	27.60 ± 0.29

Table E10: continued from previous page

T	$\tilde{m}_{\text{EvA34}}$	$\tilde{m}_{\text{CO}_2}$	ρ	η
K	$\text{mol}_{\text{EvA34}}/\text{kg}_{\text{H}_2\text{O}}$	$\text{mol}_{\text{CO}_2}/\text{kg}_{\text{H}_2\text{O}}$	g/cm^3	mPa·s
	2.257	$1.976\ ^{+0.042}_{-0.003}$	1.050	30.99 ± 0.33
	2.257	$2.296\ ^{+0.053}_{-0.004}$	1.059	32.80 ± 0.33
	2.257	$2.661\ ^{+0.063}_{-0.005}$	1.067	34.79 ± 0.36
303.15	2.257	$3.113\ ^{+0.072}_{-0.005}$	1.077	36.70 ± 0.37
	2.247	$3.603\ ^{+0.088}_{-0.006}$	1.086	37.93 ± 0.39
	2.239	$4.537\ ^{+0.205}_{-0.011}$	1.103	40.07 ± 0.41
	2.235	$0.340\ ^{+0.008}_{-0.001}$	1.001	11.91 ± 0.12
	2.246	$1.449\ ^{+0.035}_{-0.003}$	1.030	16.29 ± 0.17
	2.257	$1.976\ ^{+0.042}_{-0.003}$	1.043	18.21 ± 0.19
	2.257	$2.296\ ^{+0.053}_{-0.004}$	1.052	19.26 ± 0.19
313.15	2.257	$2.661\ ^{+0.063}_{-0.005}$	1.060	20.44 ± 0.21
	2.257	$3.113\ ^{+0.072}_{-0.005}$	1.070	21.69 ± 0.23
	2.247	$3.603\ ^{+0.088}_{-0.006}$	1.080	22.65 ± 0.23
	2.239	$4.537\ ^{+0.205}_{-0.011}$	1.097	24.42 ± 0.25
	2.235	$0.340\ ^{+0.008}_{-0.001}$	0.994	7.74 ± 0.08
	2.246	$1.449\ ^{+0.035}_{-0.003}$	1.022	10.42 ± 0.11
	2.257	$1.976\ ^{+0.042}_{-0.003}$	1.036	11.59 ± 0.12
	2.257	$2.296\ ^{+0.053}_{-0.004}$	1.045	12.25 ± 0.13
323.15	2.257	$2.661\ ^{+0.063}_{-0.005}$	1.052	12.99 ± 0.14
	2.257	$3.113\ ^{+0.072}_{-0.005}$	1.063	13.83 ± 0.15
	2.247	$3.603\ ^{+0.088}_{-0.006}$	1.073	14.54 ± 0.16
	2.239	$4.537\ ^{+0.205}_{-0.011}$	1.091	15.95 ± 0.17
	2.235	$0.340\ ^{+0.008}_{-0.001}$	0.986	5.34 ± 0.07
	2.246	$1.449\ ^{+0.035}_{-0.003}$	1.015	7.09 ± 0.08
	2.257	$1.976\ ^{+0.042}_{-0.003}$	1.029	7.84 ± 0.08
	2.257	$2.296\ ^{+0.053}_{-0.004}$	1.037	8.29 ± 0.09
333.15	2.257	$2.661\ ^{+0.063}_{-0.005}$	1.045	8.79 ± 0.09
	2.257	$3.113\ ^{+0.072}_{-0.005}$	1.056	9.38 ± 0.10
	2.247	$3.603\ ^{+0.088}_{-0.006}$	1.066	9.92 ± 0.10
	2.239	$4.537\ ^{+0.205}_{-0.011}$	1.084	11.03 ± 0.13
	2.235	$0.340\ ^{+0.008}_{-0.001}$	0.978	3.87 ± 0.04
	2.257	$1.976\ ^{+0.042}_{-0.003}$	1.021	5.59 ± 0.06
	2.257	$2.296\ ^{+0.053}_{-0.004}$	1.030	5.90 ± 0.06
343.15	2.257	$2.661\ ^{+0.063}_{-0.005}$	1.037	6.26 ± 0.06
	2.257	$3.113\ ^{+0.072}_{-0.005}$	1.048	6.69 ± 0.07
	2.247	$3.603\ ^{+0.088}_{-0.006}$	1.059	7.11 ± 0.07
	2.235	$0.340\ ^{+0.008}_{-0.001}$	0.970	2.90 ± 0.05
	2.257	$1.976\ ^{+0.042}_{-0.003}$	1.013	4.15 ± 0.04
353.15	2.257	$2.296\ ^{+0.053}_{-0.004}$	1.022	4.38 ± 0.05
	2.257	$2.661\ ^{+0.063}_{-0.005}$	1.029	4.64 ± 0.05
	2.257	$3.113\ ^{+0.072}_{-0.005}$	1.041	5.03 ± 0.06

Table E10: continued from previous page

T	$\tilde{m}_{\text{EvA34}}$	$\tilde{m}_{\text{CO}_2}$	ρ	η
K	$\text{mol}_{\text{EvA34}}/\text{kg}_{\text{H}_2\text{O}}$	$\text{mol}_{\text{CO}_2}/\text{kg}_{\text{H}_2\text{O}}$	g/cm^3	mPa·s
353.15	2.247	3.603 $^{+0.088}_{-0.006}$	1.051	5.22 ± 0.12

T: temperature with the expanded uncertainty $U(T) = 0.1$ K (0.99 level of confidence), $\tilde{m}_{\text{EvA34}}$: molality of EvA34 with the relative expanded uncertainty $U_r(\tilde{m}_{\text{EvA34}}) = 0.001$ (0.99 level of confidence), $\tilde{m}_{\text{CO}_2}$: molality of CO$_2$ with the intervals representing the expanded uncertainty $U(\tilde{m}_{\text{CO}_2})$ (0.99 level of confidence), ρ: density with the standard uncertainty $u(\rho) = 0.001$ g/cm^3, η: dynamic viscosity with the intervals representing the standard uncertainty $u(\eta)$. The experiments were performed at ambient pressure, which was $p = 977 \pm 20$ mbar.

Table E11: Liquid heat capacity of the system (EvA34 + H$_2$O).

T	$\tilde{m}_{\text{EvA34}}$	c_p
K	$\text{mol}_{\text{EvA34}}/\text{kg}_{\text{H}_2\text{O}}$	kJ/(kg·K)
	0	4.152 ± 0.062
	0.335 ± 0.001	4.111 ± 0.064
	0.837 ± 0.001	4.100 ± 0.066
298.15	2.230 ± 0.003	3.803 ± 0.058
	5.008 ± 0.003	3.428 ± 0.059
	13.403 ± 0.014	2.957 ± 0.045
	30.009 ± 0.060	2.550 ± 0.044
	pure EvA34	2.049 ± 0.044
	0	4.151 ± 0.064
	0.335 ± 0.001	4.165 ± 0.066
	0.837 ± 0.001	4.135 ± 0.066
308.15	2.230 ± 0.003	3.861 ± 0.060
	5.008 ± 0.003	3.530 ± 0.058
	13.403 ± 0.014	3.039 ± 0.047
	30.009 ± 0.060	2.617 ± 0.044
	pure EvA34	2.090 ± 0.045
	0	4.159 ± 0.064
	0.335 ± 0.001	4.192 ± 0.065
	0.837 ± 0.001	4.150 ± 0.064
318.15	2.230 ± 0.003	3.904 ± 0.060
	5.008 ± 0.003	3.613 ± 0.064
	13.403 ± 0.014	3.122 ± 0.047
	30.009 ± 0.060	2.675 ± 0.044
	pure EvA34	2.122 ± 0.044
	0	4.164 ± 0.065
	0.335 ± 0.001	4.214 ± 0.069
328.15	0.837 ± 0.001	4.159 ± 0.064
	2.230 ± 0.003	3.945 ± 0.060
	5.008 ± 0.003	3.703 ± 0.060

Table E11: continued from previous page

T	$\tilde{m}_{\text{EvA34}}$	c_p
K	$\text{mol}_{\text{EvA34}}/\text{kg}_{\text{H}_2\text{O}}$	kJ/(kg·K)
	13.403 ± 0.014	3.183 ± 0.051
328.15	30.009 ± 0.060	2.732 ± 0.045
	pure EvA34	2.155 ± 0.046
	0	4.167 ± 0.063
	0.335 ± 0.001	4.231 ± 0.069
	0.837 ± 0.001	4.167 ± 0.064
	2.230 ± 0.003	3.985 ± 0.061
338.15	5.008 ± 0.003	3.786 ± 0.057
	13.403 ± 0.014	3.257 ± 0.049
	30.009 ± 0.060	2.790 ± 0.046
	pure EvA34	2.193 ± 0.047
	0	4.175 ± 0.066
	0.335 ± 0.001	4.251 ± 0.073
	0.837 ± 0.001	4.174 ± 0.064
	2.230 ± 0.003	4.026 ± 0.061
348.15	5.008 ± 0.003	3.859 ± 0.059
	13.403 ± 0.014	3.325 ± 0.053
	30.009 ± 0.060	2.851 ± 0.049
	pure EvA34	2.238 ± 0.046

T: temperature with the expanded uncertainty $U(T) = 0.1$ K (0.99 level of confidence), $\tilde{m}_{\text{EvA34}}$: molality of EvA34 with the intervals representing the standard uncertainty $u(\tilde{m}_{\text{EvA34}})$, c_p: liquid heat capacity with the intervals representing the standard uncertainty $u(c_p)$. The pressure inside the pans was not measured as it has no significant influence on the measured c_p values.

Table E12: Vapor pressure of pure EvA34.

T	p^{s}
K	mbar
486.31 ± 0.18	49.94 ± 2.31
482.38 ± 0.23	40.33 ± 2.17
479.55 ± 0.21	29.82 ± 2.01
474.01 ± 0.17	20.11 ± 1.87

T: temperature with the intervals representing the standard uncertainty $u(T)$, p^{s}: vapor pressure of EvA34 with the intervals representing the standard uncertainty $u(p^{\text{s}})$.

Table E13: Density and dynamic viscosity of the system (MDEA + PZ).

T	ρ	η
K	g/cm^3	mPa·s
293.15	1.036	150.46 ± 1.50
303.15	1.029	79.46 ± 0.91
313.15	1.021	45.07 ± 0.56
323.15	1.014	27.24 ± 0.34
333.15	1.006	17.41 ± 0.23
343.15	0.999	11.68 ± 0.18
353.15	0.991	8.18 ± 0.12
363.15	0.983	5.93 ± 0.09

T: temperature with the expanded uncertainty $U(T) = 0.1$ K (0.99 level of confidence), The mass fraction of MDEA in the mixture was $\tilde{w}_{MDEA} = 0.874$ with the relative expanded uncertainty $U_r(\tilde{w}_{MDEA}) = 0.01$ (0.99 level of confidence), ρ: density with the standard uncertainty $u(\rho) = 0.001$ g/cm^3, η: dynamic viscosity with the intervals representing the standard uncertainty $u(\eta)$. The experiments were performed at ambient pressure, which was $p = 977 \pm 20$ mbar.

Table E14: Density and dynamic viscosity of the system (MDEA + PZ + H$_2$O).

T	$\tilde{m}_{MDEA}$	$\tilde{m}_{PZ}$	ρ	η
K	mol$_{MDEA}$/kg$_{H_2O}$	mol$_{PZ}$/kg$_{H_2O}$	g/cm^3	mPa·s
293.15			1.037	7.37 ± 0.07
303.15			1.032	4.92 ± 0.07
313.15			1.026	3.47 ± 0.05
323.15	4.912	1.022	1.019	2.56 ± 0.04
333.15			1.013	1.96 ± 0.04
343.15			1.006	1.54 ± 0.03
353.15			0.998	1.24 ± 0.02

T: temperature with the expanded uncertainty $U(T) = 0.1$ K (0.99 level of confidence), $\tilde{m}_{MDEA}$ molality of MDEA with the relative expanded uncertainty $U_r(\tilde{w}_{MDEA}) = 0.001$ (0.99 level of confidence), $\tilde{m}_{PZ}$ molality of PZ with the relative expanded uncertainty $U_r(\tilde{w}_{PZ}) = 0.001$ (0.99 level of confidence), ρ: density with the standard uncertainty $u(\rho) = 0.001$ g/cm^3, η: dynamic viscosity with the intervals representing the standard uncertainty $u(\eta)$. The experiments were performed at ambient pressure, which was $p = 977 \pm 20$ mbar.

E.3 System (EvA25 + H$_2$O + CO$_2$)

Table E15: Liquidus temperatures of the system (EvA25 + H$_2$O + CO$_2$).

$\tilde{m}_{\text{EvA25}}$	$\tilde{m}_{\text{CO}_2}$	T_{freeze}
mol$_{\text{EvA25}}$/kg$_{\text{H}_2\text{O}}$	mol$_{\text{CO}_2}$/kg$_{\text{H}_2\text{O}}$	K
2.001	2.100	*n.a.*
2.001	2.461	*n.a.*
2.001	2.678	*n.a.*
2.001	2.850	*n.a.*
2.001	2.995	*n.a.*
2.001	3.130	*n.a.*
2.001	3.322	*n.a.*
2.001	3.547	*n.a.*
2.001	3.862	*n.a.*
2.182	2.020	*n.a.*
2.182	2.343	314.2 ± 5.0
2.186	2.370	316.2 ± 3.0
2.182	2.711	320.2 ± 5.0
2.186	2.766	321.2 ± 3.0
2.182	2.911	320.2 ± 5.0
2.186	3.185	*n.a.*
2.182	3.264	*n.a.*
2.182	3.619	*n.a.*
2.186	3.644	*n.a.*
2.277	1.128	*n.a.*
2.277	1.458	*n.a.*
2.277	1.825	*n.a.*
2.277	2.200	316.2 ± 5.0
2.277	2.563	320.7 ± 5.0
2.277	2.579	318.7 ± 3.5
2.277	2.938	323.7 ± 4.5
2.277	2.993	320.7 ± 5.0
2.277	3.286	322.2 ± 5.0
2.277	3.389	*n.a.*
2.277	3.665	*n.a.*
2.277	3.753	325.2 ± 5.0
2.277	4.031	*n.a.*
2.277	4.408	*n.a.*
2.277	4.754	*n.a.*
2.474	0.768	*n.a.*
2.474	1.565	*n.a.*
2.475	1.890	313.7 ± 4.5

Table E15: continued from previous page

$\tilde{m}_{\mathrm{EvA25}}$	$\tilde{m}_{\mathrm{CO_2}}$	T_{freeze}
$\mathrm{mol_{EvA25}/kg_{H_2O}}$	$\mathrm{mol_{CO_2}/kg_{H_2O}}$	K
2.475	2.066	313.7 ± 4.5
2.475	2.133	315.7 ± 3.5
2.475	2.294	316.7 ± 3.5
2.474	2.319	323.2 ± 5.0
2.474	2.379	325.2 ± 5.0
2.475	2.458	322.7 ± 3.5
2.474	2.500	323.2 ± 5.0
2.474	2.594	325.2 ± 3.0
2.474	2.670	331.2 ± 4.0
2.474	2.755	329.7 ± 3.5
2.475	2.815	328.7 ± 4.5
2.475	3.231	330.7 ± 3.5
2.474	3.460	332.7 ± 3.5
2.475	3.619	328.7 ± 4.5
2.474	3.772	333.2 ± 5.0
2.475	3.845	330.7 ± 3.5
2.474	3.995	330.2 ± 5.0
2.474	4.030	328.2 ± 5.0
2.475	4.156	323.2 ± 5.0
2.474	4.189	*n.a.*
2.475	4.508	*n.a.*
2.474	4.726	*n.a.*
2.475	4.780	294.2 ± 5.0
2.475	4.954	*n.a.*
2.475	5.106	*n.a.*
2.475	5.308	*n.a.*
2.474	5.357	*n.a.*
3.035	0.873	*n.a.*
3.035	1.341	*n.a.*
3.035	1.497	*n.a.*
3.037	1.538	*n.a.*
3.037	1.657	292.2 ± 22.0
3.035	1.664	313.2 ± 3.0
3.037	2.060	319.7 ± 3.5
3.035	2.073	318.7 ± 3.5
3.035	2.472	330.2 ± 5.0
3.037	2.479	326.7 ± 4.5
3.037	2.904	331.7 ± 3.5
3.037	3.720	338.7 ± 3.5
3.037	4.155	341.7 ± 3.5
3.035	4.397	342.7 ± 3.5

Table E15: continued from previous page

$\tilde{m}_{\text{EvA25}}$	$\tilde{m}_{\text{CO}_2}$	T_{freeze}
$\text{mol}_{\text{EvA25}}/\text{kg}_{\text{H}_2\text{O}}$	$\text{mol}_{\text{CO}_2}/\text{kg}_{\text{H}_2\text{O}}$	K
3.035	4.990	342.7 ± 3.5
3.035	5.396	342.7 ± 3.5
3.037	5.601	331.7 ± 3.5
3.037	5.797	333.7 ± 3.5
3.035	5.909	*n.a.*
3.037	6.244	337.7 ± 3.5
4.530	1.217	*n.a.*
4.540	1.545	316.7 ± 3.5
4.540	2.085	325.7 ± 3.5
4.530	2.337	328.2 ± 3.0
4.530	3.560	337.7 ± 3.5
4.530	4.745	349.2 ± 4.4
4.530	5.683	348.7 ± 7.5
4.530	6.781	350.5 ± 7.2
4.530	7.290	352.5 ± 7.0
4.540	7.424	353.7 ± 6.5
4.540	7.619	351.7 ± 8.5
8.656	2.127	*n.a.*
8.656	2.666	336.7 ± 4.5
8.656	2.949	338.7 ± 3.5
8.656	3.008	332.7 ± 3.5
8.656	3.553	337.7 ± 5.5
8.656	3.923	344.7 ± 3.5
8.656	4.059	343.7 ± 3.5
8.656	4.783	348.7 ± 3.5
8.656	5.861	351.2 ± 7.1
8.656	6.047	351.2 ± 6.6
8.656	6.109	351.2 ± 6.6
8.656	6.183	351.7 ± 7.5

$\tilde{m}_{\text{EvA25}}$: molality of EvA25 with the relative expanded uncertainty $U_r(\tilde{m}_{\text{EvA25}}) = 0.001$ (0.99 level of confidence), $\tilde{m}_{\text{CO}_2}$: molality of CO_2 with the relative expanded uncertainty $U_r(\tilde{m}_{\text{CO}_2}) = 0.01$ (0.99 level of confidence). T_{freeze}: liquidus temperature with the intervals representing the standard uncertainty $u(T_{\text{freeze}})$. The pressure was not measured as it has no significant influence on the measured freezing point temperatures. [n.a.]no solids were observed in the investigated temperature range.

Table E16: Liquidus temperature of the system ($EvA25 + CO_2$).

$\tilde{\alpha}_{CO_2}$ mol_{CO_2}/mol_{EvA25}	T_{freeze} K
0.014	285.2 ± 15.0
0.048	331.7 ± 13.5
0.065	350.7 ± 7.5
0.130	352.7 ± 9.5
0.148	351.7 ± 10.5
0.192	354.7 ± 9.5
0.238	354.7 ± 11.5
0.273	350.7 ± 17.5

$\tilde{\alpha}_{CO_2}$: CO_2-loading with the relative expanded uncertainty $U_r(\tilde{\alpha}_{CO_2}) = 0.01$ (0.99 level of confidence). T_{freeze}: liquidus temperature with the intervals representing the standard uncertainty $u(T_{freeze})$. The pressure was not measured as it has no significant influence on the measured freezing point temperatures.

Table E17: Liquid-liquid equilibrium of the system ($EvA25 + H_2O$).

	aqueous phase	organic phase
T K	$\tilde{w}_{H_2O}$ g/g	$\tilde{w}_{H_2O}$ g/g
342.30 ± 0.11	0.776 ± 0.014	0.554 ± 0.016
343.19 ± 0.10	0.855 ± 0.011	0.447 ± 0.012
344.99 ± 0.21	0.876 ± 0.017	0.377 ± 0.013
347.32 ± 0.51	0.918 ± 0.011	0.341 ± 0.029
348.15 ± 0.10	0.920 ± 0.010	0.291 ± 0.028
350.84 ± 0.43	0.931 ± 0.012	0.251 ± 0.067
353.03 ± 0.62	0.943 ± 0.012	0.192 ± 0.035
357.11 ± 0.63	0.952 ± 0.011	0.149 ± 0.033
362.57 ± 0.37	0.962 ± 0.013	0.125 ± 0.025
372.66 ± 0.18	0.973 ± 0.011	0.093 ± 0.020
382.55 ± 0.33	0.979 ± 0.010	0.077 ± 0.022
392.78 ± 0.26	0.981 ± 0.011	0.072 ± 0.041
402.39 ± 0.24	0.984 ± 0.011	0.061 ± 0.022

T: temperature with the intervals representing the standard uncertainty $u(T)$, $\tilde{w}_{H_2O}$: mass fraction of H_2O with the intervals representing the standard uncertainty $u(\tilde{w}_{H_2O})$. The pressure inside the cell was not measured as it has no significant influence on the measured compositions.

Table E18: Liquid-liquid equilibrium of the system ($EvA25 + H_2O + CO_2$).

	aqueous phase		organic phase	
T	$\tilde{w}_{H_2O}$	$\tilde{w}_{CO_2}$	$\tilde{w}_{H_2O}$	$\tilde{w}_{CO_2}$
K	g/g	g/g	g/g	g/g
338.27	0.561 ± 0.010	0.052 ± 0.016	0.203 ± 0.020	0.006 ± 0.017
338.20	0.544 ± 0.010	0.056 ± 0.016	0.161 ± 0.020	0.010 ± 0.017
338.24	0.540 ± 0.010	0.062 ± 0.016	0.147 ± 0.020	0.005 ± 0.017
343.24	0.748 ± 0.010	0.009 ± 0.015	0.404 ± 0.010	0.003 ± 0.016
343.26	0.739 ± 0.010	0.014 ± 0.015	0.267 ± 0.020	0.003 ± 0.016
343.20	0.598 ± 0.010	0.053 ± 0.016	0.174 ± 0.020	0.002 ± 0.017
343.17	0.580 ± 0.010	0.061 ± 0.016	0.152 ± 0.020	0.005 ± 0.017
343.21	0.569 ± 0.010	0.066 ± 0.016	0.134 ± 0.020	0.006 ± 0.017
343.09	0.524 ± 0.010	0.086 ± 0.017	0.152 ± 0.020	0.005 ± 0.017
343.15	0.519 ± 0.010	0.087 ± 0.017	0.146 ± 0.020	0.006 ± 0.017
343.16	0.511 ± 0.010	0.092 ± 0.017	0.125 ± 0.020	0.003 ± 0.017
348.14	0.832 ± 0.010	0.011 ± 0.015	0.266 ± 0.020	0.000 ± 0.016
348.22	0.851 ± 0.010	0.016 ± 0.015	0.194 ± 0.020	0.000 ± 0.017
348.16	0.834 ± 0.010	0.016 ± 0.015	0.185 ± 0.020	0.001 ± 0.017
348.12	0.787 ± 0.010	0.020 ± 0.015	0.272 ± 0.020	0.002 ± 0.016
348.11	0.664 ± 0.010	0.043 ± 0.015	0.182 ± 0.020	0.002 ± 0.017
348.15	0.632 ± 0.010	0.053 ± 0.016	0.142 ± 0.020	0.004 ± 0.017
348.12	0.606 ± 0.010	0.062 ± 0.016	0.138 ± 0.020	0.004 ± 0.017
349.07	0.591 ± 0.010	0.066 ± 0.016	0.119 ± 0.020	0.005 ± 0.017
348.10	0.537 ± 0.010	0.087 ± 0.017	0.102 ± 0.020	0.004 ± 0.017
352.99	0.849 ± 0.010	0.013 ± 0.015	0.214 ± 0.020	0.000 ± 0.017
353.08	0.833 ± 0.010	0.015 ± 0.015	0.171 ± 0.020	0.000 ± 0.017
352.94	0.829 ± 0.010	0.015 ± 0.015	0.203 ± 0.020	0.000 ± 0.017
353.24	0.792 ± 0.010	0.026 ± 0.015	0.149 ± 0.020	0.000 ± 0.017
353.13	0.754 ± 0.010	0.030 ± 0.015	0.190 ± 0.020	0.000 ± 0.017
353.08	0.685 ± 0.010	0.042 ± 0.015	0.138 ± 0.020	0.001 ± 0.017
353.31	0.589 ± 0.010	0.080 ± 0.016	0.142 ± 0.020	0.004 ± 0.017
353.07	0.544 ± 0.010	0.088 ± 0.017	0.086 ± 0.020	0.004 ± 0.017
353.03	0.539 ± 0.010	0.092 ± 0.017	0.080 ± 0.020	0.004 ± 0.017
353.07	0.566 ± 0.010	0.093 ± 0.017	0.131 ± 0.020	0.003 ± 0.017
353.21	0.543 ± 0.010	0.100 ± 0.017	0.074 ± 0.020	0.000 ± 0.017
353.46	0.531 ± 0.010	0.100 ± 0.017	0.074 ± 0.020	0.005 ± 0.017
353.22	0.554 ± 0.010	0.101 ± 0.017	0.075 ± 0.020	0.001 ± 0.017
353.17	0.500 ± 0.010	0.113 ± 0.017	0.060 ± 0.020	0.004 ± 0.017
373.22	0.898 ± 0.010	0.013 ± 0.015	0.105 ± 0.020	0.000 ± 0.017
372.96	0.881 ± 0.010	0.014 ± 0.015	0.097 ± 0.020	0.000 ± 0.017
372.44	0.876 ± 0.010	0.017 ± 0.015	0.142 ± 0.020	0.000 ± 0.017
373.03	0.801 ± 0.010	0.024 ± 0.015	0.097 ± 0.020	0.000 ± 0.017

Table E18: continued from previous page

	aqueous phase		organic phase	
T	$\tilde{w}_{H_2O}$	$\tilde{w}_{CO_2}$	$\tilde{w}_{H_2O}$	$\tilde{w}_{CO_2}$
K	g/g	g/g	g/g	g/g
372.90	0.819 ± 0.010	0.028 ± 0.015	0.129 ± 0.020	0.000 ± 0.017
373.14	0.786 ± 0.010	0.036 ± 0.016	0.121 ± 0.020	0.000 ± 0.017
373.17	0.755 ± 0.010	0.042 ± 0.016	0.147 ± 0.020	0.000 ± 0.017
373.11	0.738 ± 0.010	0.056 ± 0.017	0.084 ± 0.020	0.001 ± 0.017
373.13	0.634 ± 0.010	0.063 ± 0.016	0.113 ± 0.020	0.003 ± 0.017
373.35	0.614 ± 0.010	0.077 ± 0.016	0.138 ± 0.020	0.005 ± 0.017
373.22	0.581 ± 0.010	0.086 ± 0.017	0.068 ± 0.020	0.005 ± 0.017
373.24	0.557 ± 0.010	0.088 ± 0.017	0.119 ± 0.020	0.005 ± 0.017
373.27	0.542 ± 0.010	0.097 ± 0.017	0.055 ± 0.020	0.001 ± 0.017
373.20	0.497 ± 0.010	0.112 ± 0.017	0.058 ± 0.020	0.018 ± 0.017
393.18	0.914 ± 0.010	0.013 ± 0.015	0.100 ± 0.020	0.000 ± 0.017
392.60	0.896 ± 0.010	0.016 ± 0.015	0.133 ± 0.020	0.000 ± 0.017
393.20	0.916 ± 0.010	0.017 ± 0.015	0.095 ± 0.020	0.000 ± 0.017
392.76	0.840 ± 0.010	0.026 ± 0.015	0.119 ± 0.020	0.000 ± 0.017
392.83	0.841 ± 0.010	0.028 ± 0.015	0.136 ± 0.020	0.004 ± 0.017
392.96	0.807 ± 0.010	0.036 ± 0.016	0.119 ± 0.020	0.000 ± 0.017
392.76	0.788 ± 0.010	0.040 ± 0.016	0.139 ± 0.020	0.004 ± 0.017
393.08	0.770 ± 0.010	0.045 ± 0.016	0.123 ± 0.020	0.000 ± 0.017
393.14	0.790 ± 0.010	0.050 ± 0.017	0.061 ± 0.020	0.000 ± 0.017
393.14	0.668 ± 0.010	0.065 ± 0.016	0.126 ± 0.020	0.008 ± 0.017
393.22	0.662 ± 0.010	0.070 ± 0.016	0.064 ± 0.020	0.002 ± 0.017
393.19	0.613 ± 0.010	0.076 ± 0.016	0.064 ± 0.020	0.003 ± 0.017
393.16	0.593 ± 0.010	0.091 ± 0.017	0.075 ± 0.020	0.002 ± 0.017
393.14	0.567 ± 0.010	0.098 ± 0.017	0.064 ± 0.020	0.001 ± 0.017
393.17	0.539 ± 0.010	0.106 ± 0.017	0.070 ± 0.020	0.009 ± 0.017

T: temperature with the expanded uncertainty $U(T) = 0.1$ K (0.99 level of confidence), $\tilde{w}_{H_2O}$: mass fraction of H_2O with the intervals representing the standard uncertainty $u(\tilde{w}_{H_2O})$, $\tilde{w}_{CO_2}$: mass fraction of CO_2 with the intervals representing the standard uncertainty $u(\tilde{w}_{CO_2})$. The pressure inside the cell was not measured as it has no significant influence on the measured compositions.

Table E19: CO_2-solubility in the system (EvA25 + H_2O + CO_2) in the low pressure region.

T	$\tilde{m}_{EvA25}$	$\tilde{m}_{CO_2}$	p_{CO_2}
K	mol_{EvA25}/kg_{H_2O}	mol_{CO_2}/kg_{H_2O}	mbar
313.16	0.685	$1.018\,^{+0.028}_{-0.006}$	27.14 ± 0.21
313.16	0.680	$1.095\,^{+0.027}_{-0.006}$	43.34 ± 0.36
313.16	0.668	$1.147\,^{+0.020}_{-0.001}$	61.60 ± 0.97
313.16	0.668	$1.230\,^{+0.026}_{-0.004}$	112.65 ± 1.62

Table E19: continued from previous page

T	$\tilde{m}_{\text{EvA25}}$	$\tilde{m}_{\text{CO}_2}$	p_{CO_2}
K	$\text{mol}_{\text{EvA25}}/\text{kg}_{\text{H}_2\text{O}}$	$\text{mol}_{\text{CO}_2}/\text{kg}_{\text{H}_2\text{O}}$	mbar
313.17	0.668	$1.269\ ^{+0.030}_{-0.006}$	161.19 ± 3.66
313.19	0.694	$1.365\ ^{+0.033}_{-0.006}$	301.79 ± 7.92
313.20	0.694	$1.387\ ^{+0.033}_{-0.006}$	375.75 ± 15.45
313.14	0.681	$1.411\ ^{+0.032}_{-0.006}$	539.16 ± 15.62
313.16	0.680	$1.419\ ^{+0.047}_{-0.013}$	569.21 ± 30.18
313.16	0.680	$1.424\ ^{+0.036}_{-0.008}$	636.08 ± 11.43
353.16	0.681	$0.277\ ^{+0.006}_{-0.001}$	24.24 ± 0.56
353.16	0.681	$0.427\ ^{+0.010}_{-0.001}$	41.14 ± 0.94
353.16	0.681	$0.554\ ^{+0.015}_{-0.003}$	58.66 ± 0.70
353.19	0.678	$0.669\ ^{+0.015}_{-0.002}$	87.86 ± 2.31
353.19	0.678	$0.837\ ^{+0.020}_{-0.003}$	154.20 ± 2.35
353.17	0.678	$0.967\ ^{+0.023}_{-0.004}$	252.08 ± 3.13
353.19	0.678	$1.078\ ^{+0.025}_{-0.004}$	418.01 ± 3.80
353.20	0.685	$1.175\ ^{+0.028}_{-0.005}$	675.94 ± 9.30
353.19	0.678	$1.232\ ^{+0.025}_{-0.003}$	1101.39 ± 14.48
393.16	0.694	$0.097\ ^{+0.002}_{-0.000}$	95.71 ± 3.54
393.15	0.690	$0.144\ ^{+0.003}_{-0.000}$	165.71 ± 4.77
393.15	0.685	$0.186\ ^{+0.004}_{-0.001}$	245.38 ± 5.30
393.14	0.690	$0.246\ ^{+0.006}_{-0.001}$	354.76 ± 5.99
393.15	0.685	$0.291\ ^{+0.007}_{-0.001}$	439.77 ± 20.94
393.14	0.685	$0.330\ ^{+0.008}_{-0.001}$	542.28 ± 8.50
393.15	0.690	$0.350\ ^{+0.008}_{-0.001}$	592.71 ± 35.28
393.15	0.690	$0.356\ ^{+0.009}_{-0.001}$	603.52 ± 27.71
393.14	0.690	$0.372\ ^{+0.009}_{-0.001}$	654.66 ± 15.27
393.18	0.694	$0.389\ ^{+0.009}_{-0.001}$	698.91 ± 7.43
313.18	2.022	$2.483\ ^{+0.056}_{-0.013}$	25.14 ± 0.46
313.16	2.022	$3.001\ ^{+0.073}_{-0.019}$	39.88 ± 0.99
313.16	2.022	$3.050\ ^{+0.071}_{-0.017}$	42.08 ± 0.70
313.16	2.026	$3.214\ ^{+0.076}_{-0.019}$	52.94 ± 1.15
313.18	2.022	$3.227\ ^{+0.072}_{-0.016}$	51.41 ± 0.58
313.17	2.022	$3.499\ ^{+0.079}_{-0.018}$	85.12 ± 2.09
313.19	2.006	$3.662\ ^{+0.081}_{-0.018}$	127.02 ± 1.43
313.18	2.006	$3.878\ ^{+0.101}_{-0.029}$	262.00 ± 8.53
313.18	2.006	$3.958\ ^{+0.096}_{-0.024}$	332.39 ± 15.60
313.18	2.006	$4.123\ ^{+0.092}_{-0.020}$	514.35 ± 7.17
313.18	2.006	$4.245\ ^{+0.096}_{-0.022}$	712.30 ± 24.38
353.13	2.004	$0.420\ ^{+0.009}_{-0.002}$	36.38 ± 1.59
353.11	2.004	$0.647\ ^{+0.017}_{-0.004}$	66.34 ± 1.07
353.13	2.004	$0.951\ ^{+0.019}_{-0.003}$	113.64 ± 2.14
353.13	2.004	$1.269\ ^{+0.029}_{-0.006}$	176.83 ± 3.65
353.16	2.026	$1.593\ ^{+0.037}_{-0.008}$	233.90 ± 1.92

Table E19: continued from previous page

T	$\tilde{m}_{\text{EvA25}}$	$\tilde{m}_{\text{CO}_2}$	p_{CO_2}
K	$\text{mol}_{\text{EvA25}}/\text{kg}_{\text{H}_2\text{O}}$	$\text{mol}_{\text{CO}_2}/\text{kg}_{\text{H}_2\text{O}}$	mbar
353.17	2.026	$1.739\ ^{+0.042}_{-0.010}$	259.44 ± 8.81
353.16	2.026	$2.155\ ^{+0.048}_{-0.009}$	391.51 ± 6.14
353.16	2.026	$2.679\ ^{+0.060}_{-0.012}$	518.40 ± 6.76
353.13	2.004	$2.939\ ^{+0.072}_{-0.017}$	683.83 ± 8.58
393.15	2.013	$0.070\ ^{+0.002}_{-0.000}$	59.26 ± 1.37
393.15	2.085	$0.088\ ^{+0.002}_{-0.000}$	78.99 ± 2.74
393.15	2.013	$0.132\ ^{+0.003}_{-0.001}$	144.61 ± 3.18
393.15	2.013	$0.186\ ^{+0.004}_{-0.000}$	247.00 ± 3.43
393.16	2.085	$0.249\ ^{+0.006}_{-0.001}$	359.97 ± 17.50
393.16	2.085	$0.276\ ^{+0.006}_{-0.001}$	419.20 ± 17.03
393.15	2.085	$0.336\ ^{+0.008}_{-0.002}$	539.67 ± 21.51
393.12	2.085	$0.416\ ^{+0.010}_{-0.002}$	707.16 ± 3.10

T: temperature with the expanded uncertainty $U(T) = 0.1$ K (0.99 level of confidence), $\tilde{m}_{\text{EvA25}}$: molality of EvA25 with the relative expanded uncertainty $U_r(\tilde{m}_{\text{EvA25}}) = 0.001$ (0.99 level of confidence), $\tilde{m}_{\text{CO}_2}$: molality of CO_2 with the intervals representing the expanded uncertainty $U(\tilde{m}_{\text{CO}_2})$ (0.99 level of confidence). p_{CO_2}: partial pressure of CO_2 with the intervals representing the standard uncertainty $u(p_{\text{CO}_2})$.

Table E20: CO_2-solubility in the system $(\text{EvA25} + H_2O + CO_2)$ in the high pressure region.

T	$\tilde{m}_{\text{EvA25}}$	$\tilde{m}_{\text{CO}_2}$	p
K	$\text{mol}_{\text{EvA25}}/\text{kg}_{\text{H}_2\text{O}}$	$\text{mol}_{\text{CO}_2}/\text{kg}_{\text{H}_2\text{O}}$	bar
313.13		1.730	4.610 ± 0.145
313.18		1.845	7.823 ± 0.031
313.15		2.083	14.435 ± 0.067
313.19		2.270	22.077 ± 0.048
313.17	0.685	2.392	28.478 ± 0.119
313.13		2.500	32.790 ± 0.054
313.25		2.617	42.453 ± 0.079
313.23		2.743	51.712 ± 0.285
313.09		2.911	66.451 ± 0.326
313.08		2.969	76.496 ± 0.305
353.15		1.397	4.881 ± 0.019
353.16		1.469	7.369 ± 0.047
353.15		1.575	11.736 ± 0.029
353.16	0.685	1.619	14.074 ± 0.040
353.16		1.683	17.213 ± 0.042
353.12		1.732	20.873 ± 0.083
353.20		1.895	30.865 ± 0.044

Table E20: continued from previous page

T	$\tilde{m}_{\mathrm{EvA25}}$	$\tilde{m}_{\mathrm{CO_2}}$	p
K	$\mathrm{mol_{EvA25}/kg_{H_2O}}$	$\mathrm{mol_{CO_2}/kg_{H_2O}}$	bar
353.20		1.996	40.985 ± 0.088
353.07	0.685	2.138	51.570 ± 0.129
353.11		2.259	62.572 ± 0.072
353.17		2.360	74.519 ± 0.190
392.90		1.033	6.309 ± 0.026
393.36		1.163	9.298 ± 0.022
393.05		1.258	13.788 ± 0.027
393.24		1.401	21.385 ± 0.065
393.15		1.470	28.801 ± 0.098
393.19	0.683	1.540	32.936 ± 0.068
393.36		1.603	38.374 ± 0.131
393.17		1.671	49.258 ± 0.170
393.09		1.814	60.099 ± 0.090
393.15		1.903	70.642 ± 0.143
313.30		4.662	3.622 ± 0.024
313.38		5.090	7.528 ± 0.015
313.31		5.262	9.763 ± 0.017
313.33	2.009	5.617	15.699 ± 0.021
313.09		5.736	19.561 ± 0.033
313.36		6.016	31.174 ± 0.038
313.34		6.313	48.736 ± 0.054
313.36		6.592	73.853 ± 0.078
353.42		3.748	3.704 ± 0.109
353.13		4.092	6.387 ± 0.032
353.16		4.228	9.829 ± 0.120
353.14	2.009	4.630	19.879 ± 0.101
353.15		4.793	28.600 ± 0.154
353.15		4.817	30.323 ± 0.162
353.13		5.268	51.674 ± 0.153
353.16		5.527	71.306 ± 0.547
393.20		1.093	4.643 ± 0.035
393.42	2.025	1.412	5.802 ± 0.047
393.39		1.796	7.408 ± 0.111
393.25		2.380	9.900 ± 0.086
393.30		3.060	14.027 ± 0.092
392.92		3.561	18.436 ± 0.047
392.95	2.009	3.825	26.083 ± 0.060
393.28		3.939	32.224 ± 0.100
393.31		4.428	64.485 ± 0.754

Table E20: continued from previous page

T	$\tilde{m}_{\text{EvA25}}$	$\tilde{m}_{\text{CO}_2}$	p
K	$\text{mol}_{\text{EvA25}}/\text{kg}_{\text{H}_2\text{O}}$	$\text{mol}_{\text{CO}_2}/\text{kg}_{\text{H}_2\text{O}}$	bar

T: temperature with the expanded uncertainty $U(T) = 0.1$ K (0.99 level of confidence), $\tilde{m}_{\text{EvA25}}$: molality of EvA25 with the relative expanded uncertainty $U_r(\tilde{m}_{\text{EvA25}}) = 0.001$ (0.99 level of confidence), $\tilde{m}_{\text{CO}_2}$: molality of CO_2 with the relative expanded uncertainty $U_r(\tilde{m}_{\text{CO}_2}) = 0.001$ (0.99 level of confidence). p bubble point pressure with the intervals representing the standard uncertainty $u(p)$.

Table E21: pK-values of EvA25 highly diluted in H_2O.

	T	$\tilde{m}_{\text{EvA25}}$	$\tilde{m}_{\text{HCl}}$	$\tilde{m}_{\text{NaOH}}$	pK
	K	$\text{mol}_{\text{EvA25}}/\text{kg}_{\text{H}_2\text{O}}$	$\text{mol}_{\text{HCl}}/\text{kg}_{\text{H}_2\text{O}}$	$\text{mol}_{\text{NaOH}}/\text{kg}_{\text{H}_2\text{O}}$	
	20.37 ± 0.22	0.033 ± 0.001	0.134 ± 0.002	0.114 ± 0.001	10.90 ± 0.10
	39.95 ± 0.25	0.029 ± 0.002	0.137 ± 0.005	0.118 ± 0.005	10.25 ± 0.15
pK_α	60.35 ± 0.45	0.028 ± 0.004	0.138 ± 0.001	0.120 ± 0.002	9.80 ± 0.20
	79.33 ± 0.33	0.033 ± 0.000	0.142 ± 0.003	0.121 ± 0.002	9.50 ± 0.10
	20.30 ± 0.18	0.034 ± 0.001	0.138 ± 0.002	0.085 ± 0.001	9.80 ± 0.10
	39.95 ± 0.25	0.030 ± 0.002	0.141 ± 0.006	0.093 ± 0.002	9.25 ± 0.15
pK_γ	60.68 ± 0.63	0.029 ± 0.004	0.142 ± 0.000	0.096 ± 0.007	8.75 ± 0.15
	79.85 ± 0.25	0.034 ± 0.000	0.147 ± 0.003	0.093 ± 0.002	8.40 ± 0.10
	20.43 ± 0.15	0.035 ± 0.001	0.143 ± 0.002	0.053 ± 0.001	6.77 ± 0.15
	39.95 ± 0.25	0.031 ± 0.002	0.145 ± 0.006	0.067 ± 0.000	6.35 ± 0.15
pK_β	61.05 ± 0.85	0.030 ± 0.005	0.146 ± 0.000	0.070 ± 0.011	5.90 ± 0.10
	80.25 ± 0.15	0.035 ± 0.000	0.152 ± 0.003	0.062 ± 0.002	5.60 ± 0.10

T: temperature with the intervals representing the standard uncertainty $u(T)$, $\tilde{m}_{\text{EvA25}}$: molality of EvA25 with the intervals representing the standard uncertainty $u(\tilde{m}_{\text{EvA25}})$, $\tilde{m}_{\text{HCl}}$: molality of HCl with the intervals representing the standard uncertainty $u(\tilde{m}_{\text{HCl}})$, $\tilde{m}_{\text{NaOH}}$: molality of NaOH with the intervals representing the standard uncertainty $u(\tilde{m}_{\text{NaOH}})$, p$K$: molal activity based p$K$-value with the intervals representing the standard uncertainty $u(\text{p}K)$. The Greek letter indicates the corresponding amino group as shown in Figure 1. The experiments were performed at ambient pressure, which was $p = 977 \pm 20$ mbar.

Table E22: pH-values of the system (EvA25 + H_2O).

T	$\tilde{m}_{\text{EvA25}}$	pH
K	$\text{mol}_{\text{EvA25}}/\text{kg}_{\text{H}_2\text{O}}$	
	0.0037	11.11 ± 0.14
	0.0111	11.32 ± 0.12
	0.0185	11.52 ± 0.12
298.15	0.0369	11.66 ± 0.14
	0.0744	11.88 ± 0.14
	0.1485	11.96 ± 0.12

Table E22: continued from previous page

T	$\tilde{m}_{\text{EvA25}}$	pH
K	$\text{mol}_{\text{EvA25}}/\text{kg}_{\text{H}_2\text{O}}$	
	0.4124	12.26 ± 0.14
298.15	1.0474	12.46 ± 0.12
	1.9985	12.72 ± 0.14
	0.0037	10.61 ± 0.11
	0.0111	10.87 ± 0.11
	0.0185	11.05 ± 0.14
	0.0369	11.18 ± 0.13
313.15	0.0744	11.37 ± 0.13
	0.1485	11.49 ± 0.12
	0.4124	11.76 ± 0.12
	1.0474	11.91 ± 0.14
	1.9985	12.13 ± 0.13
	0.0037	9.67 ± 0.15
	0.0111	9.95 ± 0.12
353.15	0.0185	10.16 ± 0.15
	0.0369	10.26 ± 0.16
	0.0744	10.48 ± 0.13
	0.1485	10.52 ± 0.15
	0.0037	8.99 ± 0.20
393.15	0.0111	9.24 ± 0.19
	0.0185	9.21 ± 0.12
	0.0369	9.39 ± 0.24

T: temperature with the expanded uncertainty $U(T) = 0.1$ K (0.99 level of confidence), $\tilde{m}_{\text{EvA25}}$: molality of EvA25 with the relative expanded uncertainty $U_r(\tilde{m}_{\text{EvA25}}) = 0.001$ (0.99 level of confidence), pH: molal activity based pH-value with the intervals representing the standard uncertainty $u(\text{pH})$. The pressure was not measured as it has no significant influence on the measured pH-values.

Table E23: pH-values of the system $(\text{EvA25} + \text{H}_2\text{O} + \text{CO}_2)$.

T	$\tilde{m}_{\text{EvA25}}$	$\tilde{m}_{\text{CO}_2}$	pH
K	$\text{mol}_{\text{EvA25}}/\text{kg}_{\text{H}_2\text{O}}$	$\text{mol}_{\text{CO}_2}/\text{kg}_{\text{H}_2\text{O}}$	
	0.419	$0.000 \, ^{+0.000}_{-0.000}$	12.39 ± 0.12
	0.419	$0.177 \, ^{+0.008}_{-0.000}$	10.77 ± 0.11
	0.419	$0.359 \, ^{+0.021}_{-0.001}$	10.22 ± 0.12
293.15	0.412	$0.542 \, ^{+0.000}_{-0.000}$	9.78 ± 0.15
	0.416	$0.558 \, ^{+0.034}_{-0.002}$	9.67 ± 0.10
	0.422	$0.721 \, ^{+0.036}_{-0.001}$	9.14 ± 0.11
	0.416	$0.790 \, ^{+0.045}_{-0.002}$	8.74 ± 0.11
	0.411	$0.912 \, ^{+0.000}_{-0.000}$	7.99 ± 0.15
333.15	0.419	$0.000 \, ^{+0.000}_{-0.000}$	11.00 ± 0.11

Table E23: continued from previous page

T	$\tilde{m}_{\text{EvA25}}$	$\tilde{m}_{\text{CO}_2}$	pH
K	$\text{mol}_{\text{EvA25}}/\text{kg}_{\text{H}_2\text{O}}$	$\text{mol}_{\text{CO}_2}/\text{kg}_{\text{H}_2\text{O}}$	
	0.419	$0.177\ ^{+0.008}_{-0.000}$	9.84 ± 0.12
	0.419	$0.359\ ^{+0.021}_{-0.001}$	9.46 ± 0.11
	0.412	$0.542\ ^{+0.000}_{-0.000}$	9.12 ± 0.15
333.15	0.416	$0.558\ ^{+0.034}_{-0.002}$	9.09 ± 0.24
	0.422	$0.721\ ^{+0.036}_{-0.001}$	8.57 ± 0.12
	0.416	$0.790\ ^{+0.045}_{-0.002}$	8.13 ± 0.16
	0.411	$0.912\ ^{+0.000}_{-0.000}$	7.49 ± 0.15
	0.422	$0.721\ ^{+0.036}_{-0.001}$	7.79 ± 0.19
373.15	0.416	$0.790\ ^{+0.045}_{-0.002}$	7.68 ± 0.16
	0.411	$0.912\ ^{+0.000}_{-0.000}$	7.23 ± 0.15
	0.663	$0.000\ ^{+0.000}_{-0.000}$	12.38 ± 0.11
	0.685	$0.186\ ^{+0.004}_{-0.001}$	11.14 ± 0.10
	0.694	$0.389\ ^{+0.009}_{-0.001}$	10.70 ± 0.14
	0.663	$0.568\ ^{+0.030}_{-0.001}$	10.25 ± 0.15
293.15	0.678	$0.837\ ^{+0.020}_{-0.004}$	9.87 ± 0.15
	0.665	$1.025\ ^{+0.057}_{-0.003}$	9.42 ± 0.14
	0.655	$1.150\ ^{+0.000}_{-0.000}$	9.02 ± 0.15
	0.668	$1.230\ ^{+0.026}_{-0.004}$	8.79 ± 0.10
	0.680	$1.334\ ^{+0.028}_{-0.004}$	8.52 ± 0.19
	0.654	$1.442\ ^{+0.000}_{-0.000}$	8.02 ± 0.15
	0.663	$0.000\ ^{+0.000}_{-0.000}$	11.17 ± 0.19
	0.685	$0.186\ ^{+0.004}_{-0.001}$	10.17 ± 0.10
	0.694	$0.389\ ^{+0.009}_{-0.001}$	9.82 ± 0.12
	0.663	$0.568\ ^{+0.030}_{-0.001}$	9.46 ± 0.15
333.15	0.678	$0.837\ ^{+0.020}_{-0.003}$	9.11 ± 0.17
	0.665	$1.025\ ^{+0.057}_{-0.002}$	8.75 ± 0.14
	0.655	$1.150\ ^{+0.000}_{-0.000}$	8.21 ± 0.15
	0.668	$1.230\ ^{+0.026}_{-0.004}$	8.14 ± 0.10
	0.680	$1.334\ ^{+0.028}_{-0.004}$	7.93 ± 0.18
	0.654	$1.442\ ^{+0.000}_{-0.000}$	7.53 ± 0.15
	0.665	$1.025\ ^{+0.057}_{-0.002}$	7.90 ± 0.22
373.15	0.668	$1.230\ ^{+0.026}_{-0.003}$	7.59 ± 0.15
	0.654	$1.442\ ^{+0.000}_{-0.000}$	7.34 ± 0.15
	2.023	$0.000\ ^{+0.000}_{-0.000}$	12.69 ± 0.12
	2.085	$0.249\ ^{+0.006}_{-0.002}$	11.45 ± 0.10
	2.004	$0.647\ ^{+0.017}_{-0.005}$	11.05 ± 0.16
	2.023	$1.214\ ^{+0.080}_{-0.008}$	10.76 ± 0.16
293.15	2.026	$1.593\ ^{+0.037}_{-0.009}$	10.61 ± 0.20
	1.993	$2.357\ ^{+0.151}_{-0.014}$	10.21 ± 0.11
	2.026	$2.679\ ^{+0.060}_{-0.014}$	10.02 ± 0.10
	2.023	$3.499\ ^{+0.079}_{-0.019}$	9.64 ± 0.17

Table E23: continued from previous page

T	$\tilde{m}_{\text{EvA25}}$	$\tilde{m}_{\text{CO}_2}$	pH
K	$\text{mol}_{\text{EvA25}}/\text{kg}_{\text{H}_2\text{O}}$	$\text{mol}_{\text{CO}_2}/\text{kg}_{\text{H}_2\text{O}}$	
	1.999	$3.860 \, ^{+0.001}_{-0.001}$	9.02 ± 0.15
293.15	2.030	$4.006 \, ^{+0.222}_{-0.014}$	8.87 ± 0.18
	1.998	$4.384 \, ^{+0.001}_{-0.001}$	8.39 ± 0.15
	2.030	$4.812 \, ^{+0.261}_{-0.016}$	7.98 ± 0.16
	2.023	$0.000 \, ^{+0.000}_{-0.000}$	11.02 ± 0.13
	2.085	$0.249 \, ^{+0.006}_{-0.001}$	10.23 ± 0.11
	2.004	$0.647 \, ^{+0.017}_{-0.005}$	9.85 ± 0.13
	2.023	$1.214 \, ^{+0.080}_{-0.007}$	9.59 ± 0.17
	2.026	$1.593 \, ^{+0.037}_{-0.008}$	9.47 ± 0.15
333.15	1.993	$2.357 \, ^{+0.151}_{-0.012}$	9.09 ± 0.22
	2.026	$2.679 \, ^{+0.060}_{-0.012}$	9.07 ± 0.10
	2.023	$3.499 \, ^{+0.079}_{-0.017}$	8.71 ± 0.17
	1.999	$3.860 \, ^{+0.001}_{-0.001}$	8.21 ± 0.15
	2.030	$4.006 \, ^{+0.222}_{-0.013}$	8.10 ± 0.17
	1.998	$4.384 \, ^{+0.001}_{-0.001}$	7.73 ± 0.15
	2.023	$4.812 \, ^{+0.261}_{-0.014}$	7.39 ± 0.17
373.15	2.023	$3.499 \, ^{+0.079}_{-0.015}$	7.78 ± 0.18
	1.998	$4.384 \, ^{+0.001}_{-0.001}$	7.37 ± 0.15

T: temperature with the expanded uncertainty $U(T) = 0.1$ K (0.99 level of confidence), $\tilde{m}_{\text{EvA25}}$: molality of EvA25 with the relative expanded uncertainty $U_r(\tilde{m}_{\text{EvA25}}) = 0.001$ (0.99 level of confidence), $\tilde{m}_{\text{CO}_2}$: molality of CO_2 with the intervals representing the expanded uncertainty $U(\tilde{m}_{\text{CO}_2})$ (0.99 level of confidence), pH: molal activity based pH-value with the intervals representing the standard uncertainty $u(\text{pH})$. The pressure was not measured as it has no significant influence on the measured pH-values.

Table E24: Loading of CO_2-containing species in the system (EvA25 + H_2O + CO_2).

T	$\tilde{m}_{\text{EvA25}}$	$\tilde{\alpha}_i$	
K	$\text{mol}_{\text{EvA25}}/\text{kg}_{\text{H}_2\text{O}}$	$\text{mol}_i/\text{mol}_{\text{EvA25}}$	
		β-carbamate	(bi)carbonate
	0.663	0.02 ± 0.02	0.42 ± 0.02
	0.663	0.07 ± 0.02	0.69 ± 0.02
	0.663	0.09 ± 0.02	0.82 ± 0.02
293.15	0.663	0.19 ± 0.02	1.14 ± 0.03
	0.665	0.25 ± 0.02	1.38 ± 0.04
	0.695	0.29 ± 0.02	1.57 ± 0.05
	0.665	0.29 ± 0.02	2.01 ± 0.06
	0.665	0.24 ± 0.02	2.28 ± 0.07
	0.663	0.02 ± 0.02	0.43 ± 0.02
313.15	0.663	0.07 ± 0.02	0.67 ± 0.02
	0.663	0.09 ± 0.02	0.91 ± 0.03

Table E24: continued from previous page

T	$\tilde{m}_{\text{EvA25}}$	$\tilde{\alpha}_i$	
K	$\text{mol}_{\text{EvA25}}/\text{kg}_{\text{H}_2\text{O}}$	$\text{mol}_i/\text{mol}_{\text{EvA25}}$	
		β-carbamate	(bi)carbonate
	0.663	0.15 ± 0.02	1.20 ± 0.04
	0.665	0.18 ± 0.02	1.46 ± 0.04
313.15	0.695	0.20 ± 0.02	1.60 ± 0.05
	0.665	0.21 ± 0.02	1.94 ± 0.06
	0.665	0.18 ± 0.02	2.24 ± 0.07
	0.663	0.00 ± 0.02	0.39 ± 0.02
	0.663	0.05 ± 0.02	0.76 ± 0.02
	0.663	0.07 ± 0.02	0.86 ± 0.03
333.15	0.663	0.11 ± 0.02	1.27 ± 0.04
	0.665	0.15 ± 0.02	1.50 ± 0.05
	0.695	0.16 ± 0.02	1.71 ± 0.05
	0.665	0.16 ± 0.02	2.09 ± 0.06
	0.665	0.12 ± 0.05	1.58 ± 0.13
	0.655	0.14 ± 0.05	1.81 ± 0.14
353.15	0.665	0.14 ± 0.05	1.94 ± 0.16
	0.665	0.15 ± 0.05	1.97 ± 0.16
	0.654	0.13 ± 0.05	1.94 ± 0.16
	0.655	0.08 ± 0.05	1.67 ± 0.13
	0.665	0.06 ± 0.05	1.70 ± 0.14
373.15	0.665	0.06 ± 0.05	1.60 ± 0.13
	0.654	0.07 ± 0.05	1.89 ± 0.15
	2.023	0.04 ± 0.02	0.25 ± 0.02
	2.023	0.10 ± 0.02	0.52 ± 0.02
	1.993	0.24 ± 0.02	0.97 ± 0.03
	1.993	0.36 ± 0.02	1.24 ± 0.04
293.15	2.030	0.38 ± 0.02	1.62 ± 0.05
	2.030	0.29 ± 0.02	2.15 ± 0.06
	2.008	0.24 ± 0.02	2.44 ± 0.07
	2.008	0.24 ± 0.02	2.40 ± 0.07
	2.023	0.04 ± 0.02	0.26 ± 0.02
	2.023	0.09 ± 0.02	0.53 ± 0.02
313.15	1.993	0.20 ± 0.02	1.04 ± 0.03
	1.993	0.28 ± 0.02	1.37 ± 0.04
	2.030	0.32 ± 0.02	1.69 ± 0.05
	2.030	0.25 ± 0.02	2.16 ± 0.06
	2.023	0.03 ± 0.02	0.26 ± 0.02
	2.023	0.07 ± 0.02	0.53 ± 0.02
333.15	1.993	0.16 ± 0.02	1.06 ± 0.03
	1.993	0.22 ± 0.02	1.35 ± 0.04
	2.030	0.27 ± 0.02	1.75 ± 0.05

Table E24: continued from previous page

T	$\tilde{m}_{\text{EvA25}}$	$\tilde{\alpha}_i$	
K	$\text{mol}_{\text{EvA25}}/\text{kg}_{\text{H}_2\text{O}}$	$\text{mol}_i/\text{mol}_{\text{EvA25}}$	
		β-carbamate	(bi)carbonate
333.15	2.030	0.20 ± 0.02	2.15 ± 0.06
	2.030	0.21 ± 0.05	1.82 ± 0.15
353.15	1.999	0.17 ± 0.05	1.63 ± 0.13
	1.998	0.18 ± 0.05	2.06 ± 0.16
	1.999	0.08 ± 0.05	1.77 ± 0.14
373.15	1.998	0.07 ± 0.05	2.02 ± 0.16

T: temperature with the expanded uncertainty $U(T) = 1$ K (0.99 level of confidence), $\tilde{m}_{\text{EvA25}}$: molality of EvA25 with the relative expanded uncertainty $U_r(\tilde{m}_{\text{EvA25}}) = 0.001$ (0.99 level of confidence), $\tilde{\alpha}_i$: loading of CO_2-containing species (cf. Figure C4) with the intervals representing the standard uncertainty $u(\tilde{\alpha}_i)$. The pressure was not measured as it has no significant influence on the loadings of CO_2-containing species.

Table E25: Density and dynamic viscosity of the system (EvA25 + H_2O).

T	$\tilde{m}_{\text{EvA25}}$	ρ	η
K	$\text{mol}_{\text{EvA25}}/\text{kg}_{\text{H}_2\text{O}}$	g/cm^3	mPa·s
	0.000	998.2	1.00 ± 0.01
	0.680	998.5	2.92 ± 0.03
	2.010	996.3	15.20 ± 0.15
	3.710	990.3	60.35 ± 0.61
293.15	5.551	981.6	151.96 ± 1.53
	8.622	968.9	360.18 ± 3.80
	14.824	952.0	604.30 ± 6.28
	33.179	926.5	392.94 ± 4.12
	pure EvA25	886.1	19.12 ± 0.20
	0.000	995.6	0.80 ± 0.01
	0.680	994.1	2.11 ± 0.02
	2.010	989.4	9.11 ± 0.10
	3.710	982.2	30.07 ± 0.30
303.15	5.551	973.2	65.82 ± 0.67
	8.622	960.3	134.73 ± 1.35
	14.824	943.2	201.69 ± 2.04
	33.179	918.3	136.90 ± 1.38
	pure EvA25	878.7	11.71 ± 0.12
	0.000	992.2	0.65 ± 0.01
	0.680	989.2	1.61 ± 0.02
313.15	2.010	982.2	5.98 ± 0.06
	3.710	973.7	16.76 ± 0.17
	5.551	964.4	32.46 ± 0.33

Table E25: continued from previous page

T	$\tilde{m}_{EvA25}$	ρ	η
K	mol_{EvA25}/kg_{H_2O}	g/cm^3	mPa·s
	8.622	951.4	58.56 ± 0.60
	14.824	934.0	80.32 ± 0.83
313.15	33.179	909.6	56.45 ± 0.57
	pure EvA25	871.3	7.77 ± 0.08
	0.000	988.0	0.55 ± 0.01
	0.680	983.6	1.29 ± 0.01
	2.010	974.4	4.20 ± 0.04
	3.710	964.8	10.23 ± 0.11
323.15	5.551	955.2	17.79 ± 0.18
	8.622	942.1	28.86 ± 0.29
	14.824	925.2	36.97 ± 0.38
	33.179	901.2	27.46 ± 0.29
	pure EvA25	863.8	5.44 ± 0.06
	0.000	983.2	0.47 ± 0.01
	0.680	977.3	1.07 ± 0.01
	2.010	965.9	3.13 ± 0.05
	3.710	955.3	6.73 ± 0.07
333.15	5.551	945.4	10.64 ± 0.11
	8.622	932.5	15.78 ± 0.16
	14.824	915.9	19.23 ± 0.19
	33.179	891.1	14.44 ± 0.15
	pure EvA25	856.4	4.04 ± 0.04
	0.000	977.8	0.40 ± 0.01
	8.622	922.3	9.41 ± 0.10
343.15	14.824	906.4	11.07 ± 0.11
	33.179	882.9	8.96 ± 0.09
	pure EvA25	849.0	3.12 ± 0.03
	0.000	971.8	0.35 ± 0.00
353.15	33.179	873.0	5.75 ± 0.06
	pure EvA25	841.6	2.48 ± 0.03
	0.000	965.3	0.31 ± 0.00
363.15	33.179	865.6	4.00 ± 0.04
	pure EvA25	834.3	2.03 ± 0.02

T: temperature with the expanded uncertainty $U(T) = 0.1$ K (0.99 level of confidence), $\tilde{m}_{EvA25}$: molality of EvA25 with the relative expanded uncertainty $U_r(\tilde{m}_{EvA25}) = 0.001$ (0.99 level of confidence), ρ: density with the standard uncertainty $u(\rho) = 0.001$ g/cm^3, η: dynamic viscosity with the intervals representing the standard uncertainty $u(\eta)$. The experiments were performed at ambient pressure, which was $p = 977 \pm 20$ mbar.

Table E26: Density and dynamic viscosity of the system ($EvA25 + H_2O + CO_2$).

T	$\tilde{m}_{EvA25}$	$\tilde{m}_{CO_2}$	ρ	η
K	mol_{EvA25}/kg_{H_2O}	mol_{CO_2}/kg_{H_2O}	g/cm^3	mPa·s
	0.655	$0.366\,^{+0.000}_{-0.000}$	1.015	2.98 ± 0.03
	0.655	$0.642\,^{+0.000}_{-0.000}$	1.025	2.99 ± 0.03
293.15	0.655	$0.839\,^{+0.000}_{-0.000}$	1.031	2.95 ± 0.03
	0.654	$1.090\,^{+0.000}_{-0.000}$	1.036	2.92 ± 0.05
	0.668	$1.269\,^{+0.030}_{-0.006}$	1.039	2.93 ± 0.03
	0.655	$0.366\,^{+0.000}_{-0.000}$	1.011	2.16 ± 0.04
	0.655	$0.642\,^{+0.000}_{-0.000}$	1.021	2.19 ± 0.02
303.15	0.655	$0.839\,^{+0.000}_{-0.000}$	1.027	2.19 ± 0.03
	0.654	$1.090\,^{+0.000}_{-0.000}$	1.032	2.18 ± 0.03
	0.668	$1.269\,^{+0.030}_{-0.006}$	1.036	2.20 ± 0.02
	0.655	$0.366\,^{+0.000}_{-0.000}$	1.006	1.63 ± 0.04
	0.655	$0.642\,^{+0.000}_{-0.000}$	1.015	1.67 ± 0.02
313.15	0.655	$0.839\,^{+0.000}_{-0.000}$	1.022	1.70 ± 0.02
	0.654	$1.090\,^{+0.000}_{-0.000}$	1.027	1.69 ± 0.03
	0.668	$1.269\,^{+0.030}_{-0.006}$	1.031	1.71 ± 0.02
	0.655	$0.366\,^{+0.000}_{-0.000}$	1.000	1.30 ± 0.02
	0.655	$0.642\,^{+0.000}_{-0.000}$	1.011	1.39 ± 0.14
323.15	0.655	$0.839\,^{+0.000}_{-0.000}$	1.015	1.35 ± 0.03
	0.654	$1.090\,^{+0.000}_{-0.000}$	1.022	1.36 ± 0.02
	0.655	$0.366\,^{+0.000}_{-0.000}$	0.993	1.06 ± 0.02
333.15	0.655	$0.642\,^{+0.000}_{-0.000}$	1.003	1.05 ± 0.03
	0.655	$0.839\,^{+0.000}_{-0.000}$	1.009	1.10 ± 0.01
	2.004	$0.420\,^{+0.009}_{-0.002}$	1.012	17.72 ± 0.18
	1.999	$0.755\,^{+0.001}_{-0.001}$	1.026	18.92 ± 0.21
293.15	1.999	$1.635\,^{+0.002}_{-0.002}$	1.049	22.33 ± 0.24
	1.999	$2.387\,^{+0.002}_{-0.002}$	1.068	24.41 ± 0.28
	1.999	$3.298\,^{+0.003}_{-0.003}$	1.085	25.06 ± 0.27
	1.994	$3.805\,^{+0.001}_{-0.001}$	1.094	25.43 ± 0.58
	2.004	$0.420\,^{+0.009}_{-0.002}$	1.005	10.46 ± 0.11
	1.999	$0.755\,^{+0.001}_{-0.001}$	1.018	11.07 ± 0.11
303.15	1.999	$1.635\,^{+0.002}_{-0.002}$	1.042	12.86 ± 0.14
	1.999	$2.387\,^{+0.002}_{-0.002}$	1.061	14.25 ± 0.15
	1.999	$3.298\,^{+0.003}_{-0.003}$	1.079	15.19 ± 0.16
	1.994	$3.805\,^{+0.001}_{-0.001}$	1.089	15.59 ± 0.20
	2.004	$0.420\,^{+0.009}_{-0.002}$	0.997	6.72 ± 0.09
	1.999	$0.755\,^{+0.001}_{-0.001}$	1.010	7.08 ± 0.08
313.15	1.999	$1.635\,^{+0.002}_{-0.002}$	1.034	8.13 ± 0.09
	1.999	$2.387\,^{+0.002}_{-0.002}$	1.053	9.04 ± 0.09
	1.999	$3.298\,^{+0.003}_{-0.003}$	1.073	9.91 ± 0.11

Table E26: continued from previous page

T	$\tilde{m}_{\mathrm{EvA25}}$	$\tilde{m}_{\mathrm{CO_2}}$	ρ	η
K	$\mathrm{mol_{EvA25}/kg_{H_2O}}$	$\mathrm{mol_{CO_2}/kg_{H_2O}}$	$\mathrm{g/cm^3}$	mPa·s
313.15	1.994	$3.805\ ^{+0.001}_{-0.001}$	1.083	10.47 ± 0.17
323.15	2.004	$0.420\ ^{+0.009}_{-0.002}$	0.989	4.66 ± 0.05
	1.999	$0.755\ ^{+0.001}_{-0.001}$	1.002	4.85 ± 0.05
	1.999	$1.635\ ^{+0.002}_{-0.002}$	1.026	5.51 ± 0.07
	1.999	$2.387\ ^{+0.002}_{-0.002}$	1.046	6.15 ± 0.07
	1.999	$3.298\ ^{+0.003}_{-0.003}$	1.066	6.86 ± 0.07
	1.994	$3.805\ ^{+0.001}_{-0.001}$	1.077	7.37 ± 0.17
333.15	2.004	$0.420\ ^{+0.009}_{-0.002}$	0.981	3.42 ± 0.03
	1.999	$0.755\ ^{+0.001}_{-0.001}$	0.993	3.54 ± 0.04
	1.999	$1.635\ ^{+0.002}_{-0.002}$	1.017	3.96 ± 0.05
	1.999	$2.387\ ^{+0.002}_{-0.002}$	1.038	4.42 ± 0.05
	1.999	$3.298\ ^{+0.003}_{-0.003}$	1.059	5.01 ± 0.07

T: temperature with the expanded uncertainty $U(T) = 0.1$ K (0.99 level of confidence), $\tilde{m}_{\mathrm{EvA25}}$: molality of EvA25 with the relative expanded uncertainty $U_r(\tilde{m}_{\mathrm{EvA25}}) = 0.001$ (0.99 level of confidence), $\tilde{m}_{\mathrm{CO_2}}$: molality of CO_2 with the intervals representing the expanded uncertainty $U(\tilde{m}_{\mathrm{CO_2}})$ (0.99 level of confidence), ρ: density with the standard uncertainty $u(\rho) = 0.001$ $\mathrm{g/cm^3}$, η: dynamic viscosity with the intervals representing the standard uncertainty $u(\eta)$. The experiments were performed at ambient pressure, which was $p = 977 \pm 20$ mbar.

Table E27: Liquid heat capacity of the system (EvA25 + H_2O).

T	$\tilde{m}_{\mathrm{EvA25}}$	c_p
K	$\mathrm{mol_{EvA25}/kg_{H_2O}}$	kJ/(kg·K)
298.15	0.000 ± 0.000	4.141 ± 0.065
	2.009 ± 0.000	3.987 ± 0.068
	5.551 ± 0.008	3.430 ± 0.072
	14.824 ± 0.034	2.961 ± 0.076
	pure EvA25	2.198 ± 0.083
308.15	0.000 ± 0.000	4.141 ± 0.067
	2.009 ± 0.000	4.031 ± 0.070
	5.551 ± 0.008	3.517 ± 0.072
	14.824 ± 0.034	3.037 ± 0.069
	pure EvA25	2.287 ± 0.081
318.15	0.000 ± 0.000	4.149 ± 0.067
	2.009 ± 0.000	4.062 ± 0.068
	5.551 ± 0.008	3.604 ± 0.071
	14.824 ± 0.034	3.121 ± 0.065
	pure EvA25	2.351 ± 0.078
328.15	0.000 ± 0.000	4.154 ± 0.067
	2.009 ± 0.000	4.118 ± 0.066

Table E27: continued from previous page

T	$\tilde{m}_{\text{EvA25}}$	c_p
K	$\text{mol}_{\text{EvA25}}/\text{kg}_{\text{H}_2\text{O}}$	kJ/(kg·K)
	5.551 ± 0.008	3.698 ± 0.066
328.15	14.824 ± 0.034	3.198 ± 0.066
	pure EvA25	2.419 ± 0.078
	0.000 ± 0.000	4.157 ± 0.066
	5.551 ± 0.008	3.799 ± 0.072
338.15	14.824 ± 0.034	3.287 ± 0.067
	pure EvA25	2.486 ± 0.071
	0.000 ± 0.000	4.175 ± 0.068
348.15	14.824 ± 0.034	3.366 ± 0.066
	pure EvA25	2.555 ± 0.068

T: temperature with the expanded uncertainty $U(T) = 0.1$ K (0.99 level of confidence), $\tilde{m}_{\text{EvA25}}$: molality of EvA25 with the intervals representing the standard uncertainty $u(\tilde{m}_{\text{EvA25}})$, c_p: liquid heat capacity with the intervals representing the standard uncertainty $u(c_p)$. The pressure inside the pans was not measured as it has no significant influence on the measured c_p values.

Table E28: Vapor pressure of pure EvA25.

T	p^{s}
K	mbar
437.75 ± 0.51	14.85 ± 1.30
443.06 ± 0.36	19.99 ± 1.37
447.97 ± 0.25	25.19 ± 1.45
451.75 ± 0.27	30.11 ± 1.52
455.33 ± 0.27	35.29 ± 1.61
457.72 ± 0.28	40.15 ± 1.78
460.88 ± 0.22	45.16 ± 1.78
463.27 ± 0.22	50.13 ± 1.85

T: temperature with the intervals representing the standard uncertainty $u(T)$, p^{s}: vapor pressure of EvA25 with the intervals representing the standard uncertainty $u(p^{\text{s}})$.

E.4 Speciation in CO_2-loaded aqueous solutions of EvAs

Table E29: Loading of CO_2-containing species in the system (EvA01 + H_2O + CO_2).

T	$\tilde{m}_{EvA}$	$\tilde{\alpha}_i$	
K	mol_{EvA}/kg_{H_2O}	mol_i/mol_{EvA}	
		β-carbamate	(bi)carbonate
	0.723	0.18 ± 0.03	0.14 ± 0.03
	0.725	0.48 ± 0.03	0.25 ± 0.03
	0.725	0.67 ± 0.03	0.32 ± 0.03
293.15	0.730	0.62 ± 0.03	0.52 ± 0.03
	0.723	0.61 ± 0.03	0.62 ± 0.03
	0.723	0.46 ± 0.03	1.04 ± 0.05
	0.725	0.34 ± 0.03	1.29 ± 0.06
	0.723	0.17 ± 0.03	0.12 ± 0.03
	0.725	0.48 ± 0.03	0.28 ± 0.03
	0.725	0.56 ± 0.03	0.36 ± 0.03
313.15	0.730	0.56 ± 0.03	0.52 ± 0.03
	0.723	0.55 ± 0.03	0.70 ± 0.04
	0.730	0.47 ± 0.03	0.90 ± 0.05
	0.725	0.36 ± 0.03	1.19 ± 0.06
	0.723	0.14 ± 0.03	0.19 ± 0.03
	0.725	0.39 ± 0.03	0.32 ± 0.03
333.15	0.725	0.47 ± 0.03	0.47 ± 0.03
	0.730	0.47 ± 0.03	0.59 ± 0.03
	0.730	0.41 ± 0.03	0.86 ± 0.04
353.15	0.723	0.13 ± 0.05	0.10 ± 0.05
	0.725	0.34 ± 0.05	0.37 ± 0.05
353.15	0.730	0.33 ± 0.05	0.66 ± 0.05
	0.723	0.33 ± 0.05	0.69 ± 0.06
	0.723	0.14 ± 0.05	0.15 ± 0.05
373.15	0.725	0.16 ± 0.05	0.39 ± 0.05
	0.725	0.14 ± 0.05	0.56 ± 0.05

T: temperature with the expanded uncertainty $U(T) = 1$ K (0.99 level of confidence), $\tilde{m}_{EvA}$: molality of EvA with the relative expanded uncertainty $U_r(\tilde{m}_{EvA}) = 0.001$ (0.99 level of confidence), $\tilde{\alpha}_i$: concentration of CO_2-containing species with the intervals representing the standard uncertainty $u(\tilde{\alpha}_i)$. The pressure was not measured as it has no significant influence on the speciation of CO_2-containing species.

Table E30: Loading of CO_2-containing species in the system (EvA02 + H_2O + CO_2).

T	$\tilde{m}_{EvA}$	$\tilde{\alpha}_i$		
K	mol_{EvA}/kg_{H_2O}	mol_i/mol_{EvA}		
		β-carbamate	(bi)carbonate	molecular CO_2
	0.536	0.00 ± 0.03	0.35 ± 0.03	0.00 ± 0.03
	0.536	0.00 ± 0.03	0.74 ± 0.04	0.00 ± 0.03
293.15	0.536	0.02 ± 0.03	1.24 ± 0.06	0.00 ± 0.03
	0.536	0.01 ± 0.03	1.58 ± 0.08	0.00 ± 0.03
	0.554	0.00 ± 0.03	1.83 ± 0.09	0.00 ± 0.03
	0.554	0.00 ± 0.03	1.97 ± 0.10	0.03 ± 0.03
	0.536	0.00 ± 0.03	0.30 ± 0.03	0.00 ± 0.03
	0.536	0.00 ± 0.03	0.75 ± 0.04	0.00 ± 0.03
313.15	0.536	0.00 ± 0.03	1.25 ± 0.06	0.00 ± 0.03
	0.536	0.00 ± 0.03	1.59 ± 0.08	0.00 ± 0.03
	0.554	0.00 ± 0.03	1.79 ± 0.09	0.00 ± 0.03
	0.554	0.00 ± 0.03	1.96 ± 0.10	0.05 ± 0.03
	0.536	0.00 ± 0.03	1.19 ± 0.06	0.00 ± 0.03
333.15	0.536	0.00 ± 0.03	1.60 ± 0.08	0.00 ± 0.03
	0.554	0.00 ± 0.03	1.74 ± 0.09	0.03 ± 0.03

T: temperature with the expanded uncertainty $U(T) = 1$ K (0.99 level of confidence), $\tilde{m}_{EvA}$: molality of EvA with the relative expanded uncertainty $U_r(\tilde{m}_{EvA}) = 0.001$ (0.99 level of confidence), $\tilde{\alpha}_i$: concentration of CO_2-containing species with the intervals representing the standard uncertainty $u(\tilde{\alpha}_i)$. The pressure was not measured as it has no significant influence on the speciation of CO_2-containing species.

Table E31: Loading of CO_2-containing species in the system (EvA03 + H_2O + CO_2).

T	$\tilde{m}_{EvA}$	$\tilde{\alpha}_i$		
K	mol_{EvA}/kg_{H_2O}	mol_i/mol_{EvA}		
		β-carbamate	(bi)carbonate	molecular CO_2
	0.468	0.01 ± 0.03	0.32 ± 0.03	0.00 ± 0.03
	0.468	0.05 ± 0.03	0.75 ± 0.04	0.00 ± 0.03
	0.468	0.07 ± 0.03	0.95 ± 0.05	0.00 ± 0.03
293.15	0.468	0.12 ± 0.03	1.31 ± 0.07	0.00 ± 0.03
	0.468	0.21 ± 0.03	1.75 ± 0.09	0.00 ± 0.03
	0.468	0.20 ± 0.03	2.09 ± 0.10	0.00 ± 0.03
	0.468	0.17 ± 0.03	2.28 ± 0.11	0.04 ± 0.03
	0.468	0.00 ± 0.03	0.30 ± 0.03	0.00 ± 0.03
	0.468	0.03 ± 0.03	0.74 ± 0.04	0.00 ± 0.03
313.15	0.468	0.06 ± 0.03	0.94 ± 0.05	0.00 ± 0.03
	0.468	0.10 ± 0.03	1.30 ± 0.07	0.00 ± 0.03
	0.468	0.16 ± 0.03	1.72 ± 0.09	0.00 ± 0.03

Table E31: continued from previous page

T	$\tilde{m}_{\mathrm{EvA}}$	$\tilde{\alpha}_i$		
K	$\mathrm{mol_{EvA}/kg_{H_2O}}$	$\mathrm{mol}_i/\mathrm{mol_{EvA}}$		
		β-carbamate	(bi)carbonate	molecular CO_2
313.15	0.468	0.17 ± 0.03	2.08 ± 0.10	0.00 ± 0.03
	0.468	0.13 ± 0.03	2.25 ± 0.11	0.09 ± 0.03
333.15	0.468	0.00 ± 0.03	0.32 ± 0.03	0.00 ± 0.03
	0.468	0.00 ± 0.03	0.77 ± 0.04	0.00 ± 0.03
	0.468	0.03 ± 0.03	0.96 ± 0.05	0.00 ± 0.03
	0.468	0.07 ± 0.03	1.32 ± 0.07	0.00 ± 0.03
	0.468	0.12 ± 0.03	1.71 ± 0.09	0.00 ± 0.03
	0.468	0.12 ± 0.03	2.13 ± 0.11	0.00 ± 0.03
353.15	0.468	0.00 ± 0.05	0.30 ± 0.05	0.00 ± 0.05
	0.468	0.00 ± 0.05	0.76 ± 0.06	0.00 ± 0.05
	0.468	0.00 ± 0.05	0.98 ± 0.08	0.00 ± 0.05
	0.468	0.00 ± 0.05	1.32 ± 0.11	0.00 ± 0.05
	0.468	0.01 ± 0.05	1.78 ± 0.14	0.00 ± 0.05
373.15	0.468	0.00 ± 0.05	0.31 ± 0.05	0.00 ± 0.05
	0.468	0.00 ± 0.05	0.73 ± 0.06	0.00 ± 0.05
	0.468	0.00 ± 0.05	0.95 ± 0.08	0.00 ± 0.05
	0.468	0.00 ± 0.05	1.34 ± 0.11	0.00 ± 0.05

T: temperature with the expanded uncertainty $U(T) = 1$ K (0.99 level of confidence), $\tilde{m}_{\mathrm{EvA}}$: molality of EvA with the relative expanded uncertainty $U_r(\tilde{m}_{\mathrm{EvA}}) = 0.001$ (0.99 level of confidence), $\tilde{\alpha}_i$: concentration of CO_2-containing species with the intervals representing the standard uncertainty $u(\tilde{\alpha}_i)$. The pressure was not measured as it has no significant influence on the speciation of CO_2-containing species.

Table E32: Loading of CO_2-containing species in the system (EvA04 + H_2O + CO_2).

T	$\tilde{m}_{\mathrm{EvA}}$	$\tilde{\alpha}_i$		
K	$\mathrm{mol_{EvA}/kg_{H_2O}}$	$\mathrm{mol}_i/\mathrm{mol_{EvA}}$		
		β-carbamate	(bi)carbonate	molecular CO_2
293.15	0.556	0.01 ± 0.03	0.55 ± 0.03	0.00 ± 0.03
	0.556	0.01 ± 0.03	0.95 ± 0.05	0.00 ± 0.03
	0.556	0.01 ± 0.03	1.24 ± 0.06	0.00 ± 0.03
	0.556	0.01 ± 0.03	1.49 ± 0.07	0.01 ± 0.03
313.15	0.556	0.00 ± 0.03	0.57 ± 0.03	0.00 ± 0.03
	0.556	0.01 ± 0.03	0.94 ± 0.05	0.00 ± 0.03
	0.556	0.01 ± 0.03	1.25 ± 0.06	0.00 ± 0.03
	0.556	0.01 ± 0.03	1.49 ± 0.07	0.01 ± 0.03
333.15	0.556	0.00 ± 0.03	1.24 ± 0.06	0.00 ± 0.03

Table E32: continued from previous page

T	$\tilde{m}_{\text{EvA}}$	$\tilde{\alpha}_i$		
K	$\text{mol}_{\text{EvA}}/\text{kg}_{\text{H}_2\text{O}}$	$\text{mol}_i/\text{mol}_{\text{EvA}}$		
		β-carbamate	(bi)carbonate	molecular CO_2

T: temperature with the expanded uncertainty $U(T) = 1$ K (0.99 level of confidence), $\tilde{m}_{\text{EvA}}$: molality of EvA with the relative expanded uncertainty $U_r(\tilde{m}_{\text{EvA}}) = 0.001$ (0.99 level of confidence), $\tilde{\alpha}_i$: concentration of CO_2-containing species with the intervals representing the standard uncertainty $u(\tilde{\alpha}_i)$. The pressure was not measured as it has no significant influence on the speciation of CO_2-containing species.

Table E33: Loading of CO_2-containing species in the system (EvA05 + H_2O + CO_2).

T	$\tilde{m}_{\text{EvA}}$	$\tilde{\alpha}_i$		
K	$\text{mol}_{\text{EvA}}/\text{kg}_{\text{H}_2\text{O}}$	$\text{mol}_i/\text{mol}_{\text{EvA}}$		
		β-carbamate	(bi)carbonate	molecular CO_2
	0.525	0.00 ± 0.03	0.48 ± 0.03	0.00 ± 0.03
	0.525	0.02 ± 0.03	0.87 ± 0.04	0.00 ± 0.03
293.15	0.493	0.01 ± 0.03	1.21 ± 0.06	0.00 ± 0.03
	0.525	0.02 ± 0.03	1.60 ± 0.08	0.01 ± 0.03
	0.525	0.00 ± 0.03	0.41 ± 0.03	0.00 ± 0.03
	0.525	0.01 ± 0.03	0.83 ± 0.04	0.00 ± 0.03
313.15	0.493	0.00 ± 0.03	1.19 ± 0.06	0.00 ± 0.03
	0.525	0.02 ± 0.03	1.57 ± 0.08	0.02 ± 0.03
333.15	0.493	0.02 ± 0.03	1.04 ± 0.05	0.00 ± 0.03

T: temperature with the expanded uncertainty $U(T) = 1$ K (0.99 level of confidence), $\tilde{m}_{\text{EvA}}$: molality of EvA with the relative expanded uncertainty $U_r(\tilde{m}_{\text{EvA}}) = 0.001$ (0.99 level of confidence), $\tilde{\alpha}_i$: concentration of CO_2-containing species with the intervals representing the standard uncertainty $u(\tilde{\alpha}_i)$. The pressure was not measured as it has no significant influence on the speciation of CO_2-containing species.

Table E34: Loading of CO_2-containing species in the system (EvA06 + H_2O + CO_2).

T	$\tilde{m}_{\text{EvA}}$	$\tilde{\alpha}_i$		
K	$\text{mol}_{\text{EvA}}/\text{kg}_{\text{H}_2\text{O}}$	$\text{mol}_i/\text{mol}_{\text{EvA}}$		
		β-carbamate	(bi)carbonate	molecular CO_2
	0.517	0.01 ± 0.03	0.34 ± 0.03	0.00 ± 0.03
	0.538	0.04 ± 0.03	0.67 ± 0.03	0.00 ± 0.03
293.15	0.529	0.04 ± 0.03	0.87 ± 0.04	0.00 ± 0.03
	0.538	0.05 ± 0.03	1.19 ± 0.06	0.00 ± 0.03
	0.529	0.04 ± 0.03	1.45 ± 0.07	0.03 ± 0.03
313.15	0.517	0.00 ± 0.03	0.35 ± 0.03	0.00 ± 0.03
	0.538	0.03 ± 0.03	0.74 ± 0.04	0.00 ± 0.03

Table E34: continued from previous page

T	$\tilde{m}_{\text{EvA}}$	$\tilde{\alpha}_i$		
K	$\text{mol}_{\text{EvA}}/\text{kg}_{\text{H}_2\text{O}}$	$\text{mol}_i/\text{mol}_{\text{EvA}}$		
		β-carbamate	(bi)carbonate	molecular CO_2
	0.529	0.04 ± 0.03	0.90 ± 0.05	0.00 ± 0.03
313.15	0.538	0.04 ± 0.03	1.15 ± 0.06	0.00 ± 0.03
	0.517	0.02 ± 0.03	1.52 ± 0.08	0.06 ± 0.03
	0.529	0.00 ± 0.03	1.59 ± 0.08	0.09 ± 0.03
	0.517	0.00 ± 0.03	0.33 ± 0.03	0.00 ± 0.03
	0.538	0.03 ± 0.03	0.77 ± 0.04	0.00 ± 0.03
333.15	0.529	0.02 ± 0.03	0.87 ± 0.04	0.00 ± 0.03
	0.538	0.02 ± 0.03	1.25 ± 0.06	0.00 ± 0.03
	0.517	0.02 ± 0.03	1.32 ± 0.07	0.10 ± 0.03
	0.529	0.01 ± 0.03	1.35 ± 0.07	0.12 ± 0.03
	0.517	0.00 ± 0.05	0.36 ± 0.05	0.00 ± 0.05
	0.538	0.00 ± 0.05	0.73 ± 0.06	0.00 ± 0.05
353.15	0.538	0.00 ± 0.05	1.09 ± 0.09	0.00 ± 0.05
	0.529	0.00 ± 0.05	1.21 ± 0.10	0.18 ± 0.05
	0.517	0.00 ± 0.05	1.27 ± 0.10	0.23 ± 0.05
	0.517	0.00 ± 0.05	0.23 ± 0.05	0.00 ± 0.05
373.15	0.517	0.00 ± 0.05	0.73 ± 0.06	0.00 ± 0.05
	0.529	0.00 ± 0.05	1.05 ± 0.08	0.18 ± 0.05

T: temperature with the expanded uncertainty $U(T) = 1$ K (0.99 level of confidence), $\tilde{m}_{\text{EvA}}$: molality of EvA with the relative expanded uncertainty $U_r(\tilde{m}_{\text{EvA}}) = 0.001$ (0.99 level of confidence), $\tilde{\alpha}_i$: concentration of CO_2-containing species with the intervals representing the standard uncertainty $u(\tilde{\alpha}_i)$. The pressure was not measured as it has no significant influence on the speciation of CO_2-containing species.

Table E35: Loading of CO_2-containing species in the system (EvA07 + H_2O + CO_2).

T	$\tilde{m}_{\text{EvA}}$	$\tilde{\alpha}_i$		
K	$\text{mol}_{\text{EvA}}/\text{kg}_{\text{H}_2\text{O}}$	$\text{mol}_i/\text{mol}_{\text{EvA}}$		
		β-carbamate	(bi)carbonate	molecular CO_2
	0.540	0.02 ± 0.03	0.33 ± 0.03	0.00 ± 0.03
	0.540	0.04 ± 0.03	0.74 ± 0.04	0.00 ± 0.03
293.15	0.540	0.12 ± 0.03	1.06 ± 0.05	0.00 ± 0.03
	0.540	0.18 ± 0.03	1.33 ± 0.07	0.00 ± 0.03
	0.540	0.28 ± 0.03	1.81 ± 0.09	0.00 ± 0.03
	0.540	0.30 ± 0.03	1.94 ± 0.10	0.06 ± 0.03
	0.540	0.00 ± 0.03	0.34 ± 0.03	0.00 ± 0.03
313.15	0.540	0.04 ± 0.03	0.75 ± 0.04	0.00 ± 0.03
	0.540	0.09 ± 0.03	1.05 ± 0.05	0.00 ± 0.03
	0.540	0.12 ± 0.03	1.39 ± 0.07	0.00 ± 0.03

Table E35: continued from previous page

T	$\tilde{m}_{\mathrm{EvA}}$	$\tilde{\alpha}_i$		
K	$\mathrm{mol}_{\mathrm{EvA}}/\mathrm{kg}_{\mathrm{H_2O}}$	$\mathrm{mol}_i/\mathrm{mol}_{\mathrm{EvA}}$		
		β-carbamate	(bi)carbonate	molecular CO_2
313.15	0.540	0.23 ± 0.03	1.85 ± 0.09	0.00 ± 0.03
	0.540	0.21 ± 0.03	1.91 ± 0.10	0.00 ± 0.03
333.15	0.540	0.00 ± 0.03	0.33 ± 0.03	0.00 ± 0.03
	0.540	0.03 ± 0.03	0.76 ± 0.04	0.00 ± 0.03
	0.540	0.05 ± 0.03	1.06 ± 0.05	0.00 ± 0.03
	0.540	0.08 ± 0.03	1.53 ± 0.08	0.00 ± 0.03
	0.540	0.15 ± 0.03	1.80 ± 0.09	0.00 ± 0.03
	0.540	0.16 ± 0.03	1.96 ± 0.10	0.00 ± 0.03
353.15	0.540	0.00 ± 0.05	0.32 ± 0.05	0.00 ± 0.05
	0.540	0.00 ± 0.05	0.73 ± 0.06	0.00 ± 0.05
	0.540	0.00 ± 0.05	1.00 ± 0.08	0.00 ± 0.05
	0.540	0.00 ± 0.05	1.54 ± 0.12	0.00 ± 0.05
	0.540	0.02 ± 0.05	1.88 ± 0.15	0.00 ± 0.05
373.15	0.540	0.00 ± 0.05	0.29 ± 0.05	0.00 ± 0.05
	0.540	0.00 ± 0.05	0.72 ± 0.06	0.00 ± 0.05
	0.540	0.00 ± 0.05	0.99 ± 0.08	0.00 ± 0.05
	0.540	0.00 ± 0.05	1.50 ± 0.12	0.00 ± 0.05

T: temperature with the expanded uncertainty $U(T) = 1$ K (0.99 level of confidence), $\tilde{m}_{\mathrm{EvA}}$: molality of EvA with the relative expanded uncertainty $U_r(\tilde{m}_{\mathrm{EvA}}) = 0.001$ (0.99 level of confidence), $\tilde{\alpha}_i$: concentration of CO_2-containing species with the intervals representing the standard uncertainty $u(\tilde{\alpha}_i)$. The pressure was not measured as it has no significant influence on the speciation of CO_2-containing species.

Table E36: Loading of CO_2-containing species in the system (EvA21 + H_2O + CO_2).

T	$\tilde{m}_{\mathrm{EvA}}$	$\tilde{\alpha}_i$			
K	$\mathrm{mol}_{\mathrm{EvA}}/\mathrm{kg}_{\mathrm{H_2O}}$	$\mathrm{mol}_i/\mathrm{mol}_{\mathrm{EvA}}$			
		β-carbamate	alkylcarbonate	(bi)carbonate	molecular CO_2
293.15	0.375	0.02 ± 0.03	0.01 ± 0.03	0.55 ± 0.03	0.00 ± 0.03
	0.373	0.02 ± 0.03	0.02 ± 0.03	0.88 ± 0.04	0.00 ± 0.03
	0.356	0.04 ± 0.03	0.04 ± 0.03	1.38 ± 0.07	0.00 ± 0.03
	0.375	0.05 ± 0.03	0.06 ± 0.03	1.50 ± 0.08	0.00 ± 0.03
	0.356	0.06 ± 0.03	0.06 ± 0.03	2.02 ± 0.10	0.06 ± 0.03
313.15	0.375	0.02 ± 0.03	0.02 ± 0.03	0.56 ± 0.03	0.00 ± 0.03
	0.373	0.02 ± 0.03	0.02 ± 0.03	0.94 ± 0.05	0.00 ± 0.03
	0.356	0.05 ± 0.03	0.04 ± 0.03	1.33 ± 0.07	0.00 ± 0.03
	0.375	0.05 ± 0.03	0.04 ± 0.03	1.50 ± 0.08	0.00 ± 0.03
	0.373	0.04 ± 0.03	0.04 ± 0.03	1.88 ± 0.09	0.04 ± 0.03
	0.356	0.04 ± 0.03	0.05 ± 0.03	2.09 ± 0.10	0.04 ± 0.03

Table E36: continued from previous page

T	$\tilde{m}_{EvA}$	$\tilde{\alpha}_i$			
K	mol_{EvA}/kg_{H_2O}	mol_i/mol_{EvA}			
		β-carbamate	alkylcarbonate	(bi)carbonate	molecular CO_2
	0.375	0.00 ± 0.03	0.00 ± 0.03	0.56 ± 0.03	0.00 ± 0.03
	0.373	0.02 ± 0.03	0.02 ± 0.03	0.85 ± 0.04	0.00 ± 0.03
333.15	0.356	0.03 ± 0.03	0.03 ± 0.03	1.46 ± 0.07	0.00 ± 0.03
	0.373	0.02 ± 0.03	0.03 ± 0.03	1.85 ± 0.09	0.03 ± 0.03
	0.356	0.02 ± 0.03	0.03 ± 0.03	1.95 ± 0.10	0.06 ± 0.03
	0.375	0.00 ± 0.05	0.00 ± 0.05	0.55 ± 0.05	0.00 ± 0.05
	0.373	0.01 ± 0.05	0.01 ± 0.05	0.80 ± 0.06	0.00 ± 0.05
353.15	0.356	0.02 ± 0.05	0.02 ± 0.05	1.23 ± 0.10	0.00 ± 0.05
	0.373	0.01 ± 0.05	0.02 ± 0.05	1.67 ± 0.13	0.00 ± 0.05
	0.356	0.01 ± 0.05	0.02 ± 0.05	1.87 ± 0.15	0.00 ± 0.05

T: temperature with the expanded uncertainty $U(T) = 1$ K (0.99 level of confidence), $\tilde{m}_{EvA}$: molality of EvA with the relative expanded uncertainty $U_r(\tilde{m}_{EvA}) = 0.001$ (0.99 level of confidence), $\tilde{\alpha}_i$: concentration of CO_2-containing species with the intervals representing the standard uncertainty $u(\tilde{\alpha}_i)$. The pressure was not measured as it has no significant influence on the speciation of CO_2-containing species.

Table E37: Loading of CO_2-containing species in the system (EvA24 + H_2O + CO_2).

T	$\tilde{m}_{EvA}$	$\tilde{\alpha}_i$		
K	mol_{EvA}/kg_{H_2O}	mol_i/mol_{EvA}		
		β-carbamate	(bi)carbonate	molecular CO_2
	0.409	0.02 ± 0.03	0.48 ± 0.03	0.00 ± 0.03
	0.409	0.04 ± 0.03	0.94 ± 0.05	0.00 ± 0.03
293.15	0.409	0.05 ± 0.03	1.36 ± 0.07	0.00 ± 0.03
	0.409	0.06 ± 0.03	1.88 ± 0.09	0.05 ± 0.03
	0.409	0.01 ± 0.03	0.40 ± 0.03	0.00 ± 0.03
	0.409	0.02 ± 0.03	0.99 ± 0.05	0.00 ± 0.03
313.15	0.409	0.04 ± 0.03	1.55 ± 0.08	0.00 ± 0.03
	0.409	0.05 ± 0.03	1.95 ± 0.10	0.00 ± 0.03
	0.409	0.00 ± 0.03	0.42 ± 0.03	0.00 ± 0.03
333.15	0.409	0.00 ± 0.03	0.80 ± 0.04	0.00 ± 0.03
	0.409	0.00 ± 0.03	1.37 ± 0.07	0.00 ± 0.03
	0.409	0.00 ± 0.05	0.42 ± 0.05	0.00 ± 0.05
353.15	0.409	0.00 ± 0.05	0.68 ± 0.05	0.00 ± 0.05
	0.409	0.00 ± 0.05	1.12 ± 0.09	0.00 ± 0.05

Table E37: continued from previous page

T	$\tilde{m}_{EvA}$	$\tilde{\alpha}_i$		
K	mol_{EvA}/kg_{H_2O}	mol_i/mol_{EvA}		
		β-carbamate	(bi)carbonate	molecular CO_2

T: temperature with the expanded uncertainty $U(T) = 1$ K (0.99 level of confidence), $\tilde{m}_{EvA}$: molality of EvA with the relative expanded uncertainty $U_r(\tilde{m}_{EvA}) = 0.001$ (0.99 level of confidence), $\tilde{\alpha}_i$: concentration of CO_2-containing species with the intervals representing the standard uncertainty $u(\tilde{\alpha}_i)$. The pressure was not measured as it has no significant influence on the speciation of CO_2-containing species.

Table E38: Loading of CO_2-containing species in the system (EvA25 + H_2O + CO_2).

T	$\tilde{m}_{EvA}$	$\tilde{\alpha}_i$		
K	mol_{EvA}/kg_{H_2O}	mol_i/mol_{EvA}		
		β-carbamate	(bi)carbonate	molecular CO_2
	0.419	0.02 ± 0.03	0.44 ± 0.03	0.00 ± 0.03
	0.419	0.06 ± 0.03	0.84 ± 0.04	0.00 ± 0.03
	0.422	0.11 ± 0.03	1.05 ± 0.05	0.00 ± 0.03
	0.416	0.16 ± 0.03	1.29 ± 0.06	0.00 ± 0.03
293.15	0.422	0.15 ± 0.03	1.23 ± 0.06	0.00 ± 0.03
	0.422	0.19 ± 0.03	1.48 ± 0.07	0.00 ± 0.03
	0.416	0.22 ± 0.03	1.76 ± 0.09	0.00 ± 0.03
	0.422	0.21 ± 0.03	2.08 ± 0.10	0.01 ± 0.03
	0.416	0.17 ± 0.03	2.34 ± 0.12	0.08 ± 0.03
	0.419	0.02 ± 0.03	0.41 ± 0.03	0.00 ± 0.03
	0.419	0.04 ± 0.03	0.74 ± 0.04	0.00 ± 0.03
	0.422	0.09 ± 0.03	1.08 ± 0.05	0.00 ± 0.03
	0.416	0.14 ± 0.03	1.36 ± 0.07	0.00 ± 0.03
313.15	0.422	0.13 ± 0.03	1.27 ± 0.06	0.00 ± 0.03
	0.422	0.16 ± 0.03	1.48 ± 0.07	0.00 ± 0.03
	0.416	0.18 ± 0.03	1.70 ± 0.09	0.00 ± 0.03
	0.422	0.17 ± 0.03	2.04 ± 0.10	0.03 ± 0.03
	0.416	0.15 ± 0.03	2.31 ± 0.12	0.08 ± 0.03
	0.419	0.01 ± 0.03	0.43 ± 0.03	0.00 ± 0.03
	0.419	0.03 ± 0.03	0.83 ± 0.04	0.00 ± 0.03
	0.422	0.06 ± 0.03	1.03 ± 0.05	0.00 ± 0.03
	0.416	0.10 ± 0.03	1.39 ± 0.07	0.00 ± 0.03
333.15	0.422	0.12 ± 0.03	1.46 ± 0.07	0.00 ± 0.03
	0.416	0.15 ± 0.03	1.79 ± 0.09	0.00 ± 0.03
	0.422	0.15 ± 0.03	1.99 ± 0.10	0.04 ± 0.03
	0.416	0.13 ± 0.03	2.19 ± 0.11	0.07 ± 0.03
353.15	0.412	0.08 ± 0.05	1.40 ± 0.11	0.00 ± 0.05
	0.422	0.08 ± 0.05	1.46 ± 0.12	0.00 ± 0.05

Table E38: continued from previous page

T	$\tilde{m}_{EvA}$	$\tilde{\alpha}_i$		
K	mol_{EvA}/kg_{H_2O}	mol_i/mol_{EvA}		
		β-carbamate	(bi)carbonate	molecular CO_2
	0.422	0.10 ± 0.05	1.62 ± 0.13	0.00 ± 0.05
353.15	0.411	0.12 ± 0.05	1.80 ± 0.14	0.04 ± 0.05
	0.422	0.12 ± 0.05	2.01 ± 0.16	0.06 ± 0.05
373.15	0.412	0.04 ± 0.05	1.54 ± 0.12	0.02 ± 0.05
	0.422	0.05 ± 0.05	1.81 ± 0.14	0.05 ± 0.05

T: temperature with the expanded uncertainty $U(T) = 1$ K (0.99 level of confidence), $\tilde{m}_{EvA}$: molality of EvA with the relative expanded uncertainty $U_r(\tilde{m}_{EvA}) = 0.001$ (0.99 level of confidence), $\tilde{\alpha}_i$: concentration of CO_2-containing species with the intervals representing the standard uncertainty $u(\tilde{\alpha}_i)$. The pressure was not measured as it has no significant influence on the speciation of CO_2-containing species.

Table E39: Loading of CO_2-containing species in the system (EvA26 + H_2O + CO_2).

T	$\tilde{m}_{EvA}$	$\tilde{\alpha}_i$		
K	mol_{EvA}/kg_{H_2O}	mol_i/mol_{EvA}		
		β-carbamate	(bi)carbonate	molecular CO_2
	0.436	0.05 ± 0.03	0.40 ± 0.03	0.00 ± 0.03
	0.444	0.14 ± 0.03	0.72 ± 0.04	0.00 ± 0.03
	0.444	0.22 ± 0.03	0.85 ± 0.04	0.00 ± 0.03
293.15	0.436	0.29 ± 0.03	1.09 ± 0.05	0.00 ± 0.03
	0.444	0.49 ± 0.03	1.39 ± 0.07	0.00 ± 0.03
	0.436	0.51 ± 0.03	1.52 ± 0.08	0.04 ± 0.03
	0.436	0.53 ± 0.03	1.67 ± 0.08	0.09 ± 0.03
	0.436	0.03 ± 0.03	0.40 ± 0.03	0.00 ± 0.03
	0.444	0.12 ± 0.03	0.77 ± 0.04	0.00 ± 0.03
	0.444	0.18 ± 0.03	0.93 ± 0.05	0.00 ± 0.03
313.15	0.436	0.27 ± 0.03	1.11 ± 0.06	0.00 ± 0.03
	0.444	0.38 ± 0.03	1.49 ± 0.07	0.00 ± 0.03
	0.436	0.43 ± 0.03	1.59 ± 0.08	0.03 ± 0.03
	0.436	0.43 ± 0.03	1.63 ± 0.08	0.09 ± 0.03
	0.436	0.02 ± 0.03	0.36 ± 0.03	0.00 ± 0.03
	0.444	0.09 ± 0.03	0.73 ± 0.04	0.00 ± 0.03
	0.444	0.14 ± 0.03	0.88 ± 0.04	0.00 ± 0.03
333.15	0.436	0.19 ± 0.03	1.11 ± 0.06	0.00 ± 0.03
	0.444	0.30 ± 0.03	1.46 ± 0.07	0.00 ± 0.03
	0.436	0.33 ± 0.03	1.66 ± 0.08	0.02 ± 0.03
	0.436	0.17 ± 0.05	1.13 ± 0.09	0.00 ± 0.05
353.15	0.444	0.21 ± 0.05	1.52 ± 0.12	0.00 ± 0.05
	0.436	0.21 ± 0.05	1.58 ± 0.13	0.00 ± 0.05

Table E39: continued from previous page

T	$\tilde{m}_{\text{EvA}}$	$\tilde{\alpha}_i$		
K	$\text{mol}_{\text{EvA}}/\text{kg}_{\text{H}_2\text{O}}$	$\text{mol}_i/\text{mol}_{\text{EvA}}$		
		β-carbamate	(bi)carbonate	molecular CO_2

T: temperature with the expanded uncertainty $U(T) = 1$ K (0.99 level of confidence), $\tilde{m}_{\text{EvA}}$: molality of EvA with the relative expanded uncertainty $U_r(\tilde{m}_{\text{EvA}}) = 0.001$ (0.99 level of confidence), $\tilde{\alpha}_i$: concentration of CO_2-containing species with the intervals representing the standard uncertainty $u(\tilde{\alpha}_i)$. The pressure was not measured as it has no significant influence on the speciation of CO_2-containing species.

Table E40: Loading of CO_2-containing species in the system (EvA27 + H_2O + CO_2).

T	$\tilde{m}_{\text{EvA}}$	$\tilde{\alpha}_i$			
K	$\text{mol}_{\text{EvA}}/\text{kg}_{\text{H}_2\text{O}}$	$\text{mol}_i/\text{mol}_{\text{EvA}}$			
		β-carbamate	alkylcarbonate	(bi)carbonate	molecular CO_2
293.15	0.498	0.02 ± 0.03	0.01 ± 0.03	0.48 ± 0.03	0.00 ± 0.03
	0.513	0.06 ± 0.03	0.01 ± 0.03	0.79 ± 0.04	0.00 ± 0.03
	0.498	0.05 ± 0.03	0.01 ± 0.03	1.29 ± 0.06	0.01 ± 0.03
	0.513	0.04 ± 0.03	0.00 ± 0.03	1.40 ± 0.07	0.02 ± 0.03
313.15	0.498	0.02 ± 0.03	0.01 ± 0.03	0.48 ± 0.03	0.00 ± 0.03
	0.513	0.04 ± 0.03	0.00 ± 0.03	0.81 ± 0.04	0.00 ± 0.03
	0.498	0.02 ± 0.03	0.00 ± 0.03	1.34 ± 0.07	0.00 ± 0.03
	0.513	0.01 ± 0.03	0.00 ± 0.03	1.43 ± 0.07	0.06 ± 0.03
333.15	0.498	0.00 ± 0.03	0.00 ± 0.03	0.52 ± 0.03	0.00 ± 0.03
	0.513	0.02 ± 0.03	0.00 ± 0.03	0.84 ± 0.04	0.00 ± 0.03
	0.498	0.00 ± 0.03	0.00 ± 0.03	1.29 ± 0.06	0.00 ± 0.03
	0.513	0.00 ± 0.03	0.00 ± 0.03	1.41 ± 0.07	0.07 ± 0.03
353.15	0.498	0.00 ± 0.05	0.00 ± 0.05	0.42 ± 0.05	0.00 ± 0.05
	0.498	0.00 ± 0.05	0.00 ± 0.05	1.29 ± 0.10	0.00 ± 0.05
	0.513	0.00 ± 0.05	0.00 ± 0.05	1.33 ± 0.11	0.10 ± 0.05

T: temperature with the expanded uncertainty $U(T) = 1$ K (0.99 level of confidence), $\tilde{m}_{\text{EvA}}$: molality of EvA with the relative expanded uncertainty $U_r(\tilde{m}_{\text{EvA}}) = 0.001$ (0.99 level of confidence), $\tilde{\alpha}_i$: concentration of CO_2-containing species with the intervals representing the standard uncertainty $u(\tilde{\alpha}_i)$. The pressure was not measured as it has no significant influence on the speciation of CO_2-containing species.

Table E41: Loading of CO_2-containing species in the system (EvA31 + H_2O + CO_2).

T	$\tilde{m}_{EvA}$	$\tilde{\alpha}_i$			
K	mol_{EvA}/kg_{H_2O}	mol_i/mol_{EvA}			
		β-carbamate	alkylcarbonate	(bi)carbonate	molecular CO_2
	0.552	0.04 ± 0.03	0.01 ± 0.03	0.50 ± 0.03	0.00 ± 0.03
	0.552	0.08 ± 0.03	0.01 ± 0.03	0.78 ± 0.04	0.00 ± 0.03
293.15	0.552	0.08 ± 0.03	0.02 ± 0.03	0.97 ± 0.05	0.00 ± 0.03
	0.571	0.07 ± 0.03	0.03 ± 0.03	1.25 ± 0.06	0.00 ± 0.03
	0.552	0.05 ± 0.03	0.03 ± 0.03	1.52 ± 0.08	0.02 ± 0.03
	0.552	0.03 ± 0.03	0.00 ± 0.03	0.48 ± 0.03	0.00 ± 0.03
	0.552	0.07 ± 0.03	0.01 ± 0.03	0.76 ± 0.04	0.00 ± 0.03
313.15	0.552	0.06 ± 0.03	0.02 ± 0.03	0.99 ± 0.05	0.00 ± 0.03
	0.571	0.05 ± 0.03	0.02 ± 0.03	1.28 ± 0.06	0.01 ± 0.03
	0.552	0.04 ± 0.03	0.01 ± 0.03	1.47 ± 0.07	0.05 ± 0.03
	0.552	0.02 ± 0.03	0.01 ± 0.03	0.44 ± 0.03	0.00 ± 0.03
	0.552	0.02 ± 0.03	0.01 ± 0.03	0.86 ± 0.04	0.00 ± 0.03
333.15	0.552	0.02 ± 0.03	0.01 ± 0.03	0.99 ± 0.05	0.00 ± 0.03
	0.571	0.01 ± 0.03	0.02 ± 0.03	1.26 ± 0.06	0.03 ± 0.03
	0.552	0.01 ± 0.03	0.02 ± 0.03	1.36 ± 0.07	0.09 ± 0.03
	0.552	0.00 ± 0.05	0.00 ± 0.05	0.46 ± 0.05	0.00 ± 0.05
	0.552	0.00 ± 0.05	0.00 ± 0.05	0.80 ± 0.06	0.00 ± 0.05
353.15	0.552	0.00 ± 0.05	0.00 ± 0.05	0.96 ± 0.08	0.00 ± 0.05
	0.552	0.00 ± 0.05	0.00 ± 0.05	1.33 ± 0.11	0.01 ± 0.05
	0.571	0.00 ± 0.05	0.00 ± 0.05	1.14 ± 0.09	0.00 ± 0.05
373.15	0.552	0.00 ± 0.05	0.00 ± 0.05	0.40 ± 0.05	0.00 ± 0.05
	0.552	0.00 ± 0.05	0.00 ± 0.05	0.84 ± 0.07	0.00 ± 0.05

T: temperature with the expanded uncertainty $U(T) = 1$ K (0.99 level of confidence), $\tilde{m}_{EvA}$: molality of EvA with the relative expanded uncertainty $U_r(\tilde{m}_{EvA}) = 0.001$ (0.99 level of confidence), $\tilde{\alpha}_i$: concentration of CO_2-containing species with the intervals representing the standard uncertainty $u(\tilde{\alpha}_i)$. The pressure was not measured as it has no significant influence on the speciation of CO_2-containing species.

Table E42: Loading of CO_2-containing species in the system (EvA32 + H_2O + CO_2).

T	$\tilde{m}_{EvA}$	$\tilde{\alpha}_i$		
K	mol_{EvA}/kg_{H_2O}	mol_i/mol_{EvA}		
		β-carbamate	(bi)carbonate	molecular CO_2
	0.444	0.03 ± 0.03	0.38 ± 0.03	0.00 ± 0.03
293.15	0.444	0.03 ± 0.03	0.75 ± 0.04	0.02 ± 0.03
	0.444	0.02 ± 0.03	0.82 ± 0.04	0.08 ± 0.03
313.15	0.444	0.00 ± 0.03	0.17 ± 0.03	0.00 ± 0.03
	0.444	0.00 ± 0.03	0.70 ± 0.04	0.07 ± 0.03

Table E42: continued from previous page

T	$\tilde{m}_{EvA}$	$\tilde{\alpha}_i$		
K	mol_{EvA}/kg_{H_2O}	mol_i/mol_{EvA}		
		β-carbamate	(bi)carbonate	molecular CO_2
313.15	0.444	0.00 ± 0.03	0.76 ± 0.04	0.09 ± 0.03
333.15	0.444	0.00 ± 0.03	0.36 ± 0.03	0.00 ± 0.03
	0.444	0.00 ± 0.03	0.62 ± 0.03	0.10 ± 0.03
	0.444	0.00 ± 0.03	0.67 ± 0.03	0.12 ± 0.03
353.15	0.444	0.00 ± 0.05	0.15 ± 0.05	0.00 ± 0.05
	0.444	0.00 ± 0.05	0.35 ± 0.05	0.00 ± 0.05
	0.444	0.00 ± 0.05	0.56 ± 0.05	0.00 ± 0.05
373.15	0.444	0.00 ± 0.05	0.21 ± 0.05	0.00 ± 0.05
	0.444	0.00 ± 0.05	0.35 ± 0.05	0.00 ± 0.05
	0.444	0.00 ± 0.05	0.37 ± 0.05	0.00 ± 0.05

T: temperature with the expanded uncertainty $U(T) = 1$ K (0.99 level of confidence), $\tilde{m}_{EvA}$: molality of EvA with the relative expanded uncertainty $U_r(\tilde{m}_{EvA}) = 0.001$ (0.99 level of confidence), $\tilde{\alpha}_i$: concentration of CO_2-containing species with the intervals representing the standard uncertainty $u(\tilde{\alpha}_i)$. The pressure was not measured as it has no significant influence on the speciation of CO_2-containing species.

Table E43: Loading of CO_2-containing species in the system (EvA34 + H_2O + CO_2).

T	$\tilde{m}_{EvA}$	$\tilde{\alpha}_i$		
K	mol_{EvA}/kg_{H_2O}	mol_i/mol_{EvA}		
		β-carbamate	γ-carbamate	(bi)carbonate
373.15	0.373	0.00 ± 0.05	0.06 ± 0.05	0.23 ± 0.05
	0.373	0.00 ± 0.05	0.08 ± 0.05	0.53 ± 0.05
	0.373	0.00 ± 0.05	0.22 ± 0.05	1.14 ± 0.09
	0.371	0.00 ± 0.05	0.33 ± 0.05	1.23 ± 0.10

T: temperature with the expanded uncertainty $U(T) = 1$ K (0.99 level of confidence), $\tilde{m}_{EvA}$: molality of EvA with the relative expanded uncertainty $U_r(\tilde{m}_{EvA}) = 0.001$ (0.99 level of confidence), $\tilde{\alpha}_i$: concentration of CO_2-containing species with the intervals representing the standard uncertainty $u(\tilde{\alpha}_i)$. The pressure was not measured as it has no significant influence on the speciation of CO_2-containing species. Results between 293.15 K $\leq T \leq$ 373.15 K are given in Table E8.

Table E44: Loading of CO_2-containing species in the system (EvA36 + H_2O + CO_2).

T	$\tilde{m}_{EvA}$	$\tilde{\alpha}_i$		
K	mol_{EvA}/kg_{H_2O}	mol_i/mol_{EvA}		
		β-carbamate	γ-carbamate	(bi)carbonate
293.15	0.487	0.00 ± 0.03	0.22 ± 0.03	0.22 ± 0.03
	0.488	0.03 ± 0.03	0.31 ± 0.03	0.34 ± 0.03

Table E44: continued from previous page

T	$\tilde{m}_{\text{EvA}}$	$\tilde{\alpha}_i$		
K	$\text{mol}_{\text{EvA}}/\text{kg}_{\text{H}_2\text{O}}$			
		β-carbamate	γ-carbamate	(bi)carbonate
	0.487	0.03 ± 0.03	0.36 ± 0.03	0.44 ± 0.03
	0.488	0.03 ± 0.03	0.45 ± 0.03	0.47 ± 0.03
	0.487	0.05 ± 0.03	0.46 ± 0.03	0.77 ± 0.04
293.15	0.488	0.08 ± 0.03	0.43 ± 0.03	0.88 ± 0.04
	0.488	0.15 ± 0.03	0.29 ± 0.03	1.51 ± 0.08
	0.487	0.14 ± 0.03	0.23 ± 0.03	1.88 ± 0.09
	0.487	0.13 ± 0.03	0.21 ± 0.03	2.04 ± 0.10
	0.487	0.00 ± 0.03	0.20 ± 0.03	0.27 ± 0.03
	0.488	0.02 ± 0.03	0.30 ± 0.03	0.34 ± 0.03
313.15	0.488	0.03 ± 0.03	0.38 ± 0.03	0.47 ± 0.03
	0.487	0.05 ± 0.03	0.41 ± 0.03	0.79 ± 0.04
	0.488	0.04 ± 0.03	0.38 ± 0.03	0.87 ± 0.04
	0.488	0.11 ± 0.03	0.16 ± 0.03	1.87 ± 0.09
	0.487	0.00 ± 0.03	0.19 ± 0.03	0.24 ± 0.03
	0.488	0.01 ± 0.03	0.28 ± 0.03	0.35 ± 0.03
	0.487	0.02 ± 0.03	0.31 ± 0.03	0.43 ± 0.03
	0.488	0.02 ± 0.03	0.33 ± 0.03	0.47 ± 0.03
333.15	0.487	0.05 ± 0.03	0.34 ± 0.03	0.82 ± 0.04
	0.488	0.06 ± 0.03	0.30 ± 0.03	0.92 ± 0.05
	0.488	0.08 ± 0.03	0.20 ± 0.03	1.42 ± 0.07
	0.487	0.03 ± 0.03	0.11 ± 0.03	1.94 ± 0.10
	0.488	0.02 ± 0.03	0.09 ± 0.03	1.98 ± 0.10
	0.487	0.00 ± 0.05	0.18 ± 0.05	0.24 ± 0.05
	0.488	0.00 ± 0.05	0.24 ± 0.05	0.33 ± 0.05
353.15	0.487	0.00 ± 0.05	0.27 ± 0.05	0.47 ± 0.05
	0.488	0.00 ± 0.05	0.23 ± 0.05	1.06 ± 0.08
	0.488	0.00 ± 0.05	0.10 ± 0.05	1.67 ± 0.13
	0.488	0.00 ± 0.05	0.06 ± 0.05	1.84 ± 0.15
	0.488	0.00 ± 0.05	0.18 ± 0.05	0.36 ± 0.05
373.15	0.487	0.00 ± 0.05	0.19 ± 0.05	0.47 ± 0.05
	0.488	0.00 ± 0.05	0.17 ± 0.05	0.62 ± 0.05
	0.487	0.00 ± 0.05	0.08 ± 0.05	0.94 ± 0.08

T: temperature with the expanded uncertainty $U(T) = 1$ K (0.99 level of confidence), $\tilde{m}_{\text{EvA}}$: molality of EvA with the relative expanded uncertainty $U_r(\tilde{m}_{\text{EvA}}) = 0.001$ (0.99 level of confidence), $\tilde{\alpha}_i$: concentration of CO_2-containing species with the intervals representing the standard uncertainty $u(\tilde{\alpha}_i)$. The pressure was not measured as it has no significant influence on the speciation of CO_2-containing species.

Statement on Authorship

This thesis contains material that has been published previously. These publications are listed below. In all cases, the author of the present thesis developed the experimental setup, carried out or supervised the experiments, evaluated the results, and wrote the manuscript.

- E. Kessler, L. Ninni, B. Willy, R. Schneider, M. Irfan, J. Rolker, E. v. Harbou, H. Hasse: Structure-property relationships for new amines for reactive CO_2-absorption, Chem. Eng. Trans. 69 (2018) 109–114.
  DOI:10.3303/CET1869019.

- E. Kessler, L. Ninni, T. Breug-Nissen, B. Willy, R. Schneider, M. Irfan, J. Rolker, E. von Harbou, H. Hasse: Physico-chemical properties of the system n,n-dimethyl-dipropylene-diamino-triacetonediamine (EvA34), water, and carbon dioxide for reactive absorption, J. Chem. Eng. Data 64 (2019) 2368–2379.
  DOI:10.1021/acs.jced.8b01174.

- E. Kessler, L. Ninni, D. Vasiliu, A. Yazdani, B. Willy, R. Schneider, M. Irfan, J. Rolker, E. von Harbou, H. Hasse: Triacetone-amine derivatives (EvAs) for CO_2-absorption from process gases, Int. J. Greenhouse Gas Control 95 (2020) 102932.
  DOI:10.1016/j.ijggc.2019.102932.

- E. Kessler, L. Ninni, T. Breug-Nissen, B. Willy, R. Schneider, M. Irfan, J. Rolker, W. R. Thiel, E. v. Harbou, H. Hasse: Speciation in CO_2-loaded aqueous solutions of sixteen triacetoneamine-derivates (EvAs) and elucidation of structure-property relationships, Chem. Eng. Sci. 229 (2021) 115999.
  DOI:10.1016/j.ces.2020.115999.

- E. Kessler, L. Ninni, T. Breug-Nissen, B. Willy, R. Schneider, M. Irfan, E. von Harbou, H. Hasse: Thermodynamic properties of a system for CO_2-absorption with liquid-liquid phase split: Eva25 + H_2O + CO_2, Ind. Eng. Chem. Res. 61 (2022) 15289-15300
  DOI:10.1021/acs.iecr.2c02701.

Furthermore, the author contributed to the following publications that are relevant for this thesis and cited therein:

- D. Vasiliu, A. Yazdani, N. McCann, M. Irfan, R. Schneider, J. Rolker, G. Maurer, E. v. Harbou, H. Hasse: Thermodynamic study of a complex system for carbon

capture: Butyltriacetonediamine + water + carbon dioxide, J. Chem. Eng. Data 61 (2016) 3814–3826. DOI:10.1021/acs.jced.6b00451.

The author carried out and evaluated the NMR spectroscopic experiments.

- B. Willy, R. Schneider, J. Rolker, M. Neumann, R. Steglich, H. Hasse, E. von Harbou, E. Kessler, D. Vasiliu, L. Ninni Schäfer: Patent DE102016204929: Absorptionsmedium, Verfahren und Vorrichtung zur Absorption saurer Gase aus Gasmischungen, 2017

The author investigated the amines.

- R. Behrens, E. Kessler, K. Münnemann, H. Hasse, E. v. Harbou: Monoalkylcarbonate formation in the system monoethanolamine–water–carbon dioxide, Fluid Phase Equilib. 486 (2019) 98–105. DOI:10.1016/j.fluid.2018.12.031

The author carried out a part of the NMR spectroscopic experiments and provided the species elucidation.

- D. Vasiliu, E. Kessler, E. v. Harbou, H. Hasse: Short-cut method for assessing solvents for gas cleaning by reactive absorption, Chem. Eng. Res. & D. 153 (2020) 757–767. DOI:10.1016/j.cherd.2019.10.015.

The author contributed to the completion of the study and the manuscript.

Contributions and student reports

The following colleagues and students contributed to this thesis under the supervision of the author by providing the amines (Benjamin Willy), and by carrying out measurements (Luciana Ninni-Schäfer, Tanja Breug-Nissen, Rolf Schneider, Eva Maire, William Porter, Julia Fuhlbrück, Thomas Wolf, Sara Khorshid, Sylvia Neef, Jasmin Lanzer, Christian Wolfram, Meik Albrecht, Madeline Schmiedeknecht, Anastasia Startseva, Dominik Schäfer, Silvie Müller, Johannes Koch, Lisa Hitschler, Heloisa Almeida, Erik Ingendae, Regina Steinke, Annemarie Rätz, Artin Aminzadehvahedi, Christian Alzer, Jakob Leicht, Guilherme Joaquim). The following student reports were prepared under the supervision of the author in the context of the present thesis:

- E. Maire: Physico-chemical properties of aqueous solutions of amines for reactive absorption of carbon dioxide. Student research project, Laboratory of Engineering Thermodynamics (LTD), TU Kaiserslautern (2015).

- C. Wolfram: NMR spectroscopic study of the carbamate formation of an amine in carbon dioxde containing aqueous solutions. Master thesis, Institut für organische Chemie und chemische Biologie, Goethe Universitaet Frankfurt (2015).

- W. Porter: Investigation on the kinetics of carbamate formations in CO2 loaded aqueous amine solutions using pH-measurement and NMR spectroscopy. RISE research project, Laboratory of Engineering Thermodynamics (LTD), TU Kaiserslautern (2015).

- J. Koch: Screening of new amine-mixtures for the CO2 separation from synthetic gas using reactive absorption. Bachelor thesis, Laboratory of Engineering Thermodynamics (LTD), TU Kaiserslautern (2016).

- M. Albrecht: Planing, construction and commissioning of a laboratory absorber for measuring absorption rate. Student research project, Laboratory of Engineering Thermodynamics (LTD), TU Kaiserslautern (2017).

- J. Lanzer: NMR spectroscopic study of carbonate and carbamate formation of the amines EvA02, EvA03 and EvA07 in carbon dioxide-containing aqueous solutions. Student research project, Laboratory of Engineering Thermodynamics (LTD), TU Kaiserslautern (2017).

- E. Ingendae: NMR spectroscopic study of carbonate and carbamate formation of the amines EvA06, EvA31 and EvA36 in carbon dioxide-containing aqueous solutions. Student research project, Laboratory of Engineering Thermodynamics (LTD), TU Kaiserslautern (2017).

- A. Startseva: NMR spectroscopic study of carbonate and carbamate formation of the amines EvA24 in carbon dioxide-containing aqueous solutions. RISE research project, Laboratory of Engineering Thermodynamics (LTD), TU Kaiserslautern (2017).

- M. Schmiedeknecht: Development of a thermodynamic model of the chemical equilibrium in the system EvA25 and H_2O. RISE research project, Laboratory of Engineering Thermodynamics (LTD), TU Kaiserslautern (2017).

- C. Alzer: Development of a thermodynamic model of the vapor-liquid equilibrium in the system EvA34, H_2O, CO_2. Bachelor thesis, Laboratory of Engineering Thermodynamics (LTD), TU Kaiserslautern (2017).

- L. Hitschler: Commissioning of an apparatus for the investigation of multi-component liquid liquid equilibria using quantitative NMR spectroscopy. Master thesis, Laboratory of Engineering Thermodynamics (LTD), TU Kaiserslautern (2017).

Curriculum Vitae

Personal information

Name:	Elmar Kessler
Date of birth:	24.08.1986
Place of birth:	Reutlingen, Germany

Education

09/1997 – 07/2003	Johannes Kepler Gymnasium Reutlingen
	Degree: Mittlere Reife
09/2003 – 07/2006	Laura-Schradin-Schule Reutlingen
	Degree: Allgemeine Hochschulreife
09/2006 – 04/2010	Universität Stuttgart
	Course: Verfahrenstechnik
	Degree: B.Sc.
09/2009 – 10/2012	Universität Stuttgart
	Course: Verfahrenstechnik
	Degree: M.Sc.

Professional experience

01/2013 – 05/2014	Project Engineer at
	IBH Engineering GmbH, Ludwigshafen
06/2014 – 04/2019	PhD student at
	Laboratory of Engineering Thermodynamics (LTD)
	Technische Universität Kaiserslautern
	Prof. Dr.-Ing. Hans Hasse
01/2018 – 04/2018	Research stay at
	The University of Canterbury, Christchurch, New Zealand
	Dr. D. H. Holland
01/2020 – 04/2020	Project Engineer, Team Process Support at
	FUCHS Lubritech GmbH, Kaiserslautern
since 05/2020	Team leader Process Support at
	FUCHS Lubricants Germany GmbH, Kaiserslautern